ornl

OAK RIDGE NATIONAL LABORATORY

MARTIN MARIETTA

ORNL/Sub/89-SC674/1/V2

Life Prediction Methodology for Ceramic Components of Advanced Heat Engines
Phase 1

J. C. Cuccio, P. Brehm, H. T. Fang, J. Hartman, W. Meade, M. N. Menon, A. Peralta, J. Z. Song, T. Strangman, J. Wade, J. Wimmer, and D. C. Wu

CERAMIC TECHNOLOGY PROJECT

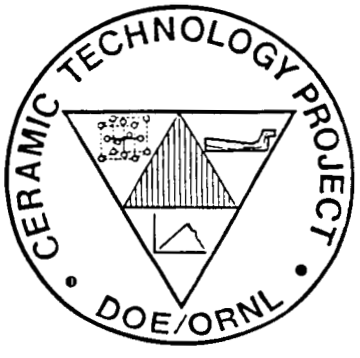

Prepared by AlliedSignal Engines
2739 E. Washington Street
Phoenix, Arizona

MANAGED BY
MARTIN MARIETTA ENERGY SYSTEMS, INC.
FOR THE UNITED STATES
DEPARTMENT OF ENERGY

DISCLAIMER

ORNL/Sub/89-SC674/1/V2

LIFE PREDICTION METHODOLOGY FOR CERAMIC COMPONENTS OF ADVANCED HEAT ENGINES

Phase 1

J. C. Cuccio, P. Brehm, H. T. Fang, J. Hartman,
W. Meade, M. N. Menon, A. Peralta, J. Z. Song,
T. Strangman, J. Wade, J. Wimmer, and D. C. Wu

Date Published: March 1995

VOLUME TWO - APPENDICES

Prepared by
AlliedSignal Engines
2739 E. Washington Street
Phoenix, Arizona
Subcontract No. 62X-SC674C

Funded by
Propulsion System Materials Program
Office of Transportation Technologies
the Assistant Secretary for
Energy Efficiency and Renewable Energy
U.S. Department of Energy
EE 51 05 00 0

for
OAK RIDGE NATIONAL LABORATORY
Oak Ridge, Tennessee 37831-6285
managed by
MARTIN MARIETTA ENERGY SYSTEMS, INC.
for the
U.S. DEPARTMENT OF ENERGY
under Contract DE-AC05-840R21400

AlliedSignal
AEROSPACE

LIFE PREDICTION METHODOLOGY FOR CERAMIC COMPONENTS OF ADVANCED HEAT ENGINES

PHASE I FINAL REPORT

Contract No. 86X-SC674C

VOLUME TWO APPENDICES

ABSTRACT

This document, the second of two volumes prepared by AlliedSignal Engines, Phoenix, Arizona, presents the Appendices for the Phase I Final Report for the Life Prediction Methodology for Ceramic Components of Advanced Heat Engines Program funded by the U.S. Dept. of Energy (DOE) and administered by the Oak Ridge National Laboratory under Contract No. 86X-SC674C, W.B.S. Element 3.2.2.3.

TABLE OF CONTENTS

Research sponsored by the U.S. Department of Energy, Assistant Secretary for Energy Efficiency and Renewable Energy, Office of Transportation Technologies, as part of the Ceramic Technology Project of the Propulsion System Materials Program, under contract DE-AC05-84OR21400 with Martin Marietta Energy Systems, Inc.

APPENDIX I

CERAMIC TEST SPECIMEN DRAWINGS AND SCHEMATICS

(7 pages)

NO.	REVISION	DATE
A	NOTE 5 LENGTH CHANGED FROM 45 TO 30	3/16/90

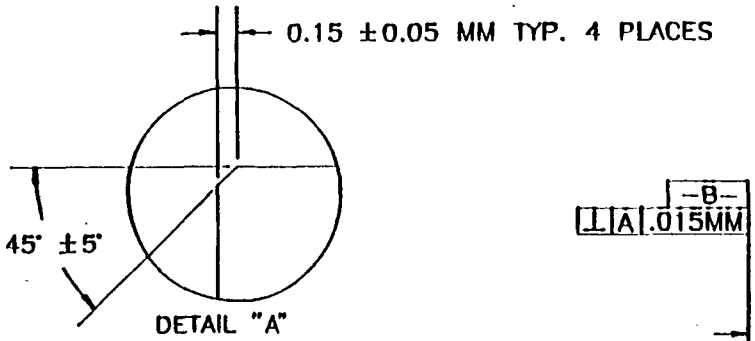

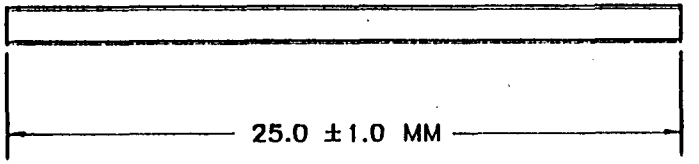

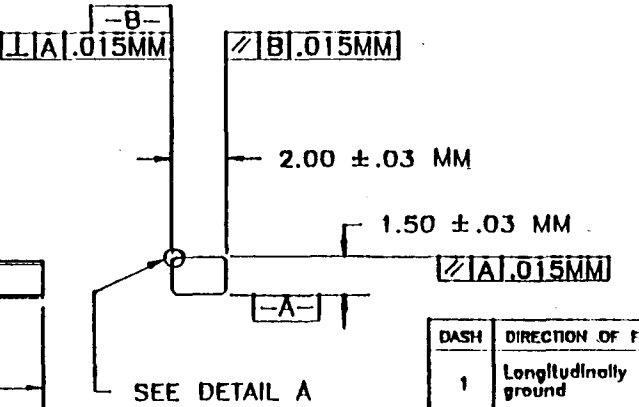

DASH	DIRECTION OF FINAL GRIND
1	Longitudinally ground
2	Transversely ground
3	45 degrees ground
4	As-processed surface

< NOTES >
1. LONGITUDINAL GRINDING REQUIRED ON ALL FACES AND CHAMFERS UNLESS OTHERWISE NOTED.
2. FINISH GRIND PER NTG-5060-01: 'FINISH SURFACE GRINDING SPECIFICATION FOR NT154'.
3. MAINTAIN TRACEABILITY TO PARENT TILE/BLANK ID
4. SURFACE FINISH SPECIFICATION: R <= 16 MICROINCHES.
5. LENGTH TOLERANCE OF 30.0 +1.0/ -0.0 IS ACCEPTABLE FOR SPECIFIC STOCK GEOMETRIES (PRIOR APPROVAL REQUIRED).

NORTON / TRW CERAMICS

TOLERENCES NOT OTHERWISE SPECIFIED X.XX = ±.020 X.XXX = ±.005 ANGLES = ±15' SURFACE FINISH 16/ DIMENSIONS ARE IN MILLIMETERS	DRAWN M.W.	DATE 12/30/89
	APPROVALS ENGINEERING: 3/16/90 QUALITY: EB 4/10/90 OPERATIONS MGR.: BJM 3/10/90 CUSTOMER: ACerniak 4/5/90	
MATERIAL: NT154 Si_3N_4		REF.DWG. #: PAP266101
TITLE: MIL-STD 1942 SIZE A FLEXURAL SPECIMEN		DWG #: NTG10004

GB11591-691

NO.	REVISION	DATE
A	UPDATE TITLEBLOCK	2/12/90
B	.03MM TOLERANCE TO .015MM	3/15/90

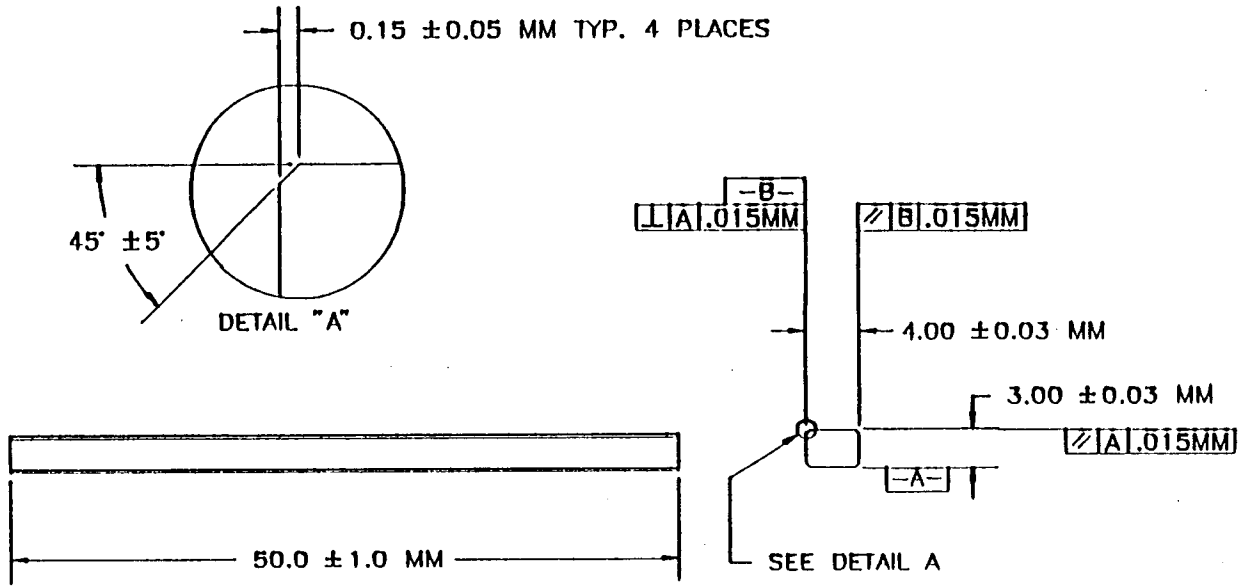

DASH	DIRECTION OF FINAL GRIND
1	Longitudinally ground
2	Transversely ground
3	45 degree ground
4	As-processed surface

< NOTES >

1. LONGITUDINAL GRINDING REQUIRED ON ALL FACES AND CHAMFERS UNLESS OTHERWISE NOTED.
2. FINISH GRIND PER NTG-5060-01: 'FINISH SURFACE GRINDING SPECIFICATION FOR NT154'.
3. MAINTAIN TRACEABILITY TO PARENT TILE/BLANK ID
4. SURFACE FINISH SPECIFICATION: R <= 16 MICROINCHES.
5. LENGTH TOLERANCE OF 45.0 +- 1.0-0.0 IS ACCEPTABLE FOR SPECIFIC STOCK GEOMETRIES (PRIOR APPROVAL REQUIRED).

NORTON / TRW CERAMICS

TOLERENCES NOT OTHERWISE SPECIFIED
X.XX = ±.020
X.XXX = ±.005
ANGLES = ±15°
SURFACE FINISH 16 √
DIMENSIONS ARE IN MILLIMETERS

DRAWN M.W. DATE 3/2/89

APPROVALS
ENGINEERING: [signature] 3/16/90
QUALITY: EB 4/10/90
OPERATIONS MGR.: BJTH 3/10/90
CUSTOMER: [signature] 4/3/90

MATERIAL: NT154 Si_3N_4
REF.DWG. #:

TITLE: MIL-STD 1942 SIZE B FLEXURAL SPECIMEN
DWG #: NTG10001

NO.	REVISION	DATE
A	4.0 ±.001 LENGTH TO 6.0 ±.005	3/16/90

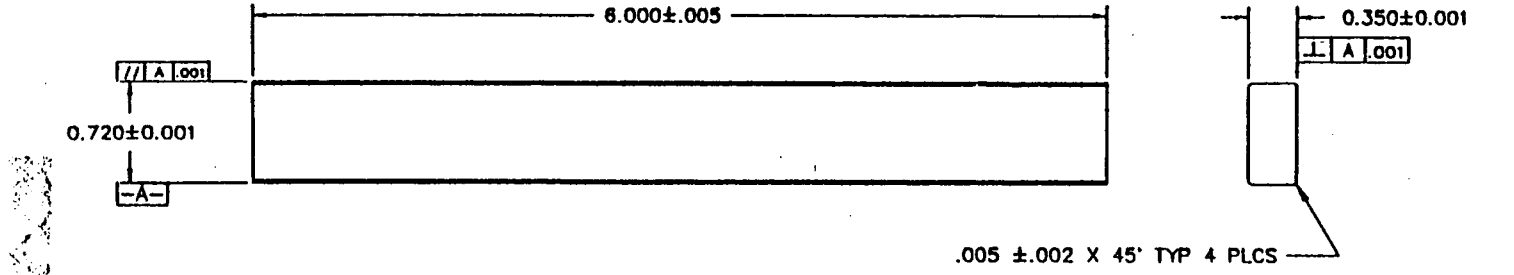

DASH	DIRECTION OF FINAL GRIND
1	Longitudinally ground
2	Transversely ground
3	45 degrees ground
4	As-processed surface

< NOTES >
1. LONGITUDINAL GRINDING REQUIRED ON ALL FACES AND CHAMFERS UNLESS OTHERWISE NOTED.
2. FINISH GRIND PER NTG-5060-01: 'FINISH SURFACE GRINDING SPECIFICATION FOR NT154'.
3. MAINTAIN TRACEABILITY TO PARENT TILE/BLANK ID
4. SURFACE FINISH SPECIFICATION: R <= 16 MICROINCHES.

NORTON / TRW CERAMICS

TOLERENCES NOT OTHERWISE SPECIFIED X.XX = ±.020 X.XXX = ±.005 ANGLES = ±15' DIMENSIONS ARE IN INCHES	DRAWN MW	DATE 2/13/90
	APPROVALS ENGINEERING: APP 4/17/90 QUALITY: EB 4/18/90 OPERATIONS MGR.: [illegible] 4/18/90 CUSTOMER: AC Contract 4/24/90	
MATERIAL: NT154 Si_3N_4		REF.DWG. #: PAP267054
TITLE: FLEXURAL SPECIMEN - SIZE E		DWG #: NTG-10005

GB11591-693

NO.	REVISION	DATE
A	.2169 GAGE ø TO .2504, R.124 TO .121	3/16/90
B	R.1210/.1190 TO R .1230/.1170	4/13/90

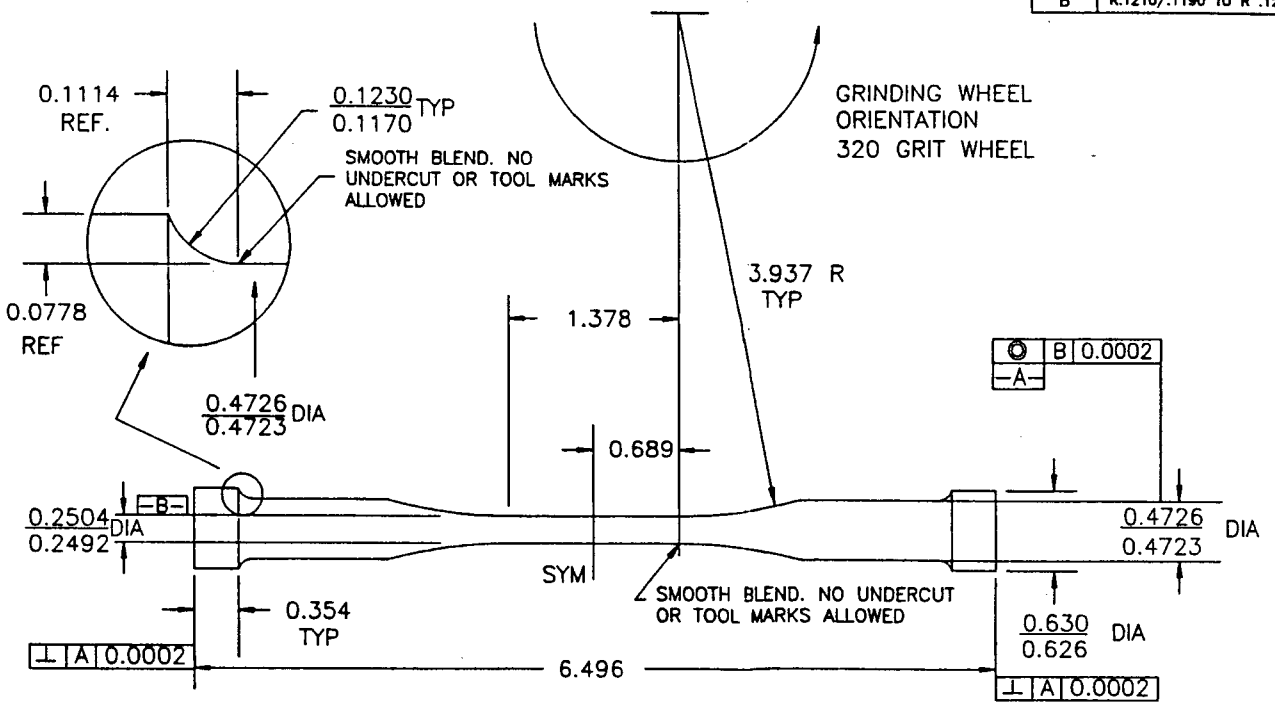

< NOTES >

1. SURFACE FINISH 16 ALL OVER EXCEPT .630ø AND ENDS WHICH CAN BE 32 .
2. FINISH GRIND PER NTG-5060-01:
   'FINISH SURFACE GRINDING SPECIFICATION FOR NT154'.
3. MAINTAIN TRACEABILITY TO PARENT TILE/BLANK ID
4. WET GRINDING REQUIRED IN FINISH GRINDING BUTTON HD RADIUS.

NORTON / TRW CERAMICS		
TOLERENCES NOT OTHERWISE SPECIFIED X.XX = ±.020 X.XXX = ±.005 ANGLES = ±15' DIMENSIONS ARE IN INCHES	DRAWN MW	DATE 3/2/89
	APPROVALS ENGINEERING: QPS 4/18/90 QUALITY: EB 4/18/90 OPERATIONS MGR.: BJM 4/18/90 CUSTOMER: A Contant 4/24/90	
MATERIAL: NT154 Si_3N_4		REF.DWG. #: PAP266126
TITLE: CYLINDRICAL BUTTON HEAD SPECIMEN		DWG #: NTG10002

GB11591-694

NO.	REVISION	DATE

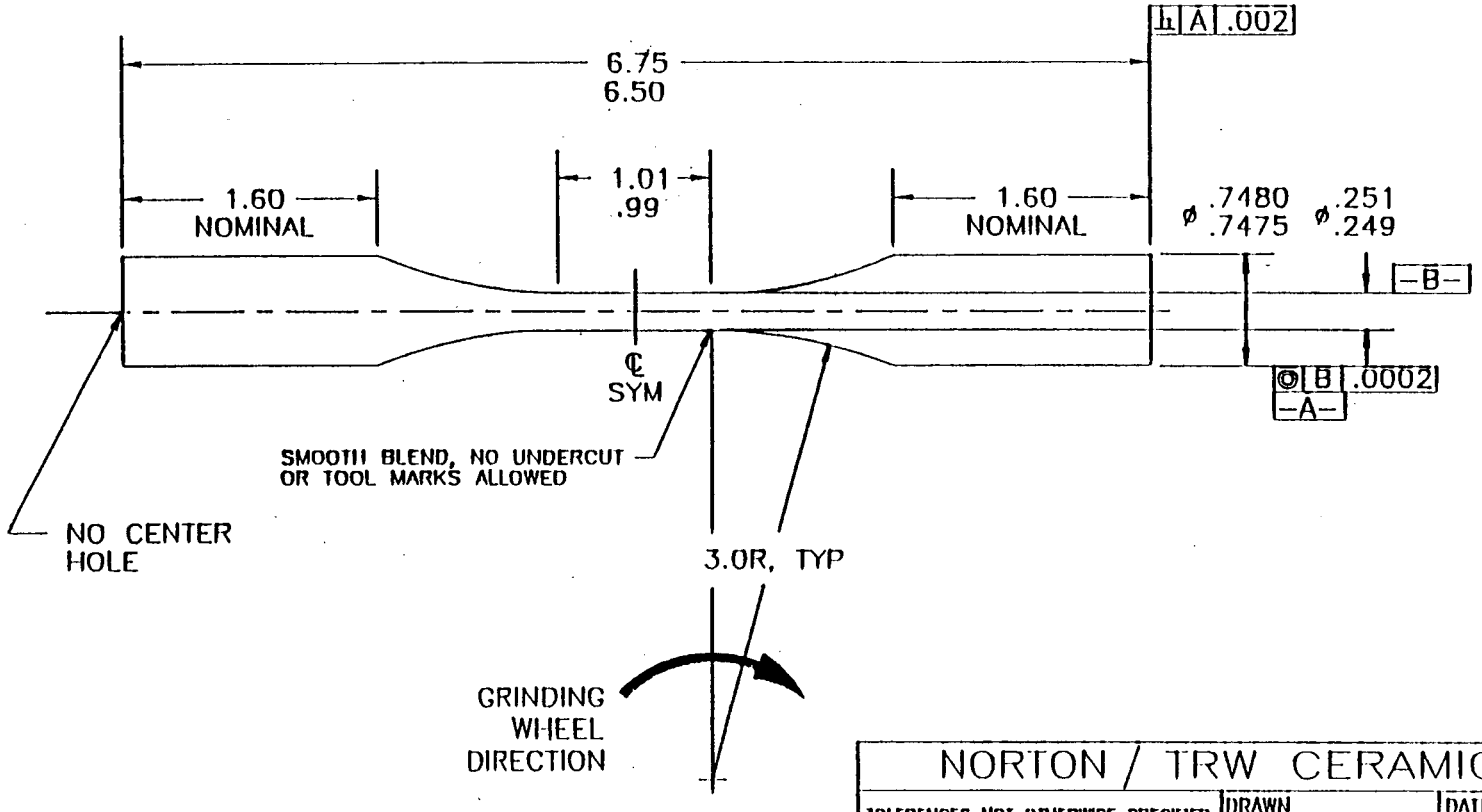

< NOTES >

1. FINISH GRIND PER NTG-5060-01:
   'FINISH SURFACE GRINDING SPECIFICATION FOR NT154'.
2. MAINTAIN TRACEABILITY TO PARENT TILE/BLANK ID.
3. SURFACE FINISH SPECIFICATION: R<=16 MICROINCHES.

NORTON / TRW CERAMICS		
TOLERENCES NOT OTHERWISE SPECIFIED X.XX = ±.020 X.XXX = ±.005 ANGLES = ±15' SURFACE FINISH 16 √ DIMENSIONS ARE IN INCHES	DRAWN L.D.LYNCH	DATE 2/21/90
	APPROVALS ENGINEERING: amg 2/21/90 QUALITY: EB 2/23/90 OPERATIONS MGR.: BJ ML 2/20/90 CUSTOMER: Accepted 3/5/90	
MATERIAL: NT154 Si_3N_4		REF.DWG. #: PAP268779
TITLE: TENSION / TORSION SPECIMEN		DWG #: NTG10011

GB11591-695

NO.	REVISION	DATE
A	R.046 ±.005 TO .100 ±.010; ADD NOTE 9	4/18/90
	ADD .10 ±.01 LENGTH TO SHAFT TIP	

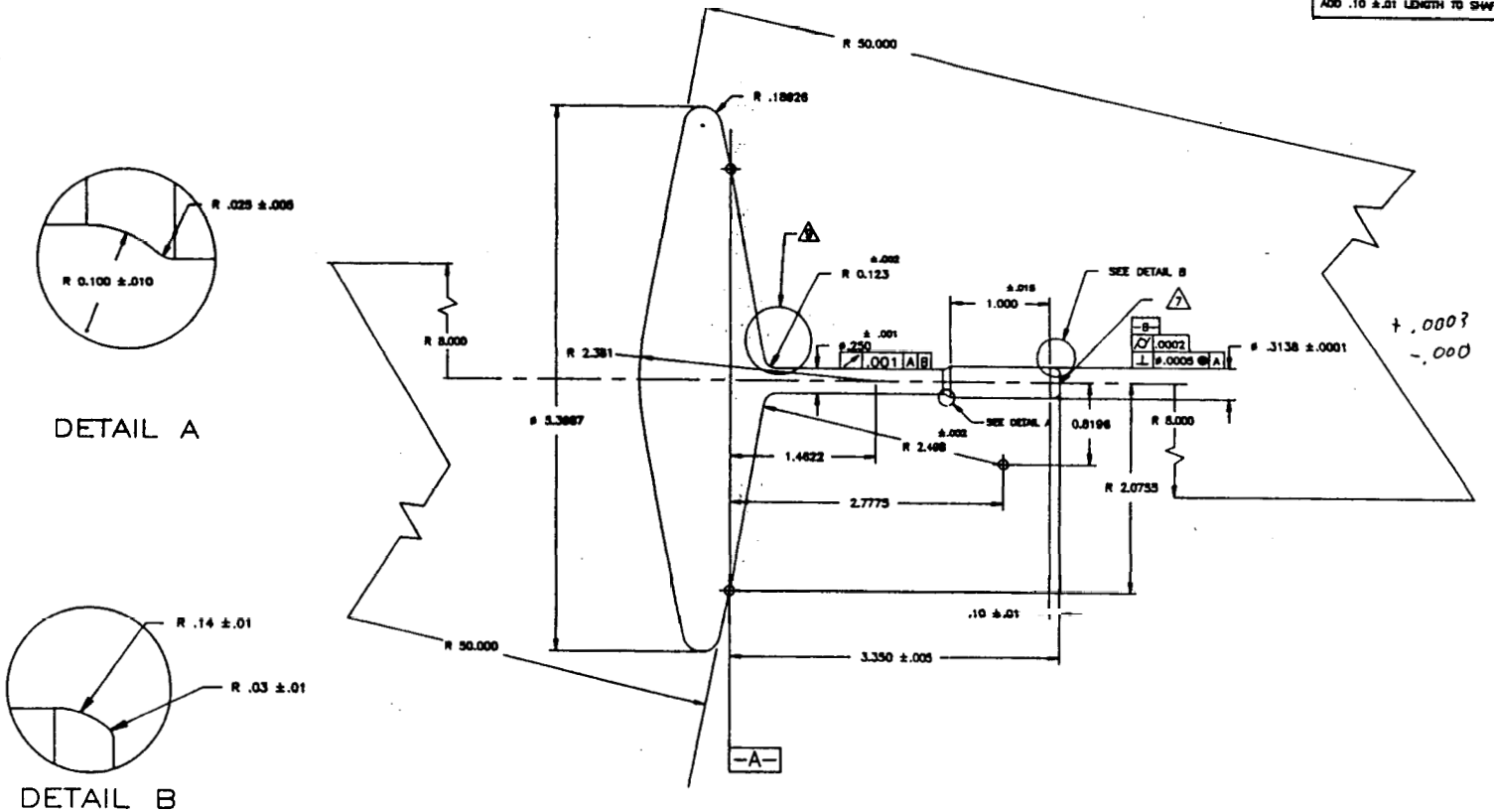

NOTES:

1. DRAWING INTERPRETATION PER SC6500
2. LOT CONTROL TO BE ESTABLISHED FOR THIS PART. SERIALIZATION TO BE APPLIED STARTING WITH RAW MAT'L.
3. UNTOLERANCED DIMENSIONS ARE BASIC.
4. ALL SURFACES DEFINED BY BASIC DIMENSIONS SHALL LIE W/IN A PROFILE TOLERANCE ZONE OF .006 REL TO DATUMS A & B.
5. MEASURE DENSITY PER ASTM C373.
6. MARK PART NO., LOT NO. AND SERIAL NO. PER MC5014 CLASS VI OR VIIIB.
7. MARK SERIAL NO. PER MC5014 CLASS XIVB, ZONE E3.
8. SIMILAR TO PA3613559.
9. SMOOTH BLEND. NO UNDERCUTS OR TOOL MARKS ALLOWED.

NORTON / TRW CERAMICS		
TOLERENCES NOT OTHERWISE SPECIFIED X.XX = ±.020 X.XXX = ±.005 ANGLES = ±15' SURFACE FINISH 16/ DIMENSIONS ARE IN INCHES	DRAWN LDL	DATE 3/14/90
	APPROVALS ENGINEERING: QP 4/17/90 QUALITY: EB 4/18/90 OPERATIONS MGR.: BTM 4/18/90 CUSTOMER: AComfort 4/24/90	
MATERIAL: NT154 Si_3N_4	REF.DWG. #: R45304	
TITLE: CERAMIC SPIN DISK	DWG #: NTG10041	

LTR	REVISION	DATE

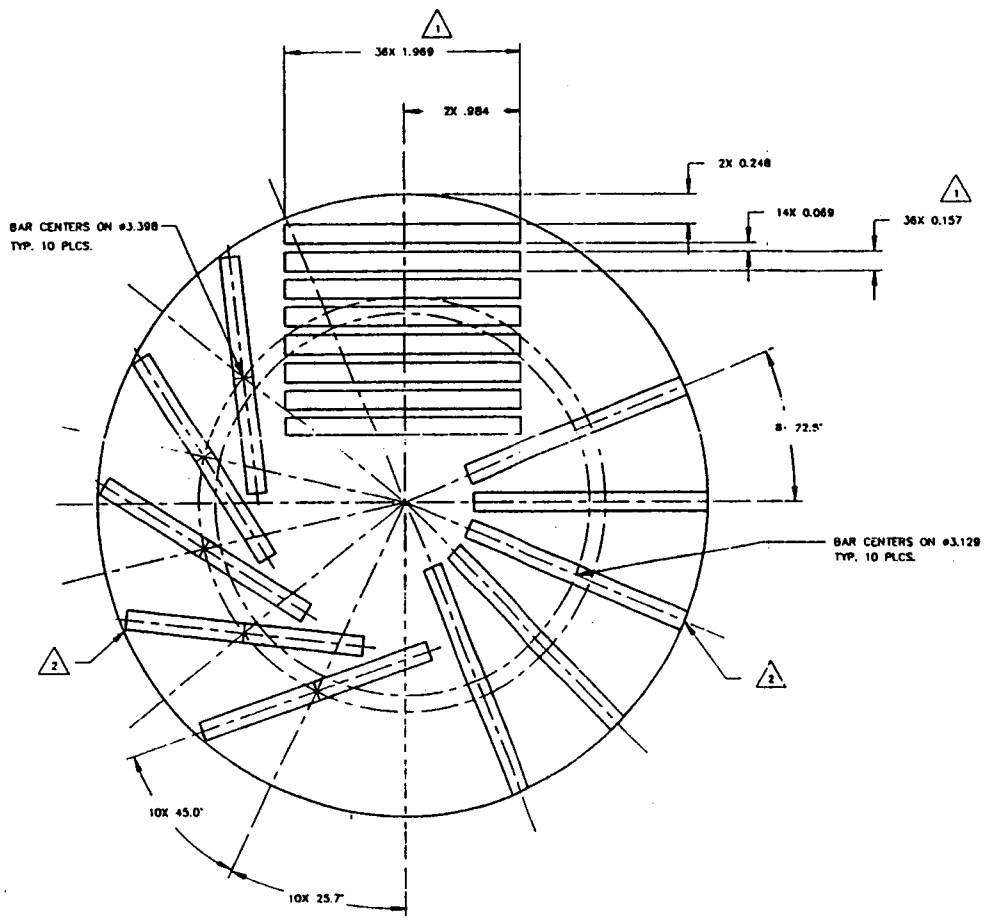

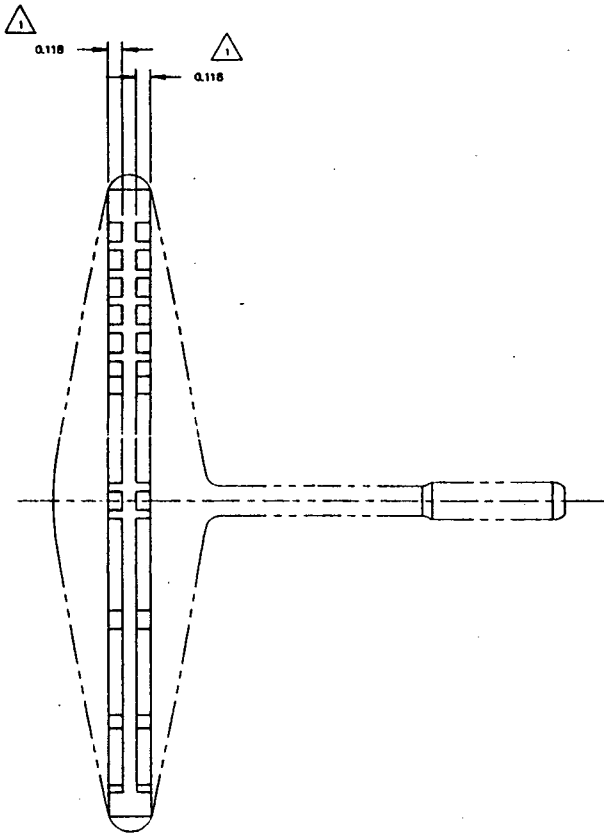

4. TRACEABILITY OF BARS WITH RESPECT TO ORIENTATION SHOWN IS REQUIRED.
5. MARK SURFACE OF EACH BAR THAT CORRESPONDS TO ORIGINAL DISK SURFACE.

△2 SLIGHT CORNER BREAK (.015 MAX.) ALLOWED.

△1 MOR BAR DIMENSIONS ARE PER DRAWING NTG10001 REV. 0. EIGHTEEN MIL. STD. 1942 B BARS ARE TO BE CUT FROM EACH SIDE OF DISK

AUTHORIZED COPY
No. ____

NORTON TRW

TOLERANCES NOT OTHERWISE SPECIFIED X.XX = ±.020 X.XXX = ±.005 ANGLES = ±15' DIMENSIONS ARE IN INCHES	DRAWN JES DATE 2/4/92 APPROVALS ENGINEERING: 2/25/92 MANUFACTURING: QUALITY: 2/25/92 TECH. DIRECTOR: 2/28/92 CUSTOMER:
MATERIAL: NT154 Si_3N_4	REF.DWG. #: NTG10001 REV. D
TITLE: SPIN DISK-MOR BAR PLACEMENT	DWG #: NTG10211

APPENDIX II

STUDIES OF MIXED-MODE AND BIAXIAL STRESS FRACTURE OF STRUCTURAL CERAMICS FOR ADVANCED VEHICULAR HEAT ENGINES

(UNIVERSITY OF UTAH REPORT)
(41 pages)

STUDIES OF MIXED-MODE AND BIAXIAL STRESS FRACTURE OF STRUCTURAL CERAMICS FOR ADVANCED VEHICULAR HEAT ENGINES

Final Report
(P.O.# 1721709)

March 1993

by

Dr. Dinesh K. Shetty
and
Dr. Luen-Yuan Chao
Department of Materials Science and Engineering
University of Utah
Salt Lake City, UT 84112

Prepared for
Allied-Signal Aerospace Company
Garrett Auxiliary Power Division
2739 East Washington Street
Phoenix, AZ 85010

ABSTRACT

Results obtained in a project entitled, " Studies of Mixed-Mode and Biaxial Fracture of Structural Ceramics for Advanced Vehicular Heat Engines", are discussed in this report. The report covers the results of two research tasks :

(A) Measurements of the combined mode I and mode II fracture toughness of a silicon nitride ceramic at room and elevated temperatures.

(B) Measurements of the fracture stresses of the silicon nitride ceramic in biaxial flexure at room temperature.

In Task A, chevron-notched-precracked silicon nitride disk specimens were tested in diametral compression with different orientatons of the notch line with respect to the loading diameter to produce different combinations of K_I and K_{II}. Tests were performed at room temperature and two elevated temperatures, 2200 ^oF and 2500 ^oF. Mixed-mode fracture toughness data could be adequately described by a commonly used empirical equation with an empirical parameter C representing the shear sensitivity. Results indicated that the shear sensitivity increased with increasing temperature. Also, slow-crack growth was detected at high temperatures.

In Task B, disk specimens were tested in biaxial flexure using uniform-pressure-on-disk tests. Fracture stresses were described by a two-parameter Weibull distribution function. The Weibull modulus (m) and characteristic strength (σ_θ) were estimated to be 10.41 and 785.2 MPa, respectively. The analysis of the biaxial flexure data using a multiaxial reliability analysis was deferred to a future date when GAPD will supply the relevant uniaxial strength data.

TABLE OF CONTENTS

I. INTRODUCTION

Martin Marietta Energy Systems, Inc., which operates Oak Ridge National Laboratory (ORNL) under contract with the Department of Energy (DOE), initiated a research project entitled, " Life Prediction Methodology for Ceramic Components of Advanced Vehicular Heat Engines ", with Garrett Auxiliary Power Division (GAPD) of Allied Signal Aerospace Company as the prime contractor. University of Utah participated in this project as a subcontractor to GAPD. The objectives of the research at University of Utah were to (A) measure the combined mode I and mode II fracture toughness at room and elevated temperatures of a candidate structural ceramic, silicon nitride†, and (B) to measure fracture stresses of the same ceramic in biaxial flexure and assess the applicability of the multiaxial reliability analysis procedure. This report describes the results of the two tasks.

II. STATEMENT OF WORK

Task A. Combined Mode I and Mode II Fracture Toughness Measurements

Fracture toughness of silicon nitride under combined mode I and mode II loading was assessed using chevron-notched disk specimens in diametral compression loading as described by Shetty et al.[1,2]. Eighty (80) disk specimens were supplied by GAPD for this task. The nominal dimensions of the as-received specimens were 31.85 mm in diameter and 3.175 mm in thickness. Specimens were chevron-notched in the center and several techniques for precracking the chevron-notched disk specimens prior to testing were investigated. These are described in the following.

Task A.1 Machining of the Chevron Notches in the Disk Specimens

A symmetrical chevron notch was machined in the center of the disk specimen using diamond-grit blades. The machining was done by an outside vendor§. Specific machining instructions were supplied to the vendor by the University of Utah. Geometry of the chevron-notched disk specimens is shown in the schematic of Figure 1. In Fig. 1, R is the disk radius and a_1 is half of the notch length measured on the surface. The normalized notch length, a_1/R (= α_1), was designed to be 0.4.

---

† Grade NT-154, Norton/TRW Ceramics, Northboro, MA.

§ Quality Magnetic Corp., Compton, CA.

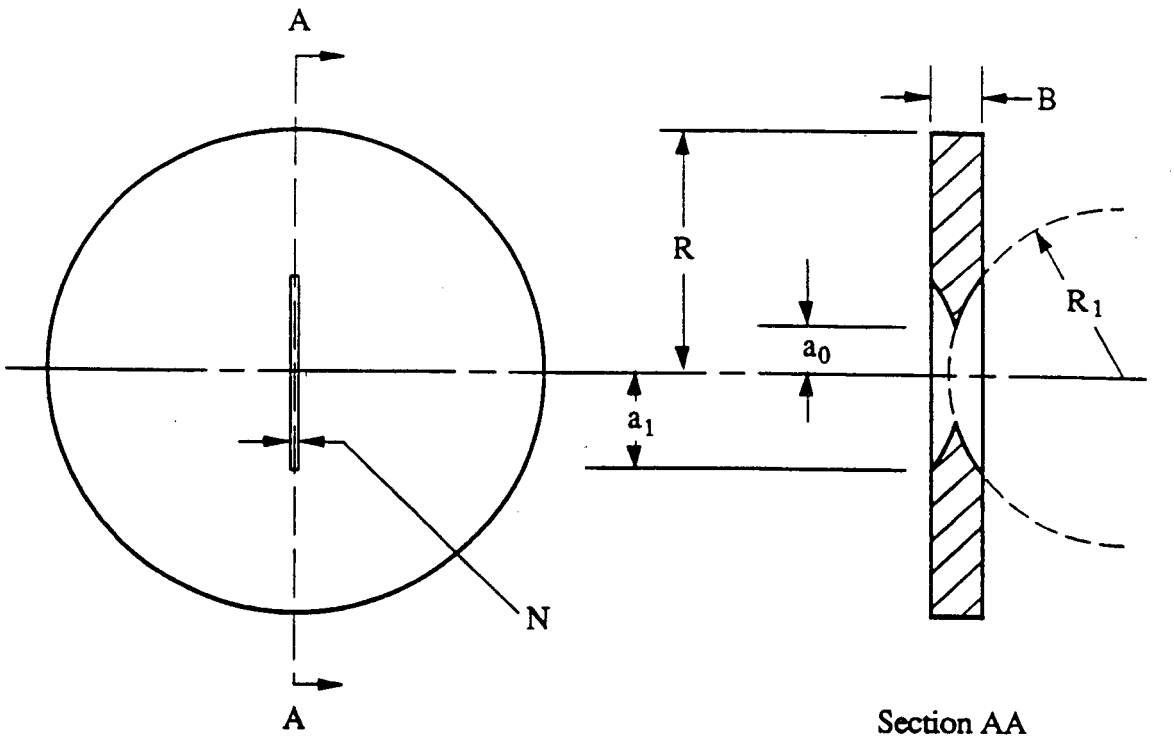

GB11591-698

Figure 1. Geometry of the Chevron-Notched Disk Specimens Used in Combined Mode I and Mode II Fracture Toughness Tests.

Task A.2 Development of Precracking Techniques for Chevron-Notched Disk Specimens

A.2-1. Theoretical Considerations:

The fracture mechanics analysis used to investigate precracking techniques starts with Irwin's relation between elastic strain energy release rate, G, and the rate of change of compliance of a cracked specimen:

$$G = \frac{P^2}{2}\frac{dC}{dA} \qquad (1)$$

where P is the load on the specimen, C is the compliance and dA is an incremental area caused by crack extension. Eq. 1 can be rewritten in terms of stress intensity factor, K_I, as :

$$K_I = P\left[\frac{E}{2(1-\nu^2)}\frac{dC}{dA}\right]^{1/2} \qquad (2)$$

where E is elastic modulus and ν is Poisson's ratio.

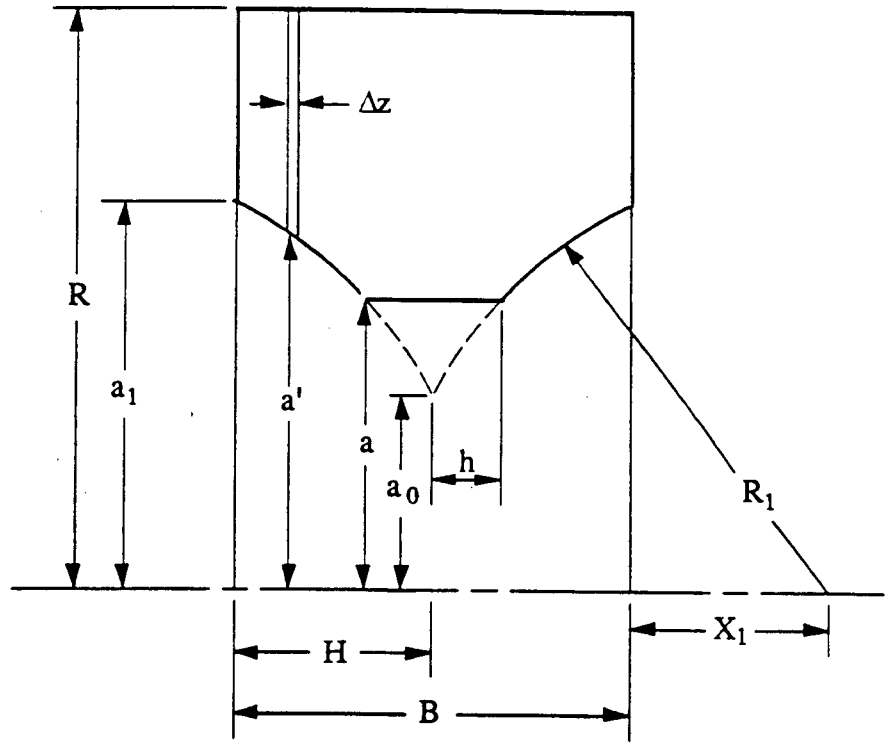

GB11591-699

Figure 2. Nomenclature of the Chevron Notch Cross-Section.

Because of the curvature of the diamond-grit blade, the chevron notch has a curved boundary. Figure 2 shows an enlarged cross-section of the chevron notch. For the curved chevron notch , the following equation is applicable :

$$(X_1 + \frac{B}{2} - h)^2 = R_1^2 - a^2 \qquad (3)$$

where a is half the crack length and the other dimensions (B, X_1, h) are indicated in Fig. 2. Equation 3 can be rearranged to write an expression for h,

$$h = X_1 + \frac{B}{2} - (R_1^2 - a^2)^{1/2} \qquad (4)$$

and for a small incremental crack extension da, the incremental area, dA, is

$$dA = 4\,h\,da \qquad (5)$$

Substitution of Eqs. 4 and 5 into Eq. 2 gives the following equation,

$$K_I = P \left[\frac{E}{2(1-\nu^2)} \frac{1}{4[X_1 + \frac{B}{2} - (R_1^2 - a^2)^{1/2}]} \frac{dC}{da} \right]^{1/2} \quad (6)$$

In analyzing chevron-notched specimens, it is commonly assumed that the rate of change of compliance (dC/da) is equal to that of a straight-through crack of the same crack length[5,6], i.e.,

$$\left(\frac{dC}{da}\right)_{CV} = \left(\frac{dC}{da}\right)_{STC} \quad (7)$$

This assumption, referred to as the straight-through-crack assumption (STCA), enables one to relate stress-intensity factor for a chevron-notched specimen to that of a straight-through-cracked specimen of otherwise similar geometry.

Stress-intensity factor solutions for straight-through cracks in diametral compression specimens have been reported by Atkinson and co-workers[7]. For a central through-crack of length 2a in a disk specimen loaded in compression, the mode I stress intensity factor is given as:

$$K_I = \frac{P}{\pi R B} (\pi a)^{1/2} N_I \quad (8)$$

where N_I is a nondimensional mode I stress-intensity factor that accounts for the effects of stress gradient. For the crack aligned in the plane of loading, i.e., pure mode I condition, N_I is a function of only the normalized crack size, $\alpha = a/R$. Atkinson et al.[7] reported numerical values for N_I for α ranging from 0.1 to 0.6. Shetty et al.[1] developed the following cubic polynomial fit to the numerical results of Atkinson et al.:

$$N_I = 0.991 + 0.141\,\alpha + 0.863\,\alpha^2 + 0.886\,\alpha^3 \quad (9)$$

The differences between the polynomial fit of Eq. 9 and the values given by Atkinson et al. are less than 0.1%.

From Eqs. 2 and 8, the rate of change of compliance for the straight-through-cracked specimen can be written as

$$\left(\frac{dC}{da}\right)_{STC} = \frac{4(1-\nu^2)}{\pi R B E}\,\alpha\,[N_I(\alpha)]^2 \qquad (10)$$

By employing the straight-through-crack assumption, i.e., substituting Eq. 10 into Eq. 6, an expression of the stress-intensity factor for the chevron-notched diametral compression specimen can be obtained :

$$K_I = \frac{PN_I}{B}\left(\frac{\alpha}{\pi R}\right)^{1/2}\left[\frac{1}{2\left[\frac{X_1}{B} + \frac{1}{2} - \frac{1}{B}(R_1^2 - R^2\alpha^2)^{1/2}\right]}\right]^{1/2} \qquad (11)$$

It should be noted that Eq. 11 is applicable only when the crack front is within the chevron notch section, i.e., $a_0 < a < a_1$. When $a > a_1$ the specimen has a straight-through crack and Eq. 8 should be applied.

Figure 3 shows a plot of load (P) vs. the normalized crack length (α) calculated using Eq. 11 and Eq. 8 based on an assumed value of K_{IC} (= 4.9 MPa$\sqrt{m}$). Note that stable crack growth occurs within the chevron notch section, i.e. the load increases with increasing crack length as described by Eq. 11. The crack becomes unstable when α reaches α_1 (0.4 in this case); for crack lengths, $\alpha > \alpha_1$, the dependence of critical load on crack length is governed by Eq. 8.

A.2-2. Precracking Experiments

Four techniques for precracking the chevron-notched silicon nitride disk specimens were investigated: (1) subcritical crack growth under constant load, (2) fatigue crack growth under cyclic compression loading, (3) wedge loading and (4) static loading and grinding. The technical approaches and the results of the four techniques are described in the following paragraphs.

Subcritical Crack Growth under Constant Load: In this technique, subcritical crack growth of ceramics was used to generate precracks. The fracture load (P_f) of a disk specimen was estimated prior to the test using Eq. 11 where the normalized crack length, α, took the specific value of a_1/R. The disk specimen was loaded in mode I condition to 80 ~ 90% of the estimated fracture load in deionized water at room temperature. The water environment was used to promote subcritical crack growth. The subcritical-crack-growth was

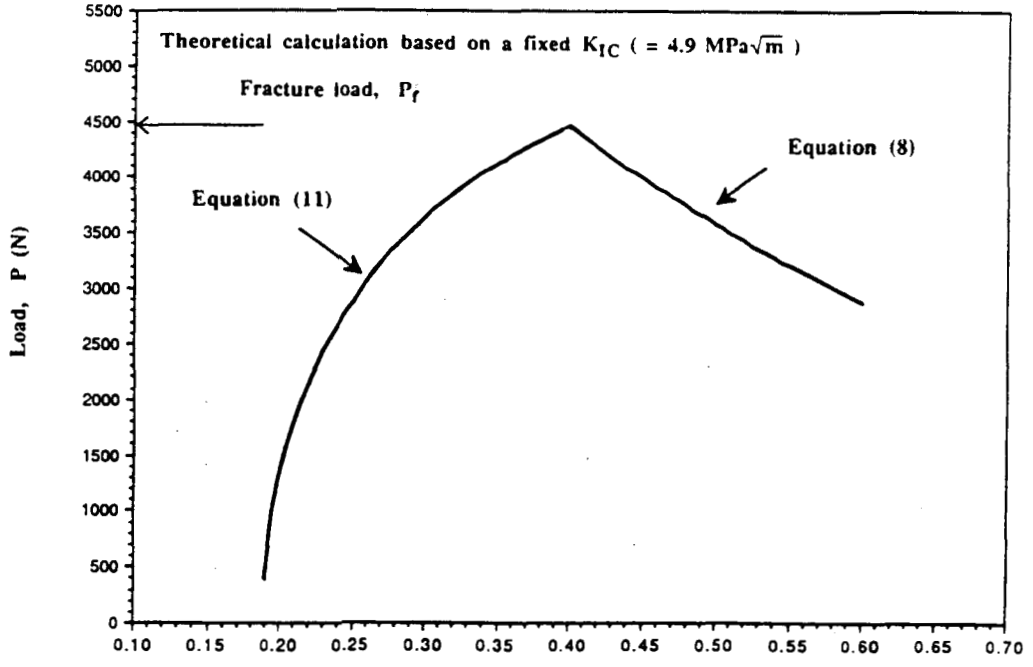

GB11591-700

Figure 3. Theoretical Relation between Load (P) and Crack Length (α) for a Chevron-Notched Diametral Compression Disk Specimen.

monitored using electrical resistance grids deposited on the specimen surface at the notch tip[3,4]. As the crack cut the grid lines it changed the resistance of the grid and caused step changes in the voltage output. The experiment was conducted in such a way that as soon as the precrack was detected on the voltage output, the specimen was unloaded. Precracking using this technique was investigated on a commercial grade alumina ceramic§ and the silicon nitride (NT-154). The technique was successful with the alumina ceramic. Figure 4 shows the SEM micrograph of the precrack obtained in the alumina specimen. The technique was, however, not successful with the silicon nitride[8]. Three disk specimens of the silicon nitride were tested assuming a fracture toughness of 5.0 MPa$\sqrt{m}$ [9] to estimate the fracture loads from Eq. 11. Possibly because of the small range of stress intensity over which subcritical crack growth occurred in the silicon nitride, it was difficult to unload the specimen in time as soon as a step change was observed on the voltage output. This resulted in rapid fracture of the specimens.

§ Grade AD-94, Coors Ceramics, Norman, OK.

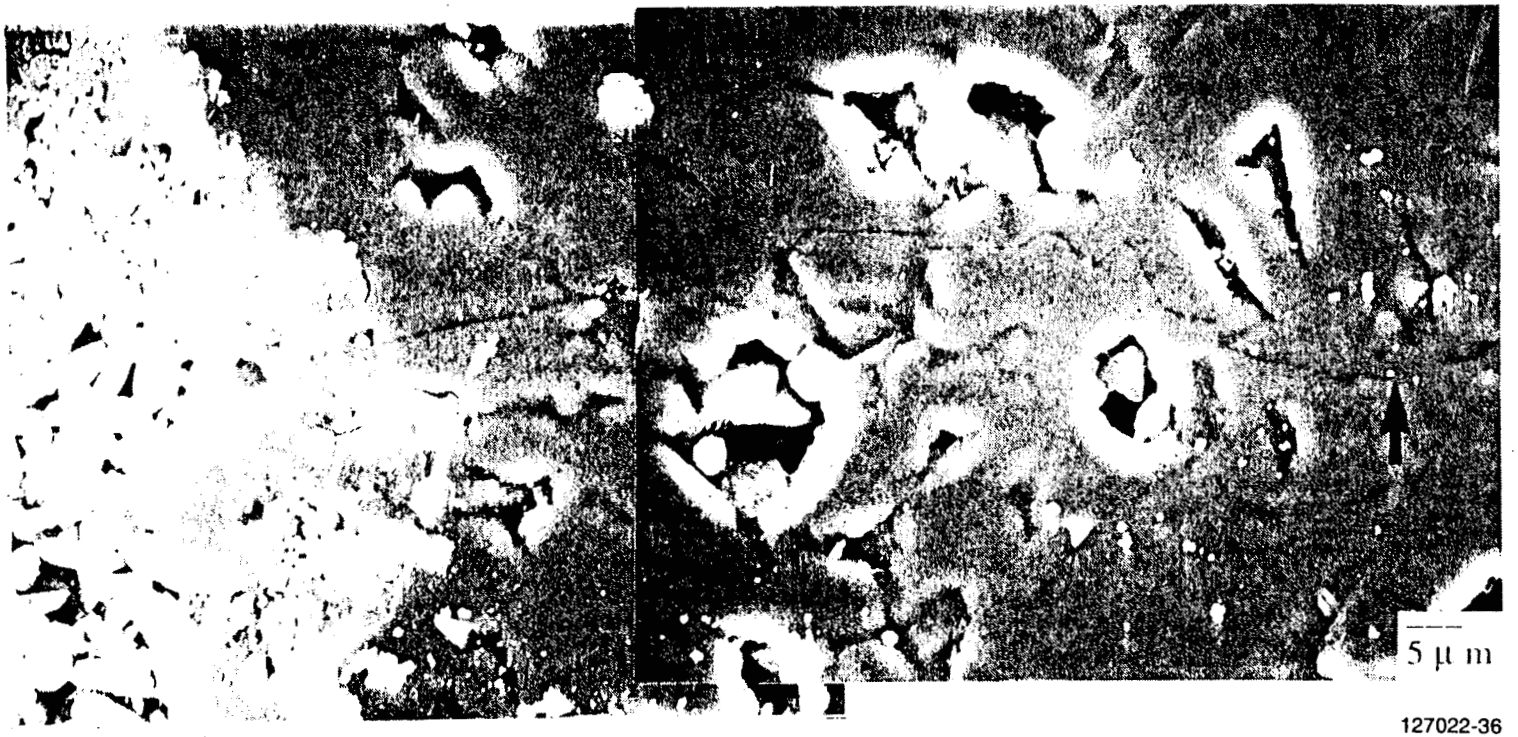

Figure 4. Precrack Obtained in Alumina (Coors, AD-94) Ceramic Using Subcritical Crack Growth under Constant Load.

Fatigue Crack Growth under Cyclic Compression Loading: Cyclic compression loading as a method of fatigue precracking chevron-notched disk specimens was investigated first on the alumina ceramic then the silicon nitride (NT-154). The disk specimen was initially loaded in pure mode I to a maximum load, $P_{max} = 0.98 \sim 0.99\ P_f$ where P_f was the anticipated fracture load based on Eq. 11, in order to generate sharp cracks in the chevron notches. The specimen was then subjected to cyclic diametral compression (mode I) loading using a servohydraulic machine and the following test conditions: sinusoidal load cycling at 20 Hz, R ratio (ratio of the minimum load to the maximum load in each cycle) = 0.1. A peak load of $P_{max} = 0.5\ P_f$ was selected for the first 100,000 cycles. After this, the peak load was increased by 5% of P_f after every 100,000 cycles. The precrack was monitored by a travelling microscope attached to the test machine. This technique was successful for the alumina ceramic[8]. A crack could be seen outside the notch tip when the peak load was 55% of P_f for 80,000 cycles. Figure 5 shows an optical micrograph of the notch and the precrack in an alumina specimen where the arrow points to the crack tip. For the silicon nitride (NT-154), no stable precracks outside the notch region could be established even after increasing the peak load to $P_{max} = 0.65\ P_f$ for 100,000 cycles. The specimen was further loaded to 67.5% of P_f where the specimen broke instantly after 98,850 cycles. This technique was, therefore, considered not applicable to silicon nitride.

In addition to this mode I fatigue precracking, two silicon nitride disk specimens with straight through notches were subjected to cyclic compression along a diameter normal to the notch. The objective of this experiment was to see if the cyclic compression loading technique for precracking edge-notched beam specimens developed by Suresh and Brockenbrough[10] could be applied to the disk specimens. Specimens were slightly ground at the two loading points initially in order to distribute the compression load. Results indicated that both specimens developed damage and cracks at the loading points without showing precracks outside the notch.

Wedge Loading: Wedge loading as a method of precracking chevron-notched disk specimen was investigated. The specimen was initially loaded in mode I condition to 95% of its fracture load. A tungsten carbide wedge was then inserted into the center of the notch perpendicular to the surface of the specimen. The wedge was lubricated with mineral oil and forced into the notch at a rate of 0.01 mm/min (0.0004 inch/min). This technique was abandoned because of its lack of control over both the extent of crack growth as well as the orientation of the cracks. Specifically, cracks were found to initiate and extend at an angle to the initial notch and the precrack orientation could not be controlled.

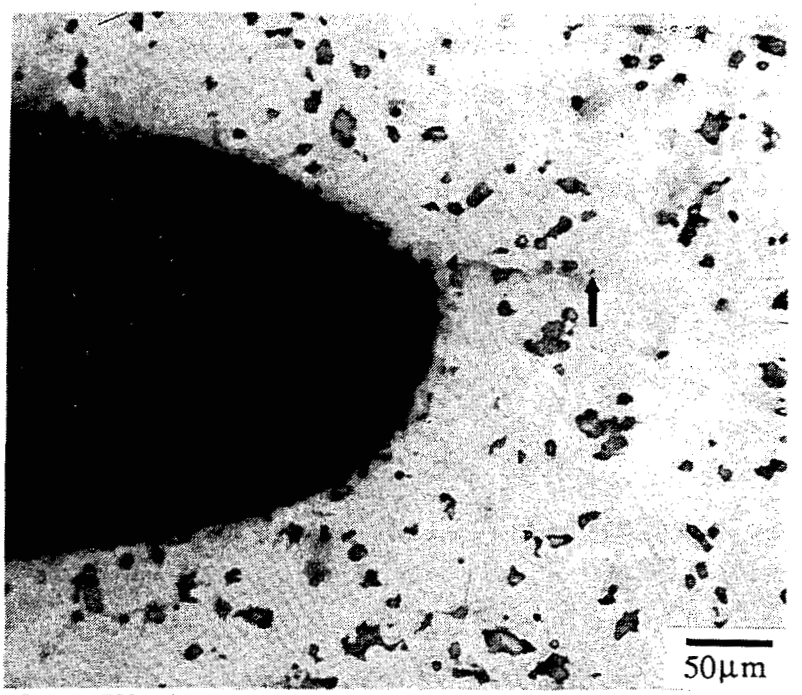

Figure 5. Stable Crack Outside the Notch in a Diametral Compression Disk Specimen of Alumina (Coors, AD-94) Produced by the Cyclic Compression Loading Technique.

Static Loading and Grinding: In this technique, the specimen was preloaded in two steps. In the first step, the specimen was loaded in mode I to about 4 kN (which is ~ 85% of the fracture load for the silicon nitride) using a crosshead speed of 0.05 mm/min. The objective of this loading was to initiate a sharp crack in the notch. In the second step, the specimen was turned upside down and again loaded in mode I to a peak load close to the fracture load (> 95% of the fracture load). The crosshead speed used in this step was 0.004 mm/min. The reason for turning the specimen upside down was to even the crack lengths in the two notch sections and extend the crack very close to the base of the notch. The specimen was then ground and polished on both faces to reveal the subsurface crack. This technique was applied to several silicon nitride disk specimens and the results indicated that in the majority of the specimens four cracks could be seen outside the notch region after grinding down 0.5 mm on both faces to reduce the thickness from its original 3.19 mm to 2.19mm. Figure 6 shows a representative SEM micrograph of the precrack revealed by grinding and polishing a silicon nitride specimen.

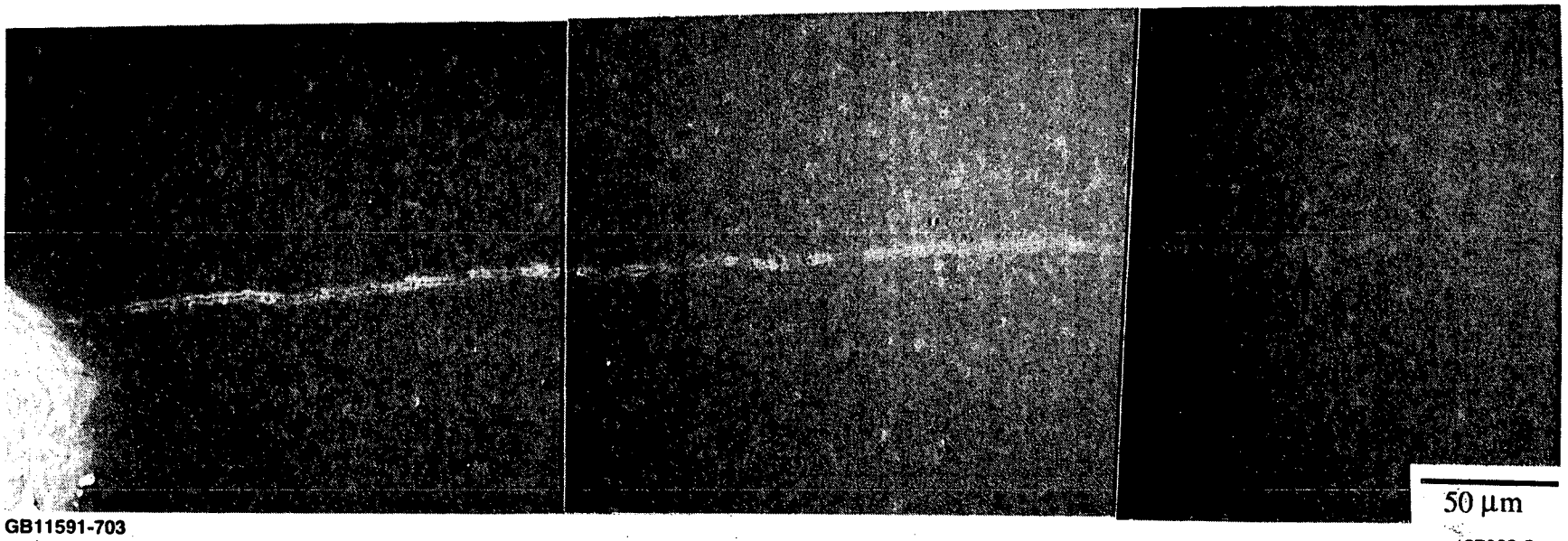

Figure 6. Stable Crack Outside the Chevron Notch in a Silicon Nitride NT-154 Disk Specimen Preloaded in Mode I and Surface Ground to Reduce the Thickness.

The static loading and grinding technique was finally selected to precrack the disk specimens for mixed-mode fracture toughness measurements since the other techniques were not successful with silicon nitride. However, it was necessary to retain a minimum thickness of 2.5 mm for the ground specimen to ensure uniform loading through the thickness. Successful precracking, therefore, depended on the position of the precrack front, which, in turn, was dependent on the magnitude of the preload. To precisely estimate the preload, fracture toughness distribution of the silicon nitride was established by loading four specimens to fracture in mode I using the procedure described above. Fracture toughness values of 4.838, 4.826, 4.827, 4.801 MPa$\sqrt{m}$ were obtained from the fracture loads using Eq. 11 and assuming the critical crack length to be a_1. A normal distribution of the fracture toughness was determined based on these values (mean = 4.823 MPa$\sqrt{m}$, standard deviation = 0.016 MPa$\sqrt{m}$). The fracture toughness corresponding to a cumulative probability of 0.17 was initially selected from the distribution. The magnitude of preload for a batch of 10 specimens was calculated based on this fracture toughness. In the process of preloading these 10 specimens, two specimens fractured and the corresponding fracture toughness values (4.794 and 4.793 MPa$\sqrt{m}$) were taken into account to establish a new fracture toughness distribution. Subsequently, the fracture toughness value used for preloading was changed to a value corresponding to a cumulative probability of 0.1 of the distribution. By the time the remaining specimens were preloaded, additional three specimens fractured and the fracture toughness values were calculated to be 4.799, 4.800 and 4,796 MPa$\sqrt{m}$. These values were taken into accout to establish a new fracture toughness distribution right after they were obtained individually.

The preloaded specimens were ground using a 600-grit diamond wheel and 0.005 mm depth of cut per pass. 0.254 mm from each face was first ground on each of the specimens. The specimen was then polished down to 1 μm on both faces and examined under the microscope[§]. If no precracks could be observed, the specimen was again ground to remove 0.13 mm from each face. After this, the specimen was again polished and examined under the microscope.

Out of the total 68 specimens, 29 specimens were found to have four cracks outside the base of the notch, eight specimens were found to have one, two or three cracks outside the base of the notch and 31 specimens were found to have no cracks revealed outside the notches. The final thickness of each specimen was recorded. For those

---

§ Nomarsky Microscope, Model BH-2, Olympus.

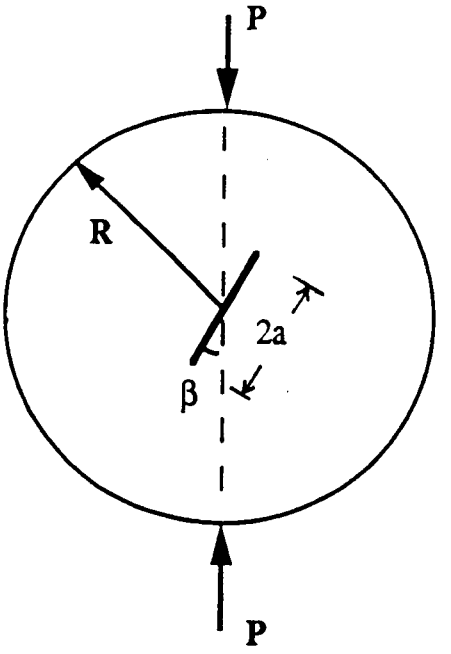

GB11591-841

Figure 7. Inclined Crack in a Disk Specimen and the Associated Coordinate System.

specimens with precracks outside the notches, the crack lengths were measured under the microscope, the normalized crack length, α, was obtained by normalizing the measured crack length with respect to the diameter of the specimen. For those specimens without precracks outside the notches, the normalized crack length, α, was calculated by normalizing the new notch length with respect to the diameter of the specimen.

Task A.3 Mixed-Mode Loading of the Disk Specimens at Room Temperature

Pure mode I, pure mode II and combined mode I and mode II loadings were obtained by orienting the notch line at various angles relative to the loading diameter (see Figure 7). Crack inclination angle, β, was varied between zero degree for pure mode I to close to 30 degrees for pure mode II. Crack inclination angle for pure mode II depends on the normalized crack length, α. Orientations between β = zero and 30 degrees produced different combinations of mode I and mode II loading.

The stress intensity factors for combined mode I (K_I) and mode II (K_{II}) loading are given by the following relationships developed by Atkinson et al.[7]:

$$K_I = \frac{P\ a^{1/2}}{\pi^{1/2}\ R\ B} N_I \tag{12}$$

$$K_{II} = \frac{P\ a^{1/2}}{\pi^{1/2}\ R\ B} N_{II} \tag{13}$$

where P is the fracture load, a is the crack length, R and B are the specimen dimensions given in Fig. 1, and N_I and N_{II} are the nondimensional coefficients that are functions of the normalized crack length, α, and the angle of inclination, β. Atkinson et al.[7] have given numerical solutions for N_I and N_{II} using a five-term approximation of series solution.

Eight orientations corresponding to $K_I / (K_I+K_{II})$ ranging from 1.0 to 0.0 were selected. The specific values of $K_I / (K_I+K_{II})$ were 1.0 (pure mode I), 0.85, 0.70, 0.56, 0.42, 0.28, 0.14 and 0 (pure mode II). One orientation at $K_I / (K_I+K_{II})$ equal to -0.05 was also selected. Two specimens were tested in each of the nine orientations, one specimen with precrack outside the notch and the other with the precrack inside the notch base. At one orientation, $K_I / (K_I+K_{II}) = 0.42$, four specimen were tested. The objective of this pairing was to compare the fracture toughness obtained from the two types of specimens. The crack inclination angle, β, for each specimen was calculated using Eqs. 12 and 13 based on the normalized crack length, α, measured after grinding and the selected orientation. Disk specimens with appropriate orientations were loaded to fracture in diametral compression in a universal testing machine# with a crosshead speed of 1.27 mm/min. Special care was taken to recover all the fractured pieces.

Extension of the cracks in the disk specimens subjected to combined mode I and mode II loading or those subjected to pure mode II loading was always noncoplanar with the original cracks, i.e. cracks always deviated from their original planes. Figure 8 shows a typical fracture pattern of a silicon nitride specimen subjected to combined mode I and mode II loading. It can be seen that the specimen has precrack outside the notch region and crack extension occurred by kinking indicating noncoplanar crack extension. Figure 9 shows a typical fracture pattern of a silicon nitride disk specimen with the precrack inside the notch region and fractured in mixed-mode loading. It can be seen that even though

Model 4206, Instron Corp., MA.

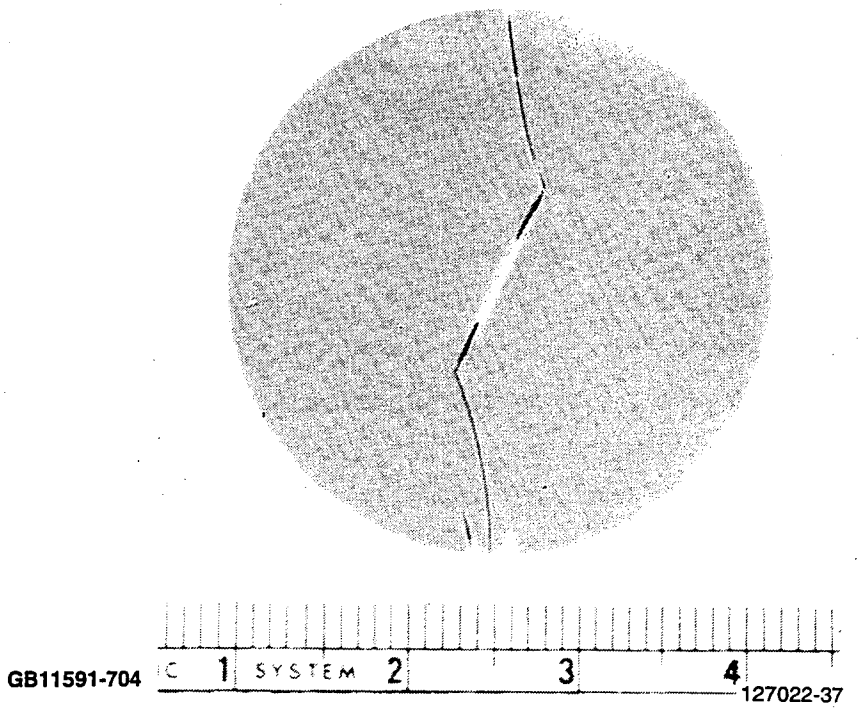

Figure 8. Fracture Pattern of a Silicon Nitride NT-154 Disk Specimen with Precrack Outside the Notch Base and Fractured in Mixed-Mode Loading.

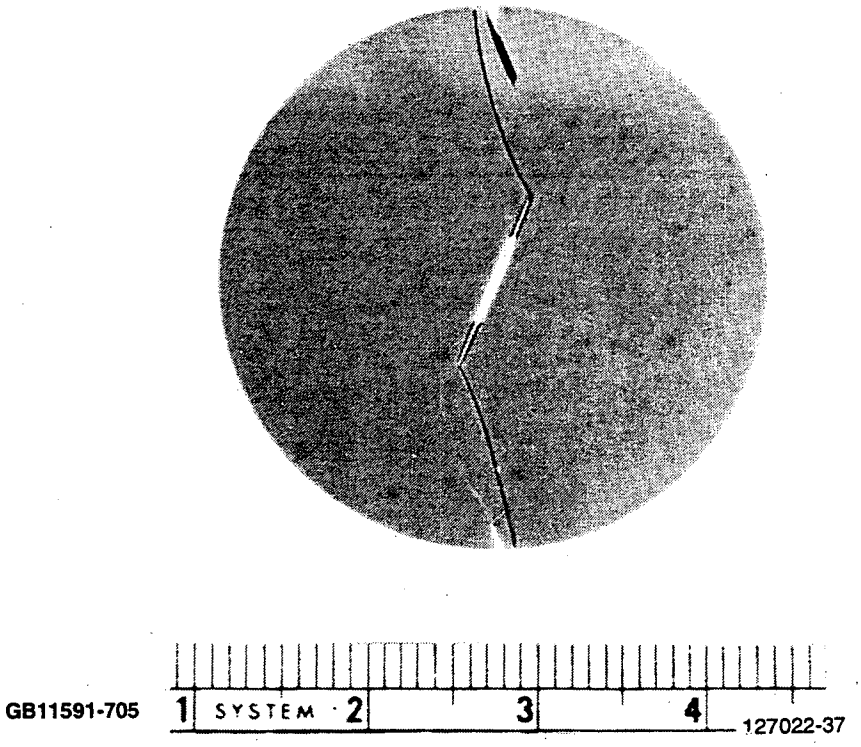

Figure 9. Fracture Pattern of a Silicon Nitride NT-154 Disk Specimen with Precrack intside the Notch Base and Fractured in Mixed-Mode Loading.

there was no precrack revealed outside the notch, stable crack growth occurred in the chevron notch during preloading and the crack front was, in fact, very close to the base of the notch.

Fractured specimens were reassembled and examined under the microscope to measure the lengths between the two kinks on either side of the notch (except the specimens tested in pure mode I). For those specimens with precracks outside the notch, these measurements were compared to the previous measurements prior to the test. Results indicated that the two measurements were only slightly different. The kink-to-kink crack length measurement was considered more accurate, and therefore, was used in Eqs. 12 and 13 to calculate the mode I and mode II stress intensity factors. For those specimens with precracks inside the notch (as shown in Fig. 9), the kink-to-kink crack lengths were less than the initial notch length, and the stress-intensity factors were determined using the kink-to-kink crack length measurements. For the two pure mode I tests, the initial crack length measurement and the initial notch length were used to calculate the stress-intensity factors for the specimen with precrack outside the notch and the specimen with precrack inside the notch, respectively.

Figure 10 shows a plot of mode I stress-intensity factor, K_I, versus mode II stress-intensity factor, K_{II}, for combined mode I - mode II fracture of the silicon nitride disks tested at room temperature (70^o F). The average value of the critical stress-intensity factor for mode I, K_{IC}, i.e. the mode I fracture toughness, was 4.96 MPa$\sqrt{m}$. With increasing mode II loading the mode I stress-intensity factor decreased monotonically and for pure mode II loading, the mode II stress-intensity factor at fracture was approximately K_{II} = 9.98 MPa$\sqrt{m}$. It should be noted that there was no significant difference between the stress-intensity factors calculated form the two types of specimens (i.e. specimens with precracks inside or outside the notch). The K_I and K_{II} values of all the data in Fig. 10 are listed in Appendix A.

Combined mode I and mode II fracture toughness envelopes for many polycrystalline ceramics are adequately described by the following empirical equation[11]:

$$\frac{K_I}{K_{IC}} + \left(\frac{K_{II}}{C\,K_{IC}}\right)^2 = 1 \qquad (14)$$

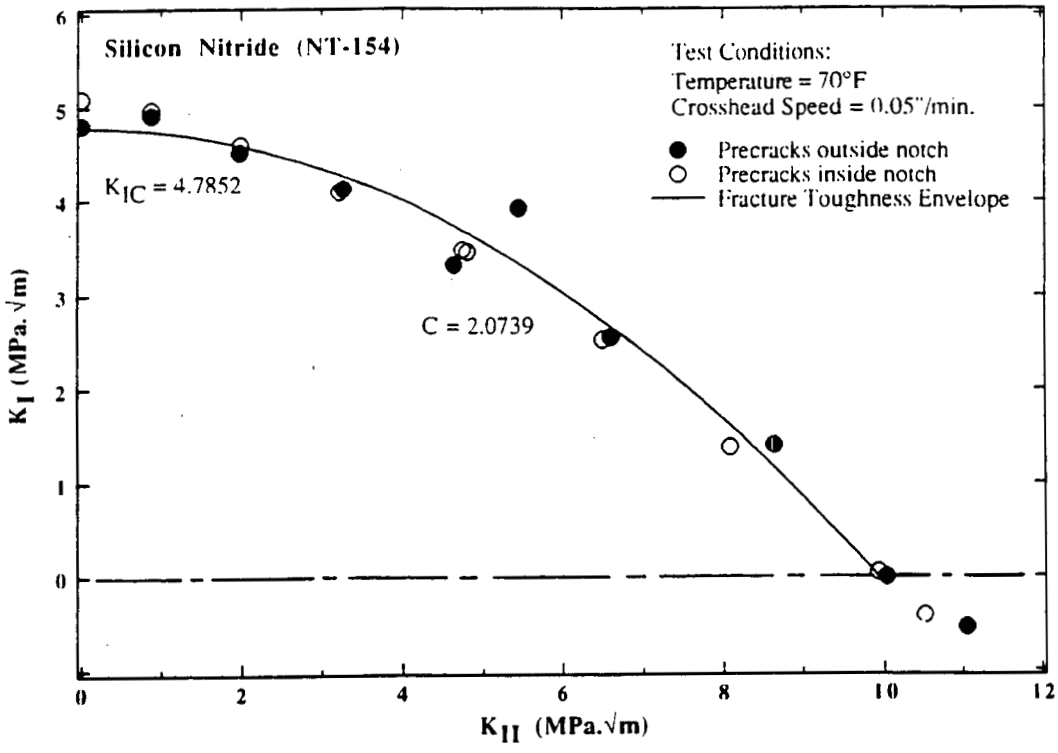

GB11591-842

Figure 10. Mode I and Mode II Stress-Intensity Factors for Mixed-Mode Fracture of Silicon Nitride Disks in Diametral-Compression Tests.

In Eq. 14, C is an empirical constant which is the ratio of the fracture toughness in pure mode II loading and the mode I fracture toughness. Palaniswamy and Knauss[12] have shown that Eq. 14 with C = 0.816 gives a very good fit to their rigorous calculations based on the maximum strain energy release rate criterion for crack extension under combined mode I and mode II loading. For polycrystalline ceramics, experimental data are described by Eq. 14 with C value ranging from 1.0 to 2.0[13,14]. In the present study, Eq. 14 was used to fit the mixed-mode fracture toughness data obtained at room temperature. The result is shown in Fig. 10 as the solid line. The best fit C value was calculated to be 2.07. The mode I fracture toughness, K_{IC}, estimated from the best fit envelope was 4.79 MPa$\sqrt{m}$.

As discussed in an earlier section, the length of the stably growing crack in the chevron-notch section can be theoretically calculated using a stress-intensity analysis developed for the disk specimen. The equilibrium growth of the crack in the chevron-notch

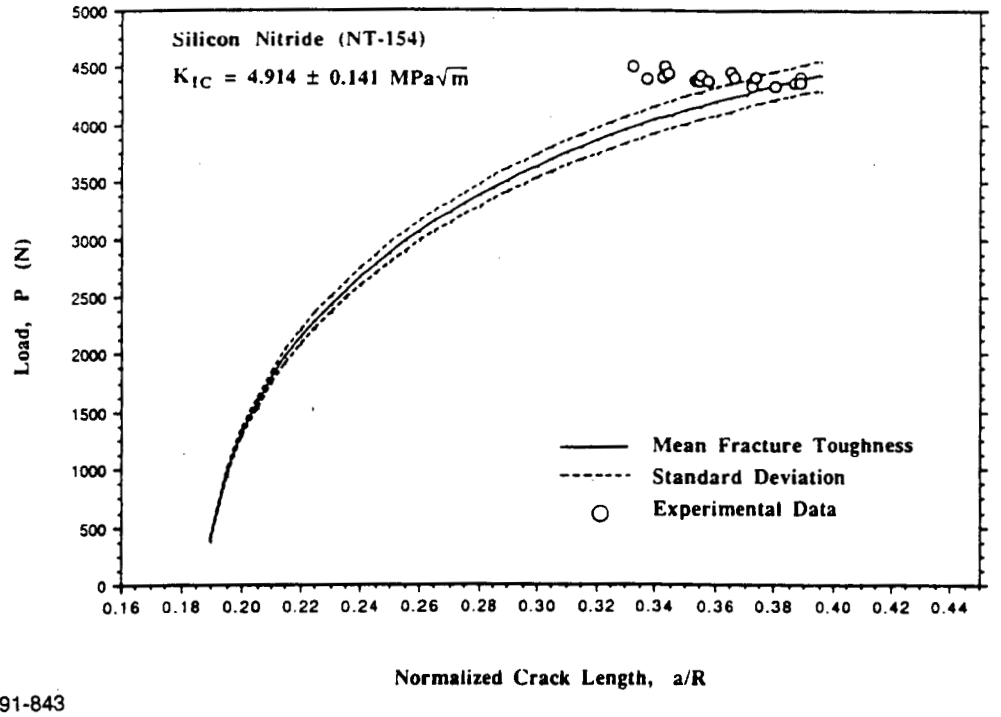

GB11591-843

Figure 11. Theoretically Calculated (Solid and Dashed Lines) and Measured Crack Lengths (Circles) in the Chevron-Notch Section of Silicon Nitride Disk Specimens.

section is governed by Eq. 11. Figure 11 shows a plot of P (load) versus α (normalized crack length) for the disk specimens used in static loading and grinding. The solid line and the two dashed lines represent the theoretical calculations using Eq. 11 based on the mean and standard deviation of the mode I fracture toughness ($K_{IC} = 4.914 \pm 0.141$ MPa$\sqrt{m}$). The mean and standard deviation of the fracture toughness were determined by taking into account all the valid K_{IC} values obtained in the precracking experiments and the two mode I fracture toughness data in Fig. 10 . The circles represent the actual crack-tip position in the notch as revealed by grinding and polishing. It is evident that in a significant number of the specimens the crack lengths in the chevron notches were shorter than what Eq. 11 predicts. It is not clear at this time what causes this disagreement. However, one possibility is the approximation involved in the calculation of Eq. 11. As discussed ealier, Eq. 11 was derived based on the STCA, i.e. the equivalent straight-through-crack assumption. The compliance of the chevron-notched disk specimen can be alternately modeled by Bluhm's slice synthesis method (SS)[15]. Investigation of the Bluhm's slice synthesis method was not performed during the course of this project. The results in Fig. 11, however, indicate the difficulty in precisely controlling the load to precrack the chevron-notched disk specimen.

Task A.4 Mixed-Mode Loading of the Disk Specimens at Elevated Temperatures.

Precracked silicon nitride disk specimens were loaded to fracture in diametral compression at two elevated temperatures, 2200 °F and 2500 °F. Two crosshead speeds, 1.27 mm/min and 0.0127 mm/min, were used at 2200 °F to examine the possible effect of crosshead speed on the fracture toughness envelope. Tests at 2500 °F used a crosshead speed of 1.27 mm/min. Mixed-mode fracture toughness values were measured at four orientations corresponding to $K_I / (K_I+K_{II})$ ranging from 1.0 to 0.0 and one angle at $K_I / (K_I+K_{II})$ equal to -0.05. The four orientations selected were $K_I / (K_I + K_{II}) = 1.0$ (pure mode I), 0.634 (i.e. $K_I / K_{II} = \tan^{-1} 60^o$), 0.366 (i.e. $K_I / K_{II} = \tan^{-1} 30^o$) and 0.0 (pure mode II). Two specimens were tested in each orientation, one specimen with precrack outside the chevron notch, the other specimen with precrack inside the chevron notch. Calculation of the stress-intensity factors followed the same procedure as described in the room temperature tests.

Task A.4-1 2200° F, Crosshead Speed = 1.27 mm/min

Figure 12 shows the results of combined mode I and mode II fracture toughness tests at 2200 °F and crosshead speed = 1.27 mm/min. Post-test microscopic examination showed, however, that the two specimens tested in pure mode II and the two specimens tested in the negative mode I orientations had fractures initiated close to the tips of the notch but not the crack tips. This phenomenon was not observed in the room temperature tests and was possibly due to excessive shielding effect of the asperity contact on the crack surfaces. This shielding effect apparently increases at elevated temperatures as well as when the crack is oriented close to pure mode II. Therefore, these four tests were considered not valid. To compensate for this, it was decided to test additional two specimens at the orientation of $K_I / K_{II} = \tan^{-1} 15^o$. These two data combined with the other data obtained from pure mode I, $K_I / K_{II} = \tan^{-1} 60^o$ and $K_I / K_{II} = \tan^{-1} 30^o$ are plotted in Fig. 12. These fracture toughness data are listed in Appendix B. Eq. 14 was fitted to these mixed-mode fracture toughness data. The result is shown in Fig. 12 as the solid line. The best fit C value was calculated to be 1.97. The mode I fracture toughness, K_{IC}, resulting from the best fit envelope was 4.43 MPa$\sqrt{m}$.

Task A.4-2 2200° F, Crosshead Speed = 0.0127 mm/min

The mixed-mode fracture toughness results of the silicon nitride tested at 2200 °F and a crosshead speed of 0.0127 mm/min are summarized in Figure 13. Based on the experience in the test series at 2200 °F and 1.27 mm/min crosshead speed, no specimens were tested in the pure mode II and the negative mode I orientations. The data shown in

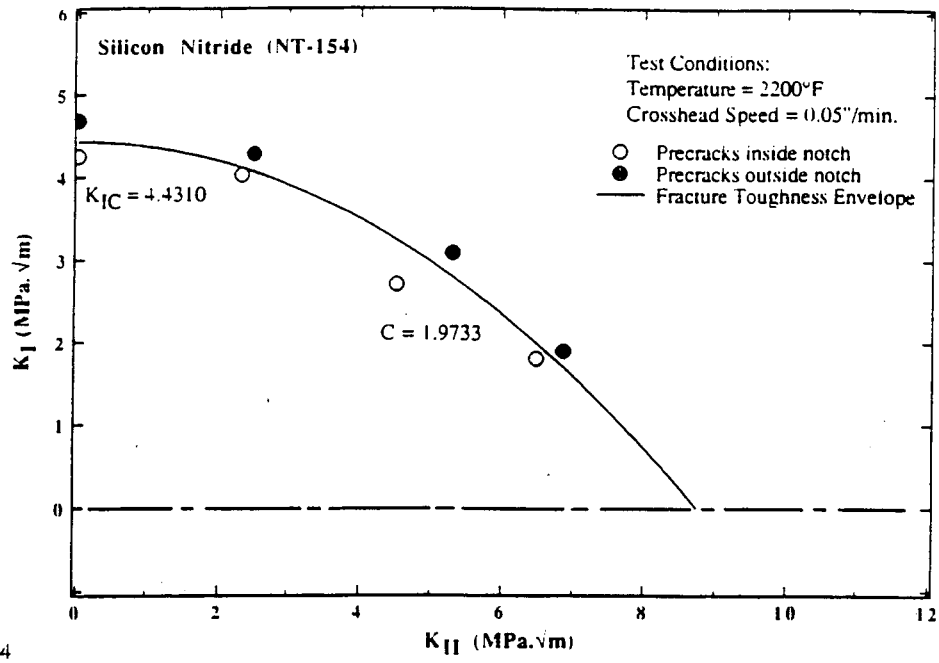

GB11591-844

Figure 12. Mode I and Mode II Stress-Intensity Factors for Mixed-Mode Fracture of Silicon Nitride Disks in Diametral-Compression Tests at 2200 °F (Crosshead Speed = 1.27 mm/min).

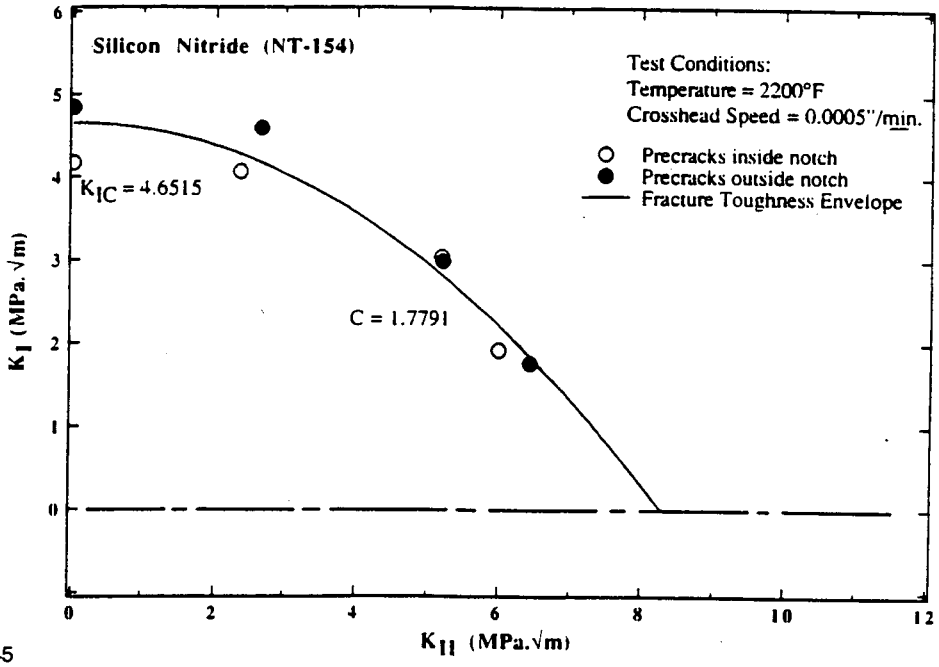

GB11591-845

Figure 13. Mode I and Mode II Stress-Intensity Factors for Mixed-Mode Fracture of Silicon Nitride Disks in Diametral-Compression Tests at 2200 °F (Crosshead Speed = 0.0127 mm/min).

Fig. 13 correspond to the specimens tested in the following orientations: pure mode I, $K_I / K_{II} = \tan^{-1} 60^o$, $K_I / K_{II} = \tan^{-1} 30^o$ and $K_I / K_{II} = \tan^{-1} 15^o$. The fracture toughness data are listed in Appendix C. Eq. 14 was also fitted to the data (shown as the solid line in Fig. 13); the best fit C value was 1.78. The mode I fracture toughness, K_{IC}, estimated from the best fit envelope was 4.65 MPa$\sqrt{m}$.

Two disk specimens from the batch tested at 2200 °F and 0.0127 mm/min crosshead speed were selected for examination of fracture surfaces in the scanning electron microscope. The two specimens selected were the specimen tested in pure mode I with the precrack outside the chevron notch and the specimen tested in a mixed-mode orientation, $K_I / K_{II} = \tan^{-1} 60^o$, with its precrack also outside the chevron notch. Figure 14 shows a SEM micrograph of the fracture surface of the first specimen (pure mode I). The first set of arrows points to the position of the crack front after stable crack growth during preloading, while the second set of arrows points to the position where fast fracture occurred. The fracture surface between the arrows (~ 40 μm) is likely due to subcritical crack growth promoted by the slow crosshead speed (0.0127 mm/min). Figure 15 shows the fracture surface of the second specimen (mixed-mode). The arrows point to the position of the precrack front. The subcritical crack growth region could not be clearly identified in this case because of the inclined surface of the kink.

Task A.4-3 2500° F, Crosshead Speed = 1.27 mm/min

Figure 16 shows the mode I - mode II fracture toughness envelope for the silicon nitride tested at 2500 °F and a crosshead speed of 1.27 mm/min. Similar to the previous tasks, the data represent the results obtained from tests in the orientations of pure mode I, $K_I / K_{II} = \tan^{-1} 60^o$, $K_I / K_{II} = \tan^{-1} 30^o$ and $K_I / K_{II} = \tan^{-1} 15^o$. The fracture toughness data are listed in Appendix D. Equation 14 with a C value of 1.68 gave a good fit to the data. The mode I fracture toughness, K_{IC}, estimated from this fit was 4.33 MPa$\sqrt{m}$.

Task B. Biaxial Disk Flexure Testing and Analysis

Forty disk specimens were supplied by GAPD. The nominal dimensions of the specimens were 50.46 mm in diameter and 3.190 mm in thickness. Both surfaces of the as-received specimens were finished using 320-grit diamond wheel. All the disk specimens had undergone a heat treatment at GAPD.

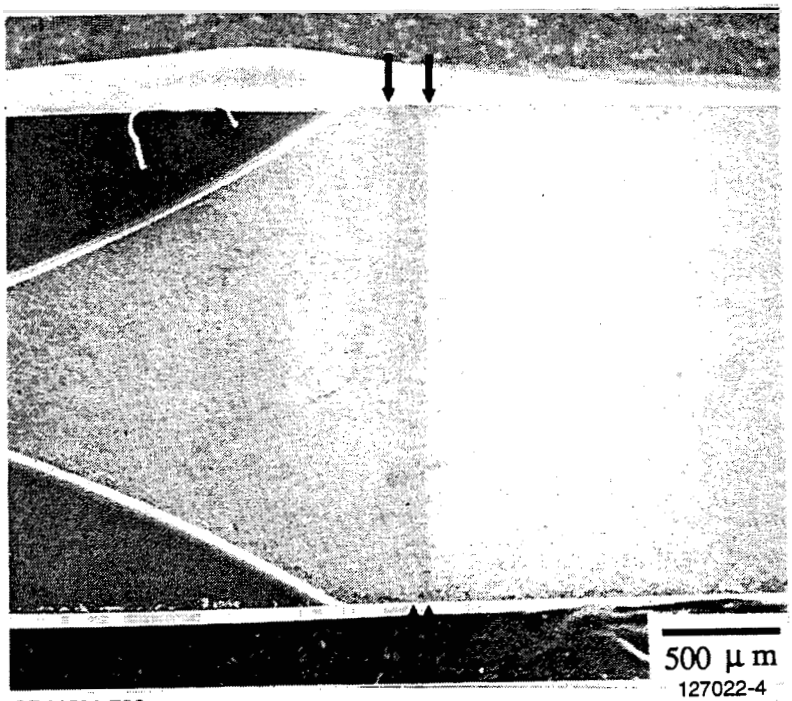

Figure 14. Fracture Surface of Chevron-Notched Diametral-Compression Specimen of Silicon Nitride Tested at 2200 °F and 0.0127 mm/min Crosshead Speed in Pure Mode I.

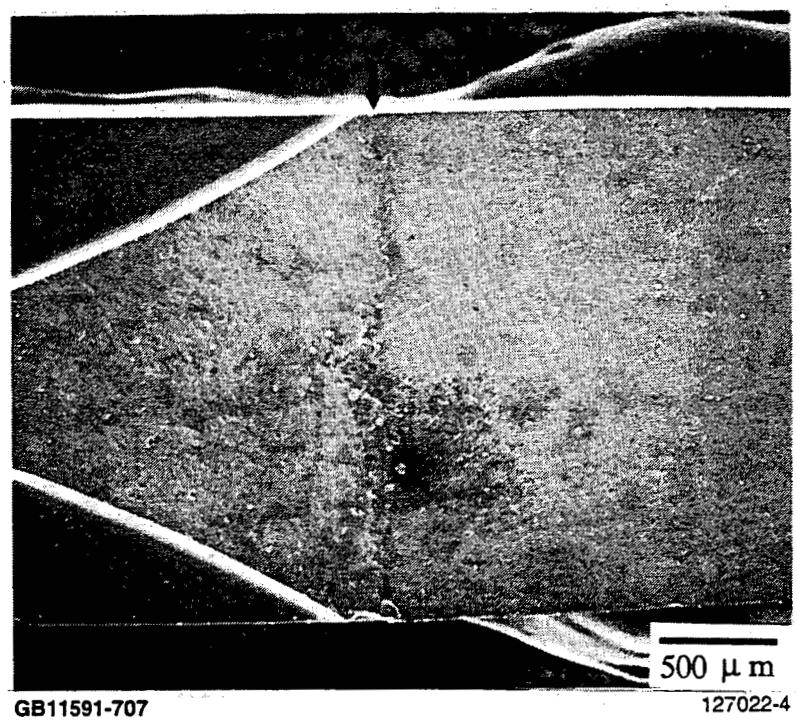

Figure 15. Fracture Surface of Chevron-Notched Diametral-Compression Specimen of Silicon Nitride Tested at 2200 °F and 0.0127 mm/min Crosshead Speed in Mixed-Mode.

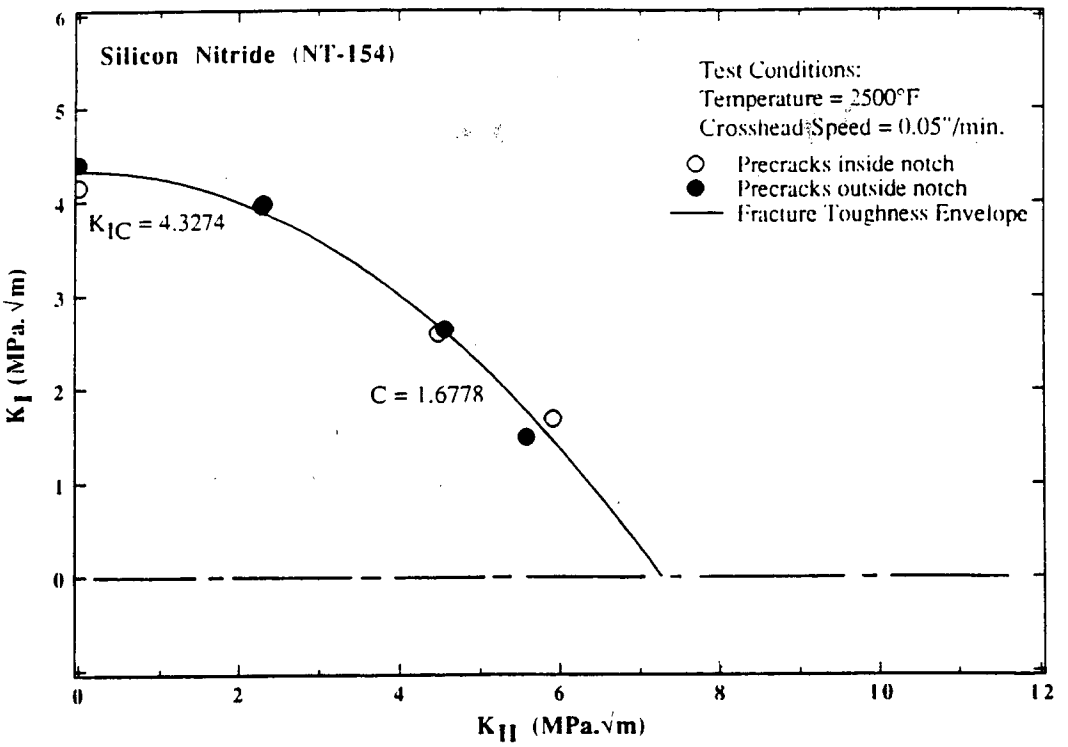

GB11591-846

Figure 16. Mode I and Mode II Stress-Intensity Factors for Mixed-Mode Fracture of Silicon Nitride Disks in Diametral-Compression Tests at 2500 °F (Crosshead Speed = 1.27 mm/min).

A hydraulic test system featuring uniform pressure loading of disks was employed in this study to measure fracture stresses in biaxial flexure[16]. Figure 17 shows the cross section of the biaxial test cell. The disk specimen was supported along its periphery on a ball-bearing support and transversely loaded by uniform pressure. The specimen support system consisted of 40 freely rotating ball bearings (3.175 mm in diameter) spaced uniformly along a circle , 48.26 mm in diameter. The ball-bearing support system was designed to minimize friction at the support points. The opposite surface of the disk was transversely loaded by uniform pressure from hydraulic oil. A brass foil diaphragm (0.0254 mm thick) separated the specimen surface and the hydraulic oil. Pressure in the test cell was generated using a system consisting of a manual hydraulic pump and a hydraulic ram (see the schematic in Figure 18). The ram assembly with its piston and cylinder was mounted on the crosshead of a universal testing machine and was connected in series with the test cell. A set of high pressure valves were used to direct the oil flow in the desired direction. The pump was first used to fully extend the piston outside the cylinder with the test cell shut-off from the line. The manual pump was, then, shut-off

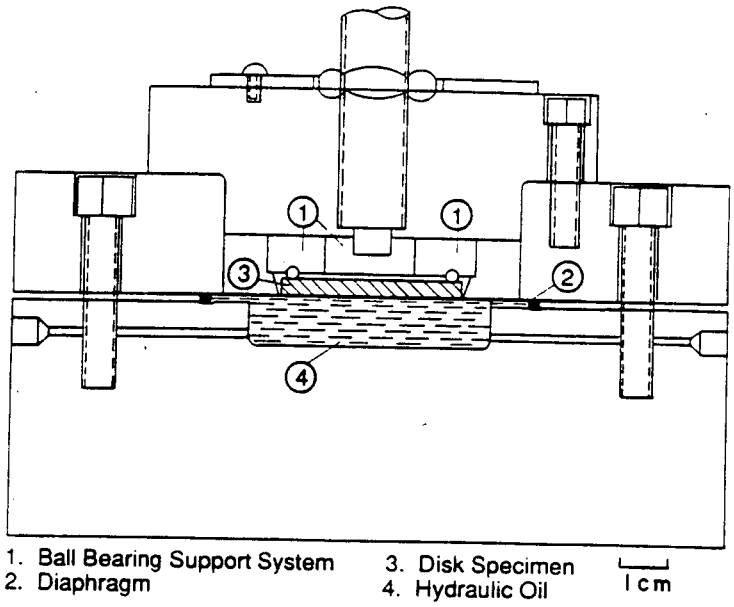

GB11591-847

Figure 17. Cross Section of the Hydraulic Test Cell Used in Biaxial Flexure Tests.

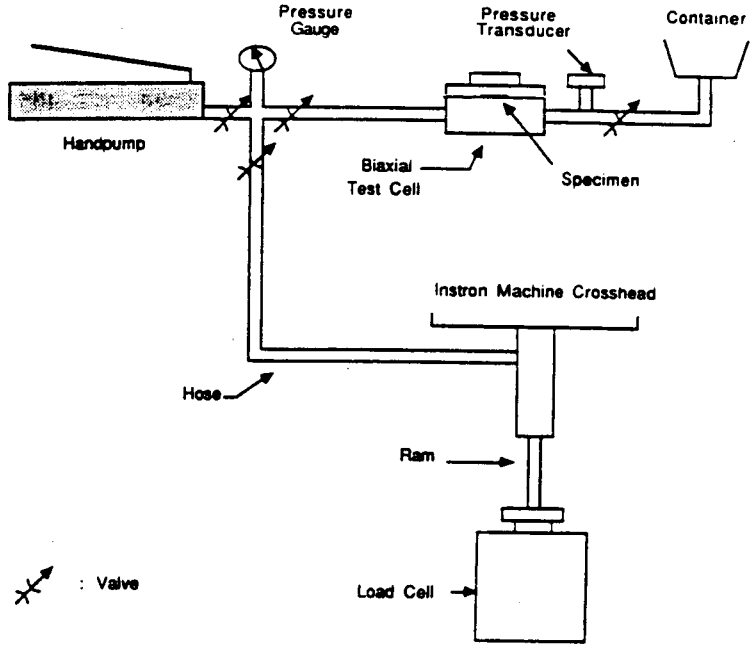

GB11591-848

Figure 18. Loading Arrangement Used in the Biaxial Flexure Tests.

from the line and the test cell was connected. The crosshead of the universal testing machine was then used to displace the piston at a uniform displacement rate, thus generating a linear pressure increase in the test cell. The pressure rise rates and, therefore, the stressing rates could be varied by varing the crosshead speed. The pressure in the test cell was measured using a pressure transducer.

Task B.1 Calibrations and Fracture Stress Measurements

A disk specimen of thickness, t, and radius, r_2, freely supported along a radius, r_1, and loaded transversely by uniform pressure, p, develops an axisymmetric stress distribution. The radial stress, σ_r, and the tangential stress, σ_t, are functions of radial position only and their variations as given by plate theory[17,18] are as follows:

$$\sigma_r = \sigma_b \left[1 - \alpha \left(\frac{r}{r_1}\right)^2 \right] \tag{15}$$

$$\sigma_t = \sigma_b \left[1 - \beta \left(\frac{r}{r_1}\right)^2 \right] \tag{16}$$

where σ_b is the maximun tensile stress at the center of the disk given as:

$$\sigma_b = \frac{3pr_1^2}{8t^2}\left[2\,(1-\nu) + (1+3\nu)\left(\frac{r_2}{r_1}\right)^2 - 4\,(1+\nu)\left(\frac{r_2}{r_1}\right)^2 \ln\left(\frac{r_2}{r_1}\right) \right] + \frac{(3+\nu)\,p}{4\,(1-\nu)} \tag{17}$$

α and β are parameters that determine the stress gradients and are given as :

$$\alpha = \frac{3\,p\,(3+\nu)\,r_1^2}{8\,t^2\,\sigma_b} \tag{18}$$

$$\beta = \frac{3\,p\,(1+3\nu)\,r_1^2}{8\,t^2\,\sigma_b} \tag{19}$$

The applicability of Eq. (17) to the disk specimens tested in this study was examined by direct measurements of strains at the disk centers. Figure 19 shows the linear variation of thickness normalized strains as function of applied pressure measured on two

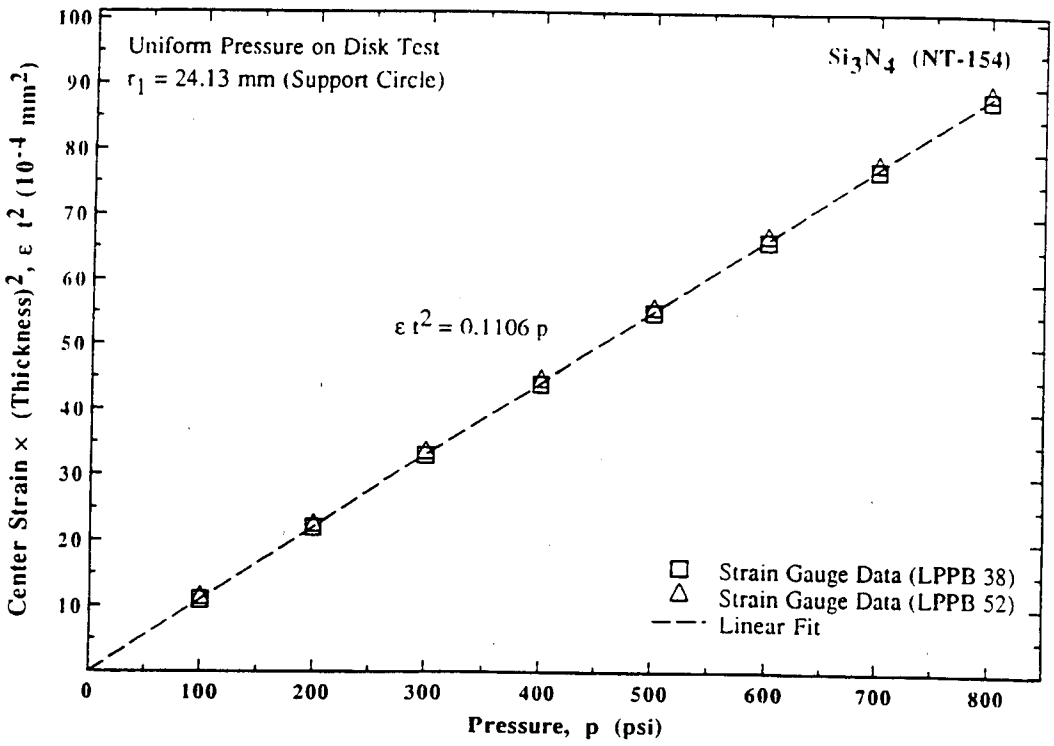

GB11591-849

Figure 19. Variation of Thickness-Normalized Strain Measured at the Center of Two Silicon Nitride Disk Specimens with Applied Pressure.

disk specimens of the silicon nitride. The two specimens showed excellent reproducibility. The dashed line in Fig. 19 represents the best fit relation to the measured strain values. The elastic modulus (E) reflected by this relation can be calculated using the following equation:

$$\varepsilon_b t^2 = \frac{\sigma_b (1-\nu) t^2}{E} \qquad (20)$$

where σ_b was calculated from Eq. (17) and ν is the Poisson's ratio. The calculated elastic modulus was 330.5 GPa. This value is in good agreement with the value obtained at GAPD using an ultrasonic method.

Thirty seven (37) out of the original 40 specimens were tested (Note: initially, three specimens were tested using a support system with a larger supporting diameter, 24.765 mm. The larger supporting circle was too close to the diameter of the specimen and

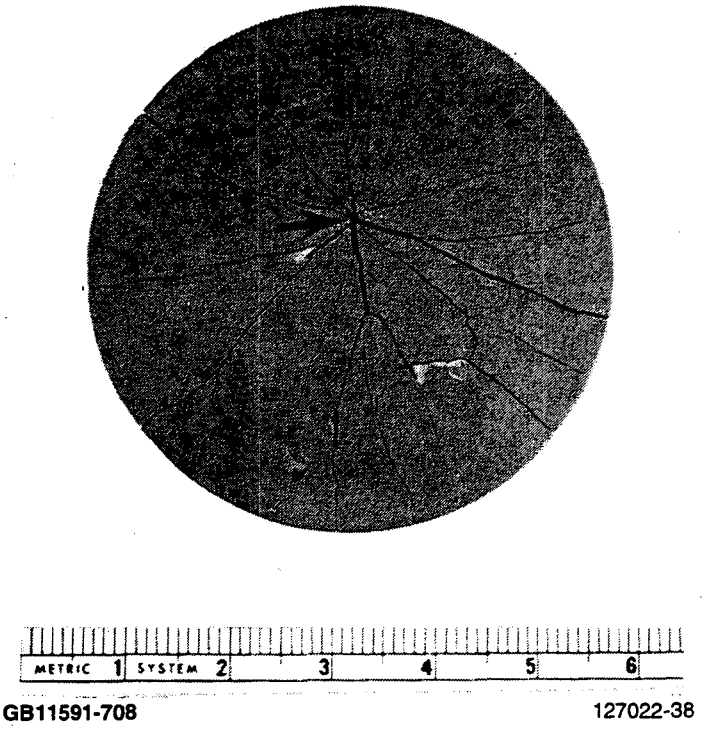

Figure 20. Typical Fracture Pattern in a Disk Specimen of Silicon Nitride Tested in Biaxial Flexure. The Arrow Points to the Fracture Origin.

this caused edge failure of two specimens). Tests were carried out at room temperature and a stressing rate of 23 MPa/s. This stressing rate was selected because it is the stressing rate of a beam specimen (3 x 4 x 45 mm) when tested in four-point bending (40 mm support span, 20 mm loading span) at a crosshead speed of 0.5 mm/min. Figure 20 shows a representative disk specimen of silicon nitride after fracture in the biaxial flexure test. The arrow points to the fracture initiation site on a short length of the fracture plane referred to as a "jog." Beyond the jog the fracture plane bifurcated repeatedly, resulting in the fracture pattern seen in the figure. The initial jog was randomly located close to the center of the disk.

Task B.2 Fracture Stress Data and Statistics

Fracture strain (ε) for each specimen was calculated from the fracture pressure (p) using the strain calibration (Fig. 19). Fracture strains were converted to fracture stresses using Eq. 20 and E = 330.5 GPa. The probability of fracture, F, for each test specimen was defined by the following rank statistics[19]:

$$F = \frac{(i - 0.5)}{N} \tag{21}$$

where i is the rank of a specimen in increasing order of fracture stress and N is the sample size. The 'best fit' fracture stress distribution was determined using the maximum likelihood method[20] and expressed in terms of the two-parameter Weibull distribution function :

$$F = 1 - \exp\left[- \left(\frac{\sigma}{\sigma_\theta}\right)^m \right] \tag{22}$$

In Equation (12), m is referred to as the Weibull modulus and σ_θ is called the characteristic strength of the distribution.

Figure 21 shows the linearized Weibull plot of the fracture stresses of the silicon nitride (NT-154) (fracture stress data are listed in Appendix E). The Weibull modulus and the characteristic strength were estimated to be 10.41 and 785.2 MPa, respectively. The statistical uncertainties of the two parameters were also determined using the 'Bootstrap' method[21]. The 90% confidence interval of m is (8.72 $\leftrightarrow$ 13.19); the 90% confidence interval of σ_θ is (762.4 MPa $\leftrightarrow$ 805.6 MPa).

Care was taken to recover fractured pieces of the disk specimens. Four specimens were selected for fractographic examination to identify the strength-controlling flaws. These four specimens were selected from different stress levels to represent the entire fracture stress distribution. Three specimens fractured from surface flaws. Fracture-initiating flaw in one specimen could not be clearly identified. Figures 22 and 23 show scanning electron micrographs of the fracture surfaces of two specimens. The two arrows in Fig. 22 (A) indicate the "jog". Fig. 22 (B) shows a higher magnification of the fracture origin. A thin layer of amorphous phase can be observed at the surface; this thin layer was suspected to be the fracture origin. In Fig. 23 (A), the "jog" is identified by the arrows. A higher magnification of the fracture origin, shown in Fig. 23 (B), indicates that the fracture origin was a surface pit.

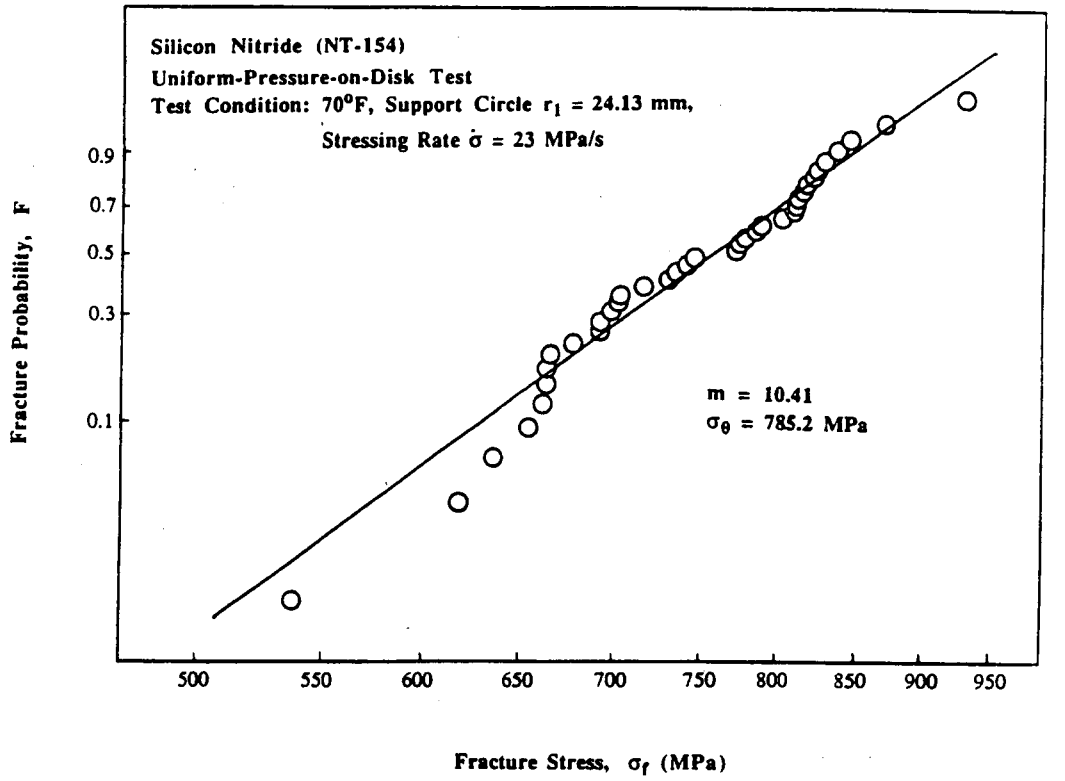

GB11591-850

Figure 21. Linearized Weibull Plots of the Fracture Stresses of Silicon Nitride Tested in Biaxial Flexure.

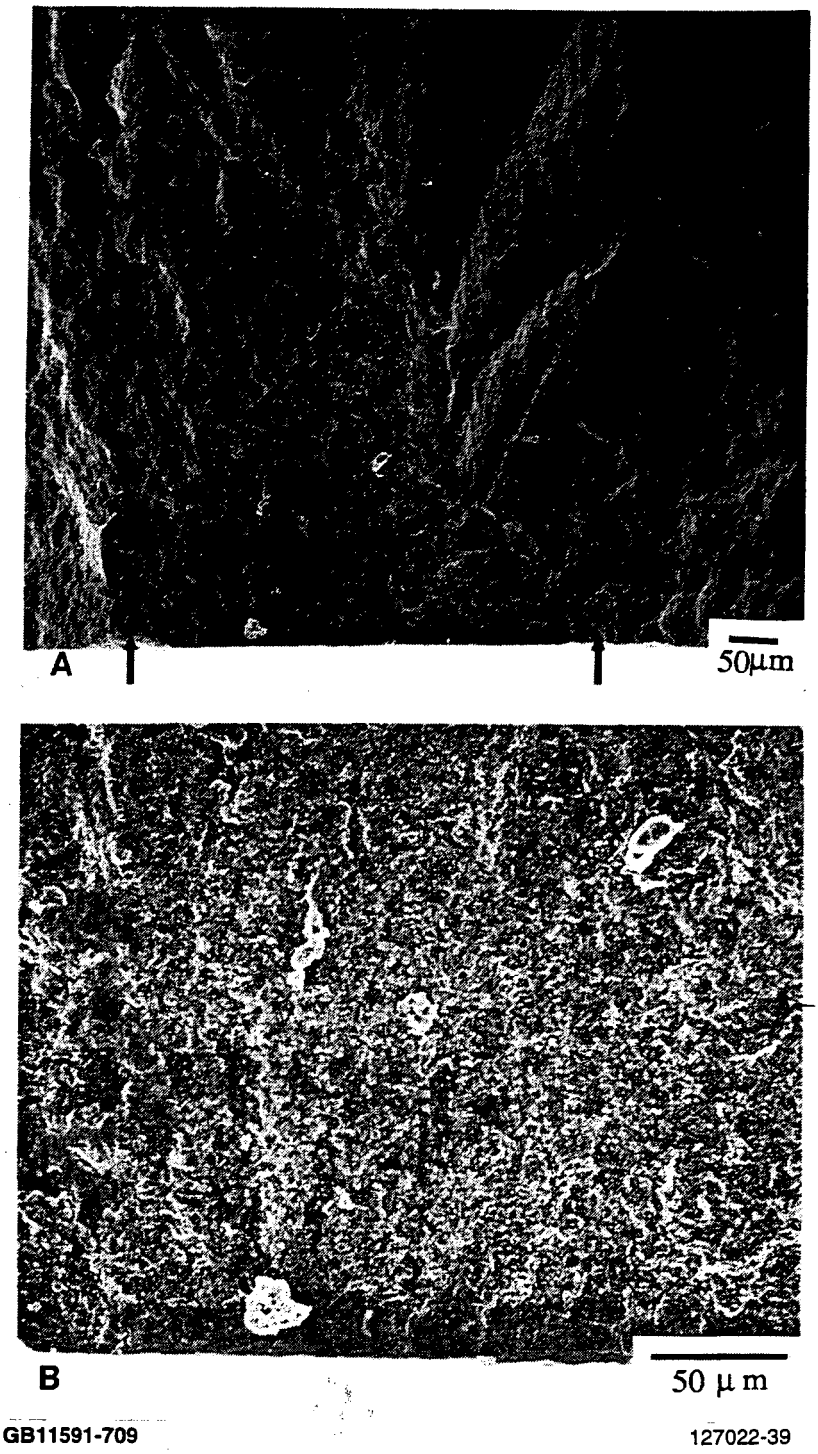

Figure 22. (A) Fracture Surface in the Vicinity of the Fracture Origin; (B) A Thin Layer of Amorphous Phase Was Suspected to be the Fracture Origin. ($\sigma_f = 694.5$ MPa)

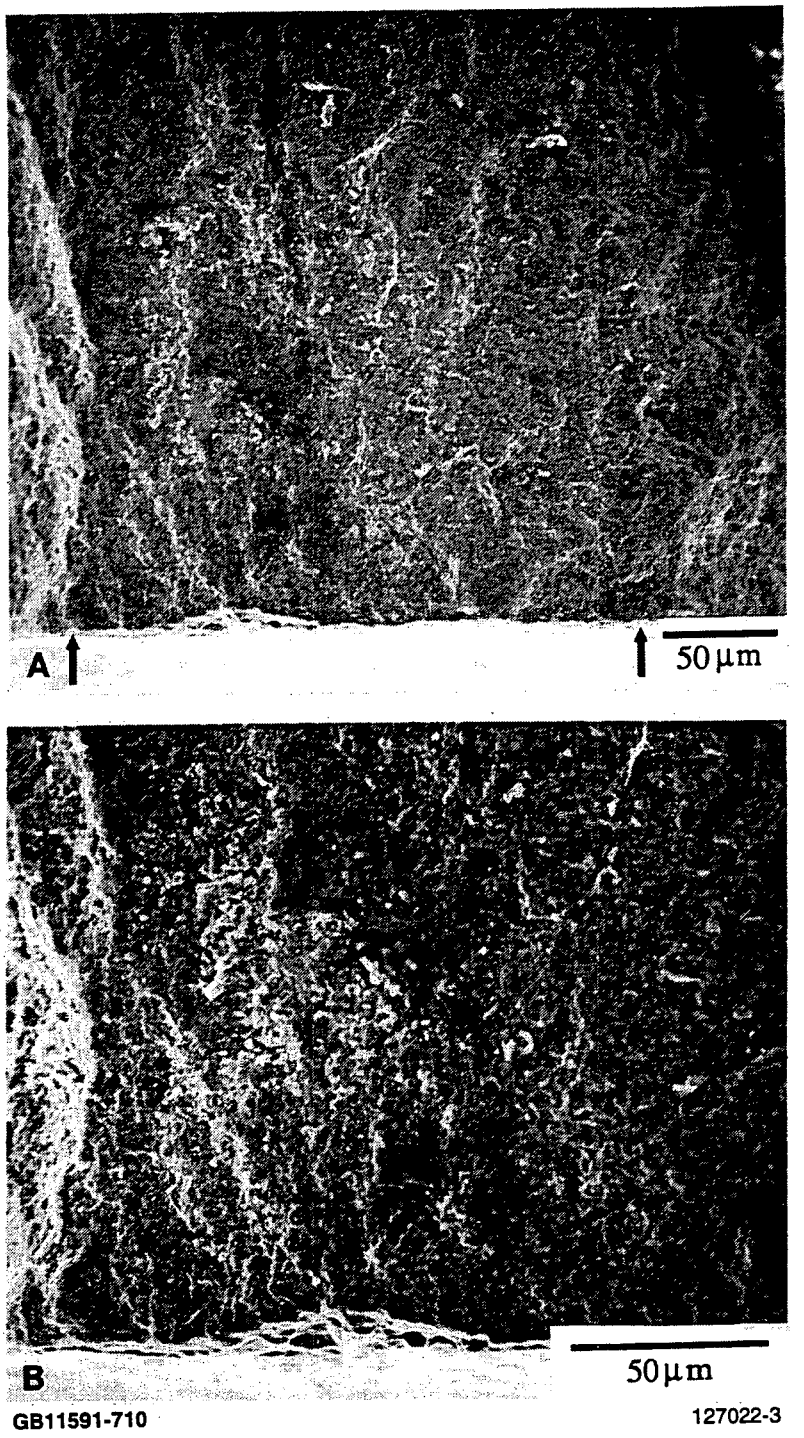

Figure 23. (A) Fracture Surface in the Vicinity of the Fracture Origin; (B) A Surface Pit Was Suspected to be the Fracture Origin. (σ_f = 848.0 MPa)

III. SUMMARY

The University of Utah participated in the project entitled, " Life Prediction Methodology for Ceramic Components of Advanced Vehicular Heat Engines," as a subcontractor to Garrett Auxiliary Power Division (GAPD) of Allied Signal Aerospace Company. The University of Utah completed the following two tasks in the subcontract:

(A) Measurements of the combined mode I and mode II fracture toughness of a silicon nitride ceramic at room and elevated temperatures.

(B) Measurements of the fracture stresses of the silicon nitride ceramic in biaxial flexure at room temperature.

In Task A, silicon nitride disk specimens were first chevron-notched in the center and then precracked using the static loading and grinding method. Specimens were tested in diametral compression with different orientatons of the notch line with respect to the loading diameter to produce different combinations of K_I and K_{II}. Tests were performed at room temperature and two elevated temperatures, 2200 ^oF and 2500 ^oF. Mixed-mode fracture toughness data could be adequately described by a commonly used empirical equation with an empirical parameter C representing the shear sensitivity. Results indicated that the shear sensitivity increased with increasing temperature. Also, slow-crack growth was detected at high temperatures when the disks were tested at a low crosshead speed (0.0127 mm / minute).

In Task B, disk specimens were tested in biaxial flexure using uniform-pressure-on-disk tests. Variation of the thickness normalized strain with applied pressure was calibrated prior to the test. The apparent elastic modulus determined from the calibration results was 330.5 GPa. Fracture stresses were described by a two-parameter Weibull distribution function. The Weibull modulus (m) and characteristic strength (σ_θ) were estimated to be 10.41 and 785.2 MPa, respectively. The analysis of the biaxial flexure data using a multiaxial reliability analysis was deferred to a future date when GAPD will supply the relevant uniaxial strength data.

REFERENCES

1. D. K. Shetty, A. R. Rosenfield and W. H. Duckworth, " Fracture Toughness of Ceramics Measured by a Chevron-Notched Diametral-Compression Test," *J. Am. Ceram. Soc.*, **68** [12] C325-C327 (1985).
2. D. K. Shetty, A. R. Rosenfield and W. H. Duckworth, " Mixed-Mode Fracture in Biaxial Stress State : Application of the Diametral-Compression (Brazilian Disk) Test," *Eng. Frac. Mech.*, **26** [6] 825-840 (1987).
3. K. Stuffle, R. A. Cutler, A. Nagar, D. K. Shetty and A. V. Virkar, " A Microcircuit Grid Technique for Crack Length Measurement in Fatigue Tests at Elevated Temperatures," *Proc. VIth Int. Cong. on Experimental Mechanics*, Portland, OR., June 1988.
4. D. Singh and D. K. Shetty, " Subcritical Crack Growth in Soda-lime Glass in Combined Mode I and Mode II Loading," *J. Am. Ceram. Soc.*, **73** [12] 3597-3608 (1990).
5. D. Munz, R. T. Bubsey and J. L. Shannon, Jr., " Fracture Toughness Determination of Al2O3 Using Four-Point Bend Specimens with Straight-Through and Chevron Notches, " *J. Am. Ceram. Soc.*, **63** [5-6] 300-305 (1980).
6. L. M. Barker; pp 483-494 in Fracture Mechanics of Ceramics, Vol. 3. Edited by R. C. Bradt, D. P. H. Hasselman and F. F. Lang, Plenum, New York, 1978.
7. C. Atkinson, R. E. Smelser and J. Sanchez, " Combined Mode Fracture Via the Cracked Brazilian Disk Test, " *Int. J. Fract.*, **18** [4] 279-291 (1982).
8. Progress Report-3, University of Utah, March 1992.
9. Carrett Auxiliary Power Division, Allied-Signal Aerospace Company, Private Communication.
10. S. Suresh and J. R. Brockenbrough, " Theory and Experiments of Fracture in Cyclic Compression : Single Phase Ceramics, Transforming Ceramics and Ceramic Composites," *Acta Metall.*, **36** [6] 1455-70 (1988).
11. D. K. Shetty, " Mixed-Mode Fracture Criteria for Reliability Analysis and Design with Structural Ceramics," ASME *J. of Eng. for Gas Turbines and Power*, Vol. 109, No. 3, pp 282-289 (1987).
12. K. Palaniswamy and W. G. Knauss, " On the Problem of Crack Extension in Brittle Solids," *Mechanics Today*, Vol. 4, pp 87-148 (1978).
13. D. Singh and D. K. Shetty, " Microstructural Effects on Fracture Toughness of Polycrystalline Ceramics in Combined Mode I and Mode II Loading," ASME paper 88-GT-208 (1988).

14. D. Singh and D. K. Shetty, " Fracture Toughness of Polycrystalline Ceramics in Combined Mode I and Mode II Laoding," *J. Am. Ceram. Soc.*, **72** [1] 78-84 (1989).
15. J. I. Bluhm, " Slice Synthesis of a Three Dimensional "Work of Fracture" Specimens," *Eng. Fract. Mech.*, Vol. **7**, 593-604 (1975).
16. L. Y. Chao and D. K. Shetty, " Reliability Analysis of Structural Ceramics Subjected to Biaxial Flexure," *J. Am. Ceram. Soc.*, **74** [2] 333-344 (1991).
17. R. Szilard, *Theory and Analysis of Plates, Classical and Numerical Methods*; pp. 628, Prentice-Hall, Englewood Cliffs, NJ (1974).
18. J. E. Field, D. A. Gorham, J. T. Hagan, M. J. Mathewson, M. V. Swain and S. Van Der Zwaag, " Liquid Jet Impact and Damage Assessment for Brittle Solids," in Proceedings of the 5th International Conference on Rain Erosion and Allied Phenomena, Cambridge, England, September 1979.
19. K. Trustrum and A. De S. Jayatilaka, " On Estimating the Weibull Modulus for a Brittle Material," *J. Mater. Sci.*, **14** [5], pp 1080-1084 (1979).
20. S. S. Pai and J. P. Gyekenyesi, " Calculation of the Weibull Strength Parameters and the Batdorf Flaw Density Constants for Volume and Surface Flaw Induced Fracture in Ceramics," in Proceedings of the 3rd International Symposium on Ceramic Materials and Components for Engines, Las Vegas, NV, 1988. American Ceramic Society, Westerville, OH (1989).
21. C, A. Johnson, W. T. Tucker, " Advanced Statistical Concepts of Fracture in Brittle Materials," Engineered Materials Handbook, Vol.4, Ceramics and Glasses, ASM International, The Materials Information Society, 1991, pp 709-715.

Appendix A

Silicon Nitride (NT-154)
Test Conditions: Temperature = 70 ^{o}F, Crosshead Speed = 0.05"/min

Precracks inside the notch ($a/R < a_1/R$)		Precracks outside the notch ($a/R > a_1/R$)	
K_I (MPa$\sqrt{m}$)	K_{II} (MPa$\sqrt{m}$)	K_I (MPa$\sqrt{m}$)	K_{II} (MPa$\sqrt{m}$)
5.0977	0.0000	4.8167	0.0000
4.9788	0.8819	4.9182	0.8787
4.6079	1.9868	4.5253	1.9757
4.0998	3.2270	4.1326	3.2744
3.4642	4.8059	3.9292	5.4628
3.4889	4.7460	3.3261	4.6343
2.5257	6.5159	2.5538	6.6148
1.3770	8.0861	1.3973	8.6383
0.0412	9.9309	-0.0086	10.0266
-0.4230	10.5066	-0.5451	11.0515

Appendix B

Silicon Nitride (NT-154)
Test Conditions: Temperature 2200 °F, Crosshead Speed = 0.05"/min

Precracks inside the notch ($a/R < a_1/R$)		Precracks outside the notch ($a/R > a_1/R$)	
K_I (MPa$\sqrt{m}$)	K_{II} (MPa$\sqrt{m}$)	K_I (MPa$\sqrt{m}$)	K_{II} (MPa$\sqrt{m}$)
4.2602	0.0000	4.6895	0.0000
4.0385	2.3051	4.2894	2.4851
2.7093	4.5274	3.0977	5.3109
1.8119	6.4768	1.9052	6.8581

Appendix C

Silicon Nitride (NT-154)
Test Conditions: Temperature = 2200 °F, Crosshead Speed = 0.0005"/min

Precracks inside the notch ($a/R < a_1/R$)		Precracks outside the notch ($a/R > a_1/R$)	
K_I (MPa$\sqrt{m}$)	K_{II} (MPa$\sqrt{m}$)	K_I (MPa$\sqrt{m}$)	K_{II} (MPa$\sqrt{m}$)
4.1780	0.0000	4.8483	0.0000
4.0471	2.3417	4.5960	2.6529
3.0439	5.2013	2.9882	5.2197
1.9214	5.9989	1.7691	6.4357

Appendix D

Silicon Nitride (NT-154)
Test Conditions: Temperature = 2500 °F, Crosshead Speed = 0.05"/min

Precracks inside the notch ($a/R < a_1/R$)		Precracks outside the notch ($a/R > a_1/R$)	
K_I (MPa$\sqrt{m}$)	K_{II} (MPa$\sqrt{m}$)	K_I (MPa$\sqrt{m}$)	K_{II} (MPa$\sqrt{m}$)
4.1556	0.0000	4.4058	0.0000
3.9657	2.2924	3.9901	2.3124
2.6019	4.4853	2.6424	4.5662
1.6885	5.9289	1.4884	5.5862

Appendix E

Silicon Nitride (NT-154, Heat Treated)
Uniform-Pressure-on-Disk Test
Support Circle, r_1 = 24.13 mm

Stressing Rate, $\dot{\sigma}$ = 23 MPa/s

Specimen #	Fracture Pressure (psi)	Fracture Strain	Fracture Stress (MPa)
LPPB 5	1998	0.002169	930.9
LPPB 6	1514	0.001641	704.5
LPPB 7	1432	0.001553	666.8
LPPB 8	1746	0.001894	813.0
LPPB 12	1662	0.001809	776.3
LPPB 13	1464	0.001584	680.0
LPPB 14	1729	0.001872	803.6
LPPB 15	1775	0.001920	823.9
LPPB 16	1549	0.001674	718.6
LPPB 17	1765	0.001908	818.8
LPPB 18	1882	0.002033	872.5
LPPB 19	1498	0.001618	694.5
LPPB 20	1338	0.001444	620.0
LPPB 21	1788	0.001937	831.5
LPPB 22	1752	0.001893	812.7
LPPB 23	1510	0.001632	700.5
LPPB 24	1578	0.001709	733.4
LPPB 25	1159	0.001259	540.3
LPPB 26	1514	0.001642	705.0
LPPB 27	1402	0.001528	655.7
LPPB 28	1736	0.001889	810.9
LPPB 29	1429	0.001550	665.4
LPPB 30	1423	0.001545	663.0
LPPB 31	1800	0.001955	839.2
LPPB 40	1687	0.001831	786.0
LPPB 41	1426	0.001549	664.8
LPPB 42	1751	0.001903	816.8
LPPB 43	1489	0.001617	694.2
LPPB 44	1774	0.001926	826.5
LPPB 45	1368	0.001484	637.0
LPPB 46	1602	0.001744	748.7
LPPB 47	1655	0.001802	773.5
LPPB 48	1668	0.001815	779.1
LPPB 49	1583	0.001735	744.5
LPPB 50	1668	0.001838	789.0
LPPB 51	1559	0.001718	737.4
LPPB 52	1794	0.001976	848.0

APPENDIX III

MODE I/MODE II FRACTURE TOUGHNESS AND TENSION/TORSION FRACTURE STRENGTH OF NT154 SILICON NITRIDE

(BROWN UNIVERSITY REPORT)

(18 pages)

Mode I/Mode III Fracture Toughness and Tension/Torsion Fracture Strength of NT154 Si_3N_4

(Preliminary Report)

A.S. Kim and S. Suresh
Division of Engineering
Brown University
Providence, RI 02912

February 1993

INTRODUCTION

The following preliminary report is a summary of the technical results of the Mode I/Mode III and tension/torsion testing program of NT154 Si_3N_4 received from Garrett Auxiliary Power Division (GAPD) under Contract Award Number 2331700/2331710. The testing program for both Mode I/Mode III and tension/torsion testing of notched and unnotched specimens, respectively, has now been completed.

The objective of this program is considered in two phases. The first phase involves determining the Mode I and Mode III fracture toughness of NT154 Si_3N_4 as well as the full fracture toughness envelope between the two pure mode fracture conditions. The second phase of the program involves evaluating the pure torsional strength and combined tensile/torsional strength of the same material. The maximum tensile loads in this phase were limited by the capacity of the testing machine. The fracture envelope between the pure torsion and maximum tension/torsion tests is also obtained.

The Mode I/Mode III tests were performed using notched, pre-cracked 19 mm diameter cylindrical rods containing a sharp pre-crack induced under cyclic compression fatigue. For the tension/torsion tests, unnotched 19 mm cylindrical rods with a reduced mid-section approximately 30.5 mm long and 6.35 mm in diameter were used. A total of 29 cylindrical rods and 40 reduced mid-section rods was received for Mode I/Mode III and tension/torsion testing, respectively. In addition, 3 reduced mid-section rods were received to be used for alignment verification of the testing machine.

All tests were carried out on an Instron Model 1322 servo-hydraulic bi-axial testing machine. The Si_3N_4 specimens were held in cylindrical hardened steel sleeves which had an inner diameter of 19 mm and slots in the direction of the tube axes and extending halfway along the length of the sleeve on opposite sides. The specimens were inserted into the sleeves and gripped by placing two split collets around the sleeves at each end of the specimen. The testing configuration is shown in Figure 1. The tests were performed in laboratory air at room temperature

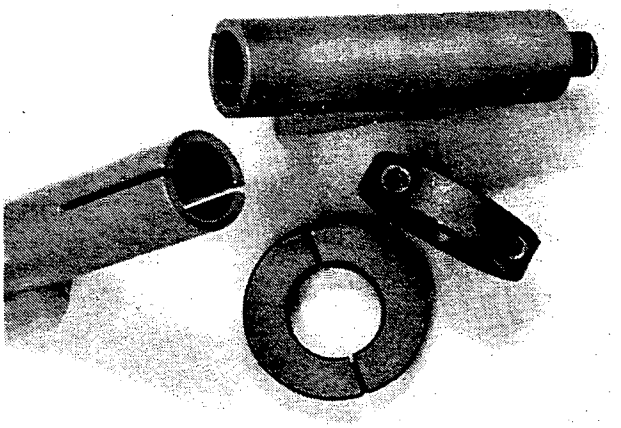

2 cm
127022-40

GB11591-711

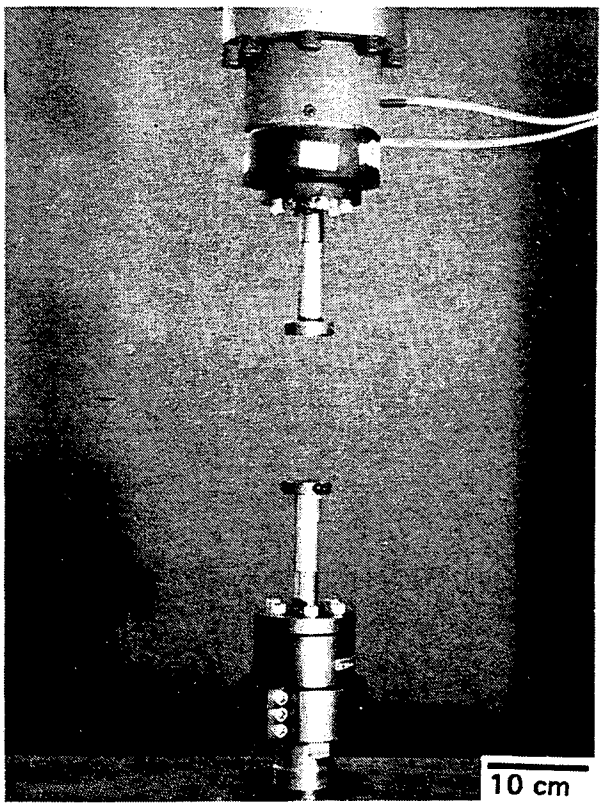

10 cm
127022-40

FIGURE 1

As reported earlier, alignment procedures were performed according to specifications prescribed by GAPD. Alignment verification results showed that the percent bending of the alignment train was less than the maximum allowed value of 5% as prescribed by both GAPD and ASTM Standard E1012-89. Strain gages were mounted on two different specimens at 90° intervals around the circumference of the specimens and the strains were recorded at various loads and specimen orientations. Two specimens were used for the verification procedure. The first specimen had 4 strain gages at the mid-section of the reduced cross-sectional area while the second specimen had 4 strain gages on each of two planes along the reduced cross-sectional area for a total of 8 strain gages on this specimen. The results of the alignment verification are summarized in Appendix A.

MODE I/MODE III FRACTURE TOUGHNESS

The 19 mm cylindrical specimens, were notched with a diamond wheel to an inner diameter of 8.9 mm and average notch root radius of 100 μm. They were then cycled on an MTS servo-hydraulic testing machine for 100,000 cycles at 20 Hz in uniaxial cyclic compression. The load and R ratio (Pmax/Pmin) values used for pre-cracking, -5 kN to -85 kN, R = 17, were systematically determined prior to testing. Three cylindrical 19 mm rods were cut into thirds, notched with a diamond wheel, and then cycled in compression at various loads and R ratios to determine these conditions.

Tests were performed on notched, pre-cracked specimens to determine the Mode I fracture toughness, the Mode III fracture toughness, and the combined Mode I/Mode III fracture envelope between these two pure mode fracture conditions. With the exception of two specimens (#LPPTT 30 and #LPPTT 38), the Mode I/Mode III tests were performed by first ramping the tension to the desired load, then ramping the torsion until failure. The loading path of the two specimens mentioned previously was reversed, i.e., they were first loaded in torsion, then ramped in tension until failure. Considering the different loading path used for these two specimens, their slight deviation (particularly for #LPPTT 30) from the general trend is not surprising.

Of the 29 cylindrical rods received from GAPD, 17 were successfully tested to generate a complete Mode I/Mode III fracture envelope. Three rods were used to determine the cyclic compression load range needed to induce, before the actual Mode I/Mode III test, a sharp pre-crack at the tip of the notch, and eight specimens were broken during handling or mounting of the specimens or at sufficiently low loads that the test was considered to be invalid. The status of the eight specimens not included in the results is listed in Appendix B. The specimens which failed during mounting were mounted in a similar manner to those which were successfully mounted and tested. The high failure rate of the specimens during mounting indicates that the sharp pre-crack at the tip of the notch made the specimens much more sensitive to loads than the notched but unpre-cracked specimens.

The results of this phase of the testing program are summarized in Table 1 and Figure 2. The Mode I fracture toughness of the material was determined to be KI_C = 4.35 MPa$\sqrt{m}$ (±3.8%). The apparent Mode III fracture toughness was found to be $KIII_C$ = 8.98 MPa$\sqrt{m}$ (±4.42%), a factor of 2.1 times the Mode I

TABLE 1

SUMMARY OF MODE I/MODE III FRACTURE TOUGHNESS TESTING OF NT154 SI3N4

Mod. of Elas., E = 3.1E+05 MPa
Poisson's ratio, v = 0.27

FILE: GVKIII.WQ1

Specimen #	KI (MPa^m)	KIII (MPa^m)	KI/KIII	KIIIc	G (N/m)	KIII/KIIIc
LPPTT 30	5.41	1.83	2.96	8.98	101.25	0.204
LPPTT 3	4.61	0.46	10.02	8.98	64.42	0.051
LPPTT 23	4.50	0.11	40.91	8.98	60.61	0.012
LPPTT 38	4.43	0.18	24.61	8.98	58.82	0.020
LPPTT 29	4.12	0.13	31.69	8.98	50.83	0.014
LPPTT 4	3.95	0.27	14.63	8.98	46.96	0.030
LPPTT 28	3.86	5.02	0.77	8.98	147.80	0.559
LPPTT 27	3.30	6.21	0.53	8.98	190.56	0.692
LPPTT 19	3.15	6.51	0.48	8.98	203.30	0.725
LPPTT 8	2.27	7.48	0.30	8.98	244.63	0.833
LPPTT 22	2.13	7.83	0.27	8.98	264.74	0.872
LPPTT 20	1.13	8.71	0.13	8.98	314.62	0.970
LPPTT 7	0.36	9.03	0.04	8.98	334.44	1.006
LPPTT 21	0.31	9.14	0.03	8.98	342.53	1.018
LPPTT 25	0.06	9.42	0.01	8.98	363.54	1.049
LPPTT 34	0.05	8.34	0.01	8.98	284.96	0.929
LPPTT 6	-0.48	8.19	-0.06	8.98	275.48	0.912

Strain Energy Release Rate, $G = (KI^2)(1-v^2)/E+(KIII^)2(1+v)/E$

Average Mode I fracture toughness based on values obtained from specimens #23, #38, and #29:

Avg. KIc:	4.35	MPa^m
STD(+/-):	0.17	MPa^m
Percent(+/-):	3.80	%

Average Mode III fracture toughness based on values obtained from specimens #7, #21, #25, and #34:

Avg. KIIIc:	8.98	MPa^m
STD(+/-):	0.40	MPa^m
Percent(+/-):	4.42	%

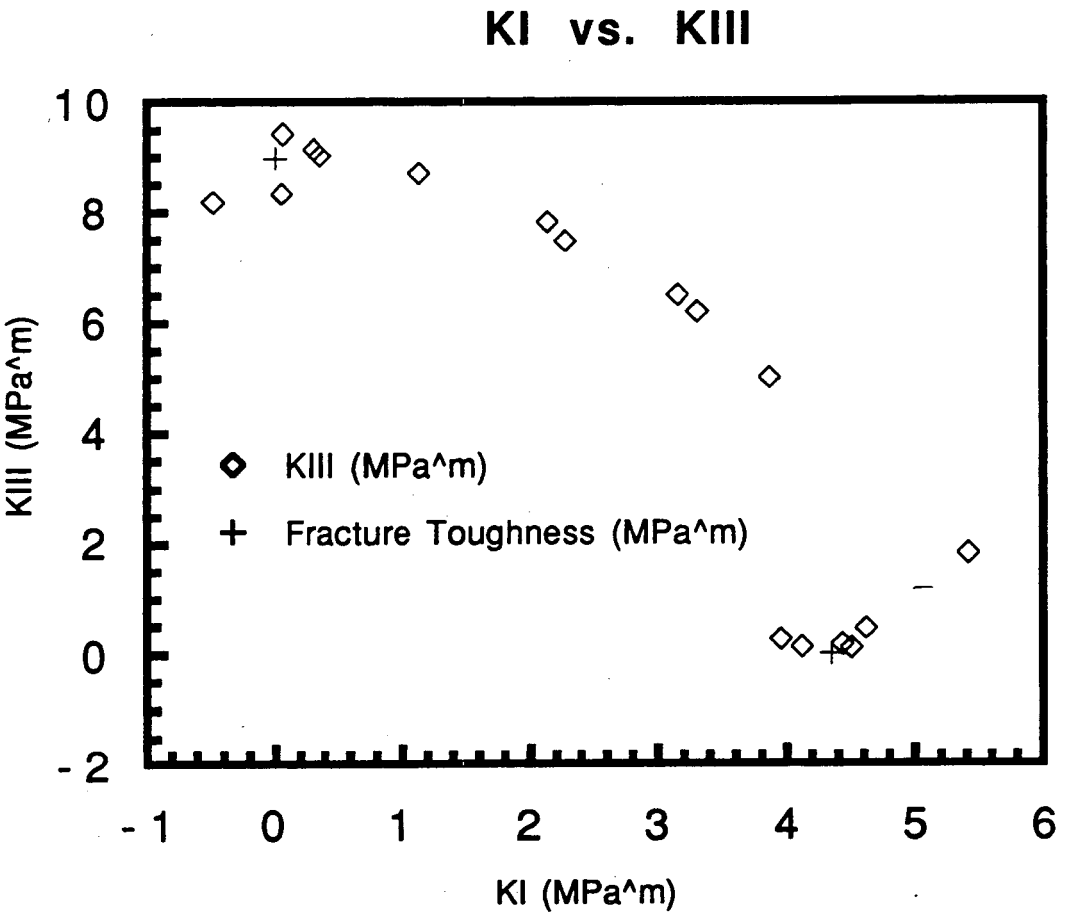

GB11591-851

FIGURE 2

fracture toughness. The higher value of the Mode III fracture toughness suggests that the effect of micro mechanisms such as crack face abrasion and locking of crack face asperities may have a significant effect on the Mode III fracture toughness values obtained.

TENSION/TORSION FRACTURE STRENGTH

The objective of the second phase of the testing program was to determine the tension and torsion loads required for failure of reduced mid-section rods with a minimum diameter of 6.35 mm along the mid-section of the rod and maximum diameter of 19 mm at each end where the specimen was gripped in the cylindrical sleeves. Tests were performed at pure torsion, maximum possible tension (as dictated by the limits of the testing machine) followed by torsion, and two points in-between, for which the tensile loads were equally spaced between zero and the maximum possible tensile load.

The distribution of tests may be summarized as follows:

Pure torsion

Applied tension 105 MPa/torsion
Applied tension 211 MPa/torsion
Applied tension 334.8 MPa/torsion

Applied torsion -624.3 MPa/tension and, as needed, further torsion
(applied torsion based on average results of the Applied tension 334.8 MPa/torsion tests)

For all but the last group of tests, the tensile load was applied first, followed by increasing torsion until failure. Results are reported for 36 of the 40 specimens and are shown in Table 2 and Figs. 3 and 4. Included in this table are the maximum load and torque for each of the tests, the normal and shear stresses, the maximum and minimum principal stresses, and the calculated angle which the maximum normal stress makes with the loading axis. The tests of the remaining 4 specimens were not included because the values obtained were considered invalid for the reasons described in Appendix B

The results of this phase of the testing program indicate an average maximum shear stress (no applied normal stress) of -796.8 MPa (± 11.5%). Under an applied normal stress of 334.8 MPa, the average shear stress was -624.3 MPa (± 10.4%). For an applied normal stress of 210.8 MPa, the average shear stress was -742.5 MPa (± 4.4%). Finally, for an applied normal stress of 105.4 MPa (750 lb), the average normal stress was -800.4 MPa (± 9.2%). For the tests performed with an initial applied shear stress of -624.3 MPa and then tension with further torsion as needed to induce failure, the average normal stress was 290.7 MPa (± 21.6%) with an average shear stress of -700.7 MPa (± 9.4%) .

TABLE 2

Garrett Hourglass Specimens — FILE: HFINAL.WQ1 — d = 0.25 in.
Tension-Torsion Test — r = 0.125 in.
February 13, 1992 — A = 0.049087 sq. in.

Spec. #	Load (lb)	Torque (lb-in)	sigma z (psi)	tau z th (psi)	sigma z (MPa)	tau z th (MPa)	Sigma 1 (MPa)	Sigma 2 (MPa)	Theta (degrees)
LPUTT12	2391.0	-315.0	48.7	-102.7	335.8	-707.9	895.5	-559.7	-38.3
LPUTT15	2385.0	-274.0	48.6	-89.3	335.0	-615.8	805.7	-470.7	-37.4
LPUTT14	2382.0	-273.0	48.5	-89.0	334.6	-613.5	803.2	-468.7	-37.4
LPUTT17	2381.0	-229.0	48.5	-74.6	334.4	-514.7	708.4	-373.9	-36.0
LPUTT18	2380.0	-298.0	48.5	-97.1	334.3	-669.7	857.4	-523.1	-38.0
Average	2383.8	-277.8	48.6	-90.5	334.8	-624.3	814.0	-479.2	-37.4
STD(+/-)	4.0	29.0	0.1	9.5	0.6	65.2	63.0	62.7	0.8
%(+/-)	0.2	-10.4	0.2	-10.4	0.2	-10.4	7.7	-13.1	-2.1
LPUTT20	1501.0	-347.0	30.6	-113.1	210.8	-779.9	892.4	-681.5	-41.2
LPUTT21	1501.0	-346.0	30.6	-112.8	210.8	-777.6	890.1	-679.3	-41.1
LPUTT22	1500.0	-329.0	30.6	-107.2	210.7	-739.4	852.2	-641.5	-40.9
LPUTT24	1500.0	-320.0	30.6	-104.3	210.7	-719.2	832.2	-621.5	-40.8
LPUTT33	1500.0	-310.0	30.6	-101.0	210.7	-696.7	810.0	-599.3	-40.7
Average	1500.4	-330.4	30.6	-107.7	210.8	-742.5	855.4	-644.6	-41.0
STD(+/-)	0.5	14.5	0.0	4.7	0.1	32.5	32.2	32.1	0.2
%(+/-)	0.0	-4.4	0.0	-4.4	0.0	-4.4	3.8	-5.0	-0.4
LPUTT25	752.0	-317.0	15.3	-103.3	105.6	-712.4	767.2	-661.6	-42.9
LPUTT28	750.0	-363.0	15.3	-118.3	105.3	-815.8	870.2	-764.8	-43.2
LPUTT29	750.0	-387.0	15.3	-126.1	105.3	-869.8	924.0	-818.7	-43.3
LPUTT32	750.0	-407.0	15.3	-132.7	105.3	-914.7	968.9	-863.5	-43.4
LPUTT34	751.0	-307.0	15.3	-100.1	105.5	-690.0	744.7	-639.2	-42.8
LPUTT35	749.0	-351.0	15.3	-114.4	105.2	-788.8	843.2	-738.0	-43.1
LPUTT36	751.0	-361.0	15.3	-117.7	105.5	-811.3	865.8	-760.3	-43.1
Average	750.4	-356.1	15.3	-116.1	105.4	-800.4	854.9	-749.4	-43.1
STD(+/-)	0.9	32.9	0.0	10.7	0.1	74.0	73.8	73.8	0.2
%(+/-)	0.1	-9.2	0.1	-9.2	0.1	-9.2	8.6	-9.9	-0.4
LPUTT3	0.0	-420.0	0.0	-136.9	0.0	-943.9	943.9	-943.9	-45.0
LPUTT4	0.0	-380.0	0.0	-123.9	0.0	-854.0	854.0	-854.0	-45.0
LPUTT5	0.0	-340.0	0.0	-110.8	0.0	-764.1	764.1	-764.1	-45.0
LPUTT6	0.0	-380.0	0.0	-123.9	0.0	-854.0	854.0	-854.0	-45.0
LPUTT7	0.0	-320.0	0.0	-104.3	0.0	-719.2	719.2	-719.2	-45.0
LPUTT8	0.0	-400.0	0.0	-130.4	0.0	-899.0	899.0	-899.0	-45.0
LPUTT9	0.0	-360.0	0.0	-117.3	0.0	-809.1	809.1	-809.1	-45.0
LPUTT10	0.0	-360.0	0.0	-117.3	0.0	-809.1	809.1	-809.1	-45.0
LPUTT45	1.2207	-371.6	0.0	-121.1	0.2	-835.1	835.2	-835.1	-45.0
LPUTT47	-1.2207	-278.3	-0.0	-90.7	-0.2	-625.5	625.4	-625.5	45.0
LPUTT48	0.0	-301.8	0.0	-98.4	0.0	-678.3	678.3	-678.3	-45.0
LPUTT49	0.0	-390.1	0.0	-127.2	0.0	-876.7	876.7	-876.7	-45.0
LPUTT50	0.0	-307.1	0.0	-100.1	0.0	-690.2	690.2	-690.2	-45.0
Average	0.0	-354.5	0.0	-115.6	0.0	-796.8	796.8	-796.8	-38.1
STD(+/-)	0.5	40.7	0.0	13.3	0.1	91.4	91.4	91.4	24.0
%(+/-)	**********	-11.5	**********	-11.5	**********	-11.5	11.5	-11.5	-63.0
LPUTT38	2379.2	-360.4	48.5	-117.5	334.2	-810.0	994.1	-659.9	-39.2
LPUTT39	1807.0	-285.0	36.8	-92.9	253.8	-640.5	779.9	-526.1	-39.4
LPUTT40	2376.7	-319.8	48.4	-104.2	333.8	-718.7	904.8	-570.9	-38.5
LPUTT42	2290.0	-285.0	46.7	-92.9	321.7	-640.5	821.2	-499.6	-38.0
LPUTT43	2386.5	-335.4	48.6	-109.3	335.2	-753.8	939.8	-604.6	-38.7
LPUTT44	1180.0	-285.0	24.0	-92.9	165.7	-640.5	728.7	-563.0	-41.3
Average	2069.9	-311.8	42.2	-101.6	290.7	-700.7	861.4	-570.7	-39.2
STD(+/-)	447.1	29.3	9.1	9.5	62.8	65.8	92.7	52.0	1.1
%(+/-)	21.6	-9.4	21.6	-9.4	21.6	-9.4	10.8	-9.1	-2.7

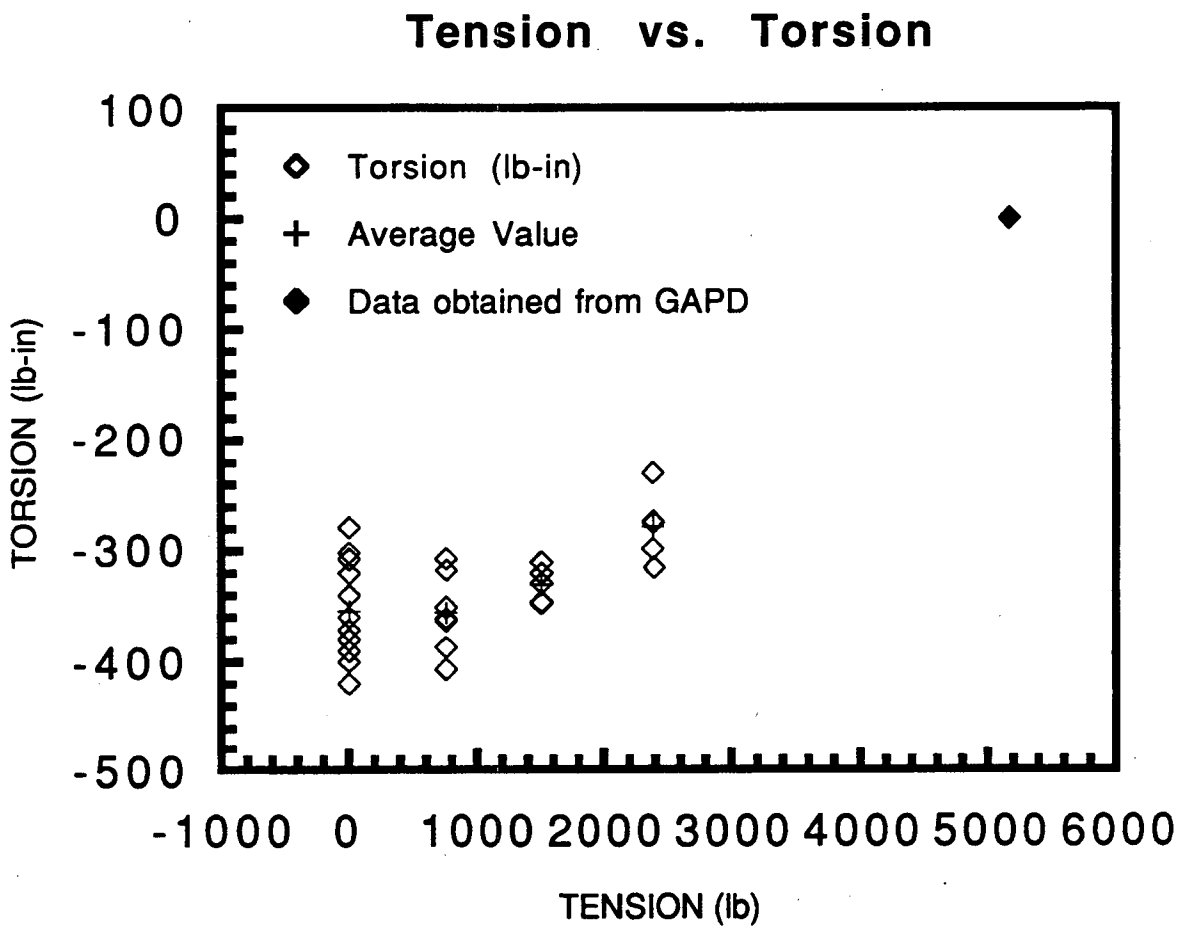

GB11591-852

FIGURE 3

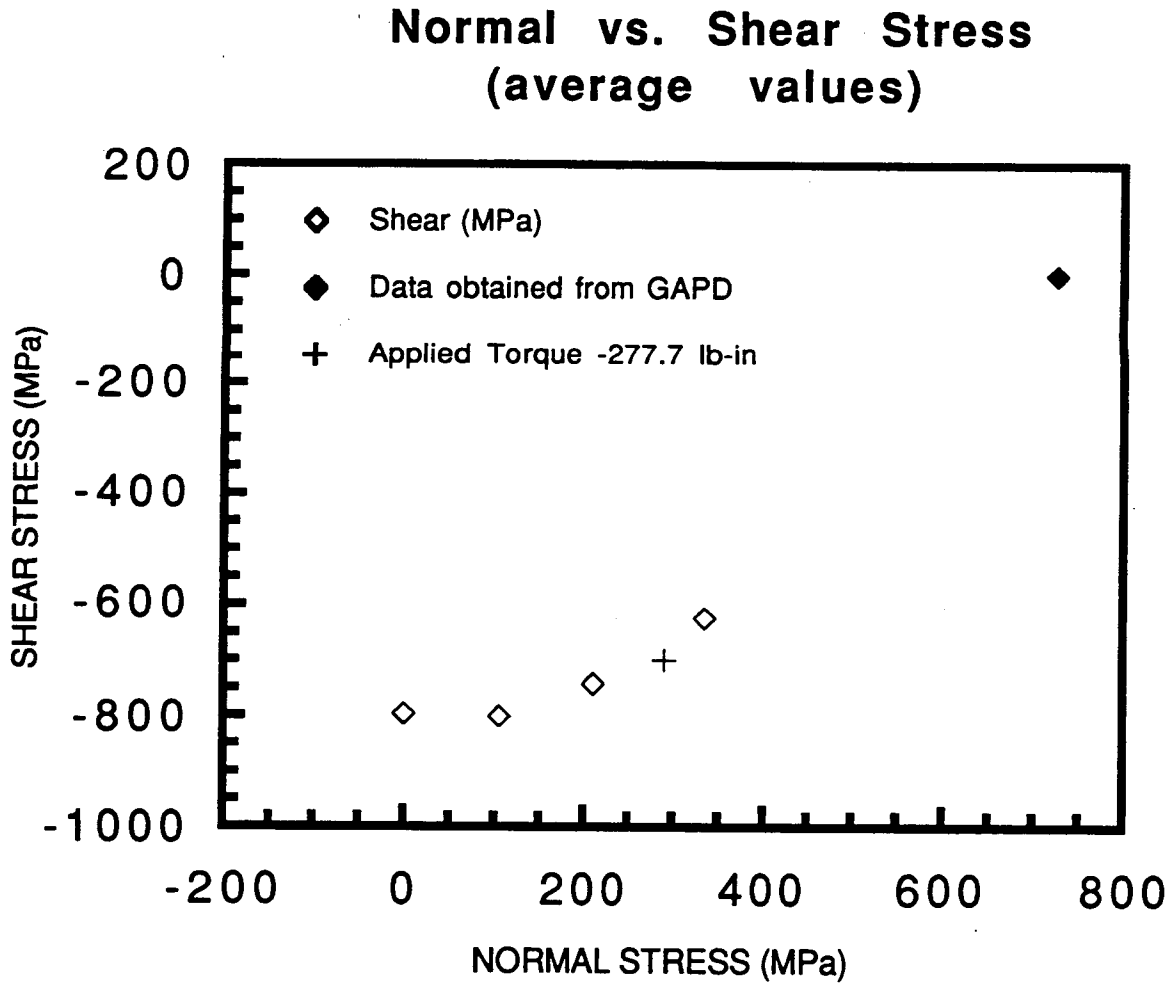

GB11591-853

FIGURE 4

CONCLUSIONS

- A sharp pre-crack approximately 100 μm long was successfully induced in notched, 19 mm cylindrical NT154 Si_3N_4 rods subjected to cyclic compression.

- Alignment of the Instron 1322 servo-hydraulic bi-axial testing machine used for this testing program was verified and found to be less than 5% bending as prescribed by both GAPD and ASTM Standard E1012-89.

- Pure Mode I and pure Mode III fracture toughness values, KI_C and $KIII_C$, respectively were obtained for NT154 Si_3N_4. KI_C was found to be 4.35 MPa$\sqrt{m}$ (± 3.8%) and $KIII_C$ was found to be 8.98 MPa$\sqrt{m}$ (± 4.42%). The full fracture envelope between these two values was also obtained.

- Pure torsion and tension/torsion strengths of NT154 Si_3N_4 were also determined. The shear strength of this material under pure torsion was found to be -796.8 MPa (± 11.5%). Under an applied tension of 334.8 MPa, the shear strength was -624.3 MPa (± 10.4%). The fracture conditions for two points between these two conditions was also obtained.

APPENDICES

APPENDIX A

SUMMARY OF PERCENT BENDING CALCULATIONS FILE: 251SUMMA.WQ1

Specimen #51
30 ksi (1500 lbs.)

		1st cycle	2nd cycle	3rd cycle	4th cycle	5th cycle
0 Degrees Rotation	(upper plane)	1.27	0.36	0.25	0.25	0.25
	(lower plane)	2.05	1.93	1.82	1.82	1.7
90 Degrees Rotation	(upper plane)	1.96	2.15	2.37	2.16	2.17
	(lower plane)	2.82	2.19	2.51	2.33	2.33
180 Degrees Rotation	(upper plane)	1.94	0.57	0.72	0.54	0.56
	(lower plane)	2.27	0.57	0.4	0.54	0.4
270 Degrees Rotation	(upper plane)	1.3	1.07	1.08	1.25	1.41
	(lower plane)	1.32	0.92	0.97	1.04	0.8
360 Degrees Rotation	(upper plane)	2.65	2.34	2.58	2.58	2.73
	(lower plane)	1.83	1.67	1.81	1.81	1.81
Best Condition	(upper plane)	2.4	1.83	1.74	1.74	1.62
	(lower plane)	2.64	2.24	2.15	2.47	2.31
Worst Condition	(upper plane)	3.6	3.54	3.29	3.62	3.89
	(lower plane)	2.38	2.53	2.54	2.7	2.73

Specimen #16
30 ksi (1500 lbs.)

		1st cycle	2nd cycle	3rd cycle	4th cycle	5th cycle
0 Degrees Rotation	(center plane)	2.59	1.84	1.59	1.56	1.51
90 Degrees Rotation	(center plane)	1.88	1.36	1.03	1.07	0.99
180 Degrees Rotation	(center plane)	1.94	1.38	1.38	1.25	1.3
270 Degrees Rotation	(center plane)	2.42	2.35	1.93	2.08	2.04
360 Degrees Rotation	(center plane)	1.91	1.75	1.69	1.83	2.14

APPENDIX B

SPECIMEN #:	REASON FOR REJECTION:
LPPTT9	Failed due to failure of pre-cracking block (no data)
LPPTT12	Failed while ramping tension (possibly defect)
LPPTT16	Failed during mounting (no data)
LPPTT18	Failed during mounting (no data)
LPPTT26	Failed during mounting (no data)
LPPTT31	Failed during test preparation (no data)
LPPTT36	Failed at very low loads (possibly defect)
LPPTT37	Failed during mounting (no data)
LPUTT2	Slipped during testing (may or may not be valid)
LPUTT11	Non-linear load-disp. curve (reason unknown)
LPUTT13	Failed at very low loads, localized area (possibly defect)
LPUTT41	Failed at very low loads

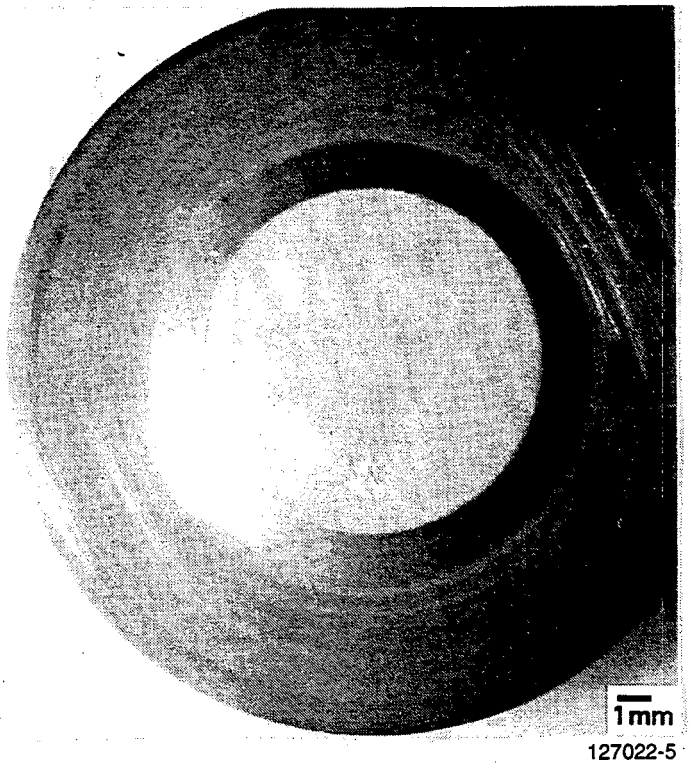

MODE I
(Specimen LPPTT23)

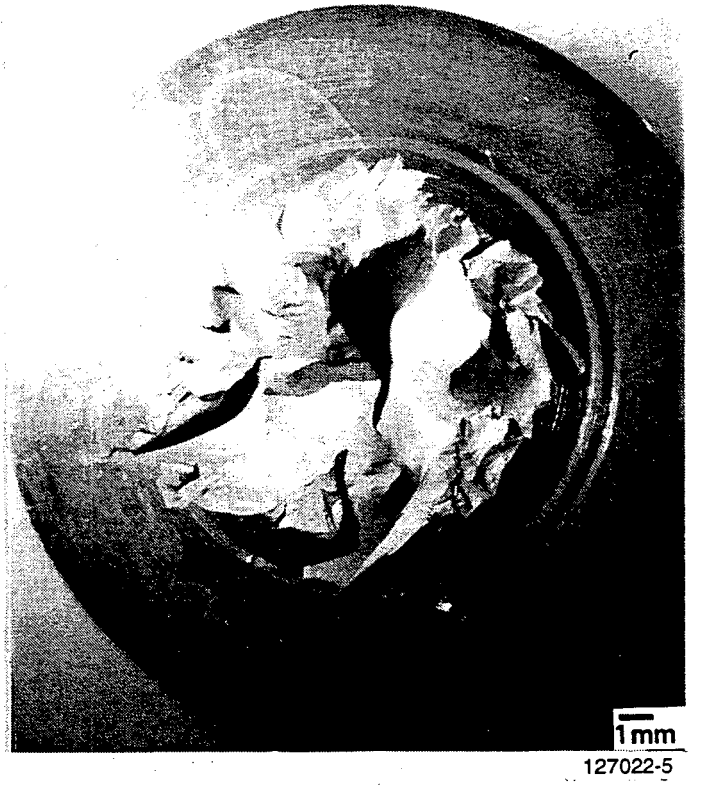

MODE III
(Specimen LPPTT7)

GB11591-712

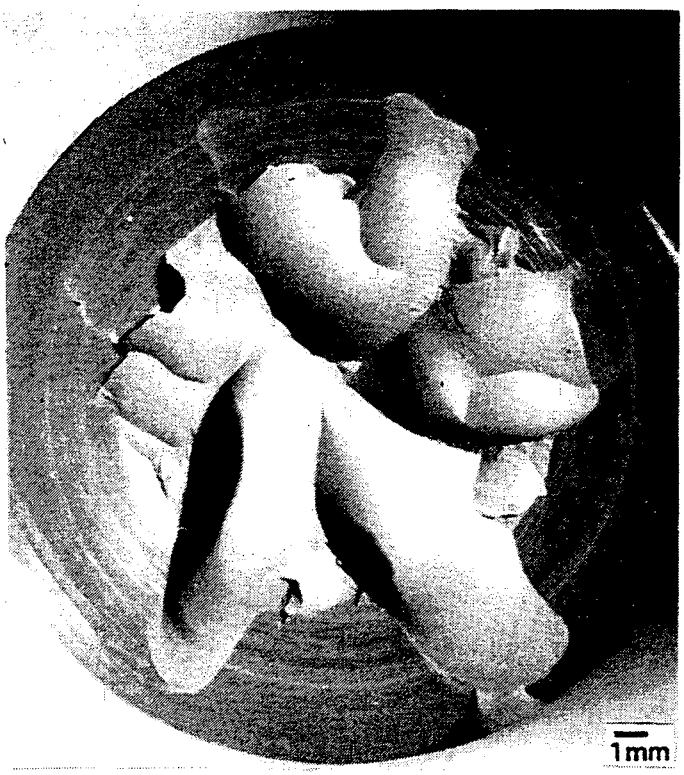

LPPTT22

LPPTT20

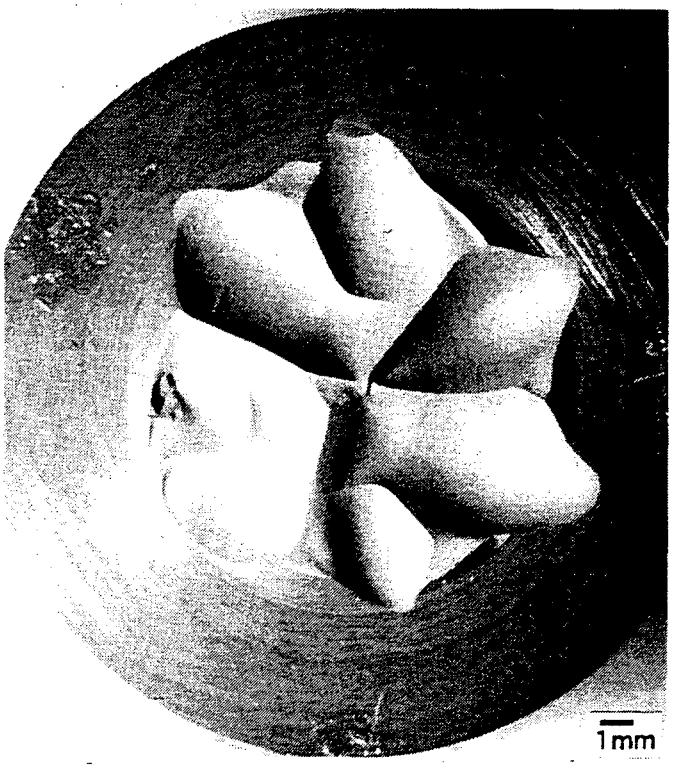

LPPTT19

GB11591-713

127022-6

APPENDIX IV

SUMMARY OF STRENGTH TEST RESULTS AND FRACTOGRAPHY

(42 pages)

AlliedSignal
AEROSPACE

TABLE 1. 4-POINT FLEXURE DATA OF MIL-A AND MIL-B SPECIMENS

LONGITUDINAL MACHINED MIL-A FLEXURE BARS

Specimen Number	Stress (ksi)	Fracture Origin Location	Fracture Origin Type	Comments
LPA-1	152.0	Surface	Surface	
LPA-2	142.5	Surface	Surface	
LPA-3	132.0	Corner	Surface	
LPA-4	136.8	Corner	Surface	Tested edgewise
LPA-5	110.0	Internal	Inclusion	Dark inclusion
LPA-6	120.4	Corner	Surface	
LPA-7	142.5	Corner	Surface	
LPA-8	159.4	Corner	Surface	
LPA-9	105.8	Corner	Surface	Possible corner damage
LPA-10	149.9	Corner	Surface	
LPA-11	130.5	Corner	Surface	
LPA-12	153.1	Surface	Surface	
LPA-13	140.4	Corner	Surface	
LPA-14	125.6	Corner	Surface	
LPA-15	144.6	Corner	Surface	
LPA-16	152.2	Corner	Surface	
LPA-17	90.8	Corner	Surface	Possible corner damage
LPA-18	110.2	Corner	Surface	
LPA-19	132.6	Corner	Surface	
LPA-20	139.8	Corner	Surface	
LPA-21	119.3	Corner	Surface	
LPA-22	138.7	Surface	Surface	
LPA-23	110.9	Corner	Surface	
LPA-24	151.0	Corner	Surface	
LPA-25	137.2	Corner	Surface	
LPA-26	87.6	Corner	Surface	Possible corner damage
LPA-27	145.3	Corner	Surface	
LPA-28	134.1	Corner	Surface	
LPA-29	137.7	Corner	Surface	
LPA-30	99.5	Corner	Surface	Possible corner damage
LPA-31	149.5	Surface	Surface	
LPA-32	151.0	Corner	Surface	
LPA-33	116.6	Corner	Surface	
LPA-34	151.0	Corner	Surface	
LPA-35	98.8	Corner	Surface	Possible corner damage
LPA-36	143.6	Surface	Surface	
LPA-37	130.9	Corner	Surface	
LPA-38	152.0	Surface	Surface	
LPA-39	133.4	Corner	Surface	
LPA-40	135.1	Corner	Surface	
LPA-41	110.2	Corner	Surface	
LPA-42	153.1	Corner	Surface	
LPA-43	111.5	Corner	Surface	

AlliedSignal
AEROSPACE

TABLE 1. 4-POINT FLEXURE DATA OF MIL-A AND MIL-B SPECIMENS (Contd)

LONGITUDINAL MACHINED MIL-A FLEXURE BARS (Contd)

Specimen Number	Stress (ksi)	Fracture Origin Location	Fracture Origin Type	Comments
LPA-44	144.6	Corner	Surface	
LPA-45	135.1	Corner	Surface	
LPA-46	122.5	Corner	Surface	
LPA-47	148.9	Corner	Surface	
LPA-48	148.2	Surface	Surface	
LPA-49	144.6	Corner	Surface	
LPA-50	135.1	Surface	Surface	
LPA-51	114.2	Corner	Surface	
LPA-52	159.4	Corner	Surface	
LPA-53	130.5	Corner	Surface	
LPA-54	140.4	Corner	Surface	
LPA-55	136.2	Corner	Surface	
LPA-56	143.6	Corner	Surface	
LPA-57	157.3	Surface	Surface	
LPA-58	80.4	Corner	Surface	Possible corner damage
LPA-59	130.5	Corner	Surface	
LPA-60	135.1	Corner	Surface	

Nominal Specimen Dimensions: Mil-A, 1.5x2x25 mm
Loading Fixture Geometry:
Four point loading with 10 mm inner span and 20 mm outer span.
Modified room temp. ORNL/HTML IEA Round-robin steel fixture.

AlliedSignal AEROSPACE

TABLE 1. 4-POINT FLEXURE DATA OF MIL-A AND MIL-B SPECIMENS (Contd)

LONGITUDINAL MACHINED MIL-B BARS

Specimen Number	Test Temp, F	Stress, ksi	Fracture Origin Location	Fracture Origin Type	Comments
LPBL-1	70	91.8	Corner	Chip	
LPBL-2	70	129.1	Internal	Pit	
LPBL-3	70	71.9	Corner	Chip	
LPBL-4	70	113.5	Corner	Surface	
LPBL-5	70	98.3	Corner	Surface	
LPBL-6	70	148.6	Corner	Surface	
LPBL-7	70	149.7	Corner	Surface	
LPBL-8	70	117.2	Corner	Surface	
LPBL-9	70	110.8	Corner	Surface	
LPBL-10	70	143.2	Surface	Surface	
LPBL-11	70	88.6	Corner	Surface	
LPBL-12	70	116.7	Corner	Surface	
LPBL-13	70	85.9	Corner	Surface	
LPBL-14	70	89.1	Surface	Surface	
LPBL-15	70	147.0	Corner	Surface	
LPBL-16	70	127.0	Corner	Surface	
LPBL-17	70	131.8	Corner	Surface	
LPBL-18	70	122.1	Corner	Surface	
LPBL-19	70	102.1	Internal	Inclusion	
LPBL-20	70	159.4	Surface	Surface	
LPBL-21	70	130.2	Corner	Surface	
LPBL-22	70	124.8	Corner	Surface	
LPBL-23	70	130.2	Corner	Surface	
LPBL-24	70	139.4	Surface	Surface	
LPBL-25	70	132.9	Corner	Surface	
LPBL-26	70	141.0	Corner	Surface	
LPBL-27	70	161.5	Corner	Surface	
LPBL-28	70	151.3	Corner	Surface	
LPBL-29	70	130.7	Surface	Surface	
LPBL-30	70	77.3	Corner	Surface	
LPBL-31	70	144.3	Corner	Surface	
LPBL-32	70	172.4	Surface	Surface	
LPBL-33	70	151.3	Surface	Surface	
LPBL-34	70	148.6	Corner	Surface	
LPBL-35	70	167.5	Surface	Surface	
LPBL-36	70	142.6	Surface	Surface	Machining line
LPBL-37	70	159.4	Surface	Surface	
LPBL-38	70	95.6	Corner	Surface	Chip with smear
LPBL-39	70	136.2	Surface	Surface	
LPBL-40	70	131.3	Corner	Surface	
LPBL-41	70	157.8	Surface	Surface	
LPBL-42	70	155.1	Corner	Surface	
LPBL-43	70	152.4	Corner	Surface	

AlliedSignal
AEROSPACE

TABLE 1. 4-POINT FLEXURE DATA OF MIL-A AND MIL-B SPECIMENS (Contd)

LONGITUDINAL MACHINED MIL-B BARS (Contd)

Specimen Number	Test Temp, F	Stress, ksi	Fracture Origin Location	Type	Comments
LPBL-44	70	144.3	Surface	Surface	
LPBL-45	70	134.0	Corner	Surface	
LPBL-46	70	157.2	Corner	Surface	
LPBL-47	70	131.3	Corner	Surface	
LPBL-48	70	157.8	Surface	Surface	
LPBL-49	70	158.8	Corner	Surface	
LPBL-50	70	127.0	Surface	Surface	
LPBL-51	70	144.3	Surface	Surface	
LPBL-52	70	115.6	Corner	Surface	
LPBL-163	70	135.7	Corner	Surface	
LPBL-164	70	137.3	Surface	Surface	
LPBL-165	70	156.2	Internal	Void	
LPBL-166	70	156.2	Corner	Surface	
LPBL-167	70	112.6	Corner	Surface	
LPBL-168	70	158.3	Internal	Inclusion	
LPBL-169	70	156.2	Corner	Surface	
LPBL-170	70	107.7	Internal	Inclusion	
LPBL-53	1800	104.2	Surface	Surface	
LPBL-54	1800	105.8	Surface	Surface	
LPBL-55	1800	133.4	Surface	Surface	
LPBL-56	1800	146.2	Surface	Surface	
LPBL-57	1800	107.9	Surface	Surface	
LPBL-58	1800	94.5	Surface	Surface	
LPBL-59	1800	100.1	Surface	Surface	
LPBL-60	1800	106.6	Surface	Surface	
LPBL-61	1800	109.6	Corner	Chip	
LPBL-62	1800	113.5	Surface	Surface	
LPBL-63	1800	136.2	Surface	Surface	Machining line
LPBL-64	1800	109.9	Surface	Surface	Good photo
LPBL-65	1800	106.4	Surface	Surface	
LPBL-66	1800	103.2	Corner	Surface	
LPBL-67	1800	107.1	Surface	Surface	
LPBL-68	1800	107.0	Surface	Surface	
LPBL-69	1800	102.7	Corner	Surface	
LPBL-70	1800	143.2	Surface	Surface	Bottom corner
LPBL-71	1800	126.4	Surface	Surface	
LPBL-72	1800	105.9	Surface	Surface	
LPBL-73	1800	108.6	Corner	Surface	
LPBL-74	1800	103.2	Corner	Surface	
LPBL-75	1800	96.7	Surface	Surface	
LPBL-76	1800	100.0	Surface	Chip	
LPBL-77	1800	114.5	Surface	Surface	
LPBL-78	1800	104.3	Surface	Surface	

TABLE 1. 4-POINT FLEXURE DATA OF MIL-A AND MIL-B SPECIMENS (Contd)

LONGITUDINAL MACHINED MIL-B BARS (Contd)

Specimen Number	Test Temp, F	Stress, ksi	Fracture Origin Location	Type	Comments
LPBL-79	1800	101.0	Corner	Surface	
LPBL-81	1800	109.1	Surface	Surface	
LPBL-82	1800	109.1	Surface	Surface	
LPBL-83	1800	107.5	Corner	Surface	
LPBL-84	2100	90.2	Surface	Surface	
LPBL-85	2100	94.6	Surface	Surface	
LPBL-86	2100	96.7	Corner	Surface	
LPBL-88	2100	88.6	Corner	Crack	
LPBL-89	2100	92.9	Surface	Surface	
LPBL-90	2100	87.5	Surface	Surface	
LPBL-91	2100	90.2	Corner	Surface	
LPBL-92	2100	90.2	Surface	Surface	
LPBL-93	2100	91.8	Surface	Surface	
LPBL-94	2100	100.5	Surface	Surface	
LPBL-95	2100	92.4	Surface	Surface	
LPBL-96	2100	99.4	Surface	Surface	
LPBL-97	2100	91.8	Surface	Surface	
LPBL-98	2100	87.5	Surface	Surface	Fe
LPBL-99	2100	80.0	Surface	Surface	
LPBL-100	2100	91.3	Surface	Surface	
LPBL-101	2100	90.2	Corner	Surface	
LPBL-102	2100	89.7	Surface	Surface	
LPBL-103	2100	105.6	Internal	Inclusion	Fe,Cr,Ni
LPBL-104	2100	100.2	Surface	Surface	
LPBL-105	2100	102.9	Surface	Surface	
LPBL-106	2100	99.6	Surface	Surface	
LPBL-107	2100	99.6	Surface	Surface	
LPBL-108	2100	96.9	Corner	Surface	
LPBL-109	2100	107.7	Surface	Surface	
LPBL-110	2100	103.4	Surface	Surface	
LPBL-111	2100	105.6	Corner	Surface	
LPBL-112	2100	100.2	Surface	Surface	
LPBL-113	2100	98.0	Surface	Surface	
LPBL-114	2100	116.3	Surface	Chip	
LPBL-115	2200	94.2	Surface	Surface	
LPBL-116	2200	99.6	Corner	Surface	
LPBL-117	2200	96.9	Corner	Surface	
LPBL-118	2200	91.6	Corner	Surface	
LPBL-119	2200	92.1	Surface	Surface	
LPBL-120	2200	94.2	Surface	Surface	
LPBL-121	2200	93.2	Surface	Surface	
LPBL-122	2200	97.5	Corner	Surface	
LPBL-123	2200	101.8	Surface	Surface	

TABLE 1. 4-POINT FLEXURE DATA OF MIL-A AND MIL-B SPECIMENS (Contd)

LONGITUDINAL MACHINED MIL-B BARS (Contd)

Specimen Number	Test Temp, F	Stress, ksi	Fracture Origin Location	Type	Comments
LPBL-124	2200	99.6	Surface	Surface	
LPBL-125	2200	94.2	Surface	Surface	
LPBL-126	2200	91.0	Surface	Surface	
LPBL-127	2200	94.8	Surface	Surface	
LPBL-128	2200	97.5	Surface	Surface	
LPBL-129	2200	99.6	Corner	Surface	
LPBL-130	2200	98.0	Surface	Surface	
LPBL-131	2200	95.3	Surface	Surface	
LPBL-132	2200	99.6	Surface	Surface	C,Fe,Co
LPBL-133	2200	95.9	Surface	Surface	
LPBL-134	2200	95.3	Surface	Surface	
LPBL-135	2200	93.7	Surface	Surface	
LPBL-136	2200	93.2	Internal	Inclusion	Fe
LPBL-137	2200	100.7	Surface	Surface	
LPBL-138	2200	93.2	Surface	Surface	
LPBL-139	2200	102.9	Surface	Surface	
LPBL-140	2200	102.3	Surface	Surface	
LPBL-141	2200	100.7	Surface	Surface	Near corner
LPBL-142	2200	104.5	Surface	Surface	
LPBL-143	2200	102.9	Surface	Surface	
LPBL-144	2200	100.2	Surface	Surface	
LPBL-145	2300	92.1	Surface	Surface	
LPBL-146	2300	94.8	Surface	Surface	
LPBL-147	2300	109.5	Surface	Surface	—
LPBL-148	2300	99.6	Surface	Surface	
LPBL-149	2300	98.6	Surface	Surface	
LPBL-150	2300	87.2	Surface	Surface	
LPBL-151	2300	99.6	Corner	Surface	
LPBL-152	2300	97.5	Corner	Surface	
LPBL-153	2300	105.0	Surface	Surface	
LPBL-154	2300	95.3	Surface	Surface	Fe
LPBL-155	2300	102.9	Surface	Surface	
LPBL-156	2300	103.4	Corner	Surface	
LPBL-157	2300	98.6	Corner	Surface	
LPBL-158	2300	100.2	Corner	Surface	
LPBL-159	2300	102.3	Surface	Surface	
LPBL-211	2300	102.9	Surface	Surface	
LPBL-212	2300	102.3	Surface	Surface	
LPBL-213	2300	94.2	Surface	Surface	
LPBL-214	2300	90.5	Surface	Surface	Possible sub-surface
LPBL-215	2300	92.6	Surface	Surface	
LPBL-216	2300	92.1	Surface	Surface	
LPBL-217	2300	91.6	Surface	Surface	

TABLE 1. 4-POINT FLEXURE DATA OF MIL-A AND MIL-B SPECIMENS (Contd)

LONGITUDINAL MACHINED MIL-B BARS (Contd)

Specimen Number	Test Temp, F	Stress, ksi	Fracture Origin Location	Fracture Origin Type	Comments
LPBL-218	2300	94.2	Surface	Surface	
LPBL-219	2300	72.7	Surface	Crack	On side. Straight
LPBL-220	2300	95.3	Corner	Surface	
LPBL-221	2300	94.8	Surface	Surface	
LPBL-222	2300	92.6	Corner	Surface	
LPBL-223	2300	88.9	Surface	Surface	
LPBL-224	2300	93.7	Surface	Surface	
LPBL-225	2300	92.1	Surface	Surface	
LPBL-226	2400	86.7	Corner	Surface	
LPBL-227	2400	87.2	Surface	Surface	
LPBL-228	2400	81.3	Surface	Surface	
LPBL-229	2400	88.3	Surface	Surface	
LPBL-230	2400	82.4	Surface	Surface	
LPBL-232	2400	81.9	Surface	Surface	
LPBL-233	2400	84.6	Surface	Surface	
LPBL-235	2400	96.4	Corner	Surface	
LPBL-236	2400	88.9	Corner	Surface	
LPBL-237	2400	91.6	Surface	Surface	Machining line
LPBL-239	2400	93.7	Surface	Surface	
LPBL-240	2400	94.2	Surface	Surface	
LPBL-241	2400	94.2	Surface	Surface	
LPBL-242	2400	86.7	Corner	Surface	
LPBL-243	2400	92.1	Surface	Surface	Machining line
LPBL-244	2400	92.6	Surface	Surface	
LPBL-245	2400	93.2	Internal	Inclusion	
LPBL-246	2400	93.2	Surface	Surface	
LPBL-247	2400	88.9	Surface	Surface	
LPBL-248	2400	98.6	Corner	Surface	
LPBL-249	2400	94.2	Corner	Surface	
LPBL-250	2400	91.0	Corner	Surface	
LPBL-251	2400	95.3	Corner	Surface	
LPBL-253	2400	95.9	Surface	Surface	
LPBL-254	2400	86.2	Surface	Surface	
LPBL-255	2400	92.1	Surface	Surface	
LPBL-256	2400	89.4	Surface	Surface	
LPBL-257	2400	90.5	Corner	Surface	
LPBL-258	2500	93.2	Surface	Surface	
LPBL-260	2500	93.2	Surface	Surface	
LPBL-261	2500	96.9	Corner	Surface	
LPBL-262	2500	92.1	Surface	Surface	
LPBL-263	2500	91.6	Surface	Surface	
LPBL-264	2500	88.9	Surface	Surface	
LPBL-265	2500	91.6	Surface	Surface	

TABLE 1. 4-POINT FLEXURE DATA OF MIL-A AND MIL-B SPECIMENS (Contd)

LONGITUDINAL MACHINED MIL-B BARS (Contd)

Specimen Number	Test Temp, F	Stress, ksi	Fracture Origin Location	Type	Comments
LPBL-266	2500	96.4	Surface	Surface	
LPBL-267	2500	95.3	Surface	Surface	
LPBL-268	2500	89.4	Surface	Surface	
LPBL-270	2500	96.9	Surface	Surface	
LPBL-271	2500	94.2	Surface	Surface	
LPBL-272	2500	91.6	Surface	Surface	
LPBL-273	2500	93.7	Surface	Surface	
LPBL-274	2500	91.0	Surface	Surface	
LPBL-275	2500	91.0	Corner	Surface	Fe,Co
LPBL-276	2500	84.0	Surface	Surface	
LPBL-277	2500	92.1	Internal	Volume	
LPBL-278	2500	93.7	Surface	Surface	
LPBL-279	2500	81.9	Internal	Void	
LPBL-280	2500	91.6	Surface	Surface	
LPBL-281	2500	94.8	Internal	Volume	
LPBL-282	2500	95.9	Surface	Surface	
LPBL-283	2500	84.6	Corner	Surface	
LPBL-284	2500	86.7	Surface	Surface	
LPBL-285	2500	87.8	Surface	Surface	
LPBL-286	2500	88.9	Surface	Surface	
LPBL-287	2500	89.9	Internal	Inclusion	~Fe,Co
LPBL-288	2500	89.9	Corner	Surface	

AlliedSignal
AEROSPACE

TABLE 1. 4-POINT FLEXURE DATA OF MIL-A AND MIL-B SPECIMENS (Contd)

45 DEGREES MACHINED MIL B BARS

Specimen Number	Test Temp, F	Stress, ksi	Fracture Origin Location	Fracture Origin Type	Comments	By or Visual
LPB451	70	116.7	Surface	Surface		
LPB452	70	80.0	Corner	Chip		
LPB453	70	103.2	Corner	Surface		
LPB454	70	101.6	Corner	Surface		
LPB455	70	102.7	Corner	Surface		
LPB456	70	136.2	Corner	Surface		
LPB457	70	122.6	Corner	Surface		
LPB458	70	124.8	Corner	Surface		
LPB459	70	94.0	Corner	Chip		
LPB4510	70	107.0	Corner	Surface		
LPB4511	70	98.3	Corner	Surface		
LPB4512	70	105.4	Corner	Surface		
LPB4513	70	122.1	Corner	Surface		
LPB4514	70	82.1	Corner	Surface		
LPB4515	70	105.9	Corner	Surface		
LPB4516	70	86.4	Corner	Chip		
LPB4517	70	127.0	Corner	Surface		
LPB4518	70	129.1	Corner	Surface		
LPB4519	70	110.8	Corner	Surface		
LPB4520	70	112.9	Corner	Surface		
LPB4521	70	114.0	Corner	Surface		
LPB4522	70	115.3	Corner	Surface		
LPB4523	70	91.6	Corner	Surface		
LPB4524	70	127.6	Corner	Chip		
LPB4525	70	99.6	Corner	Surface		
LPB4526	70	116.3	Corner	Surface		
LPB4527	70	103.9	Corner	Surface		
LPB4528	70	104.5	Corner	Surface		
LPB4529	70	80.2	Corner	Surface		
LPB4530	70	123.9	Corner	Surface		
LPB4531	70	150.8	Corner	Surface		
LPB4532	70	95.3	Corner	Surface		
LPB4533	70	96.9	Corner	Surface		
LPB4534	70	120.6	Corner	Surface		
LPB4535	70	96.9	Corner	Surface		
LPB4536	70	141.1	Surface	Surface		
LPB4537	70	137.3	Corner	Chip		
LPB4538	70	116.3	Corner	Surface		
LPB4539	70	98.0	Corner	Surface		
LPB4540	70	114.2	Corner	Surface		

AlliedSignal
AEROSPACE

TABLE 1. 4-POINT FLEXURE DATA OF MIL-A AND MIL-B SPECIMENS (Contd)

TRANSVERSE MACHINED MIL-B BARS

Specimen Number	Test Temp, F	Stress, ksi	Fracture Origin Location	Fracture Origin Type	Comments	By or Visual
LPBT-183	70	80.1	Corner	Surface		
LPBT-184	70	100.8	Corner	Surface		
LPBT-185	70	88.3	Corner	Surface		
LPBT-186	70	62.1	Corner	Surface		
LPBT-187	70	65.4	Corner	Surface		
LPBT-188	70	103.5	Surface	Surface		
LPBT-189	70	117.2	Corner	Surface		
LPBT-190	70	57.8	Corner	Surface		
LPBT-191	70	103.5	Corner	Surface		
LPBT-192	70	90.5	Corner	Surface		
LPBT-193	70	91.0	Corner	Surface		
LPBT-194	70	109.5	Corner	Surface		
LPBT-195	70	92.6	Corner	Surface		
LPBT-196	70	107.3	Corner	Surface		
LPBT-197	70	100.8	Corner	Surface		
LPBT-198	70	115.5	Corner	Surface		
LPBT-199	70	125.3	Corner	Surface		
LPBT-200	70	57.8	Corner	Chip		
LPBT-201	70	108.4	Corner	Surface		
LPBT-202	70	120.4	Corner	Surface		
LPBT-203	70	99.2	Corner	Surface		
LPBT-204	70	102.4	Corner	Surface		
LPBT-205	70	112.8	Corner	Surface		
LPBT-206	70	115.5	Surface	Surface		
LPBT-207	70	102.4	Surface	Surface		
LPBT-208	70	89.9	Corner	Surface		
LPBT-209	70	111.7	Corner	Surface		
LPBT-210	70	104.6	Corner	Surface		
LPBT-211	70	104.6	Corner	Surface		
LPBT-212	70	115.0	Corner	Surface		

Nominal Specimen Dimensions: Mil-B, 3x4x50 mm
Loading Fixture Geometry:
Four point loading with 20 mm inner span and 40 mm outer span.
Room temp - Mil-B ORNL/HTML IEA Round-robin steel fixture.
High temp - GAPD Mil-B ceramic fixture evaluated and used in IEA Rou

Note: Only specimens LPBT144, 152 and 210 failed outside/under inner span by 0.97, 0.30 and 0.23 mm respectively.

AlliedSignal
AEROSPACE

TABLE 2. SIZE E (6 INCH) FLEXURE BARS

Outer span = 5 inch, Inner span = 2.5 inch
All failures inside outer span

Specimen ID	Depth in	Width in	Stress Ksi	Location	Type	Comment
LPEL-1	0.7205	0.3500	100.6	Surface	Surface	
LPEL-4	0.7201	0.3500	97.3	Surface	Surface	
LPEL-5	0.7205	0.3500	82.0	Surface	Surface	Near back chamfer
LPEL-7	0.7205	0.3500	103.0	Surface	Surface	Machining line, near chamfer
LPEL-8	0.7205	0.3500	107.3	Surface	Surface	Near back
LPEL-9	0.7209	0.3500	109.3	Surface	Surface	On Side
LPEL-11	0.7205	0.3500	118.9	Corner	Chip	Front bottom
LPEL-12	0.7205	0.3504	101.4	Surface	Surface	Coincide with deep line
LPEL-13	0.7205	0.3500	80.1	Internal	Inclusion	Dark Inclusion
LPEL-14	0.7205	0.3500	91.9	Surface	Surface	
LPEL-15	0.7205	0.3500	116.4	Surface	Surface	Near back
LPEL-16	0.7209	0.3252	116.1	Surface	Surface	
LPEL-17	0.7205	0.3504	98.8	Surface	Surface	On Side
LPEL-18	0.7205	0.3504	105.2	Corner	Surface	
LPEL-19	0.7205	0.3500	76.9	Corner	Surface	
LPEL-20	0.7205	0.3500	82.8	Corner	Surface	Front face
LPEL-21	0.7205	0.3500	117.9	Corner	Surface	Not polished
LPEL-22	0.7205	0.3500	87.2	Surface	Surface	Near front corner
LPEL-23	0.7205	0.3500	125.4	Surface	Surface	Near chamfer
LPEL-24	0.7205	0.3500	99.3	Internal	Inclusion	Second origin surface
LPEL-25	0.7205	0.3500	119.5	Internal	Inclusion	Carbon, small
LPEL-26	0.7205	0.3500	117.4	Corner	Surface	Chamfer face
LPEL-29	0.7232	0.3500	77.8	Corner	Chip	Chip and scratch on both sides
LPEL-35	0.7205	0.3500	81.0	Corner	Surface	
LPEL-36	0.7209	0.3496	92.7	Surface	Surface	
LPEL-37	0.7205	0.3500	107.5	Surface	Surface	Near back chamfer
LPEL2-2	0.7205	0.3500	96.2	Surface	Surface	Near front
LPEL2-3	0.7205	0.3504	115.5	Surface	Surface	
LPEL2-5	0.7205	0.3504	109.3	Surface	Surface	Near Back Face
LPEL2-6	0.7205	0.3504	89.3	Corner	Surface	
LPEL2-7	0.7244	0.3504	112.0	Corner	Surface	Gaged. Not polished
LPEL2-8	0.7209	0.3500	91.5	Internal	Inclusion	
LPEL2-9	0.7205	0.3500	100.9	Surface	Surface	
LPEL2-10	0.7205	0.3504	118.0	Surface	Crack	On Side. .1" up
LPEL2-11	0.7209	0.3504	127.9	Surface	Surface	Machining line

TABLE 2. SIZE E (6 INCH) FLEXURE BARS (Contd)

Outer span = 5 inch, Inner span = 2.5 inch
All failures inside outer span

Specimen ID	Depth in	Width in	Stress Ksi	Location	Type	Comment
LPEL2-12	0.7205	0.3504	71.3	Corner	Chip	Front Metal Chip Crack
LPEL2-13	0.7205	0.3508	63.4	Corner	Surface	
LPEL2-15	0.7205	0.3504	131.1	Surface	Surface	Near Back
LPEL2-16	0.7205	0.3504	97.9	Corner	Surface	
LPEL2-19	0.7205	0.3504	131.4	Surface	Surface	Side? Bad SEM
LPEL2-20	0.7209	0.3500	109.8	Surface	Chip	On Side. Chip on both pieces
LPEL2-21	0.7209	0.3504	100.9	Internal	Inclusion	Dark Inclusion
LPEL2-22	0.7205	0.3504	113.0	Surface	Surface	
LPEL2-23	0.7205	0.3504	122.2	Surface	Crack	Existing crack?
LPEL2-24	0.7209	0.3504	57.9	Corner	Chip	Other piece chipped
LPEL2-25	0.7205	0.3504	128.9	Corner	Surface	
LPEL2-27	0.7213	0.3504	102.5	Corner	Surface	
LPEL2-28	0.7205	0.3504	134.5	Corner	Chip	Left over chips
LPEL2-29	0.7205	0.3504	86.6	Corner	Chip	
LPEL2-30	0.7205	0.3500	50.6	Corner	Crack	Chip crack. SEM both pieces
LPEL2-31	0.7205	0.3500	105.1	Surface	Surface	Near corner
LPEL2-36	0.7205	0.3504	64.2	Corner	Chip	Large chip/closed crack
LPEL2-37	0.7205	0.3504	110.5	Surface	Surface	Near chamfer
LPEL2-38	0.7205	0.3504	113.9	Surface	Surface	
LPEL2-39	0.7205	0.3504	101.2	Internal	Inclusion	Strain Gaged
LPEL2-40	0.7205	0.3500	122.2	Surface	Surface	Near front
LPEL2-41	0.7205	0.3500	80.5	Surface	Surface	On Side
LPEL2-42	0.7209	0.3504	103.3	Corner	Surface	
LPEL2-43	0.7205	0.3508	142.1	Surface	Surface	
LPEL2-46	0.7209	0.3508	99.8	Surface	Surface	On Side
LPEL2-48	0.7205	0.3500	117.7	Corner	Crack	Not polished
LPEL2-49	0.7205	0.3500	112.5	Surface	Surface	
LPEL2-50	0.7205	0.3504	66.0	Corner	Chip	Bad chamfer. SEM both pieces.
LPEL2-51	0.7205	0.3500	92.9	Internal	Inclusion	Large dark inclusion
LPEL2-52	0.7205	0.3504	115.0	Internal	Inclusion	Dark stringer inclusion, C
LPEL2-54	0.7205	0.3500	133.1	Surface	Surface	Near bottom corner. Two origins
LPEL2-55	0.7209	0.3500	125.6	Internal	Inclusion	

TABLE 2. SIZE E (6 INCH) FLEXURE BARS (Contd)

Outer span = 5 inch, Inner span = 2.5 inch
All failures inside outer span

Specimen ID	Depth in	Width in	Stress Ksi	Location	Type	Comment
LPEL2-57	0.7205	0.3500	75.1	Corner	Chip	Polished chip
LPEL2-58	0.7205	0.3500	126.5	Corner	Surface	
LPEL2-59	0.7205	0.3500	117.7	Surface	Surface	
LPEL2-63	0.7209	0.3500	107.2	Surface	Surface	
LPEL2-64	0.7205	0.3500	95.3	Corner	Surface	
LPEL2-65	0.7209	0.3500	113.4	Corner	Surface	Gaged. Not polished
LPEL3- 1	0.7197	0.3500	115.4	Internal	Inclusion	Dark inclusion near back face
LPEL3- 2	0.7197	0.3500	58.2	Surface	Surface	
LPEL3- 3	0.7201	0.3500	116.7	Surface	Surface	On Side
LPEL3- 4	0.7205	0.3508	95.4	Surface	Surface	Gaged
LPEL3- 5	0.7205	0.3500	110.2	Internal	Inclusion	Dark inclusion, C
LPEL3- 8	0.7201	0.3500	80.4	Corner	Surface	
LPEL3- 9	0.7205	0.3496	103.3	Surface	Surface	
LPEL3-10	0.7205	0.3500	118.7	Internal	Inclusion	Dark inclusion
LPEL3-11	0.7197	0.3500	127.4	Corner	Surface	Bottom corner
LPEL3-12	0.7205	0.3500	132.1	Corner	Surface	Back bottom
LPEL3-14	0.7201	0.3500	106.9	Surface	Surface	Front
LPEL3-15	0.7205	0.3504	86.2	Corner	Surface	Not polished
LPEL3-16	0.7205	0.3500	98.3	Corner	Surface	
LPEL3-17	0.7201	0.3500	117.3	Corner	Surface	
LPEL3-18	0.7201	0.3500	115.3	Surface	Surface	
LPEL3-20	0.7205	0.3500	128.0	Internal	Inclusion	Dark inclusion, C, Fe
LPEL3-21	0.7205	0.3496	70.1	Corner	Surface	
LPEL3-23	0.7205	0.3504	143.8	Surface	Surface	Estimated. Origin piece missing
LPEL3-24	0.7205	0.3500	109.6	Surface	Surface	
LPEL3-25	0.7205	0.3496	117.0	Surface	Surface	
LPEL3-26	0.7205	0.3504	104.7	Internal	Inclusion	Dark inclusion, C, Fe. Marked 3-26 (NDE & Chipped
LPEL3-31	0.7205	0.3500	72.6	Corner	Chip	Confirmed, both pcs SEM
LPEL3-33	0.7205	0.3500	126.1	Internal	Inclusion	
LPEL3-34	0.7205	0.3500	85.5	Surface	Inclusion	On Side. Surface inclusion.
LPEL3-36	0.7205	0.3504	109.3	Surface	Surface	On Side
LPEL3-37	0.7205	0.3504	133.0	Surface	Surface	On Side
LPEL3-38	0.7205	0.3500	109.4	Surface	Surface	Polished chamfer

AlliedSignal AEROSPACE

TABLE 3. FRACTOGRAPHY AND STRENGTH DATA OF FLEXURE BARS CUT FROM SPIN DISKS

Mil B bars machined from surface of special flat spin disk billets
LPD specimens were Mil B, 3x4x50 mm flexure bars tested flatwise
Outer span 40 mm, inner span 20 mm
* Radius of the concentric circle intercepting center of the flexure bar.

Specimen Number	Stress (ksi)	Disk No.	Side	Machining Direction Designed	Observed	Fracture Origin Location	Type	Comments
LPD- 1	137.3	G2-1	Stem	L(2.207R*)	Long.	Surface	Surface	
LPD- 2	124.9	G2-1	Stem	L(1.985R)	Long.	Surface	Surface	
LPD- 3	121.2	G2-1	Stem	L(1.753R)	Long.	Surface	Surface	Near chamfer
LPD- 4	133.0	G2-1	Stem	L(1.534R)	Long.	Corner	Surface	
LPD- 5	130.3	G2-1	Stem	L(1.303R)	Long-45	Surface	Surface	
LPD- 6	119.6	G2-1	Stem	L(1.072R)	Long-45	Corner	Surface	
LPD- 7	128.7	G2-1	Stem	L(0.850R)	Long-45	Surface	Surface	
LPD- 8	123.3	G2-1	Stem	L(0.626R)	Long-45	Surface	Surface	
LPD- 9	134.6	G2-1	Stem	Trans.	45-Trans	Surface	Surface	
LPD- 10	136.8	G2-1	Stem	Trans.	Trans-45	Surface	Surface	
LPD- 11	129.8	G2-1	Stem	Trans.	Trans.	Surface	Surface	
LPD- 12	128.2	G2-1	Stem	Trans.	Trans-45	Surface	Surface	
LPD- 13	124.4	G2-1	Stem	Trans.	Trans-45	Surface	Surface	
LPD- 14	114.2	G2-1	Stem	45 Deg.	45 Deg.	Surface	Surface	
LPD- 15	119.6	G2-1	Stem	45 Deg.	45 Deg.	Corner	Surface	
LPD- 16	136.8	G2-1	Stem	45 Deg.	45 Deg.	Corner	Surface	
LPD- 17	113.6	G2-1	Stem	45 Deg.	45 Deg.	Corner	Surface	
LPD- 18	109.3	G2-1	Stem	45 Deg.	45 Deg.	Surface	Surface	
LPD- 19	119.0	G2-1	Back	L(2.207R)	Long.	Corner	Surface	
LPD- 20	110.9	G2-1	Back	L(1.985R)	Long.	Corner	Chip	
LPD- 21	129.8	G2-1	Back	L(1.753R)	Long.	Surface	Surface	
LPD- 22	129.8	G2-1	Back	L(1.534R)	Long.	Surface	Surface	
LPD- 23	108.8	G2-1	Back	L(1.303R)	Long.	Internal	Inclusion	Large dark Inc.
LPD- 24	128.2	G2-1	Back	L(1.072R)	Long.	Surface	Surface	
LPD- 25	127.6	G2-1	Back	L(0.850R)	Long-45	Surface	Surface	
LPD- 26	126.0	G2-1	Back	L(0.626R)	45 Deg.	Surface	Surface	
LPD- 27	146.0	G2-1	Back	Trans.	45 Deg.	Surface	Surface	
LPD- 28	128.7	G2-1	Back	Trans.	Trans.	Surface	Surface	
LPD- 29	125.5	G2-1	Back	Trans.	Trans.	Surface	Surface	
LPD- 30	124.4	G2-1	Back	Trans.	Trans.	Surface	Surface	
LPD- 31	122.3	G2-1	Back	Trans.	Trans.	Surface	Surface	
LPD- 32	130.9	G2-1	Back	45 Deg.	45 Deg.	Corner	Surface	
LPD- 33	128.7	G2-1	Back	45 Deg.	45 Deg.	Surface	Surface	
LPD- 34	128.7	G2-1	Back	45 Deg.	45 Deg.	Surface	Surface	
LPD- 35	127.6	G2-1	Back	45 Deg.	45 Deg.	Surface	Surface	
LPD- 36	131.9	G2-1	Back	45 Deg.	45 Deg.	Surface	Surface	
LPD- 37	122.3	G2-7	Stem	L(2.207R)	Long-45	Surface	Surface	
LPD- 38	126.0	G2-7	Stem	L(1.985R)	Long-45	Surface	Surface	

TABLE 3. FRACTOGRAPHY AND STRENGTH DATA OF FLEXURE BARS CUT FROM SPIN DISKS (Contd)

Mil B bars machined from surface of special flat spin disk billets
LPD specimens were Mil B, 3x4x50 mm flexure bars tested flatwise
Outer span 40 mm, inner span 20 mm
* Radius of the concentric circle intercepting center of the flexure bar.

Specimen Number	Stress (ksi)	Disk No.	Side	Machining Direction Designed	Observed	Fracture Origin Location	Type	Comments
LPD- 39	136.8	G2-7	Stem	L(1.753R)	Long.	Surface	Surface	
LPD- 40	135.2	G2-7	Stem	L(1.534R)	Long.	Corner	Surface	
LPD- 41	112.0	G2-7	Stem	L(1.303R)	Long.	Corner	Surface	
LPD- 42	127.6	G2-7	Stem	L(1.072R)	Long-45	Surface	Surface	
LPD- 43	110.4	G2-7	Stem	L(0.850R)	Long.	Surface	Surface	
LPD- 44	121.2	G2-7	Stem	L(0.626R)	Long.	Corner	Surface	
LPD- 45	122.8	G2-7	Stem	Trans.	Trans-45	Corner	Surface	
LPD- 46	130.3	G2-7	Stem	Trans.	Trans-45	Surface	Surface	
LPD- 47	133.0	G2-7	Stem	Trans.	Trans-45	Surface	Surface	
LPD- 48	133.6	G2-7	Stem	Trans.	45 Deg.	Surface	Surface	
LPD- 49	130.9	G2-7	Stem	Trans.	Trans.	Surface	Surface	
LPD- 50	110.4	G2-7	Stem	45 Deg.	Trans.	Corner	Surface	
LPD- 51	115.3	G2-7	Stem	45 Deg.	45 Deg.	Corner	Surface	
LPD- 52	113.1	G2-7	Stem	45 Deg.	45 Deg.	Corner	Surface	
LPD- 53	124.4	G2-7	Stem	45 Deg.	45 Deg.	Corner	Surface	
LPD- 54	122.3	G2-7	Stem	45 Deg.	45 Deg.	Corner	Surface	
LPD- 55	116.3	G2-7	Back	L(2.207R)	Long.	Corner	Surface	
LPD- 56	105.0	G2-7	Back	L(1.985R)	Long.	Surface	Surface	
LPD- 57	130.9	G2-7	Back	L(1.753R)	Long-45	Surface	Surface	
LPD- 58	130.9	G2-7	Back	L(1.534R)	Long.	Surface	Surface	
LPD- 59	124.9	G2-7	Back	L(1.303R)	Long.	Corner	Surface	
LPD- 60	106.1	G2-7	Back	L(1.072R)	Long.	Corner	Surface	
LPD- 61	125.5	G2-7	Back	L(0.850R)	Long-45	Surface	Surface	
LPD- 62	117.9	G2-7	Back	L(0.626R)	Long.	Surface	Surface	
LPD- 63	121.2	G2-7	Back	Trans.	Trans.	Surface	Surface	
LPD- 64	129.8	G2-7	Back	Trans.	Trans.	Surface	Surface	
LPD- 65	124.4	G2-7	Back	Trans.	Trans-45	Surface	Surface	
LPD- 66	110.9	G2-7	Back	Trans.	45-Long	Surface	Surface	
LPD- 67	126.0	G2-7	Back	Trans.	Trans.	Surface	Surface	
LPD- 68	137.9	G2-7	Back	45 Deg.	45 Deg.	Surface	Surface	
LPD- 69	120.1	G2-7	Back	45 Deg.	45 Deg.	Corner	Surface	
LPD- 70	129.3	G2-7	Back	45 Deg.	45 Deg.	Surface	Surface	
LPD- 71	112.0	G2-7	Back	45 Deg.	45 Deg.	Surface	Surface	
LPD- 72	131.9	G2-7	Back	45 Deg.	45 Deg.	Surface	Surface	
LPD- 73	156.2	G2-10	Stem	L(2.207R)	Long.	Surface	Surface	
LPD- 74	154.0	G2-10	Stem	L(1.985R)	Long.	Surface	Surface	
LPD- 75	141.1	G2-10	Stem	L(1.753R)	Long.	Surface	Surface	
LPD- 76	142.7	G2-10	Stem	L(1.534R)	Long.	Surface	Surface	

AlliedSignal AEROSPACE

TABLE 3. FRACTOGRAPHY AND STRENGTH DATA OF FLEXURE BARS CUT FROM SPIN DISKS (Contd)

Mil B bars machined from surface of special flat spin disk billets
LPD specimens were Mil B, 3x4x50 mm flexure bars tested flatwise
Outer span 40 mm, inner span 20 mm
* Radius of the concentric circle intercepting center of the flexure bar.

Specimen Number	Stress (ksi)	Disk No.	Side	Machining Designed	Direction Observed	Fracture Location	Origin Type	Comments
LPD- 77	136.3	G2-10	Stem	L(1.303R)	Long.	Surface	Surface	
LPD- 78	137.9	G2-10	Stem	L(1.072R)	Long.	Surface	Surface	
LPD- 79	142.7	G2-10	Stem	L(0.850R)	Long-45	Surface	Surface	
LPD- 80	135.7	G2-10	Stem	L(0.626R)	Long-45	Surface	Surface	
LPD- 81	153.5	G2-10	Stem	Trans.	45 Deg.	Corner	Surface	
LPD- 82	132.5	G2-10	Stem	Trans.	Trans.	Corner	Surface	
LPD- 83	128.2	G2-10	Stem	Trans.	Trans.	Corner	Surface	
LPD- 84	123.3	G2-10	Stem	Trans.	45 Deg.	Surface	Surface	
LPD- 85	115.3	G2-10	Stem	Trans.	Trans-45	Corner	Surface	
LPD- 86	131.4	G2-10	Stem	45 Deg.	45 Deg.	Surface	Surface	
LPD- 87	145.4	G2-10	Stem	45 Deg.	45 Deg.	Surface	Surface	
LPD- 88	127.6	G2-10	Stem	45 Deg.	45 Deg.	Surface	Surface	
LPD- 89	127.6	G2-10	Stem	45 Deg.	Trans-45	Corner	Surface	
LPD- 90	144.3	G2-10	Stem	45 Deg.	45 Deg.	Surface	Surface	
LPD- 91	123.9	G2-10	Back	L(2.207R)	Long.	Surface	Surface	
LPD- 92	89.9	G2-10	Back	L(1.985R)	Long.	Corner	Chip	
LPD- 93	126.0	G2-10	Back	L(1.753R)	Long.	Corner	Surface	
LPD- 94	138.4	G2-10	Back	L(1.534R)	Long-45	Corner	Surface	
LPD- 95	132.5	G2-10	Back	L(1.303R)	Long-45	Surface	Surface	
LPD- 96	121.7	G2-10	Back	L(1.072R)	45 Deg.	Corner	Surface	
LPD- 97	139.0	G2-10	Back	L(0.850R)	Trans-45	Surface	Surface	
LPD- 98	127.6	G2-10	Back	L(0.626R)	Trans.	Surface	Surface	
LPD- 99	133.0	G2-10	Back	Trans.	45-Trans	Corner	Surface	
LPD- 100	130.3	G2-10	Back	Trans.	45 Deg.	Surface	Surface	
LPD- 101	126.6	G2-10	Back	Trans.	Trans-45	Corner	Surface	
LPD- 102	130.9	G2-10	Back	Trans.	45 Deg.	Corner	Surface	
LPD- 103	135.2	G2-10	Back	Trans.	Trans-45	Corner	Surface	
LPD- 104	125.5	G2-10	Back	45 Deg.	Trans-45	Corner	Surface	
LPD- 105	143.8	G2-10	Back	45 Deg.	45 Deg.	Corner	Surface	
LPD- 106	126.0	G2-10	Back	45 Deg.	45 Deg.	Corner	Surface	
LPD- 107	127.6	G2-10	Back	45 Deg.	Trans.	Corner	Surface	
LPD- 108	121.2	G2-10	Back	45 Deg.	45 Deg.	Corner	Surface	

TABLE 3. FRACTOGRAPHY AND STRENGTH DATA OF FLEXURE BARS CUT FROM SPIN DISKS (Contd)

Large 4 inch bars cut from inside of spin disks
Large 4 inch bar nominal dimensions were 0.525x0.400x4.0 inch. tested edgewise. Outer span 3.5 inch, inner span 1.75 inch.

Specimen Number	Stress (ksi)	Disk No.	Machining Direction	Fracture Location	Origin Type	Comments
G51- 1	116.8	G5-1	Long.	Surface	Surface	
G51- 2	107.5	G5-1	Long.	Corner	Surface	Reaction bead
G51- 3	113.8	G5-1	Long.	Surface	Surface	
G51- 4	83.7	G5-1	Long.	Internal	Inclusion	Dark inclusion.
G51- 5	82.1	G5-1	Long.	Corner	Surface	Bottom corner
G51- 6	114.8	G5-1	Long.	Surface	Surface	
G47- 1	106.9	G4-7	Long.	Internal	Inclusion	
G47- 2	121.1	G4-7	Long.	Corner	Surface	Top corner
G47- 3	100.5	G4-7	Long.	Internal	Inclusion	
G47- 4	92.9	G4-7	Long.	Internal	Inclusion	Dark Inclusion
G47- 5	58.3	G4-7	Long.	Corner	Surface	
G47- 6	114.5	G4-7	Long.	Surface	Surface	Surface reaction
G34- 1	124.3	G3-4	Long.	Surface	Surface	
G34- 2	86.0	G3-4	Long.	Surface	Surface	
G34- 3	108.3	G3-4	Long.	Internal	Inclusion	Dark Inclusion
G34- 4	114.6	G3-4	Long.	Internal	Inclusion	Dark Inclusion
G34- 5	120.2	G3-4	Long.	Corner	Surface	Top corner
G34- 6	109.8	G3-4	Long.	Surface	Surface	
G22- 1	124.5	G2-2	Long.	Surface	Surface	
G22- 2	121.7	G2-2	Long.	Corner	Surface	Top corner
G22- 3	114.5	G2-2	Long.	Surface	Surface	
G22- 4	111.9	G2-2	Long.	Surface	Surface	
G22- 5	101.0	G2-2	Long.	Corner	Surface	Reaction bead
G22- 6	65.5	G2-2	Long.	Corner	Surface	

TABLE 4. RE-HEAT TREATED MIL-B FLEXURE BAR FRACTOGRAPHY AND STRENGTH DATA

Tensile surface machining direction: LPBL = Longitudinal, LPB45 = 45 degrees, LPBT = Transverse. Chamfers were longitudinally polished
Nominal Specimen Dimensions: Mil-B, 3x4x50 mm (.1180x.1575 inch)
Loading Fixture Geometry:
Four point loading with 20 mm inner span and 40 mm outer span.
Room temp - MIL-B ORNL/HTML IEA Round-robin steel fixture.

LONGITUDINALLY MACHINED

Specimen Number	Stress (ksi)	Fracture Origin Location	Fracture Origin Type	Comments
LPBL-160	136.8	Surface	Surface	
LPBL-161	137.9	Surface	Surface	
LPBL-171	135.2	Corner	Surface	
LPBL-172	131.4	Surface	Surface	
LPBL-173	137.3	Surface	Surface	
LPBL-174	142.7	Surface	Surface	
LPBL-175	135.7	Surface	Surface	
LPBL-176	143.3	Surface	Surface	
LPBL-177	141.6	Surface	Surface	
LPBL-178	137.3	Surface	Surface	
LPBL-179	123.9	Surface	Surface	
LPBL-180	134.6	Surface	Surface	
LPBL-181	115.3	Corner	Surface	
LPBL-182	141.6	Corner	Surface	
LPBL-183	140.0	Surface	Surface	
LPBL-184	140.0	Surface	Surface	
LPBL-185	133.0	Surface	Surface	
LPBL-186	133.6	Surface	Surface	
LPBL-187	126.6	Surface	Surface	
LPBL-188	134.6	Surface	Surface	
LPBL-189	124.4	Surface	Surface	
LPBL-190	137.3	Surface	Surface	
LPBL-191	123.9	Surface	Surface	
LPBL-192	131.9	Corner	Surface	Top corner
LPBL-193	132.5	Surface	Surface	
LPBL-194	135.2	Surface	Surface	
LPBL-195	147.0	Surface	Surface	
LPBL-196	133.0	Surface	Surface	
LPBL-197	131.9	Surface	Surface	
LPBL-198	134.6	Surface	Surface	
LPBL-199	137.3	Surface	Surface	
LPBL-200	143.8	Corner	Surface	

TABLE 4. RE-HEAT TREATED MIL-B FLEXURE BAR FRACTOGRAPHY AND STRENGTH DATA (Contd)

Tensile surface machining direction: LPBL = Longitudinal, LPB45 = 45 degrees, LPBT = Transverse. Chamfers were longitudinally polished
Nominal Specimen Dimensions: Mil-B, 3x4x50 mm (.1180x.1575 inch)
Loading Fixture Geometry:
Four point loading with 20 mm inner span and 40 mm outer span.
Room temp - MIL-B ORNL/HTML IEA Round-robin steel fixture.

LONGITUDINALLY MACHINED (Contd)

Specimen Number	Stress (ksi)	Fracture Origin Location	Fracture Origin Type	Comments
LPBL-201	141.1	Surface	Surface	
LPBL-202	122.3	Surface	Surface	
LPBL-203	131.9	Surface	Surface	
LPBL-204	144.9	Surface	Surface	
LPBL-205	140.0	Surface	Surface	
LPBL-206	113.1	Surface	Surface	
LPBL-207	129.3	Surface	Surface	
LPBL-208	150.8	Surface	Surface	
LPBL-209	132.5	Surface	Surface	
LPBL-210	139.0	Surface	Surface	

TABLE 4. RE-HEAT TREATED MIL-B FLEXURE BAR FRACTOGRAPHY AND STRENGTH DATA (Contd)

Tensile surface machining direction: LPBL = Longitudinal, LPB45 = 45 degrees, LPBT = Transverse. Chamfers were longitudinally polished
Nominal Specimen Dimensions: Mil-B, 3x4x50 mm (.1180x.1575 inch)
Loading Fixture Geometry:
Four point loading with 20 mm inner span and 40 mm outer span.
Room temp - MIL-B ORNL/HTML IEA Round-robin steel fixture.

45 DEGREES MACHINED

Specimen Number	Stress (ksi)	Fracture Origin Location	Type	Comments
LPB45-41	133.0	Surface	Surface	
LPB45-42	123.9	Surface	Surface	Near chamfer
LPB45-43	128.2	Surface	Surface	
LPB45-44	128.7	Surface	Surface	
LPB45-45	130.3	Surface	Surface	
LPB45-46	114.7	Corner	Surface	
LPB45-47	138.4	Surface	Surface	
LPB45-48	131.9	Surface	Surface	
LPB45-49	132.5	Corner	Surface	
LPB45-50	129.8	Surface	Surface	
LPB45-51	130.3	Surface	Surface	
LPB45-52	122.3	Surface	Surface	
LPB45-53	86.7	Internal	Inclusion	
LPB45-54	135.7	Surface	Surface	
LPB45-55	119.0	Surface	Surface	
LPB45-56	145.4	Surface	Surface	
LPB45-57	134.6	Surface	Surface	
LPB45-58	126.6	Surface	Surface	
LPB45-59	133.6	Surface	Surface	
LPB45-60	127.1	Surface	Surface	
LPB45-61	129.3	Surface	Surface	
LPB45-62	143.8	Surface	Surface	
LPB45-63	132.5	Surface	Surface	
LPB45-64	130.3	Surface	Surface	
LPB45-65	129.8	Surface	Surface	
LPB45-66	132.5	Surface	Surface	
LPB45-67	137.9	Surface	Surface	
LPB45-68	107.7	Corner	Surface	
LPB45-69	131.9	Surface	Surface	
LPB45-70	120.6	Surface	Surface	

TABLE 4. RE-HEAT TREATED MIL-B FLEXURE BAR FRACTOGRAPHY AND STRENGTH DATA (Contd)

Tensile surface machining direction: LPBL = Longitudinal, LPB45 = 45 degrees, LPBT = Transverse. Chamfers were longitudinally polished
Nominal Specimen Dimensions: Mil-B, 3x4x50 mm (.1180x.1575 inch)
Loading Fixture Geometry:
Four point loading with 20 mm inner span and 40 mm outer span.
Room temp - MIL-B ORNL/HTML IEA Round-robin steel fixture.

TRANSVERSE MACHINED

Specimen Number	Stress (ksi)	Fracture Origin Location	Fracture Origin Type	Comments
LPBT-213	118.5	Surface	Surface	
LPBT-214	121.2	Surface	Surface	
LPBT-215	121.2	Surface	Surface	
LPBT-216	124.4	Surface	Surface	
LPBT-217	122.3	Surface	Surface	
LPBT-218	114.2	Surface	Surface	
LPBT-219	119.6	Surface	Surface	
LPBT-220	117.4	Surface	Surface	
LPBT-221	118.5	Surface	Surface	
LPBT-222	114.2	Surface	Surface	
LPBT-223	117.9	Surface	Surface	
LPBT-224	119.0	Surface	Surface	
LPBT-225	121.7	Surface	Surface	
LPBT-226	128.2	Surface	Surface	
LPBT-227	118.5	Surface	Surface	
LPBT-228	123.3	Surface	Surface	
LPBT-229	126.6	Surface	Surface	
LPBT-230	119.0	Surface	Surface	

AlliedSignal
AEROSPACE

TABLE 5A. FRACTOGRAPHY AND STRENGTH DATA OF TENSILE SPECIMENS

*Collet materials were mostly fully annealed oxygen free copper with few Inconel 718

Specimen Number	Stress (ksi)	Origin Location	Origin Type	PositioTest (mm)	T(F)	Coll* Mat.	Comment
LPTEN1-1	107.2	Buttonhead	Surface	Radius	70	718	
LPTEN1-5	119.4	Buttonhead	Surface	Radius	70	718	
LPTEN1-25	78.6	Internal	Inclusion	22.0	70	718	C,Fe,Cr,Ni
LPTEN1-29	72.3	Buttonhead	Surface	Radius	70	718	
LPTEN1-33	86.1	Surface	Line	-15.4	70	718	~45 deg scratch
LPTEN1-35	102.1	Surface	Surface	-21.1	70	Cu	
LPTEN1-37	107.4	Buttonhead	Surface	Radius	70	718	
LPTEN2-5	128.3	Internal	Inclusion	13.9	70	Cu	
LPTEN2-6	111.4	Internal	Inclusion	9.7	70	Cu	C,Fe,~Ni
LPTEN2-8	135.0	Internal	Volume	11.6	70	Cu	
LPTEN2-9	131.1	Internal	Volume	19.6	70	Cu	
LPTEN2-11	125.4	Internal	Volume	12.7	70	Cu	
LPTEN2-12	137.9	Internal	Inclusion	9.7	70	Cu	Fe, No C
LPTEN2-13	108.5	Surface	Surface	-4.9	70	Cu	
LPTEN2-14	119.8	Internal	Volume	4.6	70	Cu	
LPTEN2-15	102.3	Internal	Volume	20.7	70	Cu	
LPTEN2-16	103.7	Internal	Inclusion	-0.6	70	Cu	
LPTEN2-18	92.4	Internal	Inclusion	-8.9	70	Cu	
LPTEN2-21	48.7	Surface	Inclusion	-19.1	70	Cu	Al, ~500x40 micron
LPTEN2-22	88.4	Internal	Inclusion	21.6	70	Cu	~Fe,Al, No C,O
LPTEN2-25	91.6	Internal	Void	-5.9	70	Cu	Fe,C,O,Co. Near surfac
LPTEN2-26	90.5	Internal	Inclusion	-0.8	70	Cu	~Fe
LPTEN2-40	128.9	Internal	Volume	17.1	70	Cu	
LPTEN2-76	91.7	Surface	Surface	-6.0	70	Cu	
LPTEN2-85	97.1	Internal	Volume	18.0	70	Cu	
LPTEN2-86	101.6	Internal	Volume	19.0	70	Cu	
LPTEN2-87	100.6	Internal	Volume	6.3	70	Cu	
LPTEN2-88	113.5	Internal	Inclusion	-7.9	70	Cu	C,Fe, No Ni,Y
LPTEN2-97	100.9	Internal	Volume	12.2	70	Cu	
LPTEN2-98	108.2	Internal	Inclusion	-17.3	70	Cu	C,Fe.
LPTEN2-99	117.8	Internal	Volume	16.5	70	Cu	
LPTEN2-103	100.2	Surface	Surface	22.0	70	Cu	
LPTEN2-106	107.4	Internal	Volume	9.4	70	Cu	
LPTEN2-110	88.7	Internal	Inclusion	-18.6	70	Cu	Fe,C
LPTEN2-115	106.7	Internal	Inclusion	-9.4	70	Cu	C,Fe
LPTEN2-122	115.0	Internal	Inclusion	-19.1	70	Cu	Fe,C

AlliedSignal
AEROSPACE

TABLE 5A. FRACTOGRAPHY AND STRENGTH DATA OF TENSILE SPECIMENS (Contd)

*Collet materials were mostly fully annealed oxygen free copper with few Inconel 718

Specimen Number	Stress (ksi)	Origin Location	Origin Type	PositioTest (mm)	T(F)	Coll* Mat.	Comment
LPTEN2-135	85.6	Internal	Volume	4.0	70	Cu	
LPTEN2-144	119.0	Internal	Volume	18.2	70	Cu	15 micron large grain
LPTEN2-151	102.3	Surface	Surface	-1.1	70	Cu	
LPTEN2-154	110.4	Internal	Volume	-10.0	70	Cu	
LPTEN2-160	99.1	Internal	Inclusion	-12.2	70	Cu	
LPTEN2-163	100.6	Internal	Volume	21.5	70	Cu	
LPTEN3-28	101.9	Surface	Surface	-14.3	70	Cu	
LPTEN3-62	88.8	Surface	Surface	10.4	70	Cu	
LPTEN3-67	97.2	Surface	Surface	-10.5	70	Cu	
LPTEN3-68	120.7	Internal	Inclusion	24.6	70	Cu	Fe
LPTEN3-80	79.5	Surface	Surface	20.8	70	Cu	
LPTEN3-84	133.5	Surface	Surface	12.7	70	Cu	
LPTEN3-86	120.3	Internal	Inclusion	-9.4	70	Cu	Fe
LPTEN3-91	117.0	Internal	Inclusion	14.4	70	Cu	Fe,No C
LPTEN3-98	146.8	Surface	Surface	0.5	70	Cu	
LPTEN3-99	96.2	Surface	Surface	7.3	70	Cu	
LPTEN3-100	110.4	Surface	Surface	-21.1	70	Cu	
LPTEN3-101	104.7	Surface	Surface	14.1	70	Cu	
LPTEN3-102	110.6	Internal	Inclusion	N/A	70	Cu	
LPTEN3-104	133.0	Internal	Inclusion	14.4	70	Cu	Fe,Co, No C
LPTEN3-105	146.9	Internal	Inclusion	-6.3	70	Cu	Fe,Al,No C
LPTEN3-106	133.3	Internal	Inclusion	21.3	70	Cu	Fe, multiple inclusion
LPTEN3-107	129.7	Surface	Surface	20.1	70	Cu	
LPTEN3-108	116.5	Surface	Surface	-0.9	70	Cu	
LPTEN3-117	101.4	Surface	Surface	-8.2	70	Cu	
LPTEN3-126	83.2	Internal	Inclusion	16.5	70	Cu	C,Y, stringer
LPTEN3-127	96.9	Internal	Volume	3.3	70	Cu	
LPTEN3-130	88.9	Internal	Volume	-16.9	70	Cu	
LPTEN4-1	109.2	Internal	Inclusion	-11.7	70	Cu	C,Fe
LPTEN4-2	116.9	Internal	Inclusion	7.6	70	Cu	Ti,Fe, No. C,Si,O
LPTEN4-3	90.8	Surface	Surface	12.7	70	Cu	
LPTEN4-5	144.8	Surface	Surface	-1.6	70	Cu	
LPTEN4-7	127.9	Surface	Surface	-5.3	70	Cu	
LPTEN4-8	121.7	Surface	Surface	-13.3	70	Cu	
LPTEN4-9	143.2	Surface	Surface	18.0	70	Cu	
LPTEN4-11	125.4	Internal	Inclusion	-23.2	70	Cu	C,Fe

AlliedSignal
AEROSPACE

TABLE 5A. FRACTOGRAPHY AND STRENGTH DATA OF TENSILE SPECIMENS (Contd)

*Collet materials were mostly fully annealed oxygen free copper with few Inconel 718

Specimen Number	Stress (ksi)	Origin Location	Origin Type	Positio (mm)	Test T(F)	Coll* Mat.	Comment
LPTEN4-12	107.1	Internal	Inclusion	22.3	70	Cu	C
LPTEN4-14	101.6	Surface	Surface	-4.2	70	Cu	
LPTEN4-15	114.0	Internal	Inclusion	14.7	70	Cu	C,Y
LPTEN4-17	114.7	Internal	Inclusion	-1.3	70	Cu	~C,Fe
LPTEN4-18	124.0	Internal	Inclusion	-12.3	70	Cu	C,Fe
LPTEN4-19	123.9	Internal	Inclusion	22.0	70	Cu	Fe,Co,Ni
LPTEN4-20	91.6	Internal	Inclusion	4.4	70	Cu	Fe,C, stringer
LPTEN4-21	128.9	Surface	Surface	-3.1	70	Cu	
LPTEN4-22	118.3	Internal	Inclusion	3.8	70	Cu	Fe,~C
LPTEN4-26	108.2	Internal	Inclusion	19.5	70	Cu	C,Fe
LPTEN4-27	103.4	Internal	Inclusion	3.8	70	Cu	C,Fe
LPTEN4-28	109.2	Internal	Inclusion	-15.0	70	Cu	C,Fe,Co
LPTEN4-29	109.3	Internal	Inclusion	-3.2	70	Cu	C,Fe
LPTEN4-30	108.3	Internal	Volume	-8.9	70	Cu	
LPTEN4-32	120.8	Internal	Volume	2.0	70	Cu	
LPTEN4-34	111.1	Internal	Inclusion	-0.8	70	Cu	C,Fe,Co
LPTEN4-35	127.8	Internal	Volume	13.1	70	Cu	
LPTEN4-36	123.7	Internal	Inclusion	-18.7	70	Cu	C,Fe,Co
LPTEN4-39	124.6	Internal	Inclusion	-3.4	70	Cu	C
LPTEN4-40	124.0	Internal	Inclusion	-3.4	70	Cu	Fe,Ni, ~C
LPTEN4-42	117.4	Internal	Inclusion	-16.1	70	Cu	C,Fe
LPTEN4-43	109.8	Surface	Surface	-7.2	70	Cu	
LPTEN4-44	105.4	Internal	Inclusion	8.2	70	Cu	C,Ti Stringer
LPTEN4-45	116.1	Internal	Inclusion	23.6	70	Cu	C,Fe
LPTEN4-46	102.7	Internal	Volume	-19.1	70	Cu	~Fe
LPTEN4-47	110.4	Internal	Inclusion	-4.6	70	Cu	
LPTEN4-48	117.0	Internal	Inclusion	11.0	70	Cu	C,Fe
LPTEN4-49	109.3	Internal	Inclusion	13.1	70	Cu	C,Fe,Co
LPTEN2-49	72.6	Internal	Volume	22.3	2100	Cu	
LPTEN2-65	82.1	Internal	Inclusiom	18.2	2100	Cu	
LPTEN3-24	80.4	Internal	Void	-12.7	2100	Cu	
LPTEN3-53	80.3	Internal	Void	18.7	2100	Cu	
LPTEN3-60	89.6	Internal	Volume	-10.2	2100	Cu	
LPTEN1-39	78.3	Internal	Volume	23.1	2200	Cu	
LPTEN1-45	60.3	Internal	Inclusion	11.4	2200	Cu	Fe
LPTEN2-29	66.3	Internal	Void	1.1	2200	Cu	
LPTEN2-59	61.4	Internal	Void	7.3	2200	Cu	Crack like features
LPTEN2-96	65.3	Internal	Volume	-11.5	2200	Cu	

AlliedSignal
AEROSPACE

TABLE 5A. FRACTOGRAPHY AND STRENGTH DATA OF TENSILE SPECIMENS (Contd)

*Collet materials were mostly fully annealed oxygen free copper with few Inconel 718

Specimen Number	Stress (ksi)	Origin Location	Origin Type	Positio (mm)	Test T(F)	Coll* Mat.	Comment
LPTEN2-141	71.2	Internal	Inclusion	19.0	2200	Cu	Fe,~C
LPTEN2-143	79.3	Internal	Inclusion	-15.5	2200	Cu	Fe
LPTEN2-158	72.0	Surface	Surface	-17.0	2200	Cu	Void very near surface
LPTEN3-36	52.8	Internal	Inclusion	7.8	2200	Cu	Fe
LPTEN3-46	74.3	Internal	Volume	-7.9	2200	Cu	
LPTEN3-49	73.4	Internal	Void	2.3	2200	Cu	Crack like features
LPTEN3-56	80.1	Internal	Inclusion	20.3	2200	Cu	Fe
LPTEN3-72	76.2	Internal	Inclusion	-21.3	2200	Cu	Fe
LPTEN3-78	86.9	Internal	Volume	6.6	2200	Cu	
LPTEN3-81	96.4	Internal	Volume	-0.3	2200	Cu	Grains
LPTEN3-85	71.8	Surface	Pit	-7.2	2200	Cu	Reaction pit
LPTEN3-92	67.5	Internal	Void	-6.7	2200	Cu	Fe
LPTEN3-110	85.0	Internal	Volume	5.0	2200	Cu	
LPTEN3-131	69.5	Internal	Volume	6.6	2200	Cu	
LPTEN3-134	61.8	Internal	Inclusion	-10.1	2200	Cu	C,Fe

Nominal Specimen Dimensions: 165mm long, 6.35 mm (.250 inch) diameter gage se

Loading Fixture Geometry: Instron Supergrips and machine

Note: 0.00 mm in "Position" column indicate center of gage section. Blueprint gage length within ~+/-20 mm. ORNL-HTML defined +/-17.5.

AlliedSignal
AEROSPACE

TABLE 5B. TENSILE STRESS RUPTURE AND FRACTOGRAPHY DATA

Speicmen No.	Stress MPa	Time (hr)	Temp C	Temp F	Fracture Origin Location	Fracture Origin Type	SCG	Test	Comment
LPTEN3- 40	450	631.0	982	1800	Internal	Inclusion		HTML FF 685	C inclusion
LPTEN3- 18	455	808.0	982	1800	Button	Surface		HTML FF 884	
LPTEN3- 27	455	336.0	982	1800	Surface	Surface		HTML	
LPTEN2- 44	460	0.0	982	1800	Internal	Crack		HTML	FOL ~460 MPa
LPTEN2- 54	460	602.0	982	1800	Internal	Volume		HTML FF 805	
LPTEN2- 51	465	0.0	982	1800	Internal	Crack		HTML	FOL ~405 MPa
LPTEN2- 73	465	0.0	982	1800	Internal	Inclusion		HTML	Fe. FOL ~465 MPa
LPTEN2- 38	470	512.0	982	1800	Internal	Inclusion		HTML FF 747	C inclusion
LPTEN2- 70	475	21.0	982	1800	Internal	Void		HTML	
LPTEN1- 26	450	0.0	1149	2100	Internal	Inclusion		MPTL	Fe,Ti,Co.
LPTEN1- 41	450	1.0	1149	2100	Internal	Void		MPTL	Fe inclusion
LPTEN2- 39	450	503.0	1149	2100				MPTL FF TBD	FF
LPTEN2- 94	450	649.0	1149	2100				MPTL FF TBD	FF
LPTEN2-139	450	277.6	1149	2100	Internal	Volume	SCG	MPTL	
LPTEN2-147	450	503.0	1149	2100				MPTL FF TBD	FF
LPTEN2-150	450	513.0	1149	2100				MPTL FF TBD	FF
LPTEN2-153	450	3.2	1149	2100	Surface	Surface	SCG	MPTL	
LPTEN3- 20	450	501.0	1149	2100				MPTL FF TBD	FF
LPTEN3- 59	450	39.6	1149	2100	Internal	Volume	SCG	MPTL	
LPTEN3- 61	450	17.6	1149	2100	Internal	Volume	SCG	MPTL	
LPTEN3- 64	450	6.4	1149	2100	Internal	Inclusion	SCG	MPTL	Fe inclusion
LPTEN3- 77	450	125.4	1149	2100	Internal	Volume	SCG	MPTL	
LPTEN3- 79	450	500.0	1149	2100				MPTL FF TBD	FF
LPTEN3- 87	450	2.3	1149	2100	Internal	Inclusion		MPTL	Fe
LPTEN3- 88	450	0.4	1149	2100	Internal	Void		MPTL	Fe,Co
LPTEN3- 90	450	0.0	1149	2100	Internal	Inclusion		MPTL	Fe
LPTEN3-115	450	20.4	1149	2100	Internal	Inclusion		MPTL	Fe
LPTEN3-129	450	0.1	1149	2100	Internal	Volume	SCG	MPTL	
LPTEN3-132	450	0.0	1149	2100	Internal	Volume	SCG	MPTL	Fail on loading
LPTEN2- 61	425	0.0	1149	2100	Internal	Inclusion		HTML	Fe, C. FOL ~330 MPa
LPTEN2- 62	425	32.1	1149	2100	Internal	Void		HTML	~Fe. Failed on gage/shank trnsition
LPTEN3-109	425	509.0	1149	2100	Internal	Inclusion		HTML FF 806	Fe.
LPTEN3- 31	435	594.0	1149	2100	Surface	Pit		HTML FF 787	Reaction pit.
LPTEN2- 32	440	376.0	1149	2100	Surface	Surface		HTML	
LPTEN2- 75	445	0.0	1149	2100	Internal	Void		HTML	
LPTEN2- 47	450	0.1	1149	2100	Internal	Void		HTML	
LPTEN3- 41	450	7.0	1149	2100	Internal	Volume		HTML	
LPTEN1- 3	300	517.0	1204	2199	Missing	Missing		HTML	Specimen lost
LPTEN2- 31	315	594.0	1204	2199	Internal	Inclusion		HTML FF 589	C inclusion
LPTEN2- 74	325	68.0	1204	2199	Internal	Volume	SCG	HTML	Good SCG photo
LPTEN3- 19	335	469.0	1204	2199	Surface	Surface		HTML	
LPTEN2- 36	337	593.0	1204	2199	Surface	Oxide		HTML FF 611	Spalled oxide layer.

TABLE 5B. TENSILE STRESS RUPTURE AND FRACTOGRAPHY DATA (Contd)

Speicmen No.	Stress MPa	Time (hr)	Temp C	Temp F	Fracture Origin Location	Fracture Origin Type	SCG	Test		Comment
LPTEN2- 30	340	566.0	1204	2199	Surface	Pit		HTML	FF 774	Pit in oxide layer.
LPTEN3- 37	340	177.0	1204	2199	Surface	Surface		HTML		
LPTEN3- 39	345	636.0	1204	2199	Surface	Pit		HTML	FF 757	
LPTEN2- 28	350	612.0	1204	2199	Internal	Volume		HTML	FF 639	
LPTEN2- 71	350	2.3	1204	2199	Internal	Volume		HTML		Too vague to measure
LPTEN3- 75	375	252.0	1204	2199	Surface	Surface		HTML		
LPTEN3-121	385	501.0	1204	2199	Internal	Inclusion		HTML	FF 686	C inclusion
LPTEN3- 73	400	1.1	1204	2199	Internal	Inclusion		HTML		Fe, Cr, Ni
LPTEN2- 56	415	1.3	1204	2199	Internal	Volume		HTML		
LPTEN1- 38	375	528.0	1204	2199	Button	Surface		HTML	FF 799	
LPTEN1- 43	375	0.4	1204	2199	Internal	Volume		HTML		
LPTEN2- 72	375	0.5	1204	2199	Internal	Volume		HTML		Listed as #18, 1149C in Nanu'
LPTEN2- 93	375	40.0	1204	2199	Internal	Inclusion		HTML		Fe inclusion.
LPTEN2-146	375	12.0	1204	2199	Internal	Inclusion		HTML		Fe. .24D spots, .43(10micron)
LPTEN2-149	375	66.0	1204	2199	Internal	Inclusion		HTML		Fe. .21D spots, .43(10micron)
LPTEN2-164	375	0.8	1204	2199	Internal	Volume	SCG	HTML		
LPTEN3- 34	375	19.0	1204	2199	Internal	Inclusion		HTML		Al inclusion
LPTEN3- 48	375	525.0	1204	2199	Internal	Volume		HTML	FF 662	
LPTEN3- 54	375	43.0	1204	2199	Surface	Surface		HTML		
LPTEN3- 66	375	24.0	1204	2199	Surface	Surface		HTML		
LPTEN3- 71	375	153.0	1204	2199	Internal	Volume	SCG	HTML		
LPTEN3- 76	375	253.0	1204	2199	Surface	Surface		HTML		—
LPTEN3- 83	375	266.0	1204	2199	Internal	Volume		HTML		
LPTEN3- 93	375	80.0	1204	2199	Surface	Surface		HTML		
LPTEN3- 95	375	6.0	1204	2199	Surface	Surface		HTML		
LPTEN3-116	375	141.0	1204	2199	Internal	Volume		HTML		
LPTEN3-118	375	120.0	1204	2199	Surface	Surface		HTML		
LPTEN3-124	375	7.0	1204	2199	Surface	Surface		HTML		
LPTEN3-120	250	838.0	1260	2300	Surface	Pit		HTML	FF 571	
LPTEN1- 46	275	6.1	1260	2300	Surface	Surface		HTML		
LPTEN3- 89	275	31.0	1260	2300	Surface	Surface		HTML		
LPTEN3-112	275	474.0	1260	2300	Surface	Pit		HTML	FF 607	Reaction pit. 2cXa
LPTEN2-145	285	379.0	1260	2300	Internal	Inclusion		HTML		Fe inclusion with a small void inside
LPTEN3- 44	295	560.0	1260	2300	Internal	Volume	SCG	HTML		
LPTEN1- 36	300	0.4	1260	2300	Surface	Surface		HTML		
LPTEN2-142	305	46.0	1260	2300	Internal	Volume	SCG	HTML		
LPTEN2-102	325	1.2	1260	2300	Surface	Surface		HTML		
LPTEN2- 66	200	530.0	1295	2363	Surface	Surface		HTML	RO	Run out. Broken during removal
LPTEN1- 23	300	0.4	1295	2363	Surface	Surface		HTML		Reaction patch.

AlliedSignal
AEROSPACE

TABLE 5B. TENSILE STRESS RUPTURE AND FRACTOGRAPHY DATA (Contd)

Speicmen No.	Stress MPa	Time (hr)	Temp C	Temp F	Fracture Origin Location	Fracture Origin Type	SCG	Test	Comment
LPTEN1- 11	375	0.4	1295	2363	Surface	Surface		HTML	
LPTEN1- 15	225	675.0	1315	2399	Surface	Surface		HTML	FF 489 Reaction patch.
LPTEN2-128	227.5	20.0	1315	2399	Surface	Surface	SCG	HTML	
LPTEN2- 37	230	244.0	1315	2399	Surface	Surface	SCG	HTML	
LPTEN2-112	230	168.0	1315	2399	Surface	Surface		HTML	
LPTEN2-111	232.5	297.0	1315	2399	Surface	Surface		HTML	
LPTEN2- 64	235	52.0	1315	2399	Surface	Surface	SCG	HTML	
LPTEN1- 24	240	2.9	1315	2399	Internal	Volume	SCG	HTML	
LPTEN1- 2	250	24.4	1315	2399	Surface	Surface	SCG	HTML	
LPTEN2-121	125	728.0	1371	2500	Surface	Surface	SCG	HTML	
LPTEN2-119	130	588.0	1371	2500	Surface	Surface	SCG	HTML	
LPTEN2-117	135	587.0	1371	2500	Surface	Surface	SCG	HTML	
LPTEN2-130	135	280.0	1371	2500	Surface	Surface	SCG	HTML	
LPTEN2-124	140	586.0	1371	2500	Surface	Surface	SCG	HTML	
LPTEN1- 12	145	368.0	1371	2500	Surface	Surface		HTML	
LPTEN1- 13	145	266.0	1371	2500	Surface	Surface	SCG	HTML	
LPTEN1- 17	145	111.0	1371	2500	Surface	Surface	SCG	HTML	
LPTEN2- 7	145	373.0	1371	2500	Surface	Surface		HTML	
LPTEN2- 45	145	57.0	1371	2500	Surface	Surface		HTML	
LPTEN2- 46	145	73.0	1371	2500	Surface	Surface	SCG	HTML	
LPTEN2- 50	145	90.0	1371	2500	Surface	Surface		HTML	
LPTEN2- 57	145	364.0	1371	2500	Surface	Surface		HTML	
LPTEN2- 63	145	293.0	1371	2500	Surface	Surface	SCG	HTML	
LPTEN2- 92	145	368.0	1371	2500	Surface	Surface	SCG	HTML	
LPTEN2-101	145	112.0	1371	2500	Surface	Surface	SCG	HTML	
LPTEN2-120	145	385.0	1371	2500	Surface	Surface	SCG	HTML	
LPTEN2-136	145	122.0	1371	2500	Surface	Surface	SCG	HTML	
LPTEN2-162	145	117.0	1371	2500	Surface	Surface		HTML	
LPTEN3- 35	145	236.0	1371	2500	Surface	Surface	SCG	HTML	
LPTEN3- 50	145	443.0	1371	2500	Surface	Surface	SCG	HTML	
LPTEN2-113	150	208.0	1371	2500	Surface	Surface	SCG	HTML	
LPTEN2-134	150	171.0	1371	2500	Surface	Surface	SCG	HTML	
LPTEN3- 33	150	75.0	1371	2500	Surface	Surface	SCG	HTML	
LPTEN1- 20	160	209.0	1371	2500	Surface	Surface	SCG	HTML	
LPTEN1- 6	180	62.0	1371	2500	Surface	Surface	SCG	HTML	
LPTEN1- 7	180	6.8	1371	2500	Surface	Surface		HTML	
LPTEN1- 8	180	14.0	1371	2500	Surface	Surface	SCG	HTML	
LPTEN1- 16	180	0.8	1371	2500	Surface	Surface	SCG	HTML	
LPTEN1- 19	180	1.6	1371	2500	Surface	Surface		HTML	
LPTEN2- 34	180	5.6	1371	2500	Surface	Surface	SCG	HTML	
LPTEN2- 60	180	19.0	1371	2500	Internal	Volume	SCG	HTML	Y inclusion
LPTEN2- 69	180	0.2	1371	2500	Surface	Surface		HTML	
LPTEN2- 77	180	0.2	1371	2500	Surface	Surface		HTML	

AlliedSignal AEROSPACE

TABLE 5B. TENSILE STRESS RUPTURE AND FRACTOGRAPHY DATA (Contd)

Speicmen No.	Stress MPa	Time (hr)	Temp C	Temp F	Fracture Origin Location	Fracture Origin Type	SCG	Test		Comment
LPTEN2- 91	180	8.6	1371	2500	Surface	Surface	SCG	HTML		
LPTEN2-109	180	0.1	1371	2500	Surface	Surface		HTML		
LPTEN2-116	180	6.8	1371	2500	Surface	Surface	SCG	HTML		
LPTEN2-118	180	28.0	1371	2500	Internal	Inclusion	SCG	HTML		Y spots. Good photo of SCG and Y spots.
LPTEN2-140	180	25.0	1371	2500	Internal	Volume	SCG	HTML		
LPTEN3- 32	180	64.0	1371	2500	Surface	Surface		HTML		
LPTEN3- 69	180	1.8	1371	2500	Internal	Volume		HTML		
LPTEN1- 9	190	68.0	1371	2500	Internal	Volume	SCG	HTML		
LPTEN2- 55	210	1.4	1371	2500	Surface	Surface	SCG	HTML		
LPTEN2- 35	85	597.0	1400	2552	Surface	Oxide		HTML	FF 385	Spalled oxide layer.
LPTEN2-123	90	476.0	1400	2552	Surface	Pit		HTML	FF 323	Surface cavities at high mag.
LPTEN2- 68	100	462.0	1400	2552	Surface	Surface	SCG	HTML		
LPTEN2-114	110	411.0	1400	2552	Surface	Surface	SCG	HTML		
LPTEN1- 4	125	341.0	1400	2552	Surface	Surface	SCG	HTML		
LPTEN1- 10	130	192.0	1400	2552	Surface	Surface	SCG	HTML		
LPTEN2-125	130	139.0	1400	2552	Internal	Volume	SCG	HTML		
LPTEN1- 21	140	96.0	1400	2552	Surface	Surface	SCG	HTML		
LPTEN3- 29	150	80.0	1400	2552	Internal	Volume	SCG	HTML		

Nominal Specimen Dimensions: 165mm long, 6.35 mm (.250 inch) diameter gage section.
Loading Fixture Geometry: Instron Supergrips and Instron machine or ATS frame

AlliedSignal
AEROSPACE

TABLE 6. PLATE BENDING FRACTOGRAPHY AND STRENGTH RESULTS

Specimen Number	Pressure (psi)	Strain	Fracture Stress* (MPa)	Angle** (deg.)	Fracture Origin Location	Type	Support Circle Radius (mm)
LPPB- 5	1998	0.002169	958.7	0	Surface	Surface	24.130
LPPB- 6	1514	0.001641	725.3	35	Surface	Surface	24.130
LPPB- 7	1432	0.001553	686.4	61	Surface	Inclusion	24.130
LPPB- 8	1746	0.001894	837.1	35	Surface	Surface	24.130
LPPB- 12	1662	0.001809	799.6	0	Surface	Surface	24.130
LPPB- 13	1464	0.001584	700.1	22	Surface	Pit	24.130
LPPB- 14	1729	0.001872	827.4	70	Surface	Surface	24.130
LPPB- 15	1775	0.001920	848.6	18	Surface	Surface	24.130
LPPB- 16	1549	0.001674	739.9	60	Surface	Inclusion	24.130
LPPB- 17	1765	0.001908	843.3	68	Surface	Surface	24.130
LPPB- 18	1882	0.002033	898.6	72	Surface	Surface	24.130
LPPB- 19	1498	0.001618	715.1	2	Surface	Surface	24.130
LPPB- 20	1338	0.001444	638.2	37	Surface	Surface	24.130
LPPB- 21	1788	0.001937	856.1	11	Surface	Surface	24.130
LPPB- 22	1752	0.001893	836.7	23	Surface	Surface	24.130
LPPB- 23	1510	0.001632	721.3	29	Surface	Inclusion	24.130
LPPB- 24	1578	0.001709	755.4	54	Surface	Surface	24.130
LPPB- 25	1159	0.001259	556.5	75	Surface	Crack	24.130
LPPB- 26	1514	0.001642	725.7	10	Surface	Pit	24.130
LPPB- 27	1402	0.001528	675.4	0	Surface	Surface	24.130
LPPB- 28	1736	0.001889	834.9	0	Surface	Surface	24.130
LPPB- 29	1429	0.001550	685.1	5	Surface	Surface	24.130
LPPB- 30	1423	0.001545	682.9	67	Surface	Surface	24.130
LPPB- 31	1800	0.001955	864.1	71	Surface	Surface	24.130
LPPB- 40	1687	0.001831	809.3	44	Surface	Inclusion	24.130
LPPB- 41	1426	0.001549	684.6	48	Surface	Surface	24.130
LPPB- 42	1751	0.001903	841.1	55	Surface	Surface	24.130
LPPB- 43	1489	0.001617	714.7	68	Surface	Surface	24.130
LPPB- 44	1774	0.001926	851.3	19	Surface	Surface	24.130
LPPB- 45	1368	0.001484	655.9	3	Surface	Pit	24.130
LPPB- 46	1602	0.001744	770.8	52	Surface	Inclusion	24.130

*Fracture stress calculated from fracture pressure and calibrated strain.
**The samller angle between fracture plane and the machining direction,
Note 0 degrees is equivalent to 90 degrees
Elastic modulus used = 330.5 GPa.
Poisson's Ratio = 0.27 (AlliedSignal Engines Grindosonic data)
Note: Disks 1,2,3,33,34,36 tested with larger (24.765 mm) supporting radius
Updated fracture stress x 1.029722 (same ratio as other disks)
Disks 33,34,36 NTC AR heat treated, no AlliedSignal new treatment

AlliedSignal
AEROSPACE

TABLE 6. PLATE BENDING FRACTOGRAPHY AND STRENGTH RESULTS (Contd)

Specimen Number	Pressure (psi)	Strain	Fracture Stress* (MPa)	Angle** (deg.)	Fracture Origin Location	Type	Support Circle Radius (mm)
LPPB- 47	1655	0.001802	796.5	6	Surface	Surface	24.130
LPPB- 48	1668	0.001815	802.2	89	Surface	Surface	24.130
LPPB- 49	1583	0.001735	766.8	7	Surface	Surface	24.130
LPPB- 50	1668	0.001838	812.4	15	Surface	Surface	24.130
LPPB- 51	1559	0.001718	759.3	46	Surface	Surface	24.130
LPPB- 52	1794	0.001976	873.4	49	Surface	Surface	24.130
LPPB- 1	1614	0.001872	804.6	N/A	Edge	Surface	24.765
LPPB- 2	1686	0.001958	841.6	38	Surface	Surface	24.765
LPPB- 3	1602	0.001864	801.2	N/A	Edge	Surface	24.765
LPPB- 33	1155	0.001343	577.3	0	Surface	Surface	24.765 NTC HT
LPPB- 34	1086	0.001265	543.8	0	Surface	Surface	24.765 NTC HT
LPPB- 36	1752	0.002041	877.3	25	Internal Inclusion		24.765 NTC HT

*Fracture stress calculated from fracture pressure and calibrated strain.
**The samller angle between fracture plane and the machining direction,
Note 0 degrees is equivalent to 90 degrees
Elastic modulus used = 330.5 GPa.
Poisson's Ratio = 0.27 (AlliedSignal Engines Grindosonic data)
Note: Disks 1,2,3,33,34,36 tested with larger (24.765 mm) supporting radius
Updated fracture stress x 1.029722 (same ratio as other disks)
Disks 33,34,36 NTC AR heat treated, no AlliedSignal new treatment

TABLE 7. FRACTOGRAPHY AND TEST RESULTS OF UNOTCHED TENSION TORSION SPECIMENS

Gage diameter = .250 inch, length = 1.378 inch
Specimen length = 7.0/7.2 inch

Specimen Number	Tensile Load	Torque (lb.in)	Fracture Origin Location	Fracture Origin Type	From Side (in)	From End (in)	Top or Bottom End	First Applied Load Type
LPUTT- 45	1	-372	Internal	Inclusion	0.042	Gage	N/A	Tension
LPUTT- 47	-1	-278	Internal	Inclusion	0.008	Gage	N/A	Tension
LPUTT- 48	0	-302	Internal	Inclusion	0.002	Gage	N/A	Tension
LPUTT- 49	0	-390	Internal	Inclusion	0.028	Gage	N/A	Tension
LPUTT- 50	0	-307	Internal	Inclusion	0.013	Gage	N/A	Tension
LPUTT- 3	0	-420	Missing	(Est. Surf/Surf)		N/A	N/A	Tension
LPUTT- 4	0	-380	Surface	Surface	0.0	Gage	N/A	Tension
LPUTT- 5	0	-340	Surface	Surface	0.0	Gage	N/A	Tension
LPUTT- 6	0	-380	Surface	Surface	0.0	Gage	N/A	Tension
LPUTT- 7	0	-320	Surface	Surface	0.0	Gage	N/A	Tension
LPUTT- 8	0	-400	Surface	Surface	0.0	Gage	N/A	Tension
LPUTT- 9	0	-360	Surface	Surface	0.0	Gage	N/A	Tension
LPUTT- 10	0	-360	Surface	Surface	0.0	Gage	N/A	Tension
LPUTT- 28	750	-363	Internal	Inclusion	0.007	Gage	N/A	Tension
LPUTT- 29	750	-387	Internal	Inclusion	0.001	Gage	N/A	Tension
LPUTT- 34	751	-307	Internal	Inclusion	0.003	Gage	N/A	Tension
LPUTT- 35	749	-351	Internal	Inclusion	0.013	Gage	N/A	Tension
LPUTT- 36	751	-361	Missing	(Est. Surf/Surf)		N/A	N/A	Tension
LPUTT- 25	752	-317	Surface	Surface	0.0	3.17	Bottom	Tension
LPUTT- 32	750	-407	Surface	Surface	0.0	Gage	N/A	Tension
LPUTT- 44	1180	-285	Surface	Surface	0.0	Gage	N/A	Torsion
LPUTT- 20	1501	-347	Internal	Inclusion	0.051	Gage	N/A	Tension
LPUTT- 24	1500	-320	Internal	Inclusion	0.040	2.82	Top	Tension
LPUTT- 21	1501	-346	Surface	Surface	0.0	Gage	N/A	Tension
LPUTT- 22	1500	-329	Surface	Surface	0.0	Gage	N/A	Tension
LPUTT- 33	1500	-310	Surface	Surface	0.0	2.80	Bottom	Tension
LPUTT- 39	1807	-285	Internal	Inclusion	0.033	Gage	N/A	Torsion
LPUTT- 15	2385	-274	Missing	(Est. Surf/Surf)		Gage	N/A	Tension
LPUTT- 18	2380	-298	Internal	Inclusion	0.013	Gage	N/A	Tension
LPUTT- 38	2379	-360	Internal	Inclusion	0.002	Gage	N/A	Torsion
LPUTT- 42	2290	-285	Internal	Inclusion	0.006	Gage	N/A	Torsion
LPUTT- 43	2386	-335	Internal	Inclusion	0.011	Gage	N/A	Torsion
LPUTT- 12	2391	-315	Surface	Surface	0.0	Gage	N/A	Tension
LPUTT- 14	2382	-273	Surface	Surface	0.0	2.81	Bottom	Tension
LPUTT- 17	2381	-229	Surface	Surface	0.0	Gage	N/A	Tension
LPUTT- 40	2376	-320	Surface	Surface	0.0	Gage	N/A	Torsion

AlliedSignal
AEROSPACE

TABLE 8A. SPIN DISK TEST AND FRACTOGRAPHY RESULTS

Disk No.	Test Temp, F	Test Type	Test Sequence	Failure Speed, krpm	Failure Time Hours, (min)	Loc. Type
30*	RT	FF	1	102.70	0 (FF)	Sur Surf
38*	RT	FF	2	43.13	0 (FF)	Sur Line
27*	RT	FF	3	89.20	0 (FF)	Sur Surf
16*	RT	FF	4	80.60	0 (FF)	Sur Surf
21	RT	FF	5	82.80	0 (FF)	Sur Surf
18	RT	FF	6	99.10	0 (FF)	Sur Surf
4	RT	FF	7	92.80	0 (FF)	Sur Surf
3	RT	FF	8	107.10	0 (FF)	Int Incl
31	RT	FF	9	90.20	0 (FF)	Int Incl
36	RT	FF	10	96.60	0 (FF)	Sur Surf
9	RT	FF	11	105.00	0 (FF)	Sur Surf
17	RT	FF	12	102.60	0 (FF)	Sur Surf
34	RT	FF	13	88.50	0 (FF)	Int Incl
40	RT	FF	14	46.80	0 (FF)	Sur Line
6	2200	FF	1	93.00	0 (FF)	Int Incl
29	2200	FF	2	80.40	0 (FF)	Int Incl
25	2200	FF	3	60.80	0 (FF)	Sur Line
13	2200	FF	4	83.00	0 (FF)	Sur Surf
42	2200	FF	5	85.80	0 (FF)	Sur Surf
23	2200	FF	6	83.00	0 (FF)	Sur Surf
32	2200	FF	7	76.00	0 (FF)	Sur Surf
33	2200	FF	8	76.00	0 (FF)	Sur Surf
37	2200	FF,S/R	2	74	FOL to 75 KRPM	Int Incl
12	2200	FF,S/R	5	72.2	FOL to 75 KRPM	Sur Surf
39	2200	FF,S/R	7	47	FOL to 75 KRPM	Sur Line
41	2200	S/R	1	67/75	150/27	Sur Surf
22	2200	S/R	3	71	27.33	Sur Surf
7	2200	S/R	4	71/75/82	100/10/Burst	Sur Surf
5	2200	S/R	6	75/80/85/88.4	50/10/10/Burst	Sur Surf
1	2200	S/R	8	75	3.0	Int Volume
19	2200	S/R	9	75/84.5	50/FOL	Sur Line
14	2500	S/R	1	55.000	.95 (57 min)	Sur Surf
15	2500	S/R	2	45/50	10/0.4(600/24 min)	Sur Surf
24	2500	S/R	3	50.000	~.0166 (1 min)	Sur Surf
26	2500	S/R	4	50.000	11.08 (665 min)	Sur Surf
8	2500	S/R	5	41.800	6.966 (418 min)	Sur Surf
28	2500	S/R	6	N/A	N/A	Sur Surf

*As received NTC post machining heat treat.

AlliedSignal
AEROSPACE

TABLE 8B. SPIN DISK FRACTOGRAPHY RESULTS

Disk No.	Test Temp, F	Loc.	Type	Comments	Distance (in) From Center	Top Surf.
30*	RT	Surf	Surf	Trans. Machining	~1.0	Prob. Top
38*	RT	Surf	Line	Machining lines/scratches	0.125	On Shaft
27*	RT	Surf	Surf	Trans. Machining	0.731	Top
16*	RT	Surf	Surf	Transverse Machining direction	0.176	Top
21	RT	Surf	Surf	Long. machining direction	1.365	Bottom
18	RT	Surf	Surf	20 Deg Trans. Machining	0.940	Bottom
4	RT	Surf	Surf	Trans. Machining	0.349	Top
3	RT	Int	Incl	Dark inclusion	0.649	0.185
31	RT	Int	Incl	Dark Inclusion	0.450	0.630
36	RT	Surf	Surf		N/A	N/A
9	RT	Surf	Surf	Near deep machining groove	0.800	Top
17	RT	Surf	Surf		N/A	N/A
34	RT	Int	Incl	Dark inclusion	N/A	0.551
40	RT	Surf	Line	Machining lines/scratches	0.125	On Shaft
6	2200	Int	Incl	Dark Inclusion	~.30	~.20
29	2200	Int	Incl	Dark Long Inclusion	0.320	0.210
25	2200	Surf	Line	Circular machining line/scratch	0.593	Top
13	2200	Surf	Surf	Transverse machining line	0.590	Top
42	2200	Surf	Surf	At shaft transition	0.125	Top
23	2200	Surf	Surf		N/A	N/A
32	2200	Surf	Surf		0.498	Top
33	2200	Surf	Surf		0.560	Top
37	2200	Int	Incl	Dark inclusion	N/A	0.233 from top
12	2200	Surf	Surf	At shaft/disk transition. Disk	0.150	
39	2200	Surf	Line	Machining scratch at disk/shaft	0.140	Top
41	2200	Surf	Surf	At shaft/disk transition		
22	2200	Surf	Surf	At shaft/disk transition	0.149	Top
7	2200	Surf	Surf		1.010	Top
5	2200	Surf	Surf	At shaft/disk transition	0.125	Top
1	2200	Int	Vol.	Volume	0.417	Bottom?
19	2200	Surf	Line	Machining scratch at disk/shaft	0.229	Top
14	2500	Surf	Surf		0.819	Top
15	2500	Surf	Surf		0.907	Top
24	2500	Surf	Surf	At shaft/shaft transition		N/A
26	2500	Surf	Surf	Decided by expert opinion	N/A	Top
8	2500	Surf	Surf		0.402	Top
28	2500	Surf	Surf	On shaft inside joint		N/A

*As received NTC post machining heat treat.

TABLE 9. FRACTOGRAPHY AND STRENGTH DATA OF OXIDATION STUDY FLEXURE BARs

Nominal Specimen Dimensions: Mil-B, 3x4x50 mm
Loading Fixture Geometry: Mil-B ORNL/HTML IEA Roun
Four point loading with 20 mm inner span and 40 mm

Specimen Number	Stress (ksi)	Origin Location	Origin Type	Exposur Temp(F)	Time (hr)
LPBT- 183	80.1	Corner	Surface	70	0
LPBT- 184	100.8	Corner	Surface	70	0
LPBT- 185	88.3	Corner	Surface	70	0
LPBT- 186	62.1	Corner	Surface	70	0
LPBT- 187	65.4	Corner	Surface	70	0
LPBT- 188	103.5	Surface	Surface	70	0
LPBT- 189	117.2	Corner	Surface	70	0
LPBT- 190	57.8	Corner	Surface	70	0
LPBT- 191	103.5	Corner	Surface	70	0
LPBT- 192	90.5	Corner	Surface	70	0
LPBT- 193	91.0	Corner	Surface	70	0
LPBT- 194	109.5	Corner	Surface	70	0
LPBT- 195	92.6	Corner	Surface	70	0
LPBT- 196	107.3	Corner	Surface	70	0
LPBT- 197	100.8	Corner	Surface	70	0
LPBT- 198	115.5	Corner	Surface	70	0
LPBT- 199	125.3	Corner	Surface	70	0
LPBT- 200	57.8	Corner	Chip	70	0
LPBT- 201	108.4	Corner	Surface	70	0
LPBT- 202	120.4	Corner	Surface	70	0
LPBT- 203	99.2	Corner	Surface	70	0
LPBT- 204	102.4	Corner	Surface	70	0
LPBT- 205	112.8	Corner	Surface	70	0
LPBT- 206	115.5	Surface	Surface	70	0
LPBT- 207	102.4	Surface	Surface	70	0
LPBT- 208	89.9	Corner	Surface	70	0
LPBT- 209	111.7	Corner	Surface	70	0
LPBT- 210	104.6	Corner	Surface	70	0
LPBT- 211	104.6	Corner	Surface	70	0
LPBT- 212	115.0	Corner	Surface	70	0
LPBT- 48	127.1	Corner	Surface	1800	100
LPBT- 49	130.3	Corner	Surface	1800	100
LPBT- 50	148.1	Surface	Surface	1800	100
LPBT- 51	116.3	Corner	Surface	1800	100
LPBT- 52	132.5	Surface	Surface	1800	100
LPBT- 53	132.5	Corner	Surface	1800	100
LPBT- 54	142.7	Surface	Surface	1800	100
LPBT- 55	127.1	Surface	Surface	1800	100

TABLE 9. FRACTOGRAPHY AND STRENGTH DATA OF OXIDATION STUDY FLEXURE BARs (Contd)

Nominal Specimen Dimensions: Mil-B, 3x4x50 mm
Loading Fixture Geometry: Mil-B ORNL/HTML IEA Roun
Four point loading with 20 mm inner span and 40 mm

Specimen Number	Stress (ksi)	Origin Location	Origin Type	Exposur Temp(F)	Time (hr)
LPBT- 56	121.2	Surface	Surface	1800	100
LPBT- 57	136.3	Surface	Surface	1800	100
LPBT- 43	148.8	Surface	Surface	1900	100
LPBT- 44	126.0	Surface	Surface	1900	100
LPBT- 45	116.8	Surface	Surface	1900	100
LPBT- 46	133.6	Surface	Surface	1900	100
LPBT- 47	139.1	Surface	Surface	1900	100
LPBT- 38	146.7	Surface	Surface	2000	100
LPBT- 39	141.8	Surface	Surface	2000	100
LPBT- 40	109.7	Corner	Surface	2000	100
LPBT- 41	148.8	Surface	Surface	2000	100
LPBT- 42	151.5	Surface	Surface	2000	100
LPBT- 33	117.5	Surface	Oxide	2100	100
LPBT- 34	72.6	Corner	Crack	2100	100
LPBT- 35	125.5	Surface	Surface	2100	100
LPBT- 36	129.8	Surface	Surface	2100	100
LPBT- 37	128.7	Surface	Surface	2100	100
LPBT- 58	136.3	Surface	Surface	2200	10
LPBT- 59	137.9	Surface	Surface	2200	10
LPBT- 60	141.6	Surface	Surface	2200	10
LPBT- 61	141.1	Surface	Surface	2200	10
LPBT- 62	120.6	Surface	Surface	2200	10
LPBT- 63	123.3	Surface	Surface	2200	36
LPBT- 64	136.3	Surface	Surface	2200	36
LPBT- 105	130.9	Surface	Surface	2200	36
LPBT- 106	134.0	Corner	Surface	2200	36
LPBT- 107	137.9	Surface	Surface	2200	36
LPBT- 108	131.8	Surface	Surface	2200	100
LPBT- 109	134.0	Surface	Surface	2200	100
LPBT- 110	128.6	Surface	Surface	2200	100
LPBT- 111	127.0	Surface	Surface	2200	100
LPBT- 112	132.9	Surface	Oxide	2200	100
LPBT- 113	138.3	Surface	Oxide	2200	100
LPBT- 114	134.0	Surface	Surface	2200	100
LPBT- 115	128.6	Surface	Surface	2200	100
LPBT- 116	132.9	Surface	Surface	2200	100
LPBT- 117	136.7	Surface	Surface	2200	100
LPBT- 118	142.1	Corner	Surface	2200	360

TABLE 9. FRACTOGRAPHY AND STRENGTH DATA OF OXIDATION STUDY FLEXURE BARs (Contd)

Nominal Specimen Dimensions: Mil-B, 3x4x50 mm
Loading Fixture Geometry: Mil-B ORNL/HTML IEA Roun
Four point loading with 20 mm inner span and 40 mm

Specimen Number	Stress (ksi)	Origin Location	Origin Type	Exposur Temp(F)	Time (hr)
LPBT- 119	143.2	Surface	Surface	2200	360
LPBT- 120	122.6	Corner	Surface	2200	360
LPBT- 121	128.0	Surface	Surface	2200	360
LPBT- 122	150.2	Surface	Oxide	2200	360
LPBT- 123	143.7	Surface	Surface	2200	1000
LPBT- 124	135.6	Surface	Surface	2200	1000
LPBT- 125	141.6	Surface	Surface	2200	1000
LPBT- 126	138.3	Surface	Surface	2200	1000
LPBT- 127	138.9	Surface	Surface	2200	1000
LPBT- 128	142.6	Surface	Surface	2200	1000
LPBT- 129	116.2	Surface	Oxide	2200	1000
LPBT- 130	124.8	Surface	Surface	2200	1000
LPBT- 131	136.2	Internal	Inclusion	2200	1000
LPBT- 132	137.2	Surface	Surface	2200	1000
LPBT- 149	131.8	Corner	Surface	2300	6
LPBT- 150	130.7	Surface	Surface	2300	6
LPBT- 151	135.1	Surface	Surface	2300	6
LPBT- 152	111.8	Surface	Oxide	2300	6
LPBT- 153	126.4	Surface	Surface	2300	6
LPBT- 154	121.6	Surface	Surface	2300	59
LPBT- 155	131.3	Surface	Surface	2300	59
LPBT- 156	95.1	Surface	Surface	2300	59
LPBT- 157	121.0	Surface	Surface	2300	59
LPBT- 158	121.0	Surface	Surface	2300	59
LPBT- 159	105.9	Corner	Surface	2300	100
LPBT- 160	133.5	Surface	Surface	2300	100
LPBT- 161	120.4	Surface	Surface	2300	100
LPBT- 162	95.6	Corner	Pit	2300	100
LPBT- 163	117.2	Surface	Surface	2300	100
LPBT- 164	118.3	Surface	Surface	2300	585
LPBT- 165	124.3	Surface	Surface	2300	585
LPBT- 166	116.7	Surface	Surface	2300	585
LPBT- 167	119.4	Surface	Surface	2300	585
LPBT- 168	127.0	Surface	Surface	2300	585
LPBT- 169	119.9	Surface	Surface	2300	585
LPBT- 170	130.7	Surface	Surface	2300	585
LPBT- 171	122.1	Corner	Chip	2300	585
LPBT- 172	129.1	Surface	Surface	2300	585

TABLE 9. FRACTOGRAPHY AND STRENGTH DATA OF OXIDATION STUDY FLEXURE BARs (Contd)

Nominal Specimen Dimensions: Mil-B, 3x4x50 mm
Loading Fixture Geometry: Mil-B ORNL/HTML IEA Roun
Four point loading with 20 mm inner span and 40 mm

Specimen Number	Stress (ksi)	Origin Location	Origin Type	Exposur Temp(F)	Time (hr)
LPBT- 173	110.8	Surface	Surface	2300	585
LPBT- 65	127.6	Corner	Surface	2400	1
LPBT- 66	124.4	Surface	Surface	2400	1
LPBT- 67	130.3	Corner	Surface	2400	1
LPBT- 68	133.0	Corner	Surface	2400	1
LPBT- 69	120.6	Corner	Surface	2400	1
LPBT- 70	113.1	Corner	Surface	2400	4
LPBT- 71	124.9	Surface	Surface	2400	4
LPBT- 72	120.1	Surface	Surface	2400	4
LPBT- 73	126.6	Surface	Surface	2400	4
LPBT- 74	119.0	Surface	Surface	2400	4
LPBT- 75	118.5	Surface	Surface	2400	10
LPBT- 76	124.4	Surface	Surface	2400	10
LPBT- 77	121.7	Surface	Surface	2400	10
LPBT- 78	119.0	Surface	Surface	2400	10
LPBT- 79	123.9	Corner	Surface	2400	10
LPBT- 80	106.1	Corner	Surface	2400	10
LPBT- 81	122.8	Surface	Surface	2400	10
LPBT- 82	118.5	Surface	Surface	2400	10
LPBT- 83	124.9	Corner	Surface	2400	10
LPBT- 84	115.8	Surface	Surface	2400	10
LPBT- 85	122.8	Surface	Surface	2400	36
LPBT- 86	123.3	Surface	Surface	2400	36
LPBT- 87	120.1	Surface	Surface	2400	36
LPBT- 88	128.7	Surface	Surface	2400	36
LPBT- 89	120.6	Surface	Surface	2400	36
LPBT- 90	121.7	Surface	Surface	2400	100
LPBT- 91	126.6	Surface	Surface	2400	100
LPBT- 92	121.2	Surface	Surface	2400	100
LPBT- 93	127.1	Surface	Surface	2400	100
LPBT- 94	110.4	Surface	Surface	2400	100
LPBT- 95	122.3	Surface	Surface	2400	100
LPBT- 96	122.3	Surface	Surface	2400	100
LPBT- 97	127.1	Surface	Surface	2400	100
LPBT- 98	123.9	Corner	Chip	2400	100
LPBT- 99	119.6	Surface	Surface	2400	100
LPBT- 100	122.3	Surface	Surface	2400	360
LPBT- 101	86.7	Corner	Oxide	2400	360

TABLE 9. FRACTOGRAPHY AND STRENGTH DATA OF OXIDATION STUDY FLEXURE BARs (Contd)

Nominal Specimen Dimensions: Mil-B, 3x4x50 mm
Loading Fixture Geometry: Mil-B ORNL/HTML IEA Roun
Four point loading with 20 mm inner span and 40 mm

Specimen Number	Stress (ksi)	Origin Location	Origin Type	Exposur Temp(F)	Time (hr)
LPBT- 102	127.6	Surface	Surface	2400	360
LPBT- 103	126.0	Corner	Surface	2400	360
LPBT- 104	102.3	Corner	Pit	2400	360
LPBT- 1	135.2	Surface	Surface	2500	3
LPBT- 2	122.3	Surface	Surface	2500	3
LPBT- 3	91.0	Corner	Surface	2500	3
LPBT- 4	117.4	Corner	Surface	2500	3
LPBT- 5	105.6	Surface	Pit	2500	3
LPBT- 6	91.6	Corner	Oxide	2500	36
LPBT- 7	116.9	Surface	Surface	2500	36
LPBT- 8	109.3	Surface	Surface	2500	36
LPBT- 9	61.4	Corner	Surface	2500	36
LPBT- 10	116.3	Surface	Oxide	2500	36
LPBT- 11	110.4	Surface	Pit	2500	36
LPBT- 12	116.9	Surface	Fiber	2500	36
LPBT- 13	116.3	Surface	Oxide	2500	36
LPBT- 14	113.1	Surface	Surface	2500	36
LPBT- 15	116.9	Surface	Surface	2500	36
LPBT- 17	108.9	Surface	Surface	2500	100
LPBT- 18	113.2	Surface	Surface	2500	100
LPBT- 19	112.1	Surface	Fiber	2500	100
LPBT- 20	112.1	Missing		2500	100
LPBT- 21	120.3	Surface	Surface	2500	100
LPBT- 22	114.8	Surface	Fiber	2500	100
LPBT- 23	119.2	Surface	Surface	2500	100
LPBT- 24	118.6	Surface	Surface	2500	100
LPBT- 25	110.2	Surface	Fiber	2500	100
LPBT- 26	121.8	Surface	Surface	2500	100
LPBT- 27	108.8	Surface	Surface	2500	360
LPBT- 28	118.6	Surface	Fiber	2500	360
LPBT- 29	106.5	Surface	Oxide	2500	360
LPBT- 31	119.8	Surface	Oxide	2500	360
LPBT- 32	110.2	Surface	Oxide	2500	360
LPBT- 133	108.6	Surface	Surface	2550	3
LPBT- 134	110.8	Surface	Surface	2550	3
LPBT- 135	116.7	Surface	Surface	2550	3
LPBT- 136	114.5	Surface	Surface	2550	3
LPBT- 137	104.8	Surface	Surface	2550	3

TABLE 9. FRACTOGRAPHY AND STRENGTH DATA OF OXIDATION STUDY FLEXURE BARs (Contd)

Nominal Specimen Dimensions: Mil-B, 3x4x50 mm
Loading Fixture Geometry: Mil-B ORNL/HTML IEA Roun
Four point loading with 20 mm inner span and 40 mm

Specimen Number	Stress (ksi)	Origin Location	Origin Type	Exposur Temp(F)	Time (hr)
LPBT- 138	109.7	Surface	Surface	2550	10
LPBT- 139	103.2	Surface	Surface	2550	10
LPBT- 140	104.8	Surface	Surface	2550	10
LPBT- 141	108.6	Surface	Surface	2550	10
LPBT- 142	107.0	Surface	Surface	2550	10
LPBT- 143	107.0	Surface	Surface	2550	10
LPBT- 144	108.6	Surface	Surface	2550	10
LPBT- 145	104.8	Corner	Surface	2550	10
LPBT- 146	110.8	Surface	Surface	2550	10
LPBT- 147	114.5	Surface	Surface	2550	10
LPBT- 148	115.1	Surface	Oxide	2550	100
LPBT- 174	104.8	Surface	Fiber	2550	100
LPBT- 175	106.4	Surface	Fiber	2550	100
LPBT- 176	112.2	Surface	Surface	2550	100
LPBT- 177	104.3	Surface	Surface	2550	100
LPBT- 178	102.7	Surface	Surface	2550	100
LPBT- 179	98.3	Surface	Fiber	2550	100
LPBT- 180	105.4	Surface	Fiber	2550	100
LPBT- 181	105.9	Surface	Surface	2550	100
LPBT- 182	98.9	Surface	Surface	2550	100

TABLE 10. NOTCHED TENSILE SPECIMENS TEST AND FRACTOGRAPHY RESULTS

Tested in-house using the same machine, Supergrips, and test procedure, as standard tensile specimens
Diameter and notch dimensions measured with optical comparator for FF specimens.
Specimens LPNTN KT=1.6, specimens LPNTK KT=2.15

SPECIMEN ID	Failure Load	P/a ksi	Test Type	Loc.	Type	Comment	Outer Dia.	Inner Dia.	Notch Depth	Notch Width	Notch Radius
LPNTN- 4	4239	85.7	RT FF	Surf	Surf		0.262	0.251	0.006	0.040	0.041
LPNTN- 5	5053	102.0	RT FF	Surf	Surf		0.262	0.251	0.006	0.042	0.041
LPNTN- 14	4428	90.4	RT FF	Surf	Surf		0.262	0.250	0.006	0.043	0.041
LPNTN- 18	4950	100.6	RT FF	Surf	Surf		0.262	0.250	0.006	0.040	0.041
LPNTN- 19	3661	74.8	RT FF	Int	Void	85x46 micron, 0.125" above notch	0.262	0.250	0.006	0.041	0.041
LPNTN- 24	4641	93.9	RT FF	Surf	Surf		0.262	0.251	0.006	0.041	0.041
LPNTN- 27	4117	83.7	RT FF	Surf	Surf		0.262	0.250	0.006	0.043	0.041
LPNTN- 33	4438	90.5	RT FF	Surf	Surf		0.263	0.250	0.006	0.042	0.041
LPNTN- 39	5017	102.0	RT FF	Surf	Surf		0.263	0.250	0.006	0.042	0.041
LPNTN- 47	4291	87.0	RT FF	Surf	Surf		0.262	0.251	0.006	0.044	0.041
LPNTK- 3	2475	49.7	RT FF	Surf	Surf		0.473	0.252	0.111	0.084	0.041
LPNTK- 4	2287	45.9	RT FF	Surf	Surf		0.473	0.252	0.111	0.084	0.041
LPNTK- 7	2112	42.8	RT FF	Surf	Surf		0.473	0.251	0.111	0.084	0.041
LPNTK- 13	2897	59.0	RT FF	Surf	Surf		0.473	0.250	0.111	0.083	0.041
LPNTK- 14	2725	55.2	RT FF	Surf	Surf		0.473	0.251	0.111	0.084	0.041
LPNTK- 33	2582	52.3	RT FF	Surf	Surf		0.473	0.251	0.111	0.084	0.041
LPNTK- 40	2010	40.2	RT FF	Surf	Surf		0.472	0.252	0.110	0.084	0.041
LPNTK- 44	2298	46.0	RT FF	Surf	Surf		0.473	0.252	0.110	0.084	0.041
LPNTK- 49	3194	64.1	RT FF	Surf	Surf		0.472	0.252	0.110	0.084	0.041
LPNTK- 38	2212	44.4	RT FF	Surf	Surf		0.473	0.252	0.111	0.084	0.041

AlliedSignal AEROSPACE

TABLE 10. NOTCHED TENSILE SPECIMENS TEST AND FRACTOGRAPHY RESULTS (Contd)

ORNL LP HIGH TEMPERATURE STRESS RUPTURE/CREEP NOTCHED TENSILE SPECIMENS

Tested at HTML using same machine, Supergrips, and test procedure as standard tensile specimens
Diameters measured with micrometer and notch dimensions estimated from RT fast fracture specimens.
Specimens LPNTN KT=1.6, specimens LPNTK KT=2.1

SPECIMEN ID	Failure Time	P/a MPa	Test Type	Loc.	Type	Comment		Outer Dia.	Inner Dia.	Notch Depth	Notch Width	Notch Radius
LPNTK- 5	547	190	1204 S/R	Buttonhead		Buttonhead surface failure.	FF338	0.473	0.251	0.111	0.084	0.041
LPNTK- 6	0	200	1204 S/R	Surf	Surf	No SCG zone.	FOL	0.473	0.250	0.111	0.084	0.041
LPNTK- 8	7	125	1371 S/R	Surf	Surf	Typical progressive surface SCG zone.	Strain to failure=4050 micro strain	0.470	0.249	0.111	0.084	0.041
LPNTK- 9	546	117	1371 S/R	Surf	Surf	Very small	FF203	0.472	0.249	0.111	0.084	0.041
LPNTK- 10	1	120	1371 S/R	Int.	Vol.	SCG zone. Very close to surface.		0.471	0.250	0.111	0.084	0.041
LPNTK- 11	28	117	1371 S/R	Surf	Surf	SCG. Crack with fiber inside.	Strain to failure=16280 micro strain	0.472	0.250	0.111	0.084	0.041
LPNTK- 12	1.6	117	1371 S/R	Surf	Surf	Typical progressive surface SCG zone.		0.472	0.250	0.111	0.084	0.041
LPNTK- 15	0	260	1204 S/R	Surf	Surf	No SCG zone	Severe machining damage evident	0.472	0.250	0.111	0.084	0.041
LPNTK- 24	160	117	1371 S/R	Surf	Surf	X - Test interrupted at 160 h (TEM)	Test interrupted at 160 h (TEM)	0.471	0.250	0.111	0.084	0.041
LPNTK- 25	0.03	260	1204 S/R	Surf	Surf	Few Fe spots in mirror. No SCG.		0.471	0.251	0.111	0.084	0.041
LPNTK- 27	0.75	200	1204 S/R	Surf	Surf	No SCG zone		0.471	0.249	0.111	0.084	0.041
LPNTK- 28	505	117	1371 S/R	Surf	Surf	No SCG. Spalled surface layer.	FF214	0.471	0.249	0.111	0.084	0.041
LPNTK- 29	593	175	1204 S/R	Surf	Surf	No SCG. Spalled surface layer.	FF427	0.472	0.251	0.111	0.084	0.041
LPNTK- 30	210	120	1371 S/R	Surf	Surf	SCG zone. Oxidized crack surface.	Strain to failure=20010 micro strain	0.471	0.250	0.111	0.084	0.041
LPNTK- 37	0.33	210	1204 S/R	Surf	Surf	Very small SCG zone.		0.473	0.251	0.111	0.084	0.041
LPNTK- 39	500	200	1204 S/R			Specimen to be send back from HTML.	FF367(TEM)	0.473	0.251	0.111	0.084	0.041
LPNTK- 41	372	115	1371 S/R	Surf	Surf	SCG zone at two levels.	Strain to failure=23700 micro strain	0.471	0.248	0.111	0.084	0.041
LPNTK- 47	500	190	1204 S/R	Surf	Surf	SCG zone.	FF413	0.473	0.251	0.111	0.084	0.041
LPNTK- 51	0.8	115	1371 S/R			Specimen to be send back from HTML.		0.473	0.252	0.111	0.084	0.041
LPNTK- 52	0.1	135	1371 S/R	Surf	Surf	Very large SCG zone.		0.471	0.251	0.111	0.084	0.041
LPNTK- 252	0.25	220	1204 S/R	Surf	Surf	No SCG zone.		0.473	0.252	0.111	0.084	0.041
LPNTN- 3	502	255	1204 S/R	Surf	Surf		FF603	0.256	0.242	0.006	0.042	0.041
LPNTN- 6	13.6	145	1371 S/R	Surf	Surf	SCG zone.		0.262	0.250	0.006	0.042	0.041
LPNTN- 7	0	130	1371 S/R	Surf	Surf	Bad test. Load loss failure.	Fractured, load loss	0.262	0.250	0.006	0.042	0.041
LPNTN- 8	0.1	275	1204 S/R	Surf	Surf	No SCG zone. Spalled layer.		0.262	0.249	0.006	0.042	0.041
LPNTN- 9	144	130	1371 S/R	Surf	Surf	SCG zone.		0.262	0.250	0.006	0.042	0.041
LPNTN- 10	To be tested		S/R					0.000	0.000	0.006	0.042	0.041
LPNTN- 12	408	130	1371 S/R	Surf	Surf			0.261	0.249	0.006	0.042	0.041
LPNTN- 17	5	260	1204 S/R	Surf	Pit	Zr and trace Al inside pit.		0.263	0.248	0.006	0.042	0.041
LPNTN- 21	1.4	300	1204 S/R	Surf	Surf	Spalled layer. Zr & Al near origin.		0.263	0.250	0.006	0.042	0.041
LPNTN- 22	In test	260	1204 S/R			To be tested. 43 hr 9:00 23 July 93.		0.263	0.249	0.006	0.042	0.041
LPNTN- 26	0.4	135	1371 S/R	Surf	Incl	SCG zone. Some Al signal.		0.262	0.250	0.006	0.042	0.041
LPNTN- 30	103	133	1371 S/R	Surf	Surf	SCG zone.		0.262	0.250	0.006	0.042	0.041
LPNTN- 32	To be tested		S/R					0.000	0.000	0.006	0.042	0.041
LPNTN- 35	211	130	1371 S/R	Surf	Surf	X - Test interrupted at 211 h (TEM).	Test interrupted at 211 h (TEM)	0.262	0.249	0.006	0.042	0.041
LPNTN- 37	To be tested		S/R					0.000	0.000	0.006	0.042	0.041
LPNTN- 38	504	125	1371 S/R	Surf	Surf	Spalled layer.	FF167 MPa	0.262	0.249	0.006	0.042	0.041
LPNTN- 40	500	115	1371 S/R	Surf	Surf	Spalled layer.	FF262 MPa	0.262	0.248	0.006	0.042	0.041
LPNTN- 42	503	240	1204 S/R			Specimen to be send back from HTML.	FF474	0.263	0.248	0.006	0.042	0.041
LPNTN- 45	521	250	1204 S/R			Specimen to be send back from HTML.	FF442	0.263	0.249	0.006	0.042	0.041
LPNTN- 49	5	135	1371 S/R	Surf	Surf	SCG zone.		0.263	0.249	0.006	0.042	0.041

APPENDIX V

FRACTOGRAPHY PHOTOGRAPHS

(41 pages)

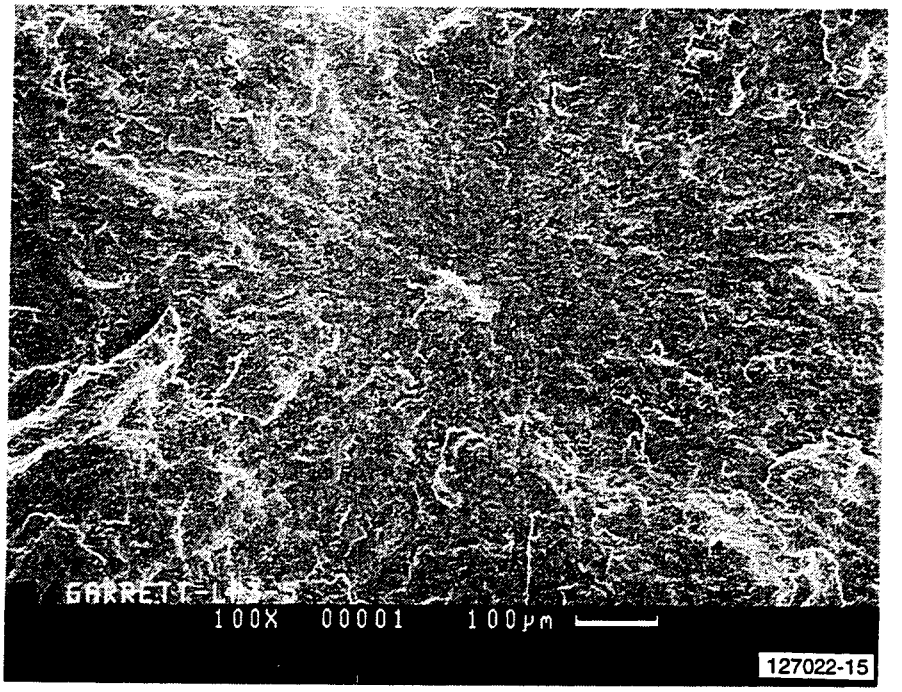

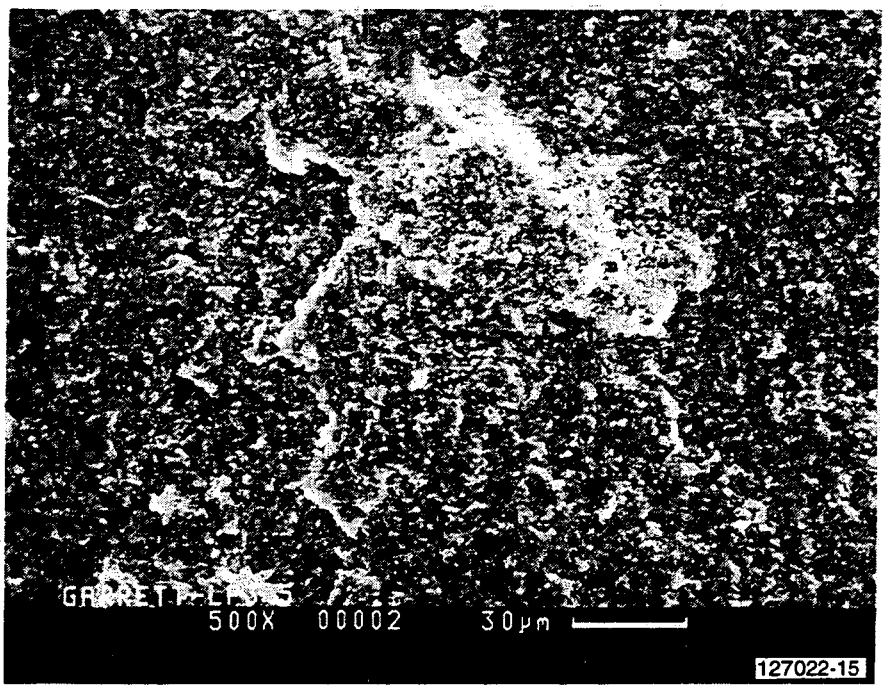

GB11591-714

Figure V-1(a). Photomicrographs Of Failure Originating From An Internal Inclusion Containing C But No Si In An E-Size Flexure Bar. MOR = 110.2 ksi.

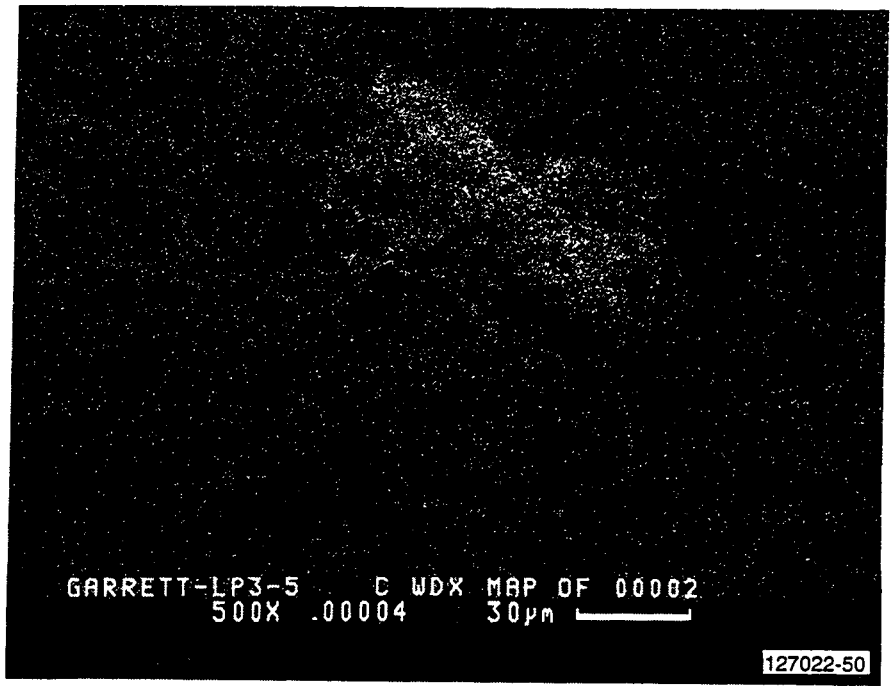

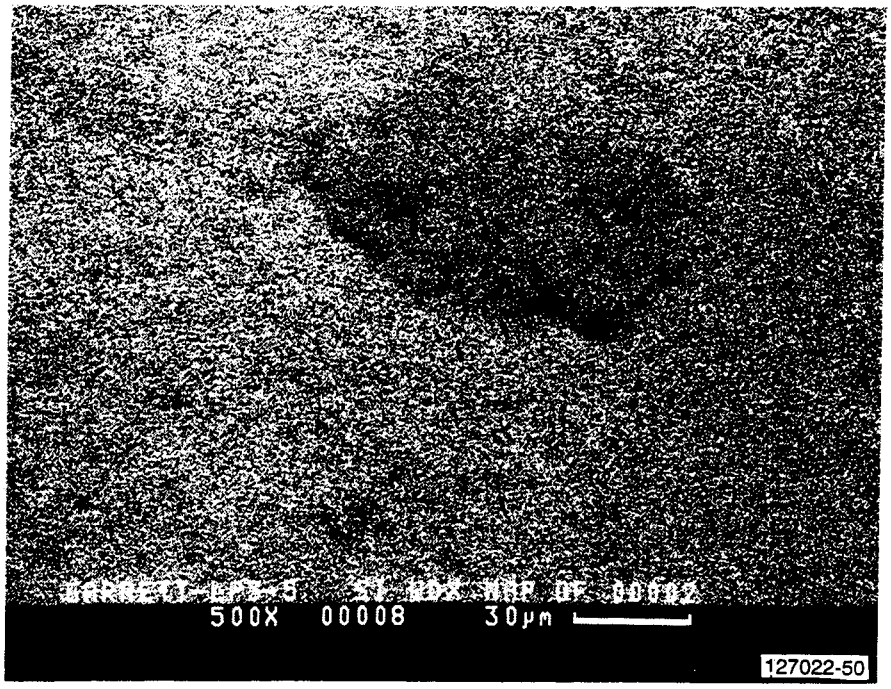

GB11591-715

Figure V-1(b). WDX Element Maps Of Failure Originating From An Internal Inclusion Containing C But No Si In An E-Size Flexure Bar. MOR = 110.2 ksi.

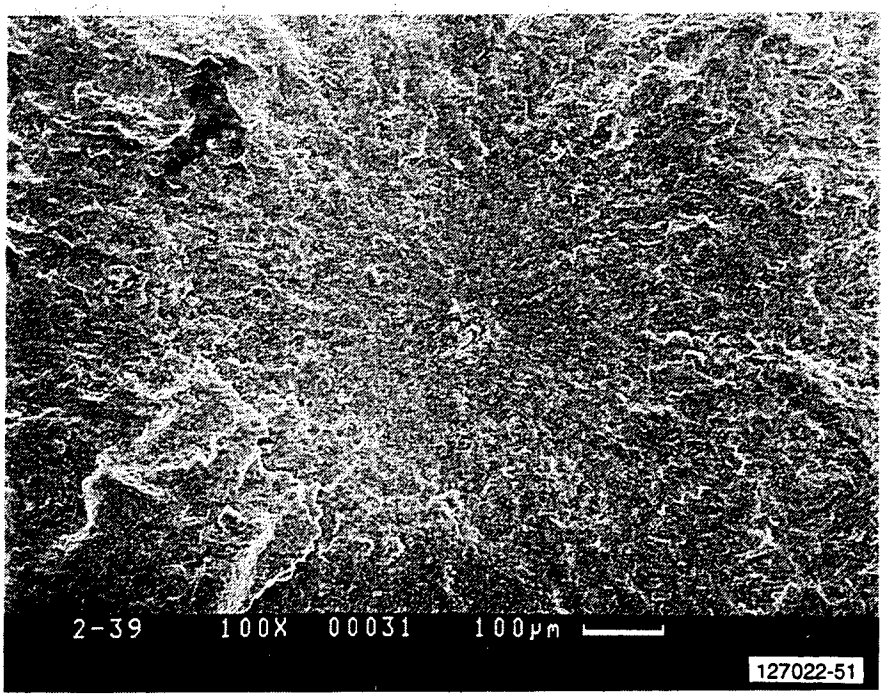

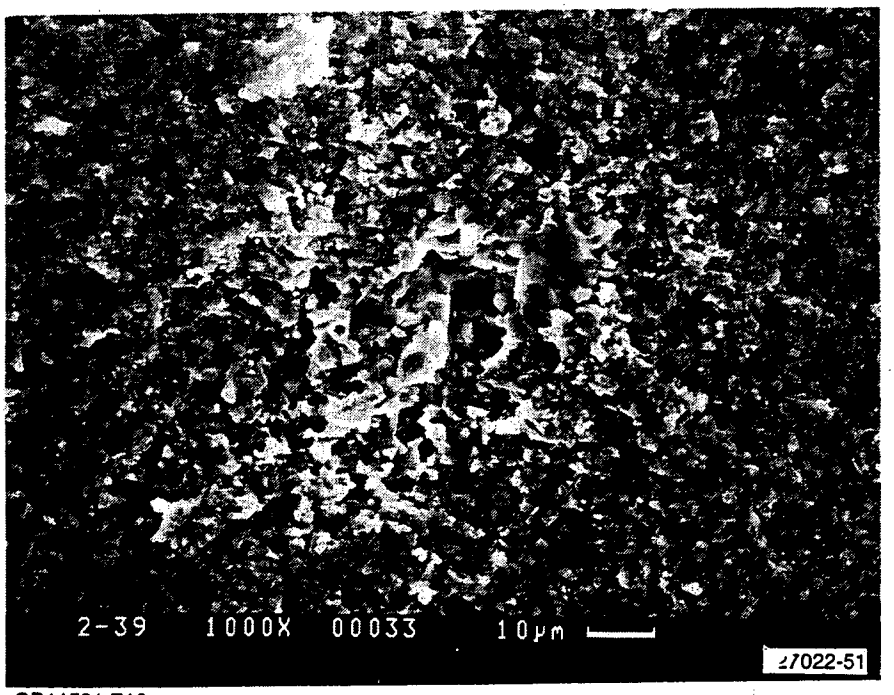

GB11591-716

Figure V-2(a). Photomicrographs Of Failure Originating From An Internal Inclusion Containing Fe And Ni In An E-Size Flexure Bar. MOR = 101.2 ksi.

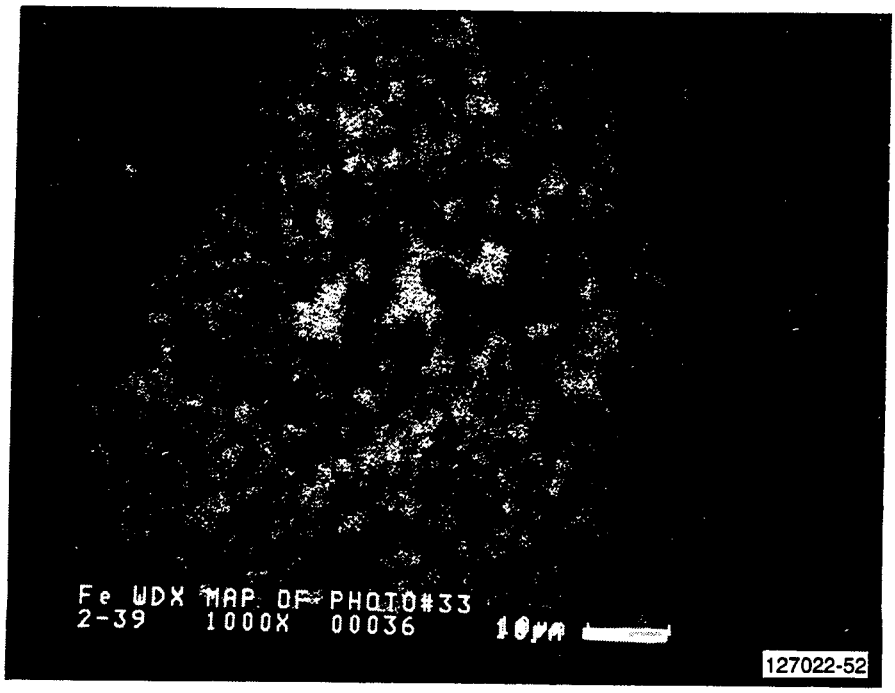

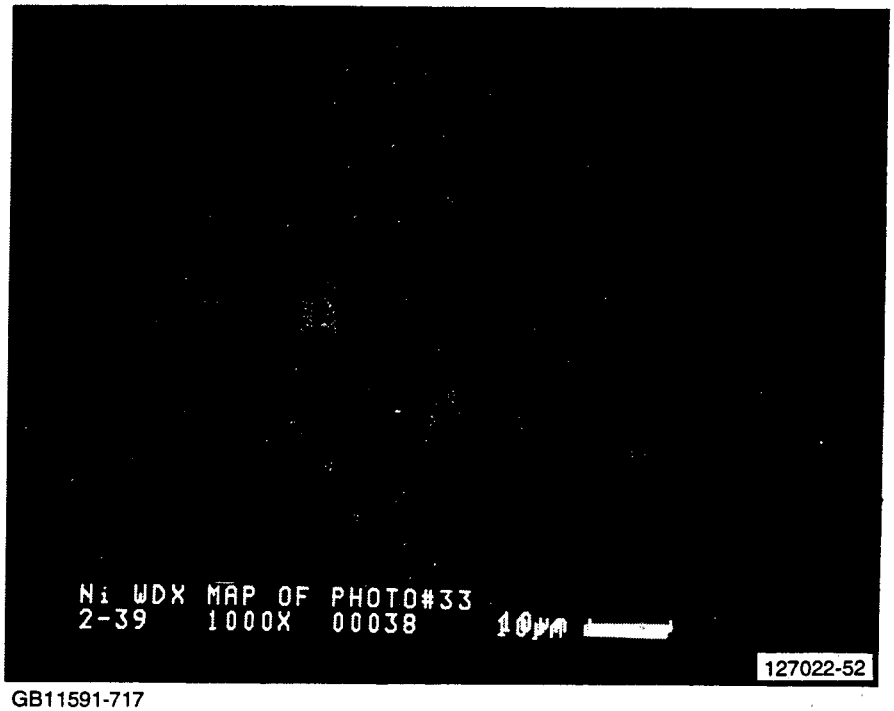

GB11591-717

Figure V-2(b). WDX Element Maps Of Failure Originating From An Internal InclusionContaining Fe And Ni In An E-Size Flexure Bar. MOR = 101.2 ksi.

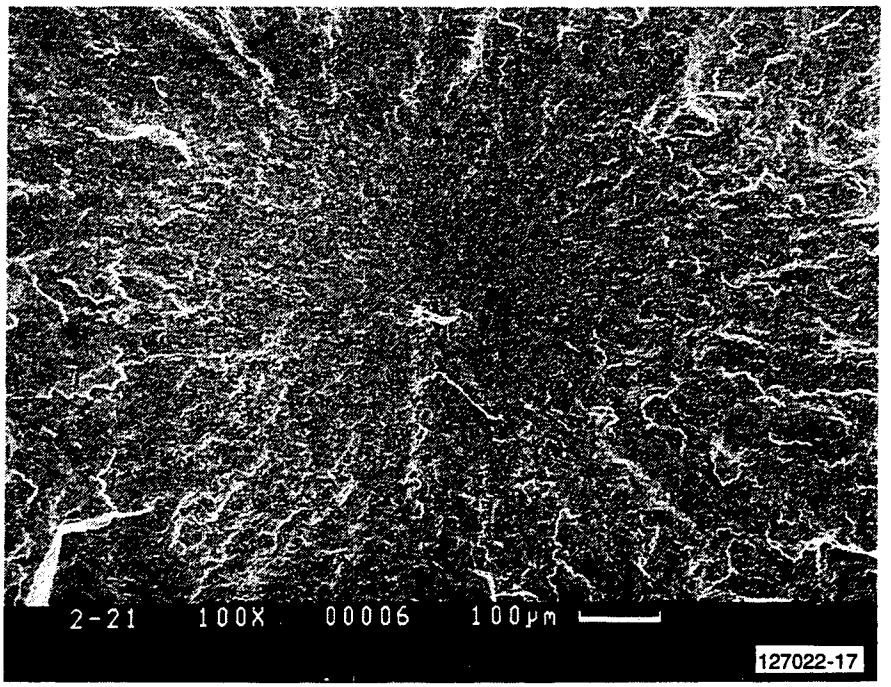

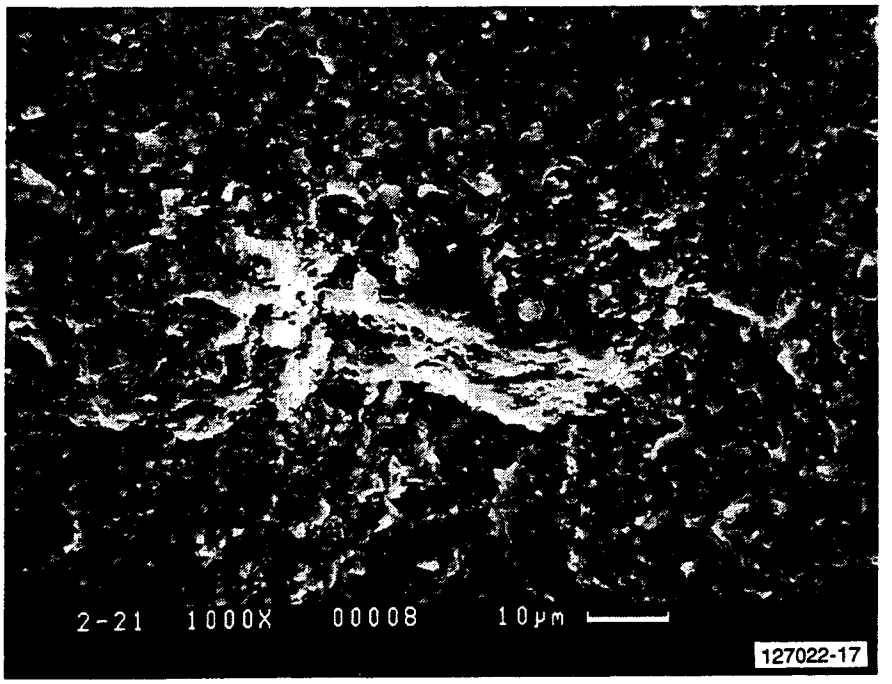

GB11591-718

Figure V-3(a). Photomicrographs Of Failure Originating From An Internal Inclusion Containing C And Traces of Fe In An E-Size Flexure Bar. MOR = 100.9 ksi.

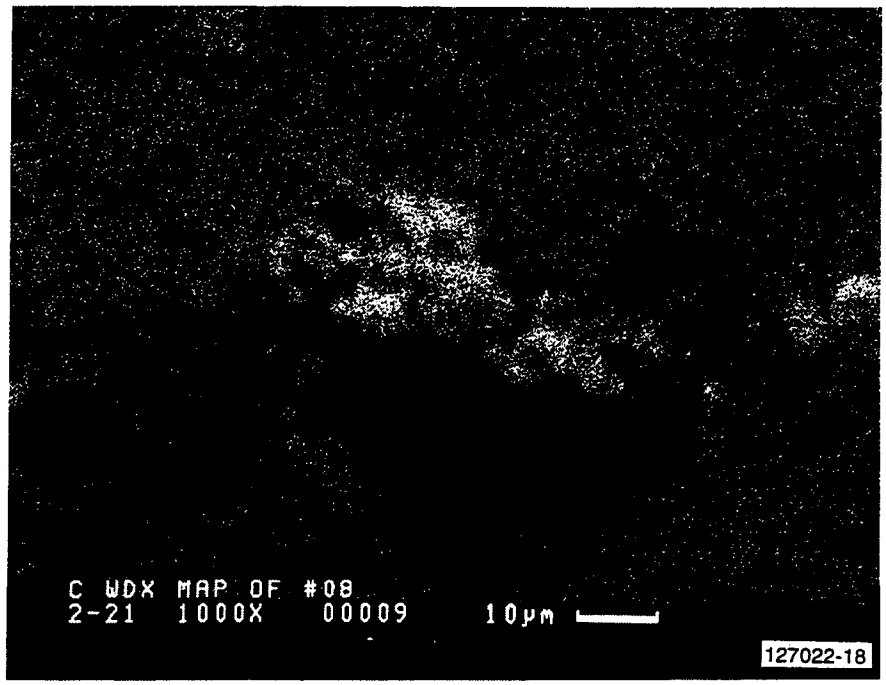

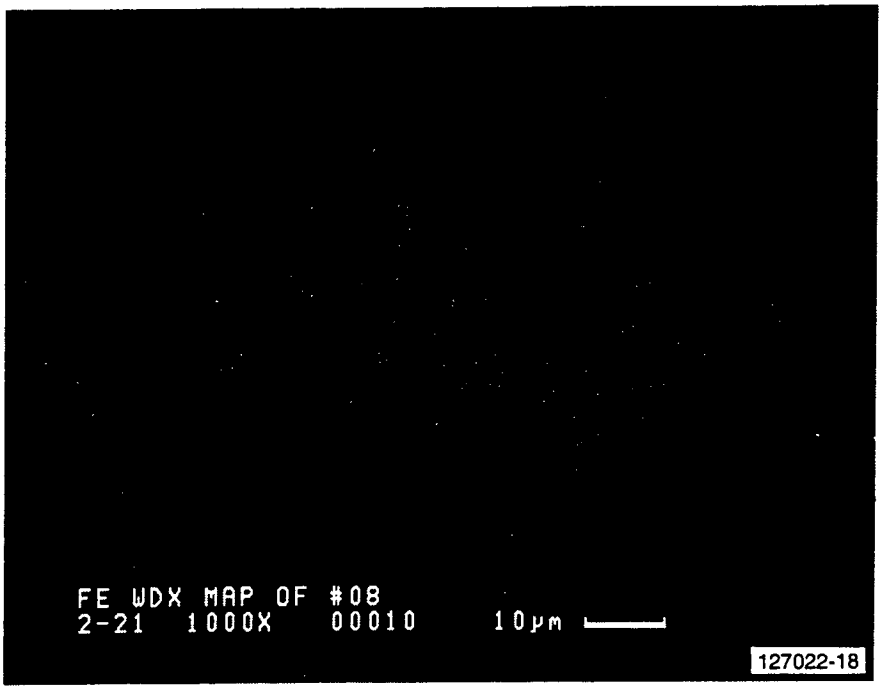

GB11591-719

Figure V-3(b). WDX Element Maps Of Failure Originating From An Internal Inclusion Containing C And Traces of Fe In An E-Size Flexure Bar. MOR = 100.9 ksi.

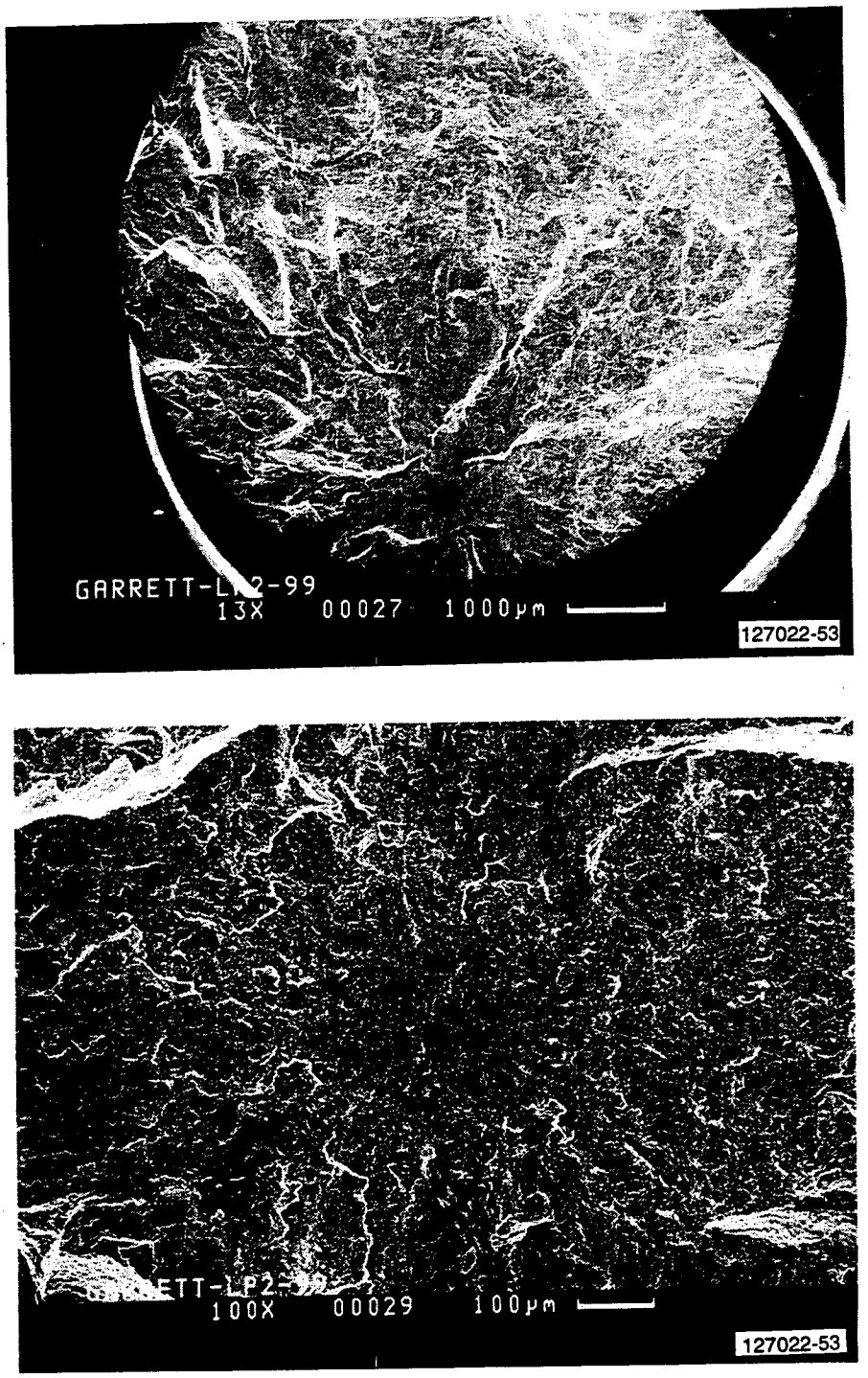

GB11591-720

Figure V-4(a). Internal Volume Fracture Origin With No Distinctive Microstructure Features. EDX And WDX Analyses Did Not Detect Any Additional Elements. Specimen Failed at 117.8 ksi at Room Temperature.

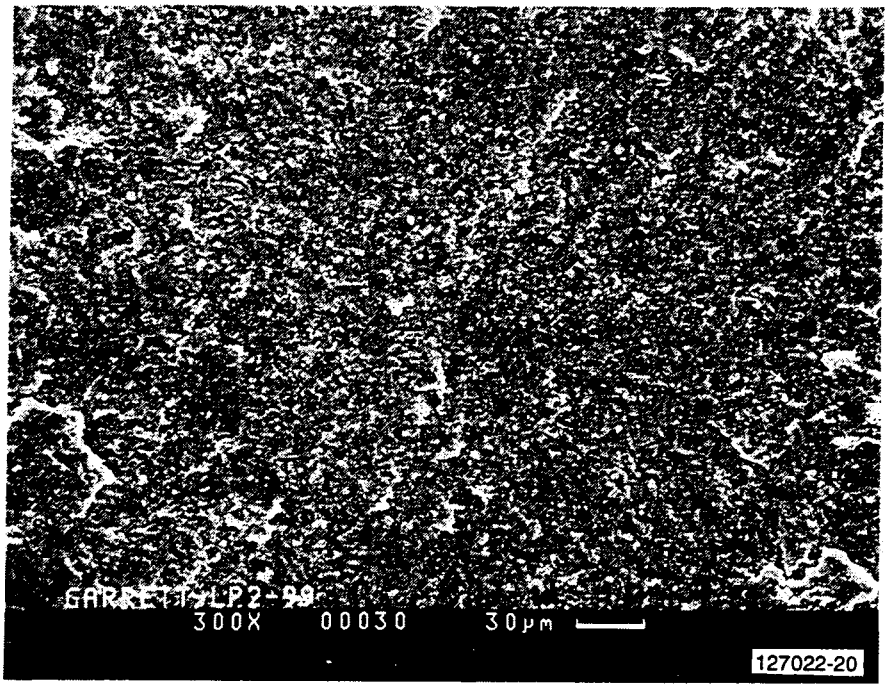

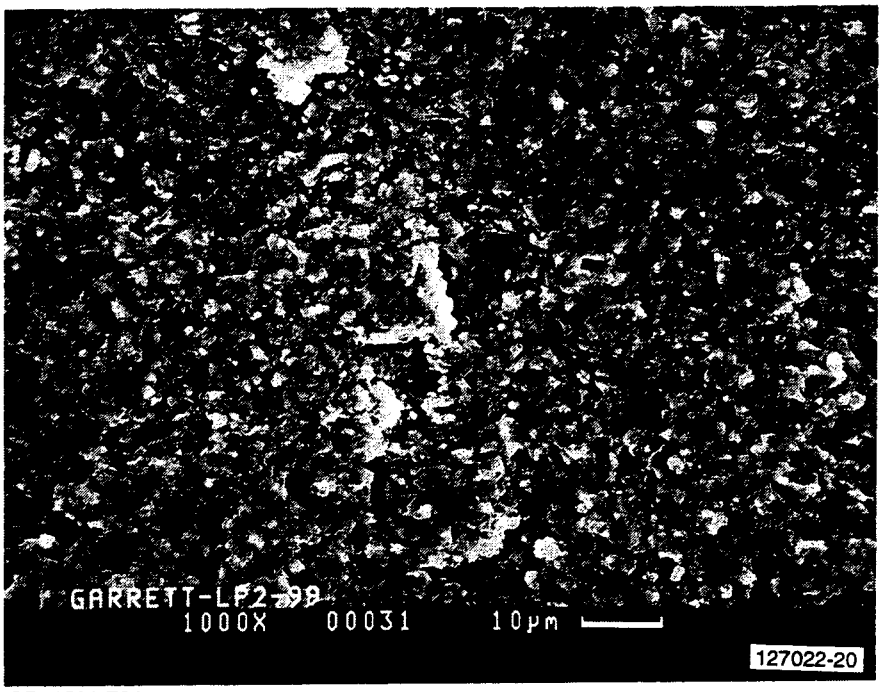

GB11591-721

Figure V-4(b). Internal Volume Fracture Origin With No Distinctive Microstructure Features. EDX And WDX Analyses Did Not Detect Any Additional Elements. Specimen Failed At 117.8 ksi At Room Temperature. (Contd)

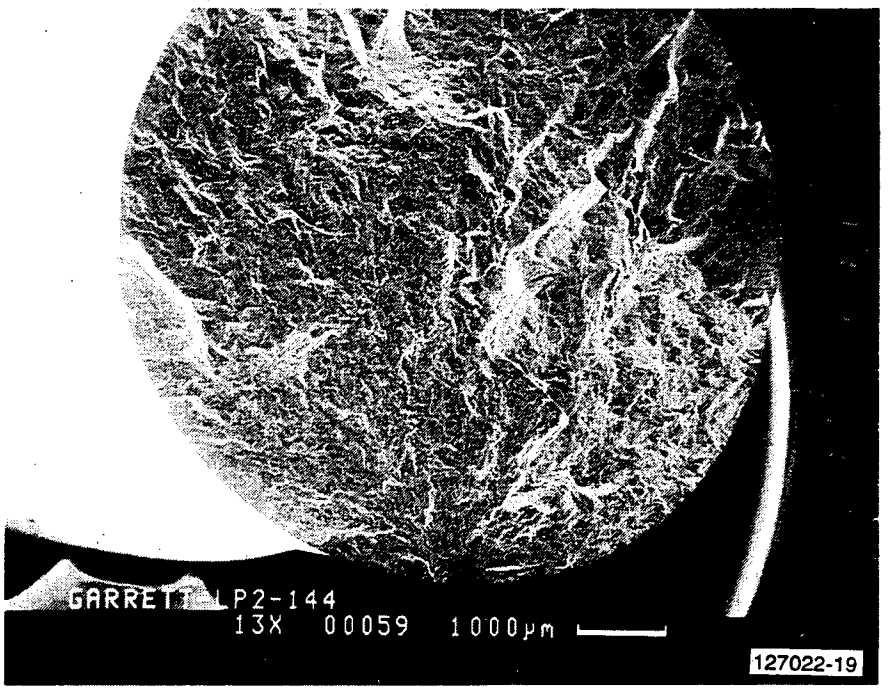

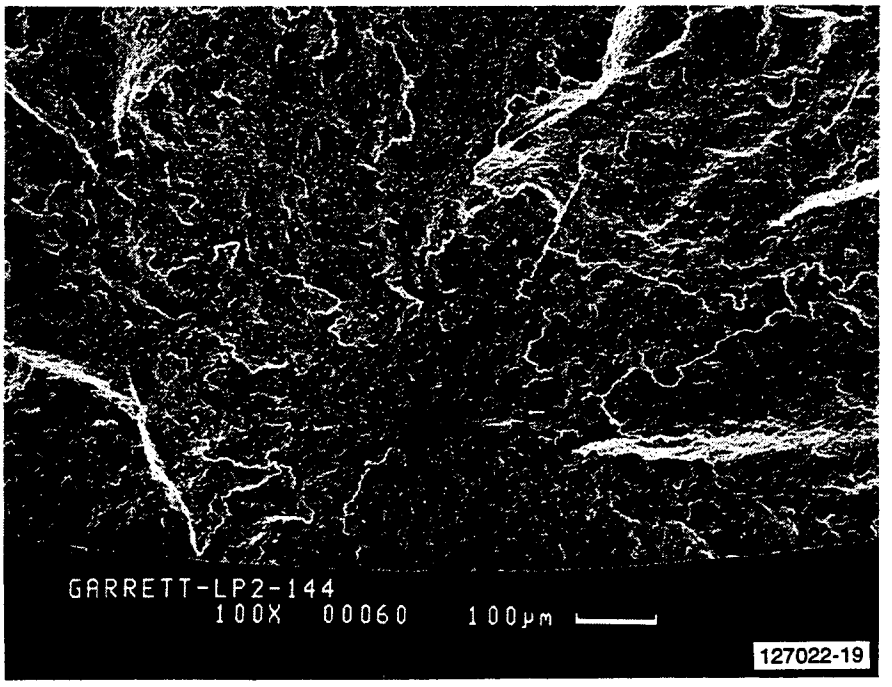

GB11591-722

Figure V-5(a). Failure Originated From Internal Volume, Possibly A Large Grain, Inside A Tensile Specimen Tested at Room Temperature And 119.0 ksi.

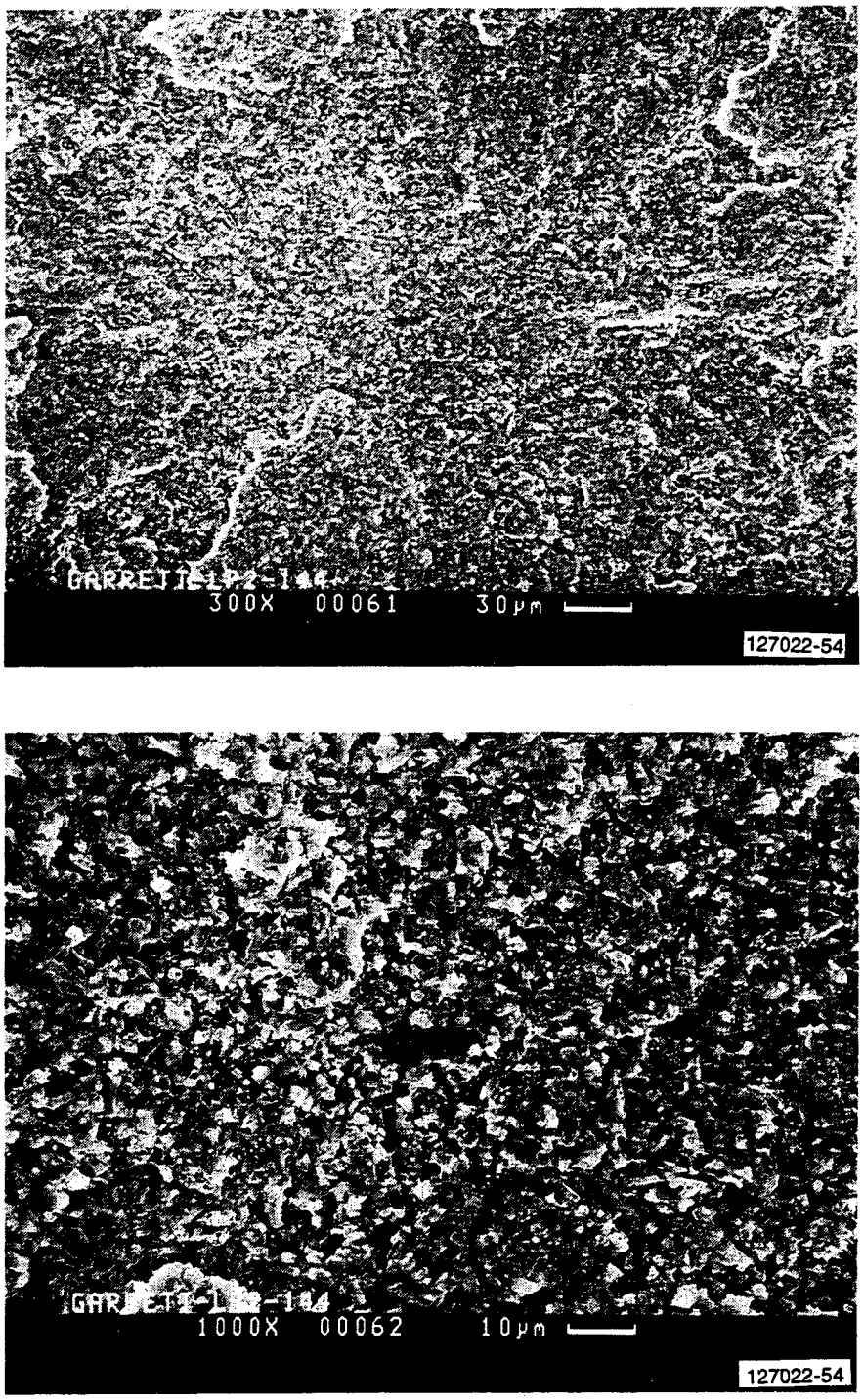

GB11591-723

Figure V-5(b). Failure Originated From Internal Volume, Possibly A Large Grain, Inside A Tensile Specimen Tested at Room Temperature And 119.0 ksi. (Contd)

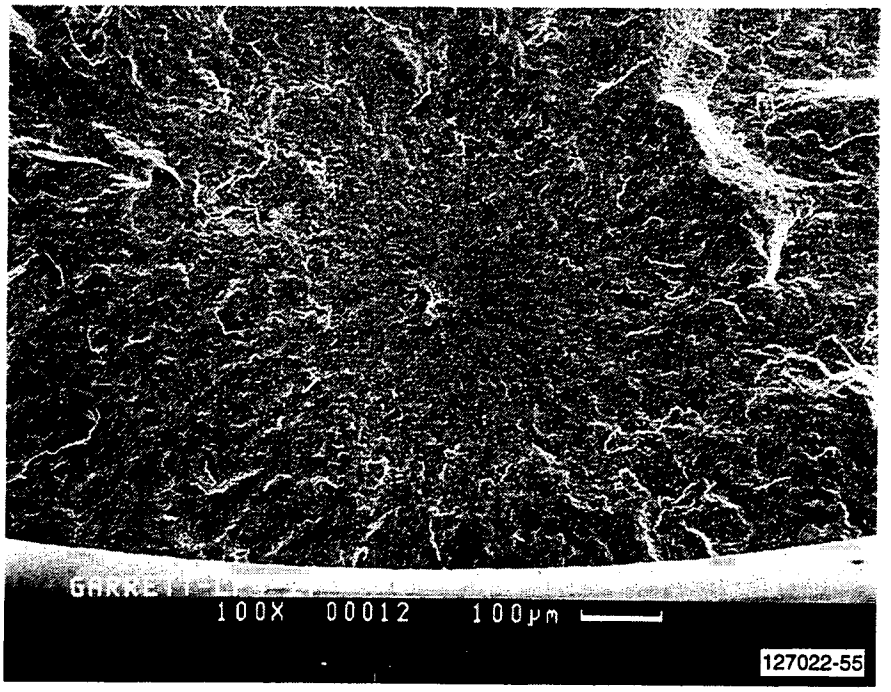

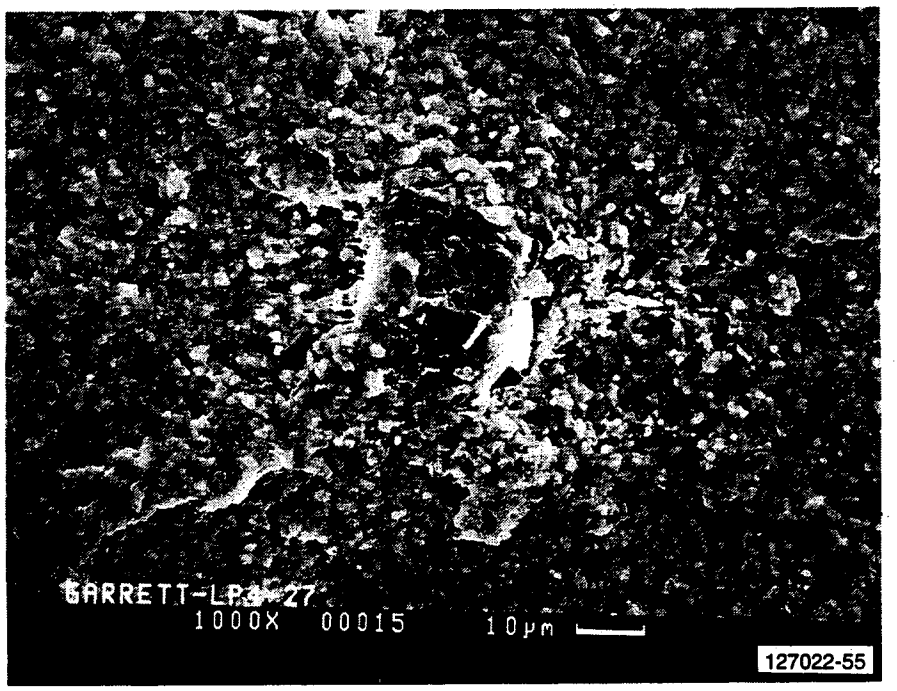

GB11591-724

Figure V-6(a). Photomicrographs Of Inclusion At Fracture Origin Of A Tensile Specimen That Failed At 103.4 ksi At Room Temperature. Inclusion Contains A Core Of C And Cluster Of Small Fe Particles.

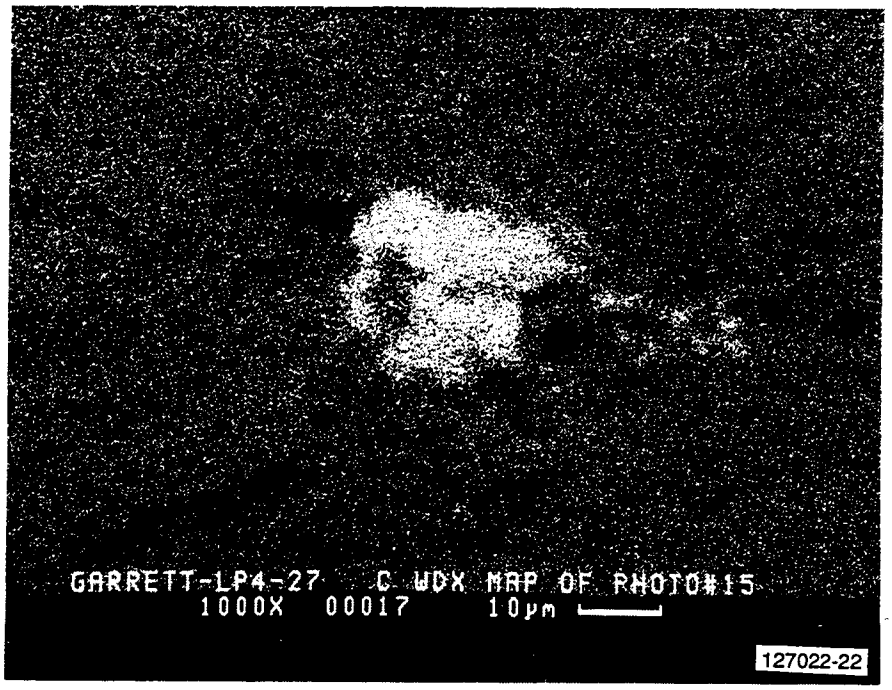

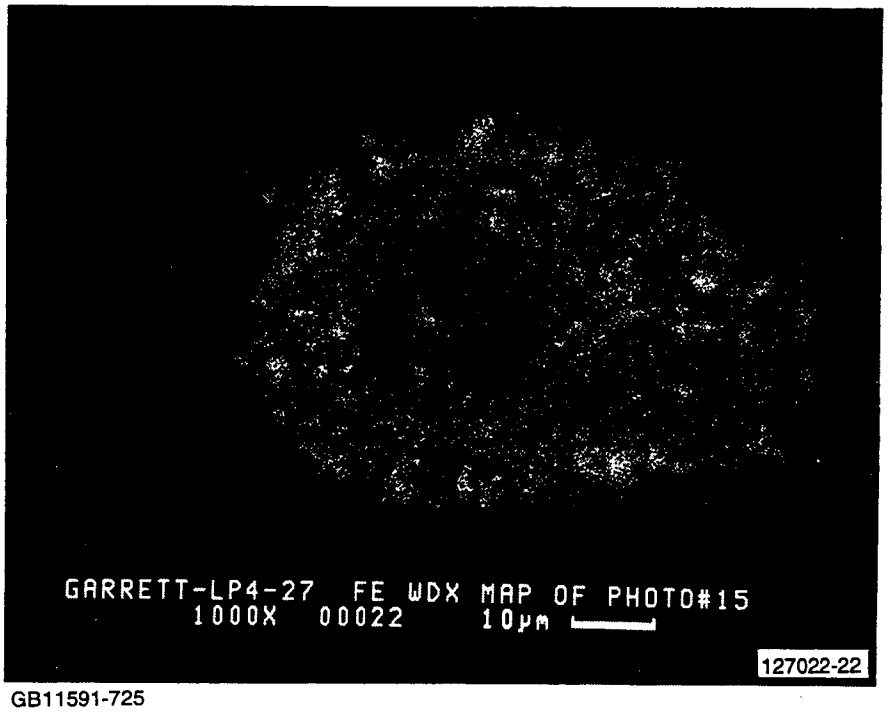

GB11591-725

Figure V-6(b). WDX Element Maps Of Inclusion At Fracture Origin Of A Tensile Specimen That Failed At 103.4 ksi At Room Temperature. Inclusion Contains A Core Of C And Cluster Of Small Fe Particles.

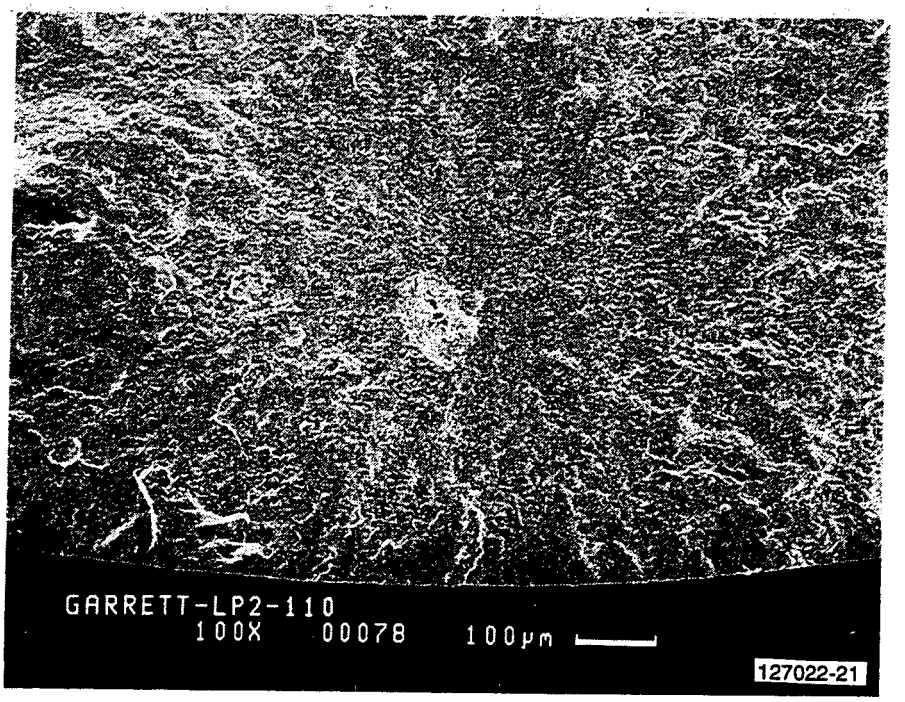

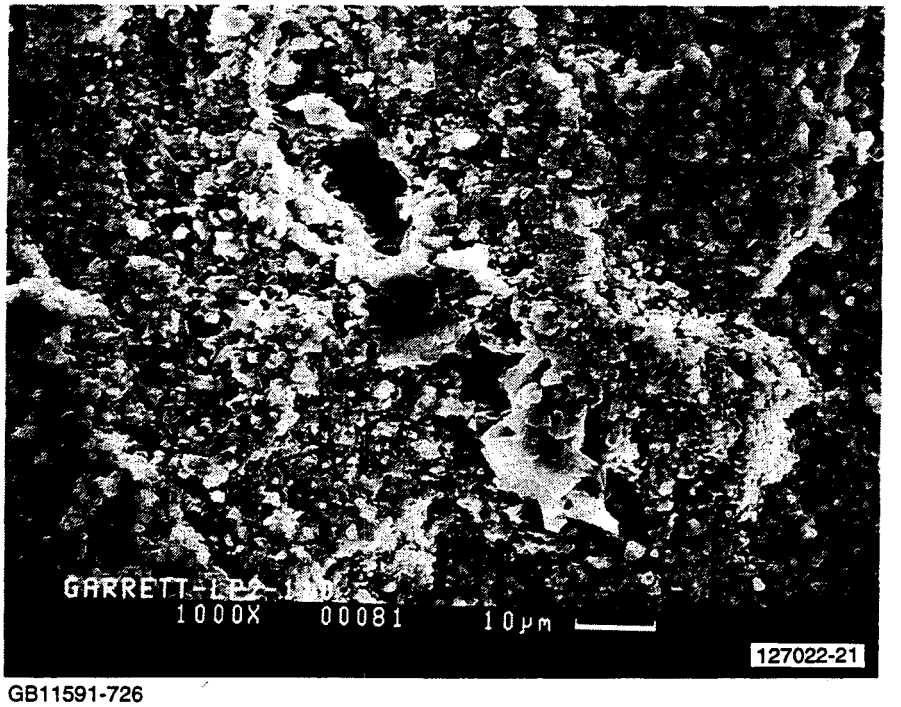

GB11591-726

Figure V-7(a). Photomicrographs Of Inclusion Zone Containing A Cluster Of Small Fe Particles And A Few Large C Particles. Tensile Specimen Failed At 88.7 ksi At Room Temperature.

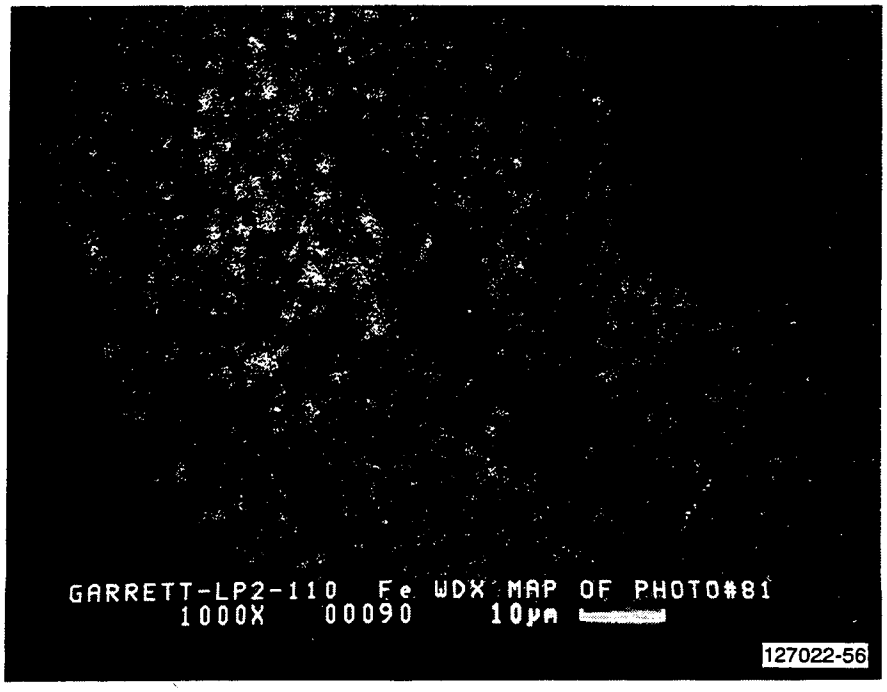

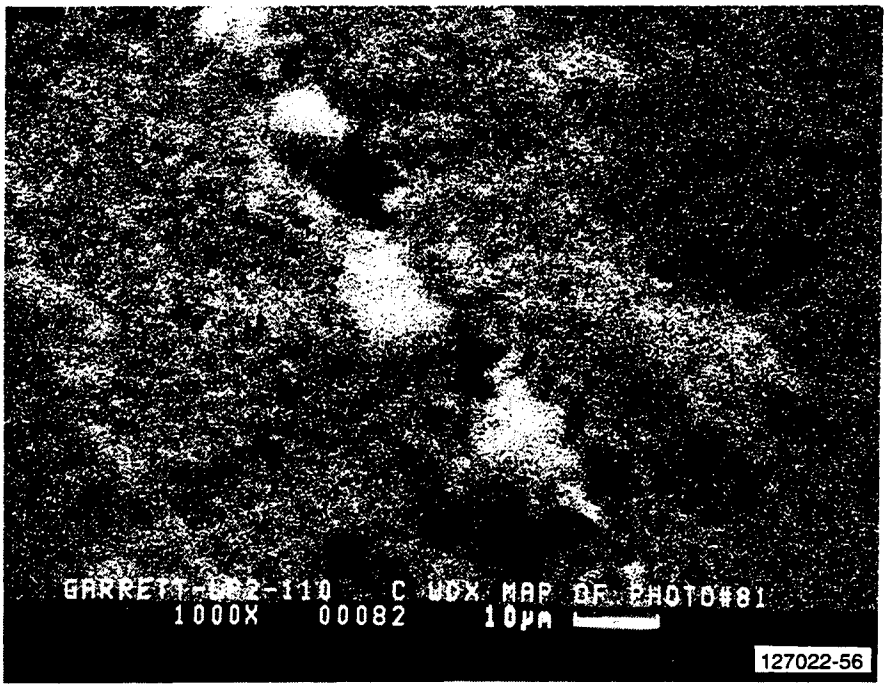

GB11591-727

Figure V-7(b). WDX element Maps Of Inclusion Zone Containing A Cluster Of Small Fe Particles And A Few Large C Particles. Tensile Specimen Failed At 88.7 ksi At Room Temperature.

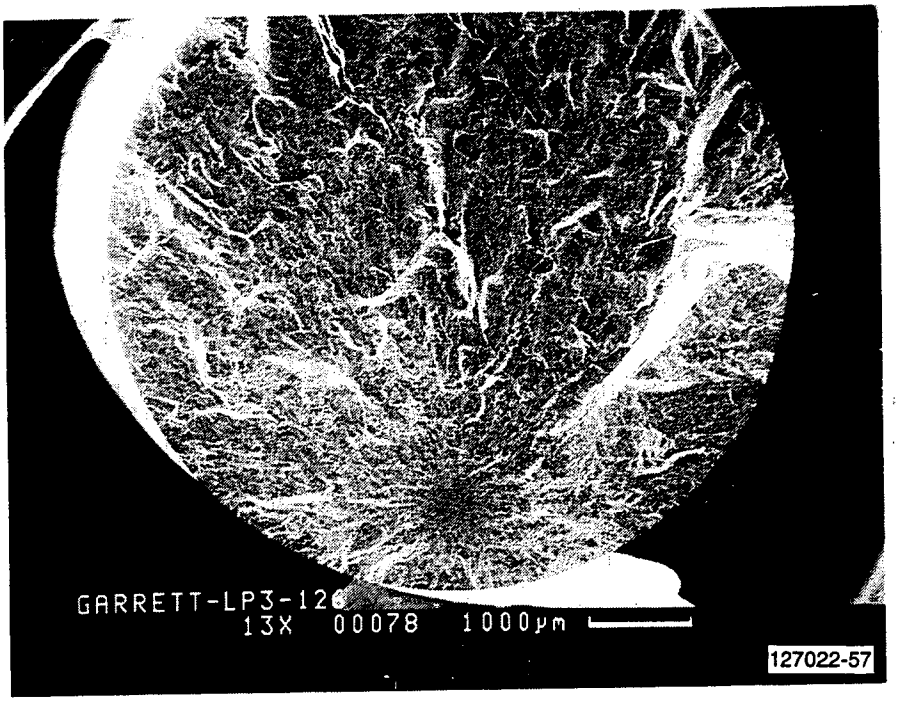

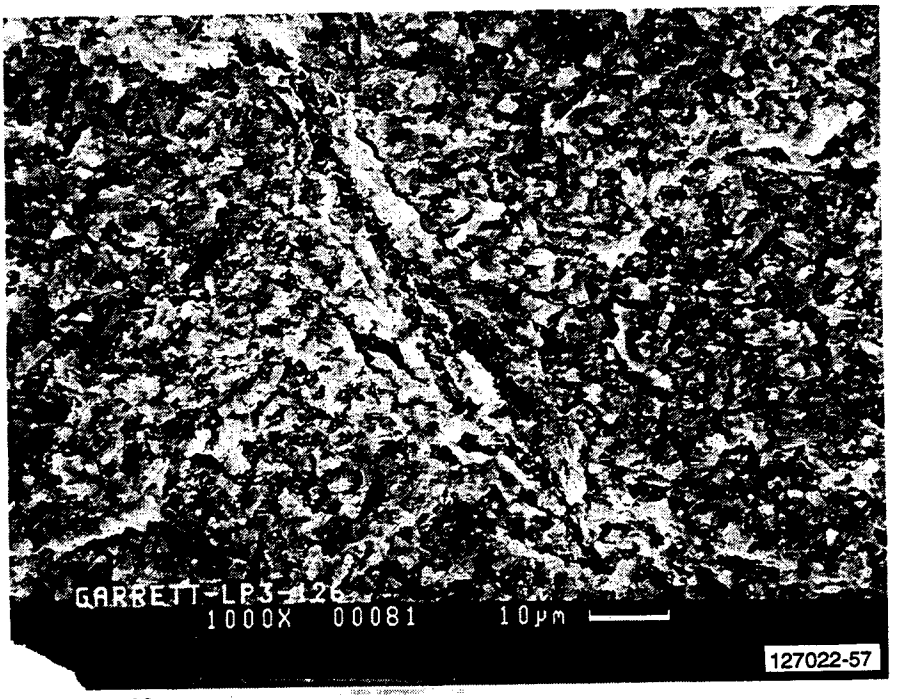

GB11591-728

Figure V-8(a). Photomicrographs Of An Elongated Inclusion Containing C And Y. Tensile Specimen Failed At Room Temperature And 83.2 ksi.

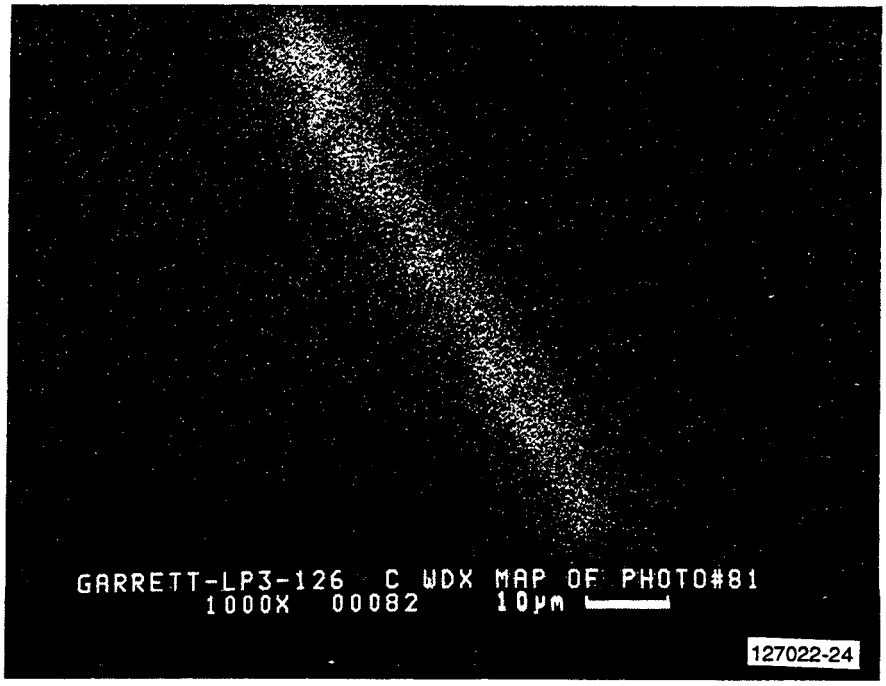

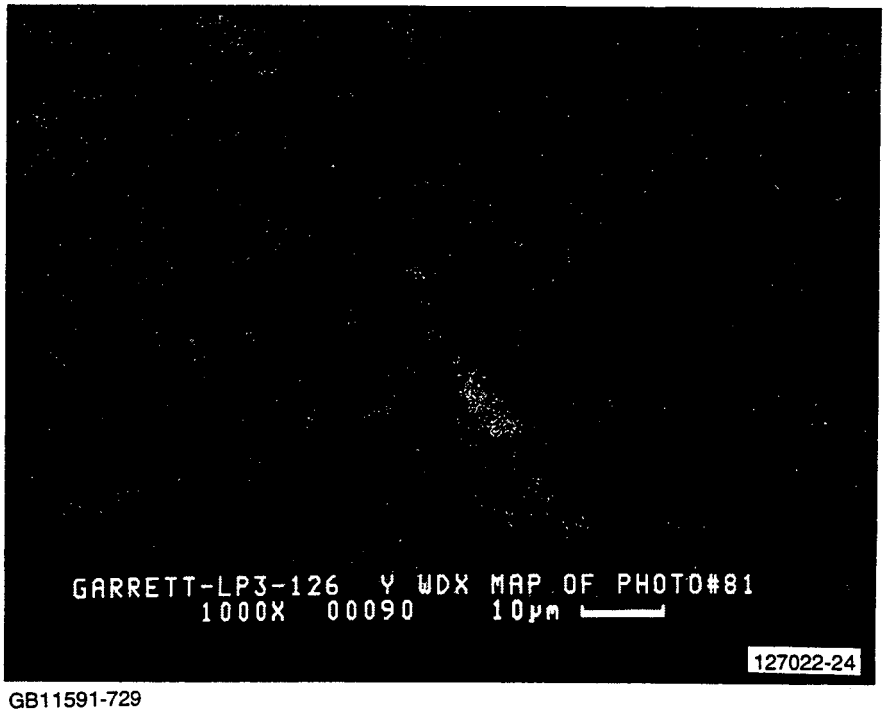

GB11591-729

Figure V-8(b). **WDX Element Maps Of An Elongated Inclusion Containing C And Y. Tensile Specimen Failed At Room Temperature And 83.2 ksi.**

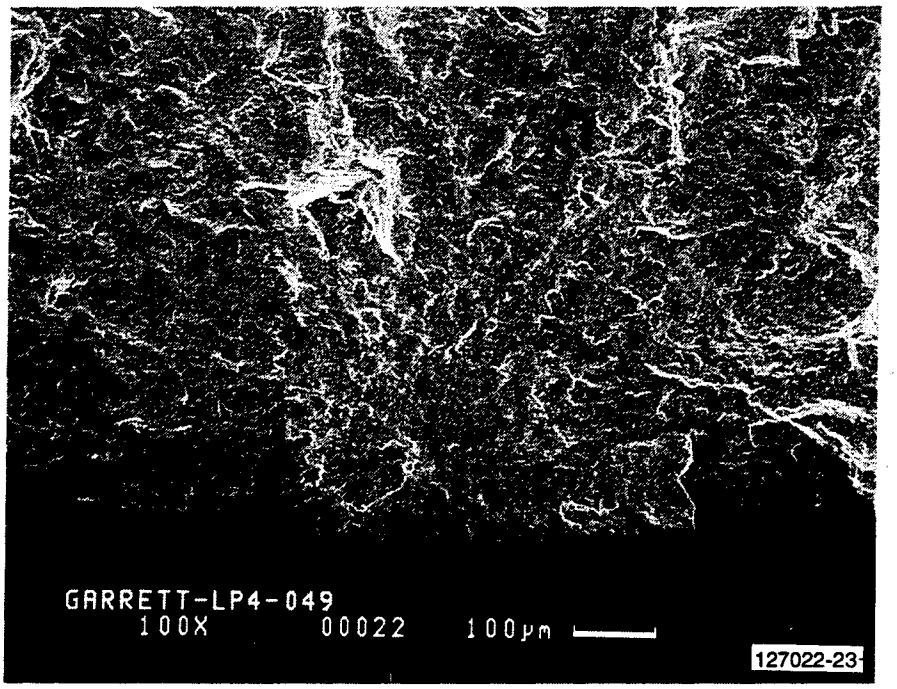

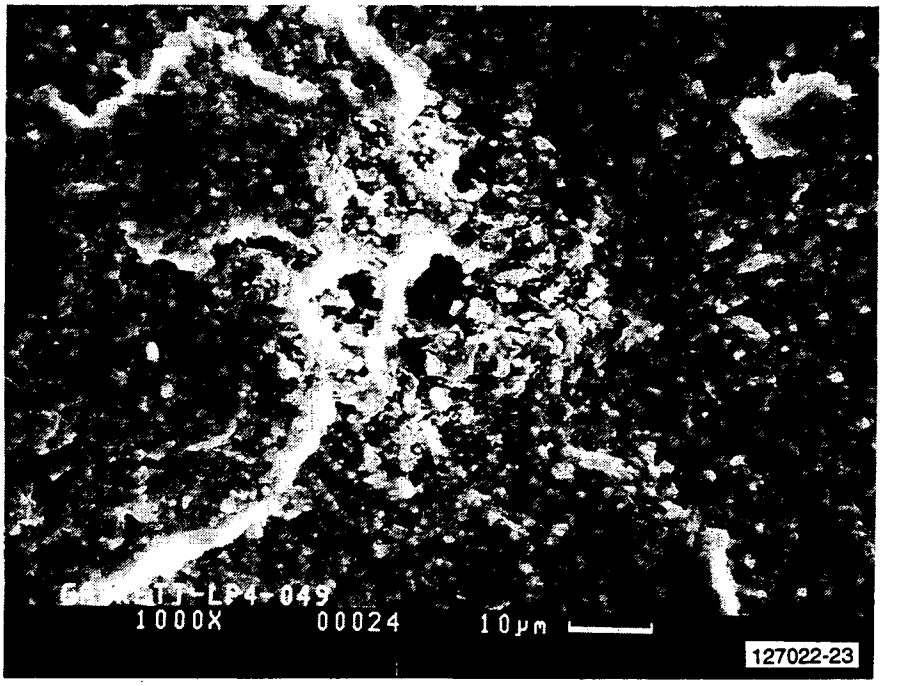

GB11591-730

Figure V-9(a). Photomicrographs Of Typical Inclusion At Fracture Origin Of Tensile Specimen That Failed At 109.3 ksi. WDX Element Maps (Following Pages) Show Inclusion Contains Clusters of C, Fe, And Co; No Si Was Present.

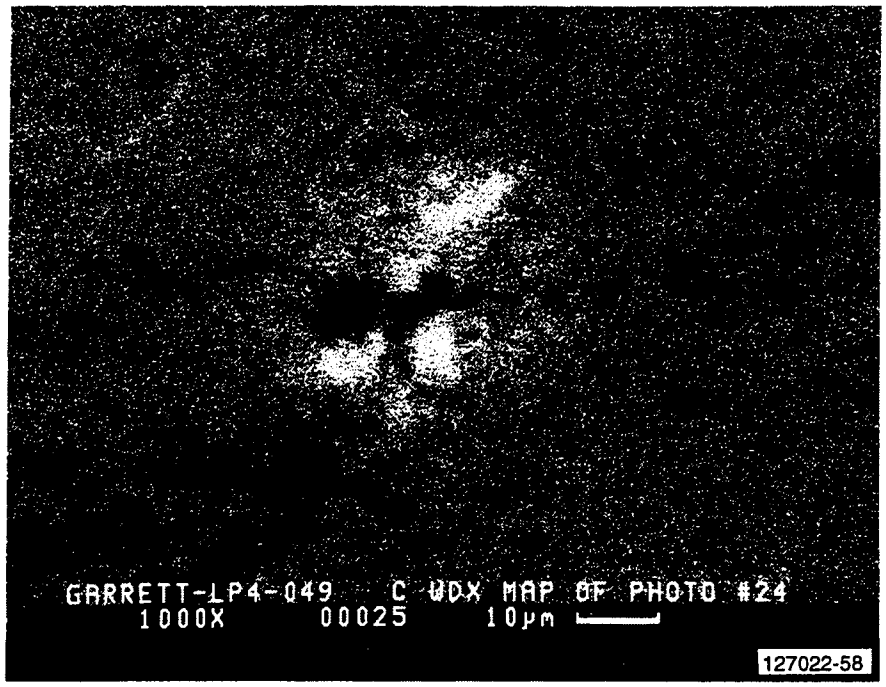

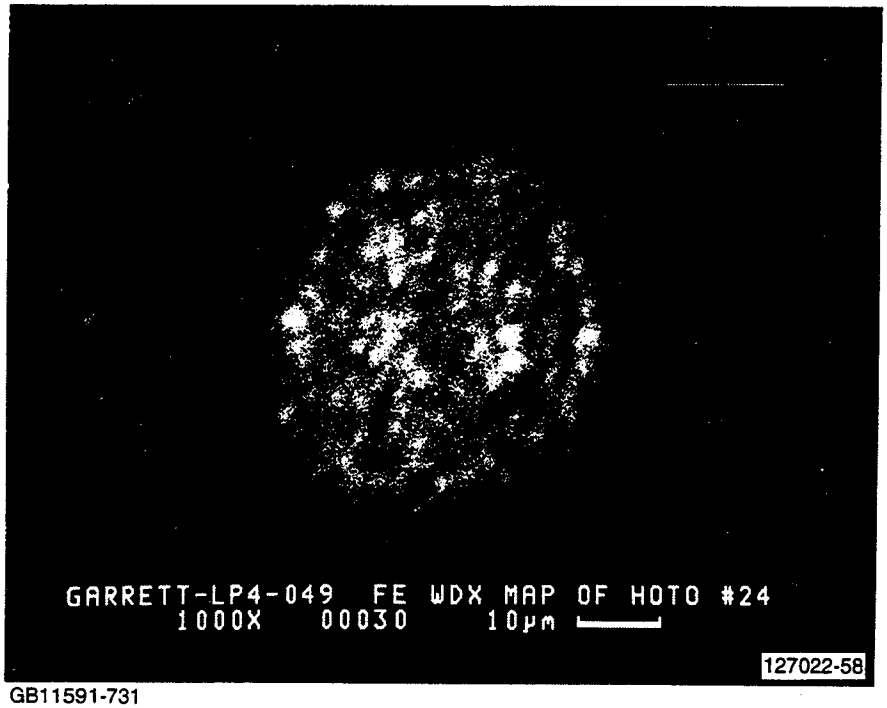

GB11591-731

Figure V-9(b). WDX Element Maps Of Typical Inclusion At Fracture Origin of Tensile Specimen That Failed at 109.3 ksi, Showing Inclusion Contains Clusters of C, Fe, And Co; No Si Was Present.

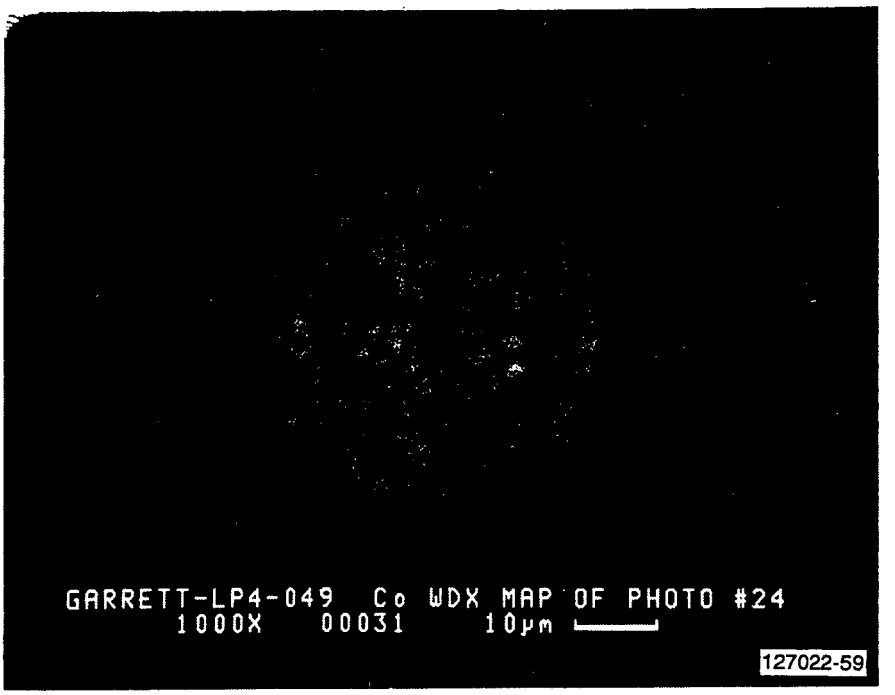

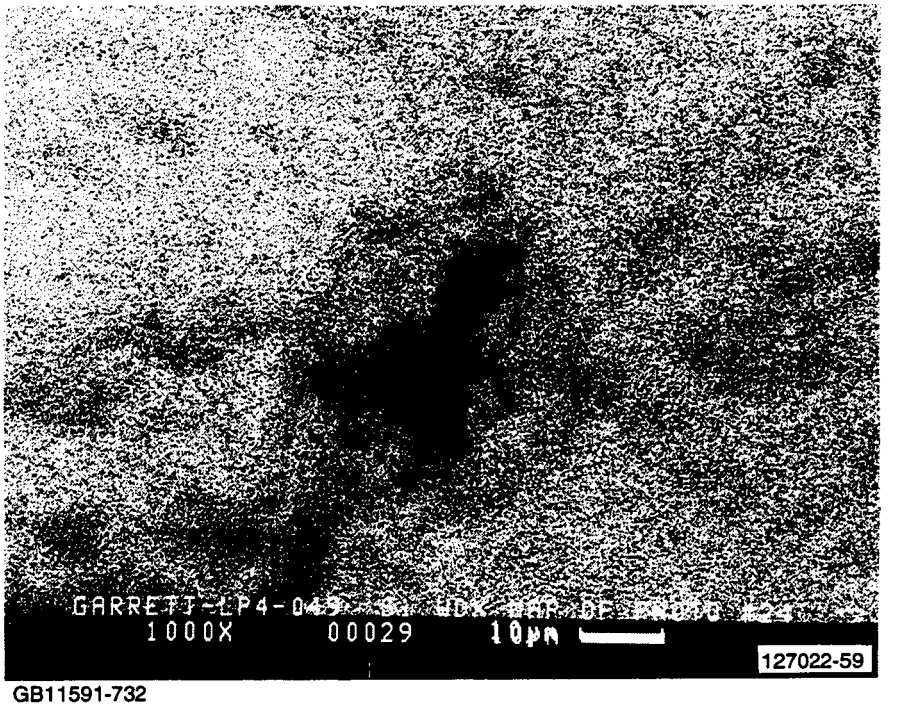

GB11591-732

Figure V-9(c). WDX Element Maps Of Typical Inclusion At Fracture Origin Of Tensile Specimen That Failed at 109.3 ksi, Showing Inclusion Contains Clusters of C, Fe, And Co; No Si Was Present. (Contd)

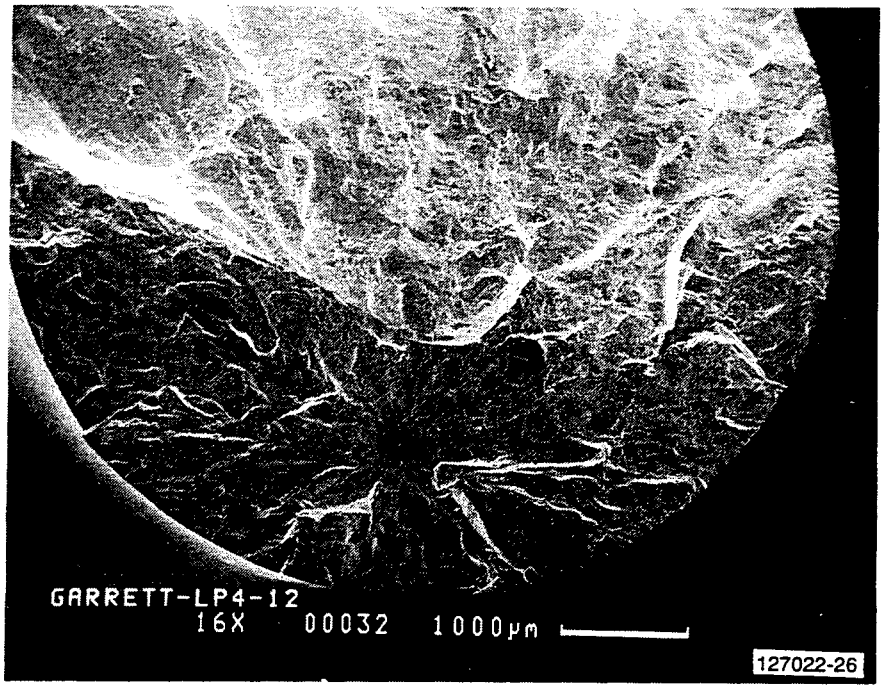

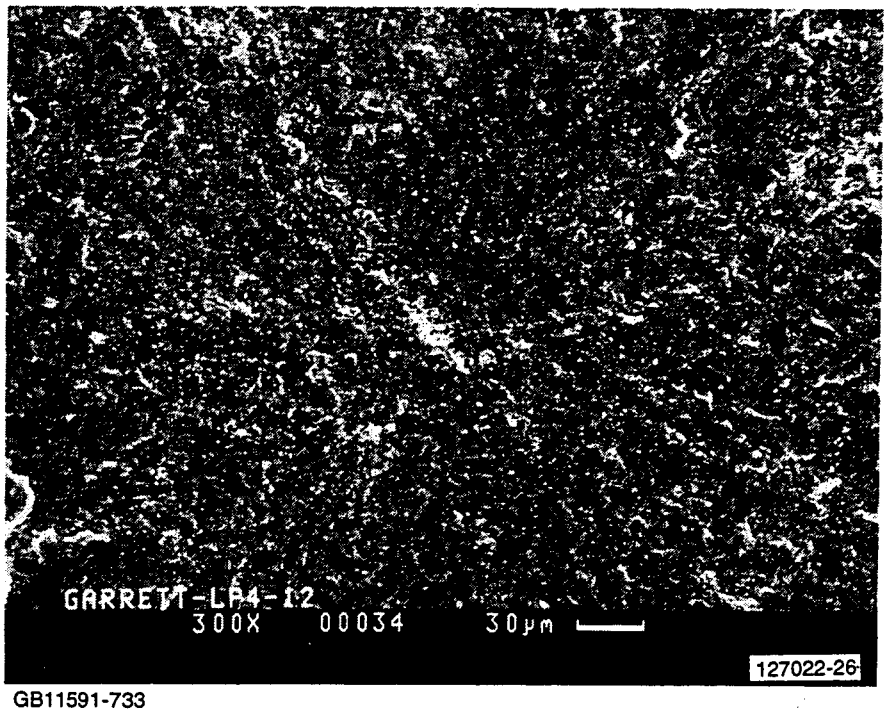

GB11591-733

Figure V-10(a). Photomicrographs Of Typical Example Of Inclusion Containing Only C At Fracture Origin Of Tensile Specimen That Failed At 107.1 ksi.

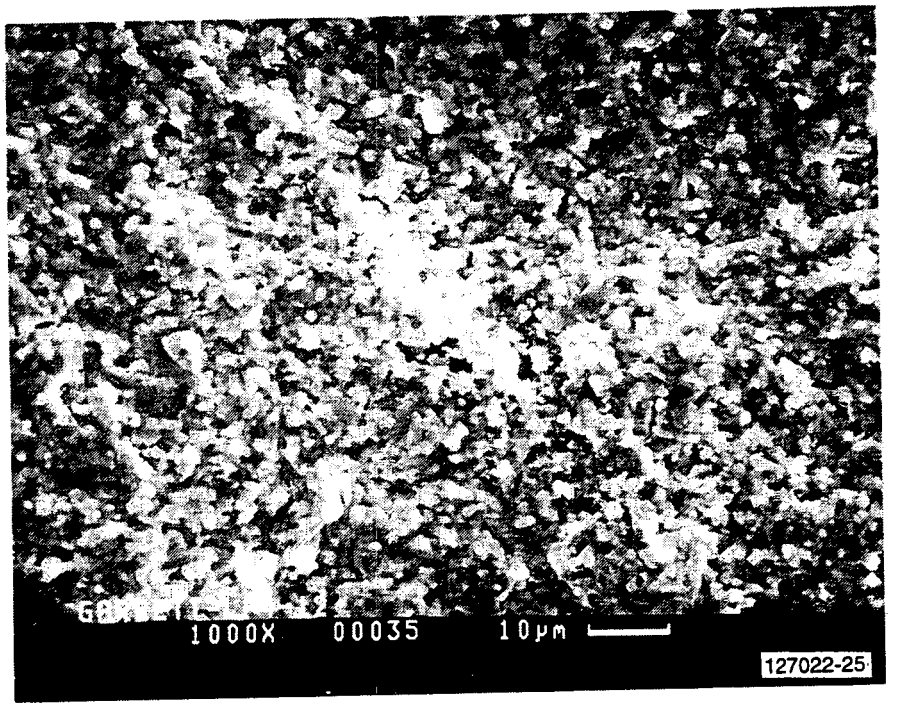

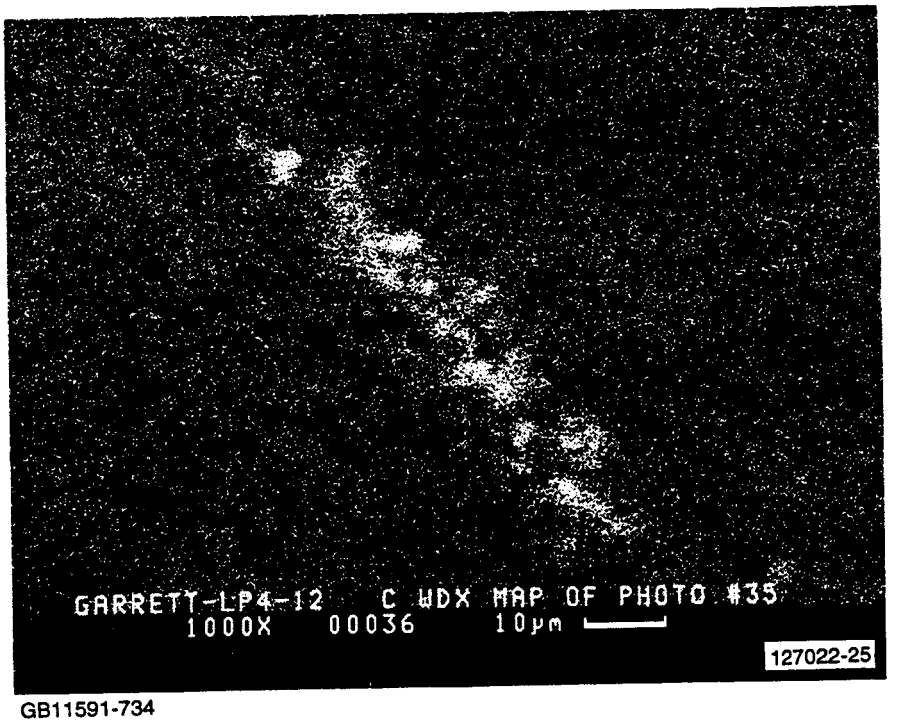

GB11591-734

Figure V-10(b). WDX Element Maps Of Typical Example of Inclusion Containing Only C At Fracture Origin Of Tensile Specimen That Failed at 107.1 ksi.

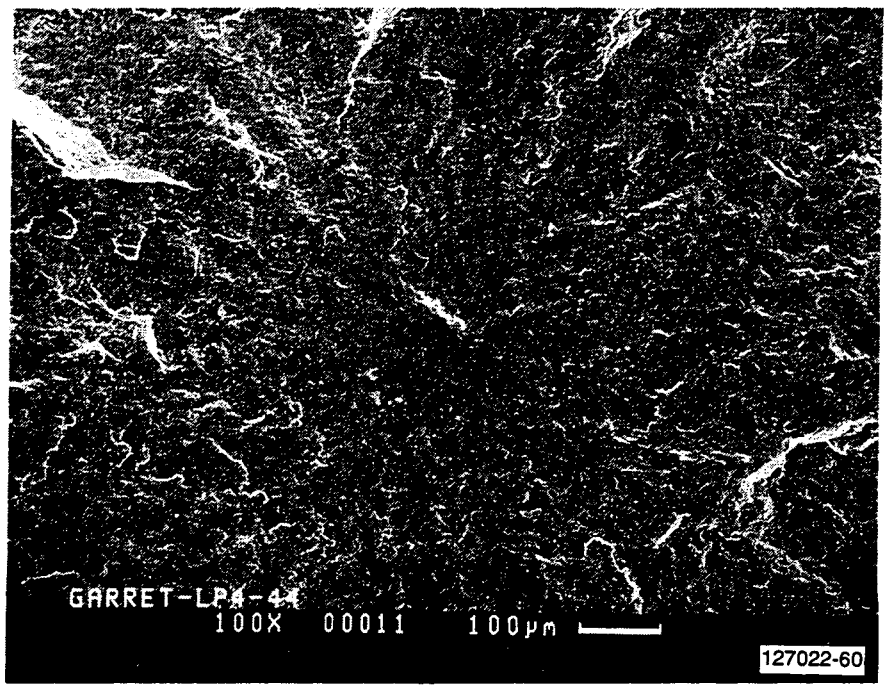

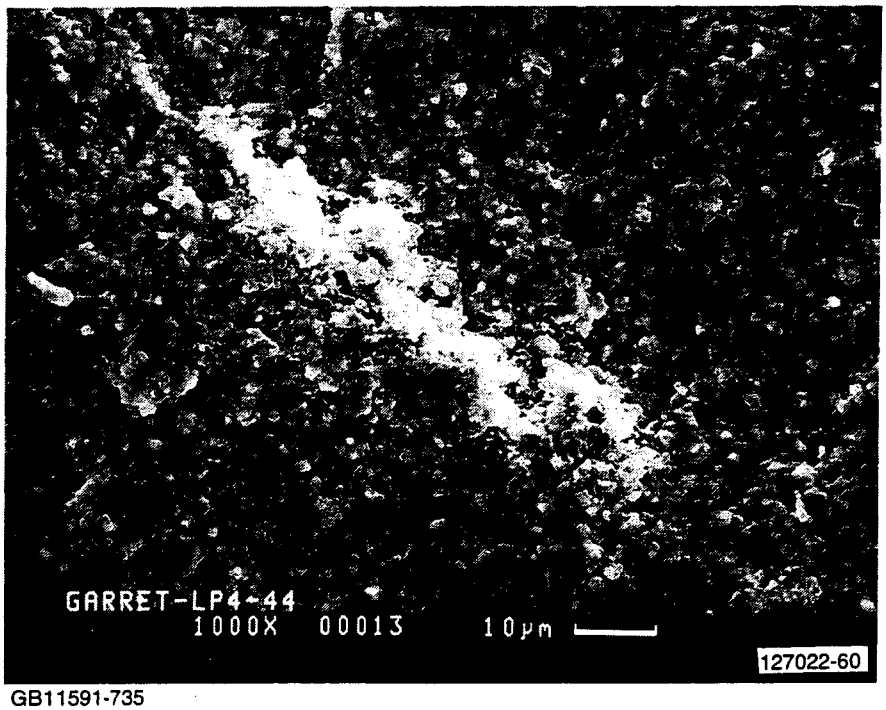

GB11591-735

Figure V-11(a). Photomicrographs Of Internal Elongated Inclusion Containing C And Ti. Tensile Specimen Failed At 105.4 ksi At Room Temperature.

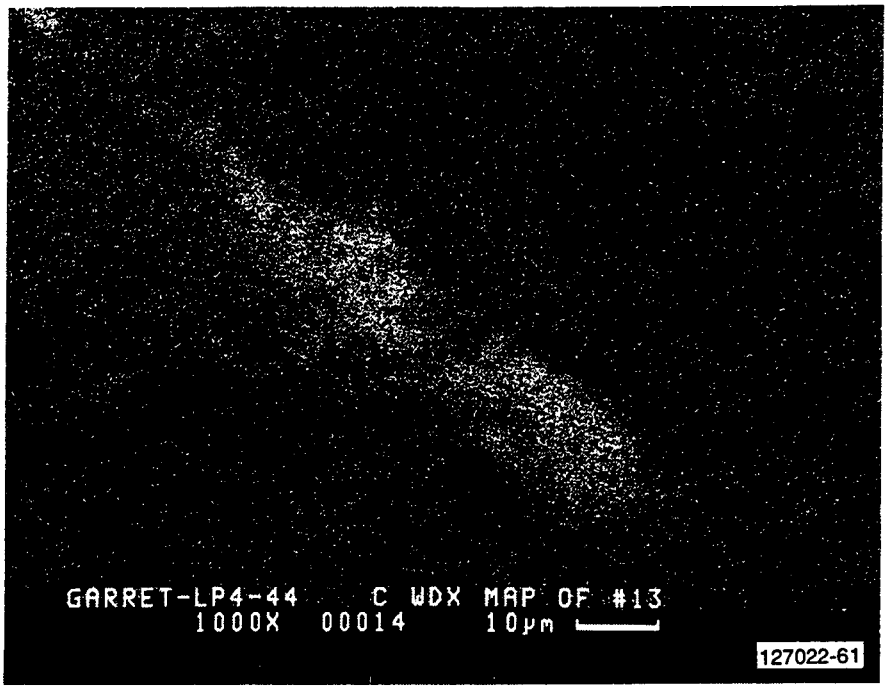

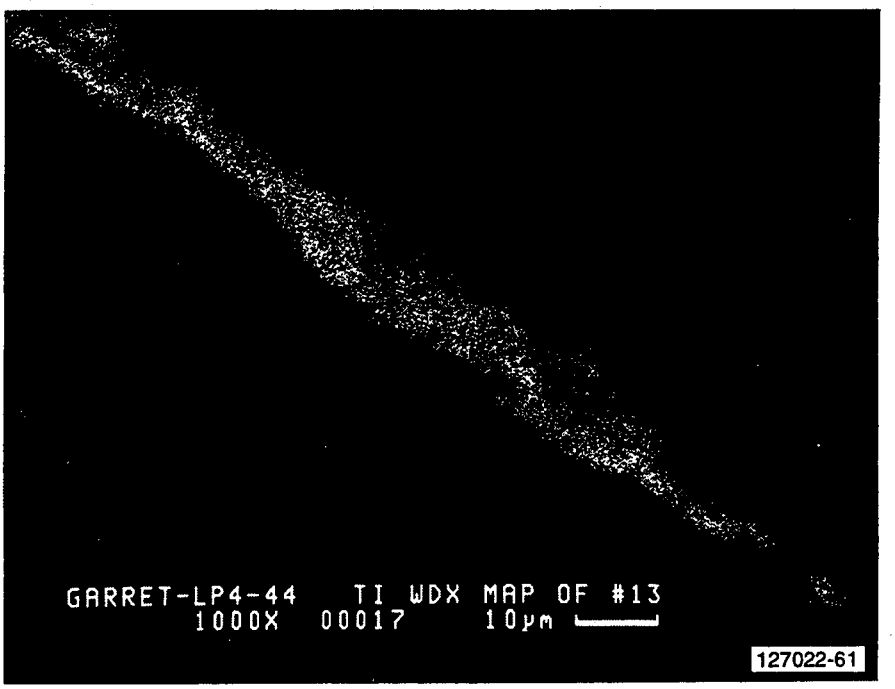

GB11591-736

Figure V-11(b). WDX Element Maps Of Internal Elongated Inclusion Containing C And Ti. Tensile Specimen Failed At 105.4 ksi At Room Temperature.

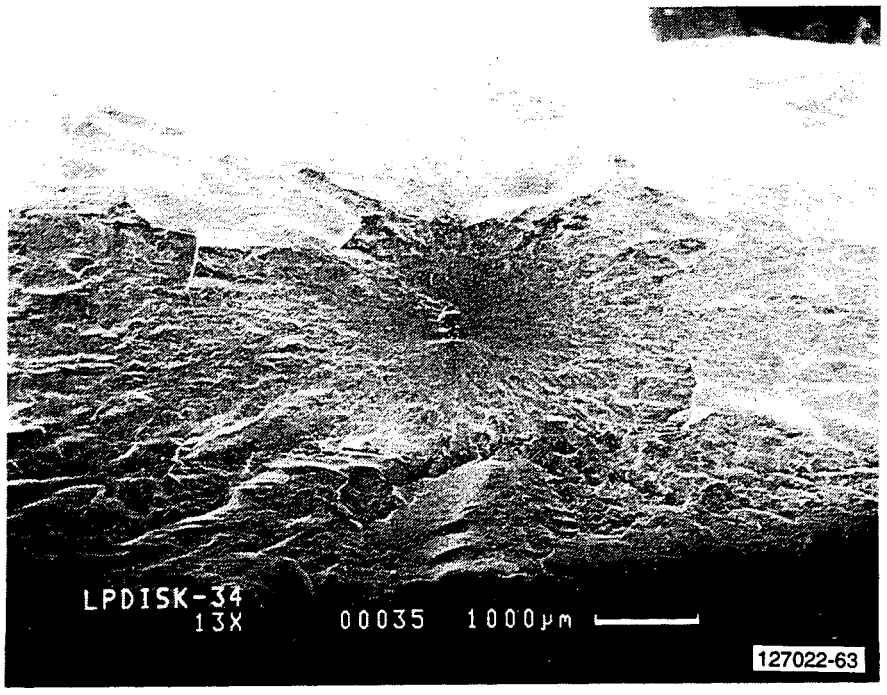

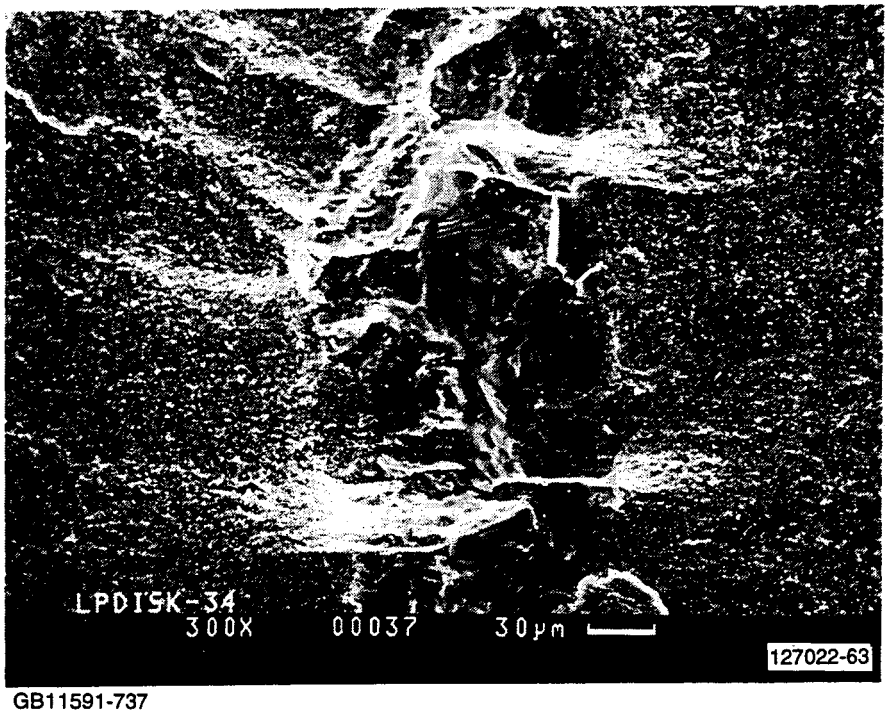

GB11591-737

Figure V-12(a). Photomicrographs Of Failure Originating From Internal Inclusion Containing Al And Possible Si. N And O WDX Element Maps (Following Pages) Indicate That Inclusion Was Not Nitride Or Silicate. Disk Burst Occurred At 88,500 rpm At Room Temperature.

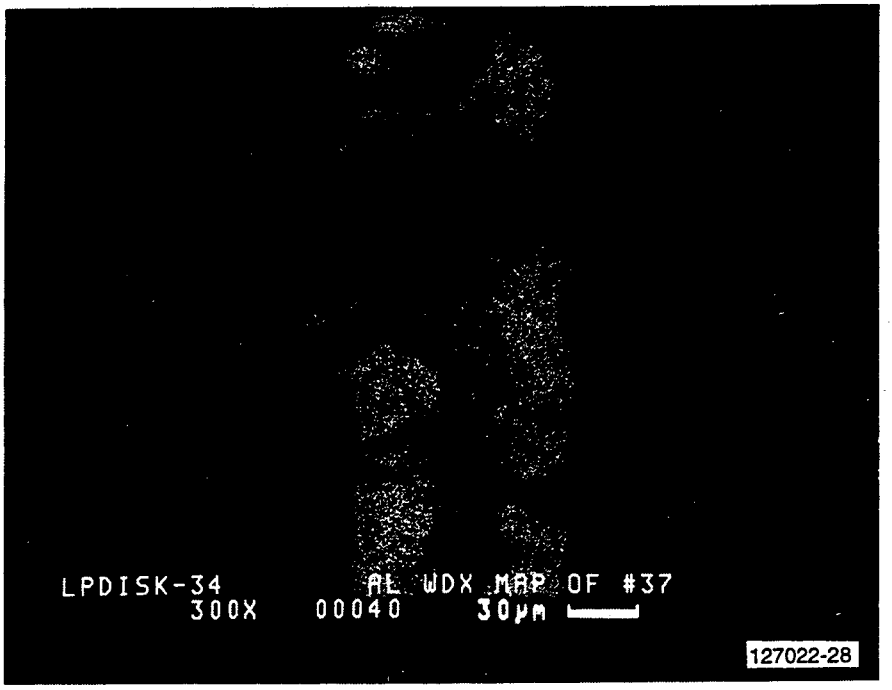

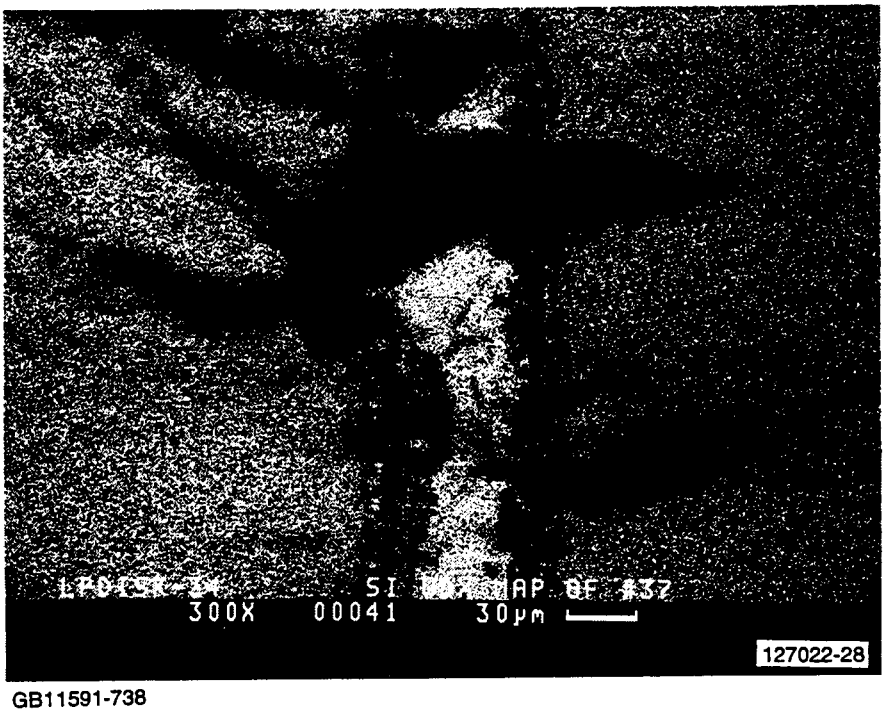

GB11591-738

Figure V-12(b). WDX Element Maps Of Failure Originating From Internal Inclusion Containing Al And Possible Si. N And O WDX Element Maps (Following Page) Indicate That Inclusion Was Not Nitride Or Silicate. Disk Burst Occurred At 88,500 rpm At Room Temperature.

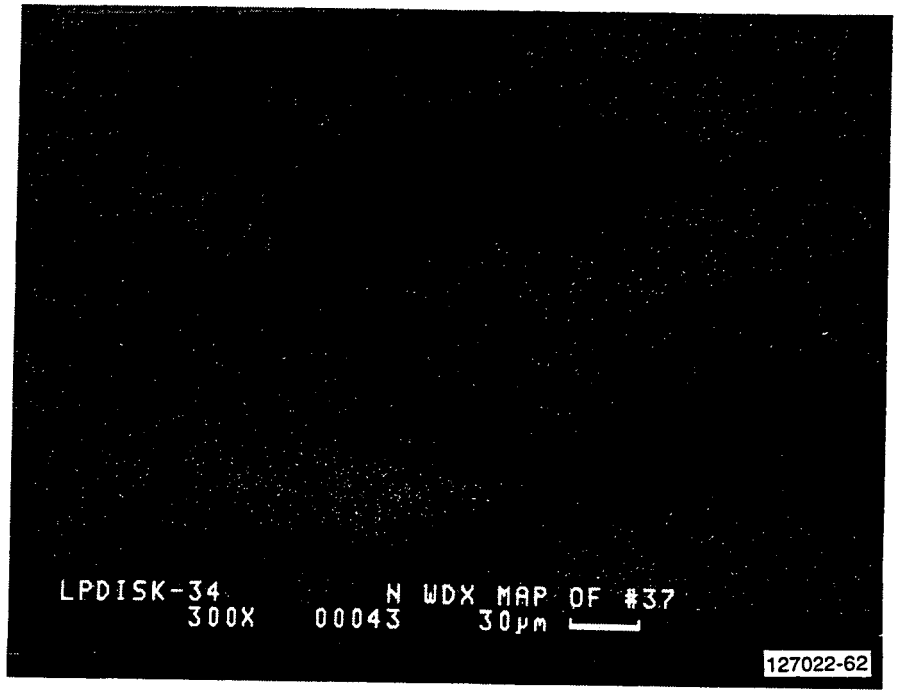

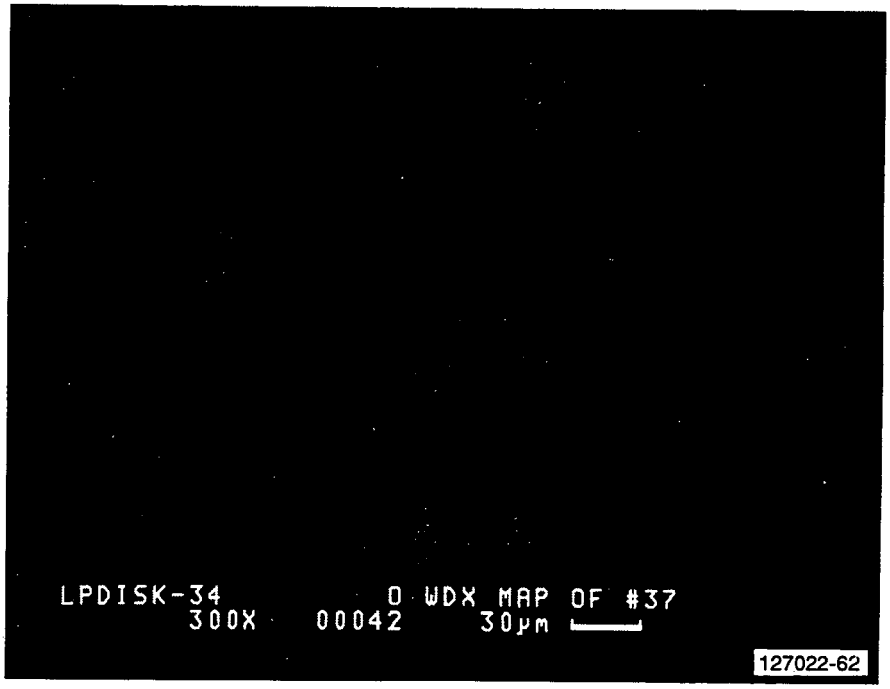

GB11591-739

Figure V-12(c). WDX Element Maps Of Failure Originating From Internal Inclusion Containing Al And Possible Si. N And O WDX Element Maps Indicate Inclusion Was Not Nitride or Silicate. Disk Burst Occurred At 88,500 rpm At Room Temperature.

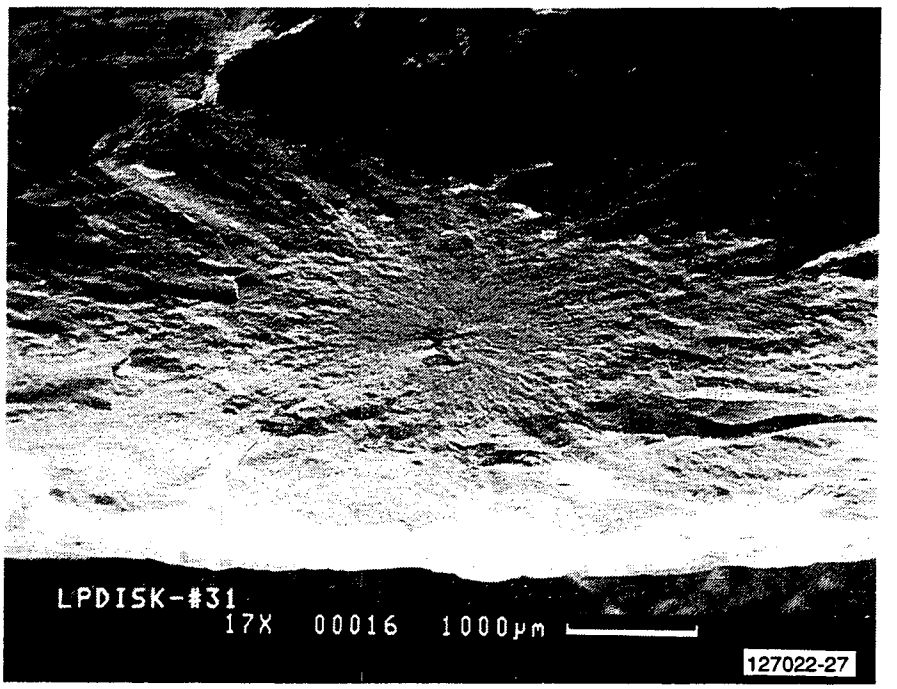

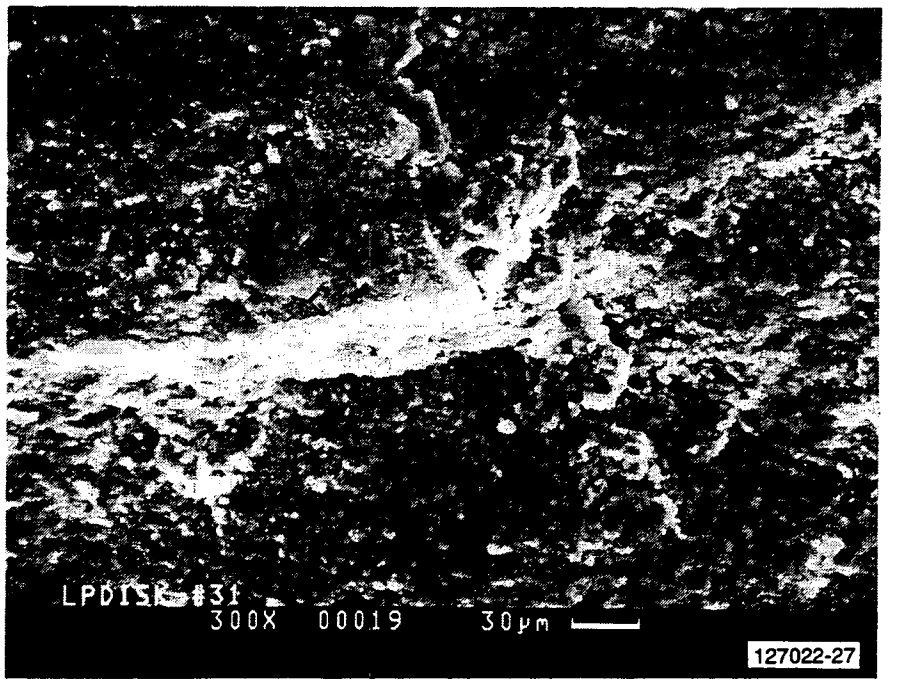

GB11591-740

Figure V-13(a). Photomicrographs Of Failure Originating From Internal Inclusion Containing Fe, Cr, Ni, And C. WDX Element Maps (Following Pages) Show Inclusion Does Not Contain O or N. Disk Burst Occurred At 90,200 rpm And Room Temperature.

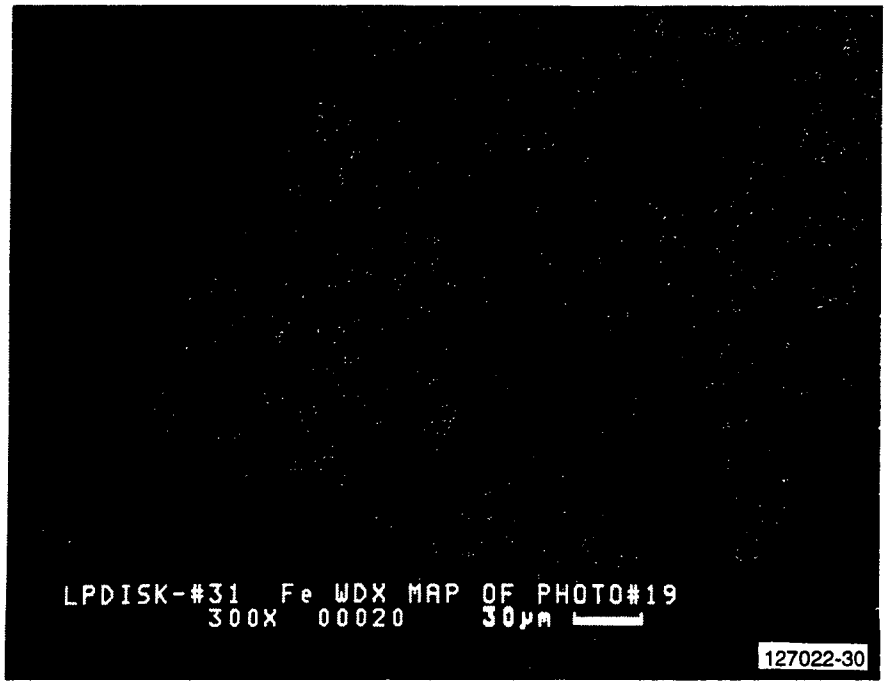

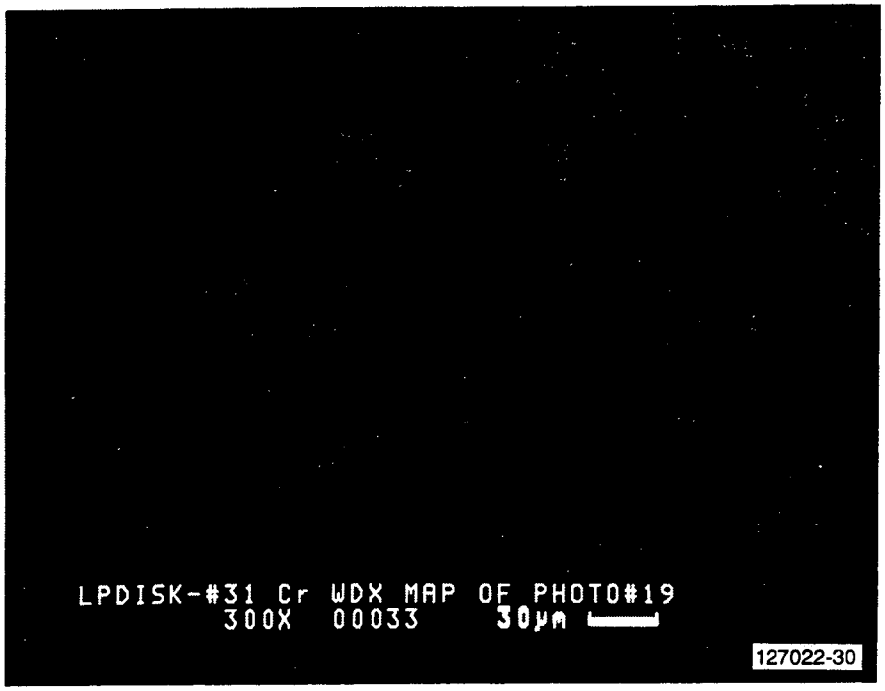

GB11591-741

Figure V-13(b). WDX Element Maps Of Failure Originating From Internal Inclusion Containing Fe, Cr, Ni, And C. Element Maps Show Inclusion Does Not Contain O Or N. Disk Burst Occurred At 90,200 rpm And Room Temperature.

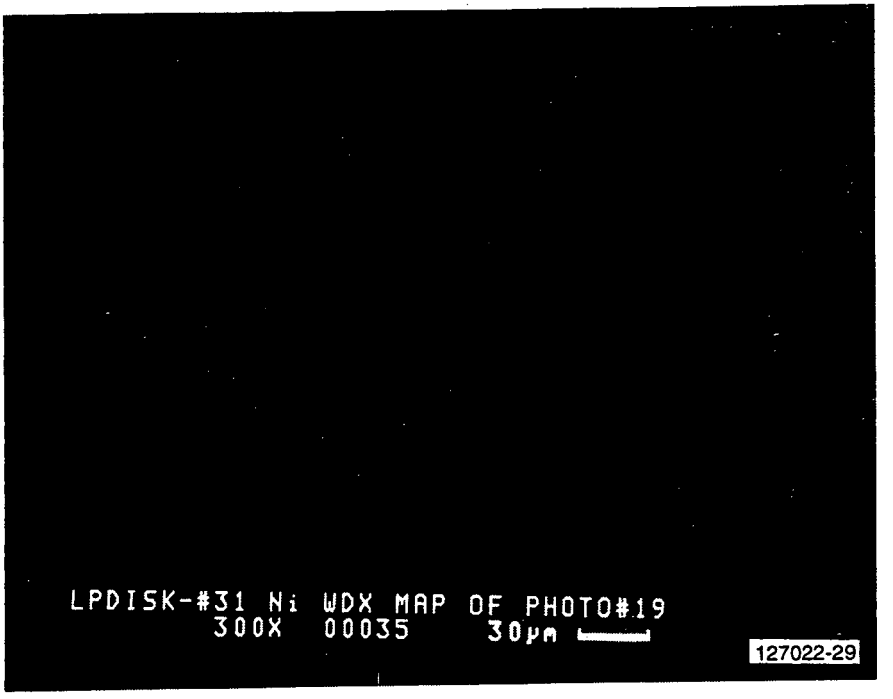

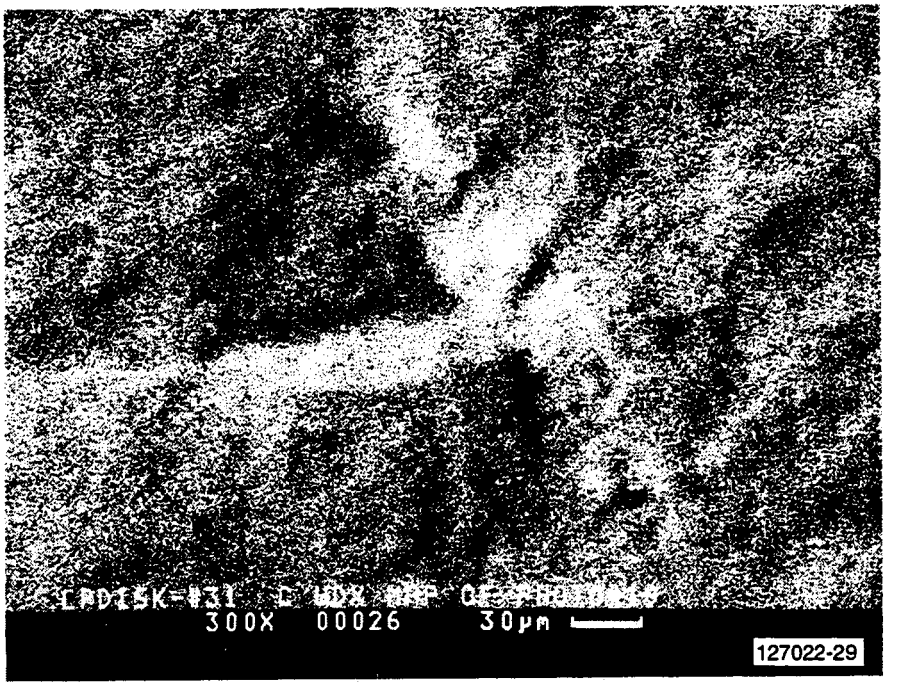

GB11591-742

Figure V-13(c). WDX Element Maps Of Failure Originating From Internal Inclusion Containing Fe, Cr, Ni, And C. Element Maps Show Inclusion Does Not Contain O Or N. Disk Burst Occurred At 90,200 rpm And Room Temperature. (Contd)

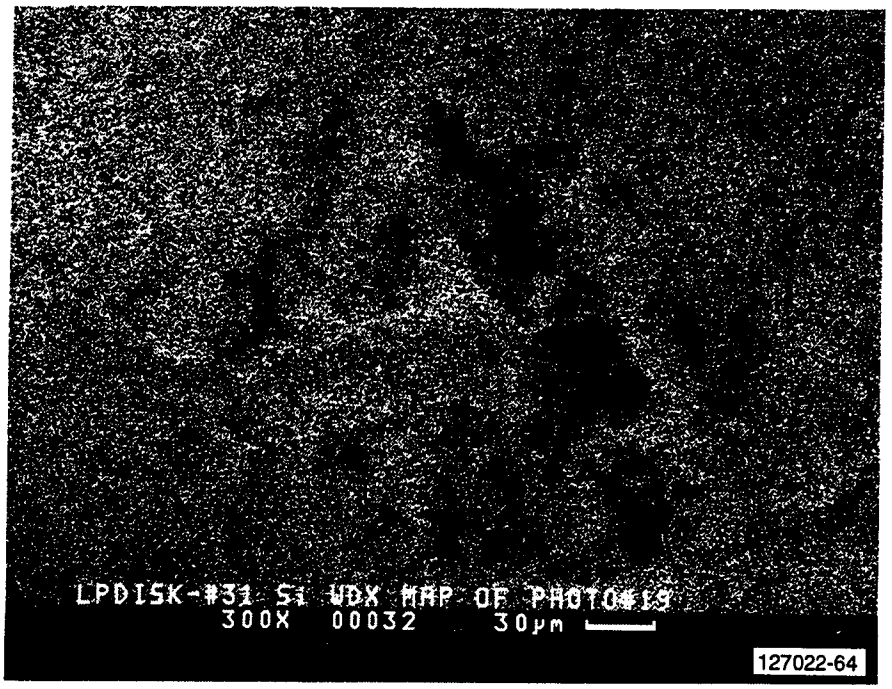

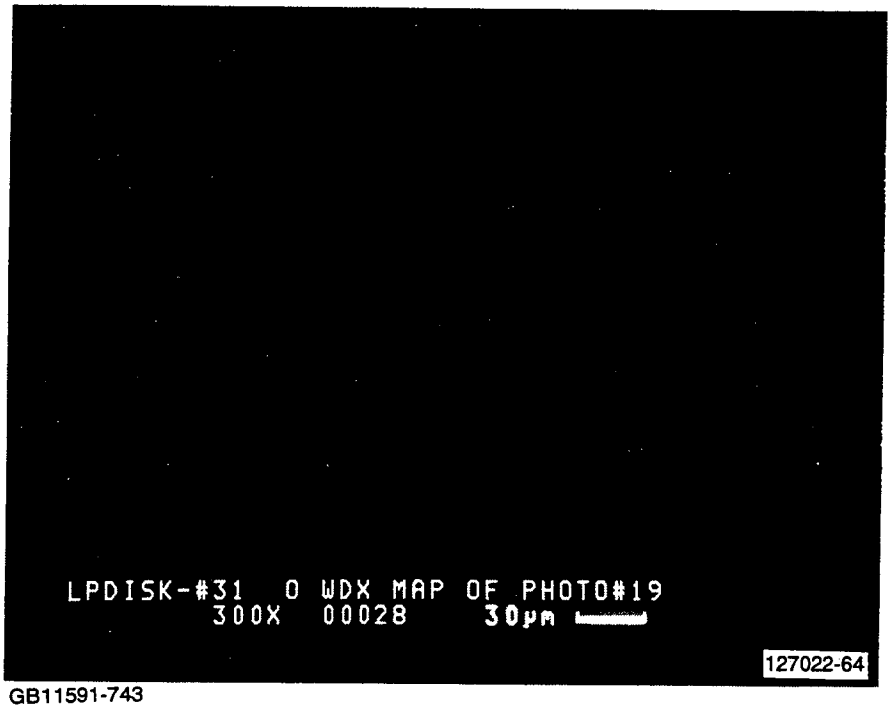

GB11591-743

Figure V-13(d). WDX Element Maps Of Failure Originating From Internal Inclusion Containing Fe, Cr, Ni, And C. Element Maps Show Inclusion Does Not Contain O Or N. Disk Burst Occurred At 90,200 rpm And Room Temperature. (Contd)

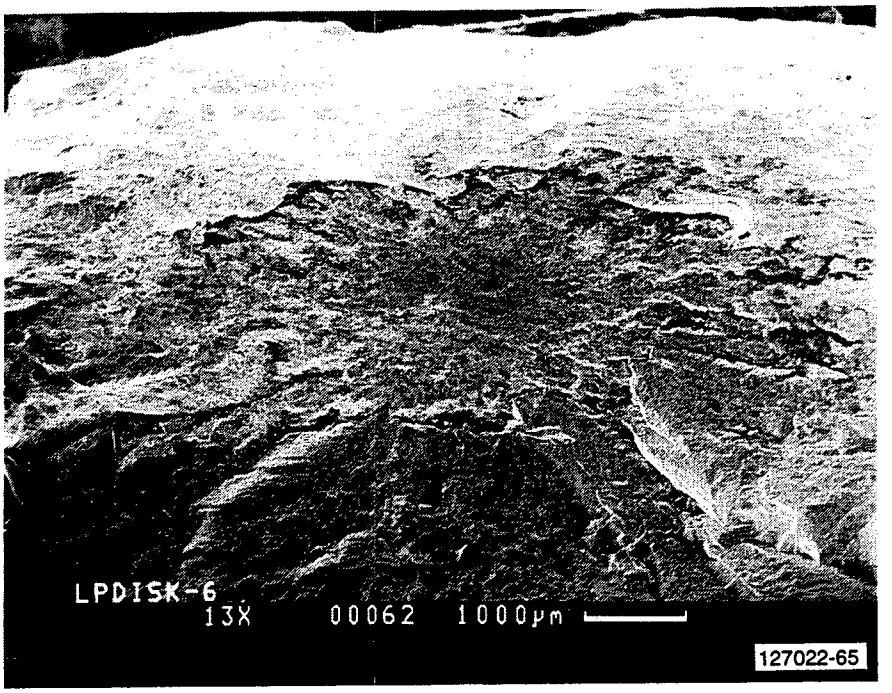

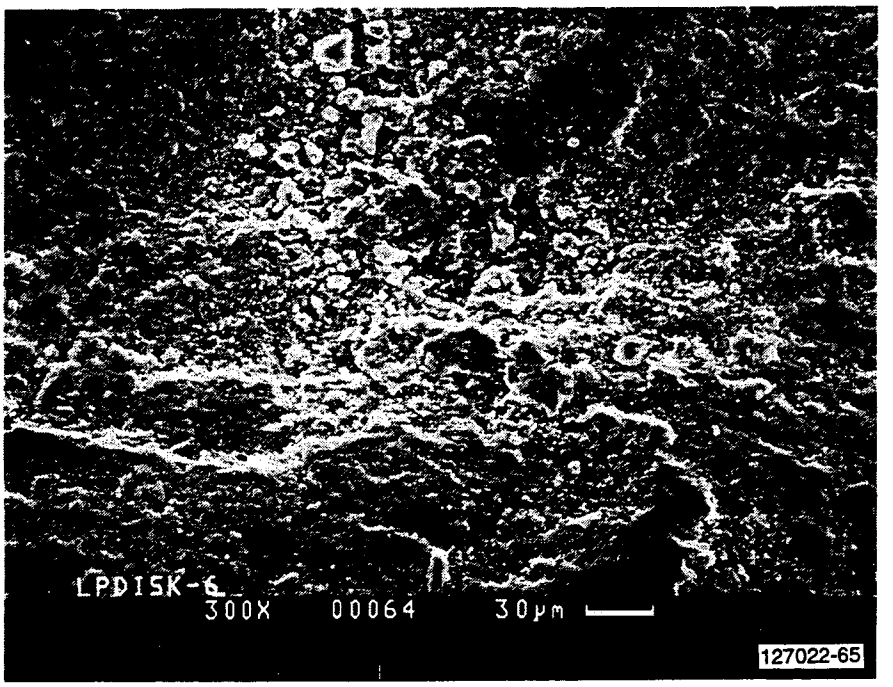

GB11591-744

Figure V-14(a). Photomicrographs Of Failure Originating From Internal Inclusion In 2200F, Fast Fracture Test Spin Disk. WDX Element Maps (Following Pages) Show Inclusion Contained Fe, Cr, Ni, And Al. Possible C Would Have Been Oxidized. Burst Occurred At 93,000 rpm.

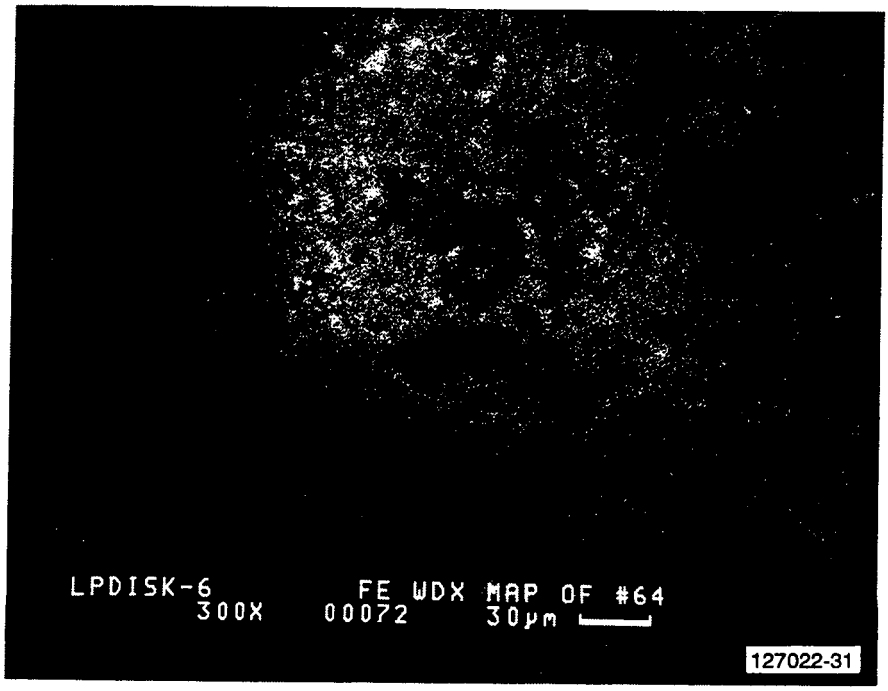

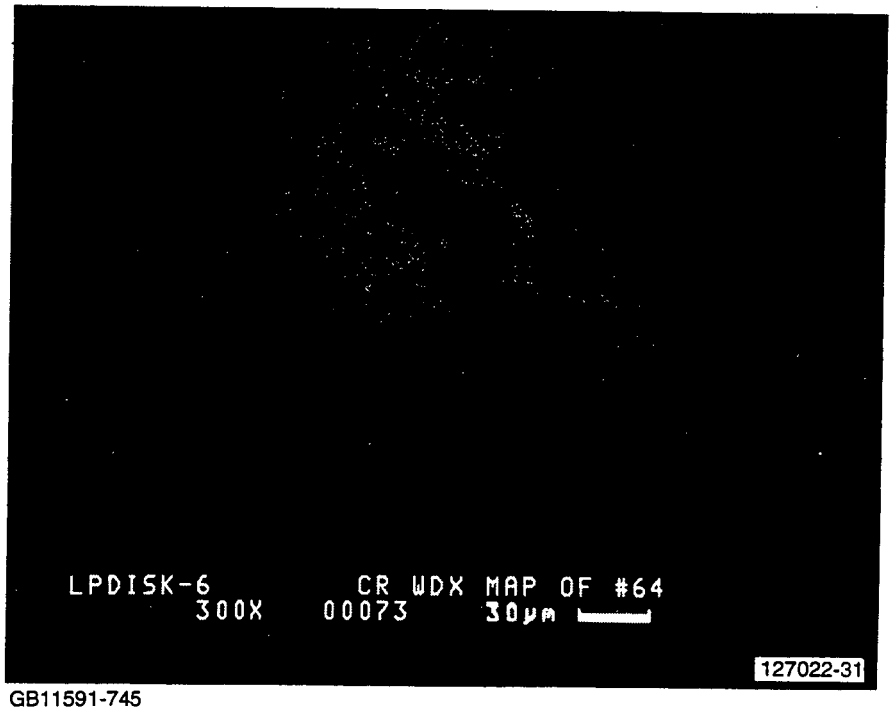

GB11591-745

Figure V-14(b). WDX Element Maps Of Failure Originating From Internal Inclusion In 2200F, Fast Fracture Test Spin Disk. Element Maps Show Inclusion Contained Fe, Cr, Ni, And Al. Possible C Would Have Been Oxidized. Burst Occurred At 93,000 rpm.

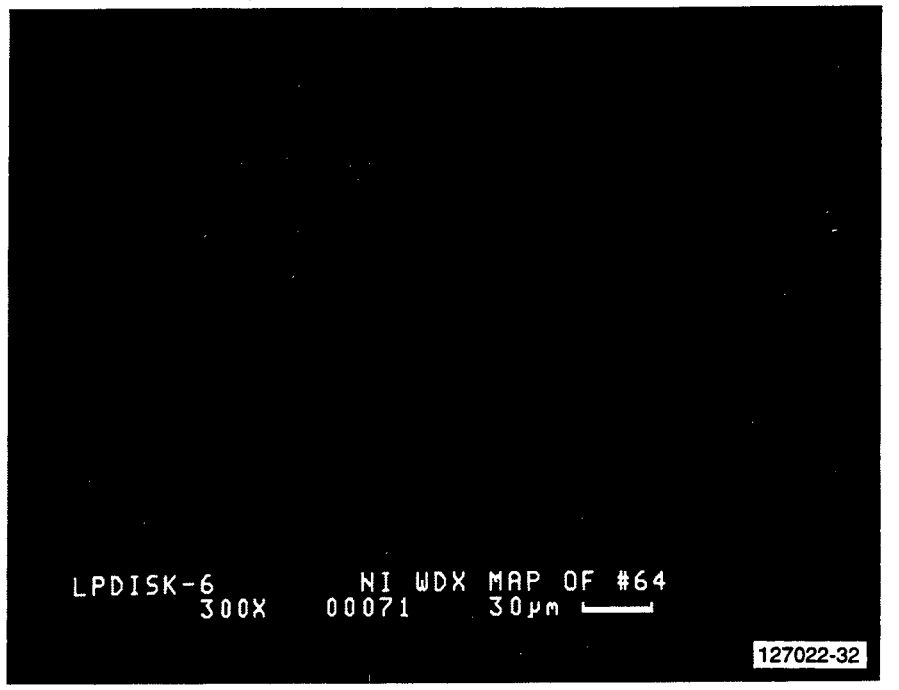

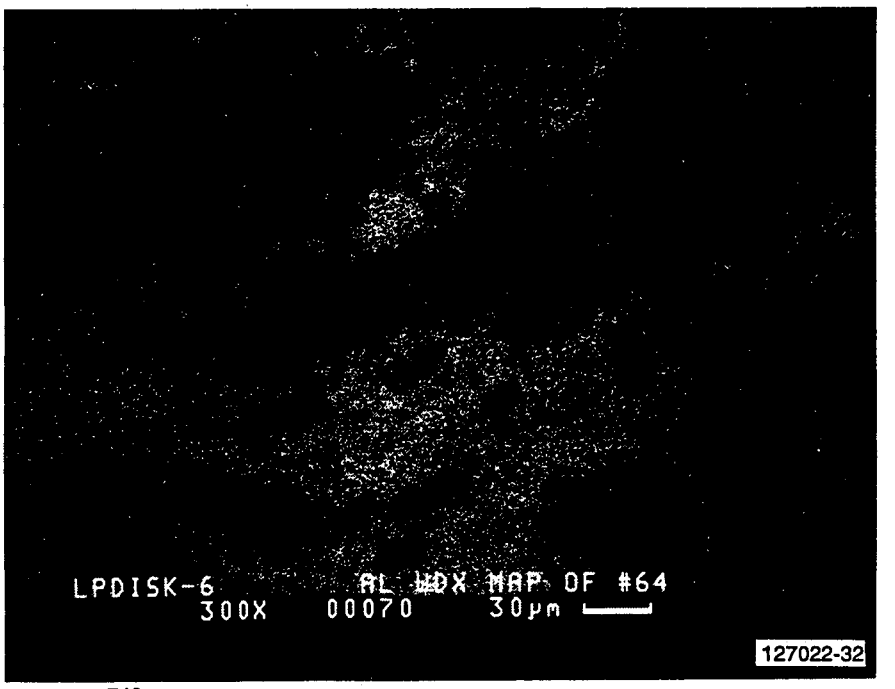

GB11591-746

Figure V-14(c). WDX Element Maps Of Failure Originating From Internal Inclusion In 2200F, Fast Fracture Test Spin Disk. Element Maps Show Inclusion Contained Fe, Cr, Ni, And Al. Possible C Would Have Been Oxidized. Burst Occurred At 93,000 rpm. (Contd)

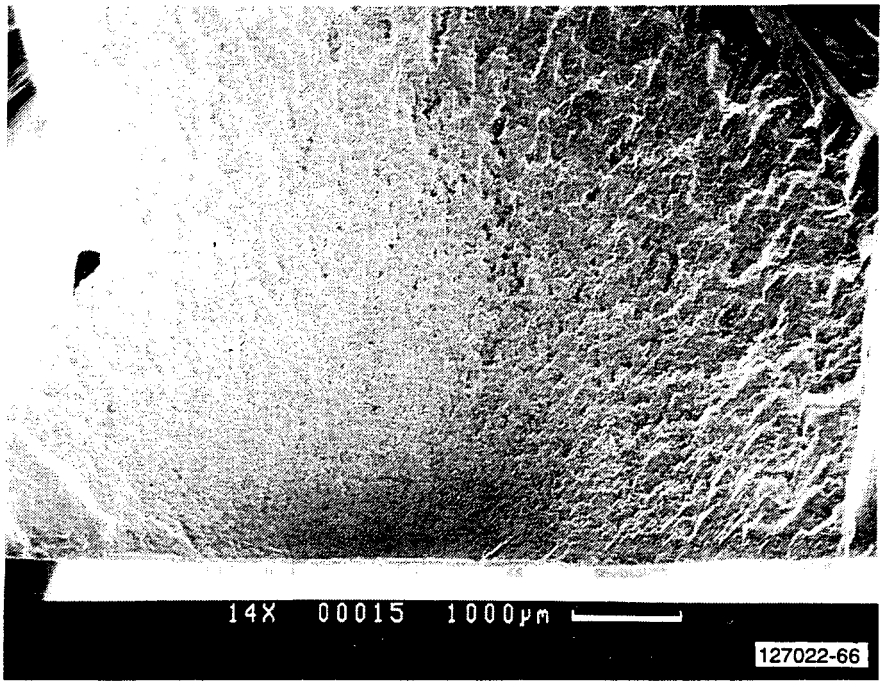

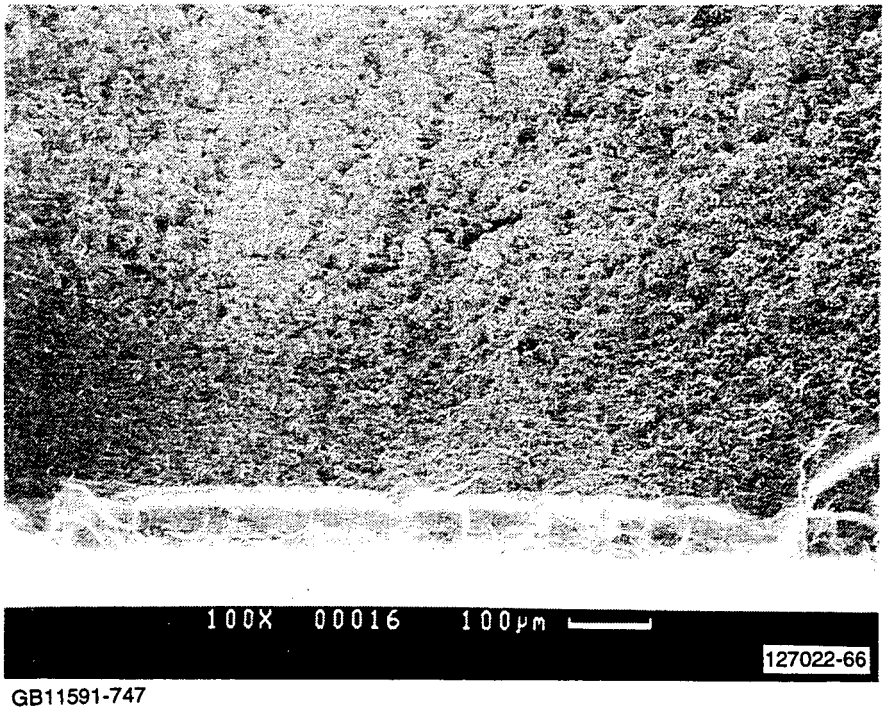

GB11591-747

Figure V-15(a). Failure Originating From Deep Surface Machining Line And Associated Damage On 2200F Fast Fracture Test Spin Disk. Burst Speed = 60,800 rpm.

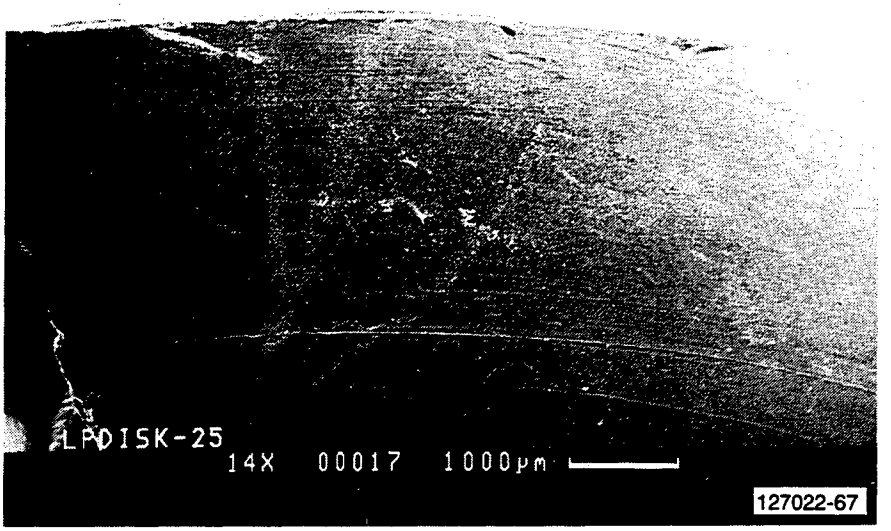

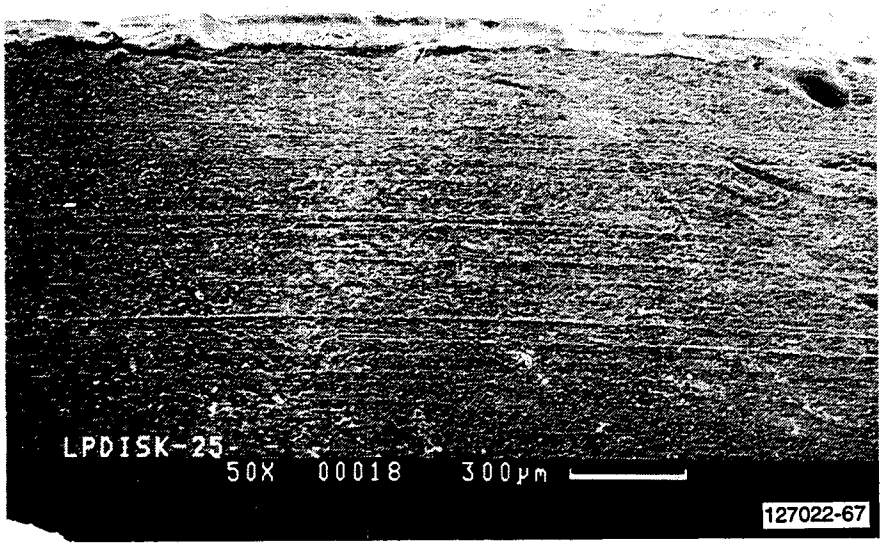

GB11591-748

Figure V-15(b). Tilting The Specimen Revealed Initial Fracture Plane Aligned With A Deep Circumferential Machining Line.

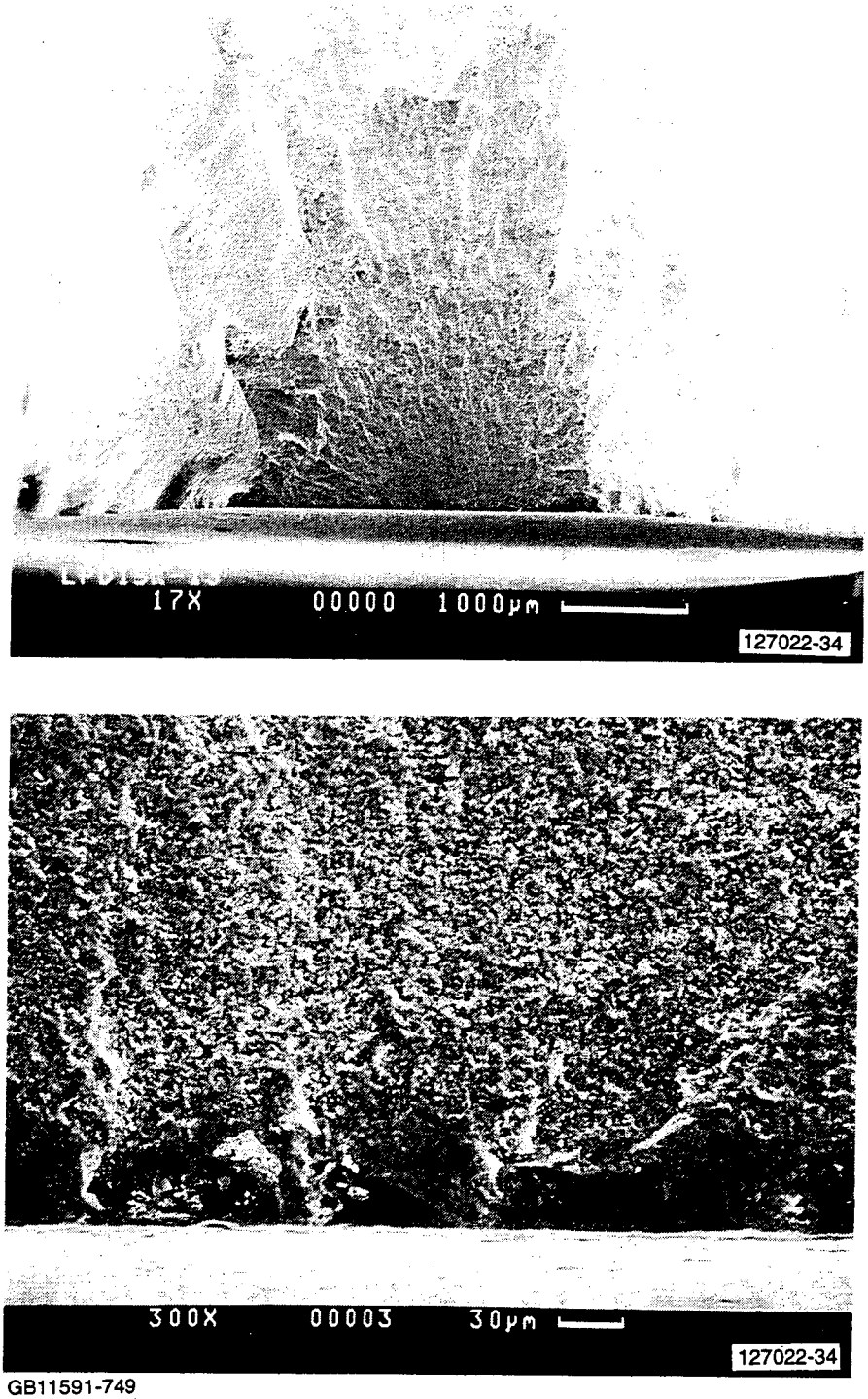

Figure V-16(a). Failure Originating From Surface Machining Damage On 2200F Fast Fracture Test Spin Disk. Burst Speed = 83,000 rpm.

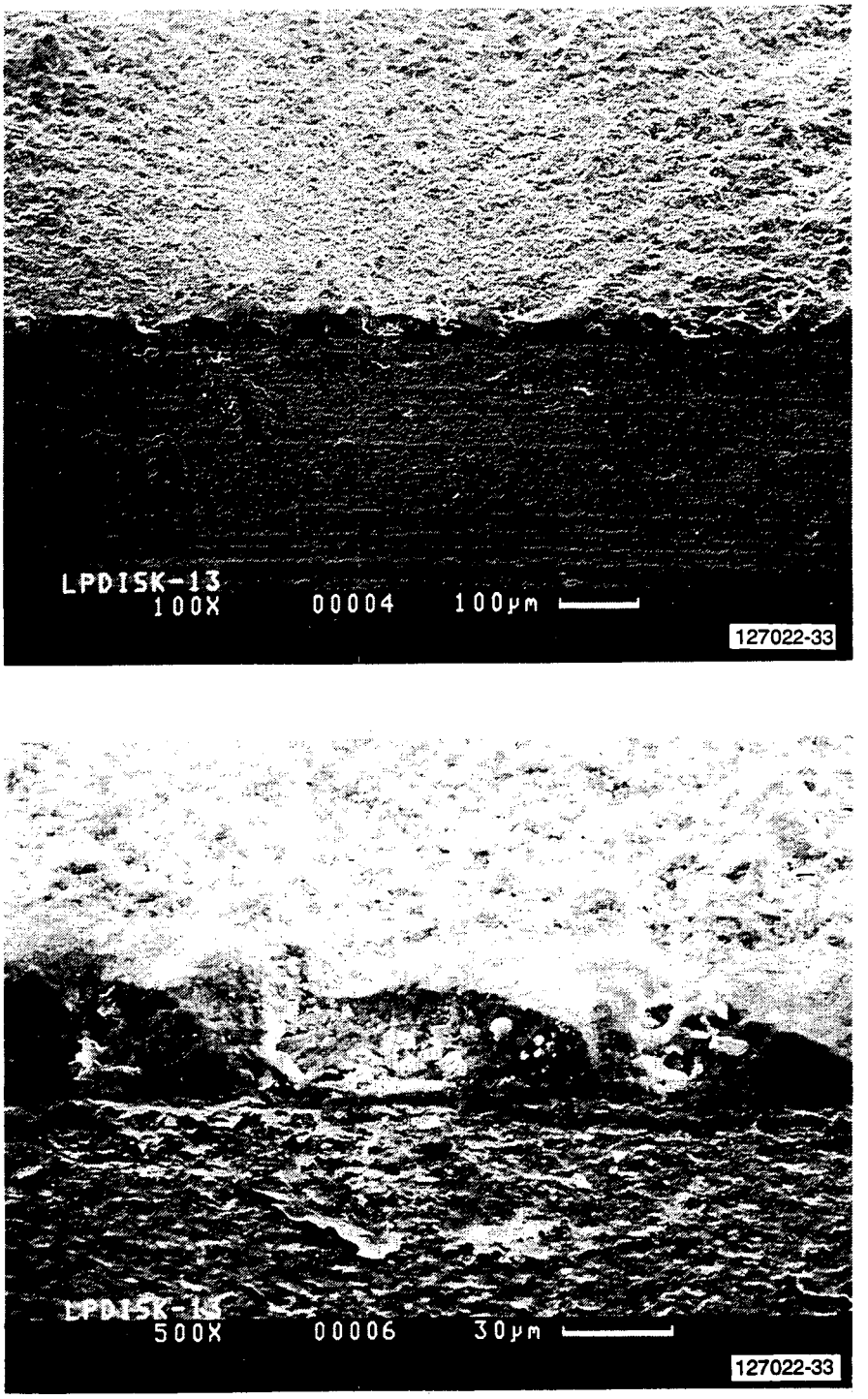

GB11591-750

Figure V-16(b). Tilting The Specimen Revealed Machining Lines Aligned With The Fracture Plane And A Series of Oxidized Microchips.

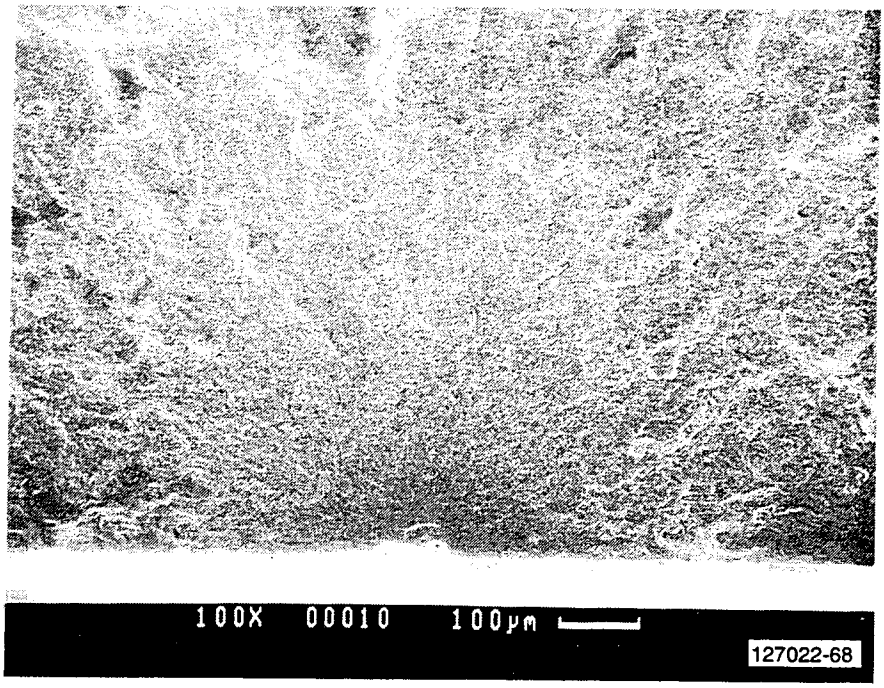

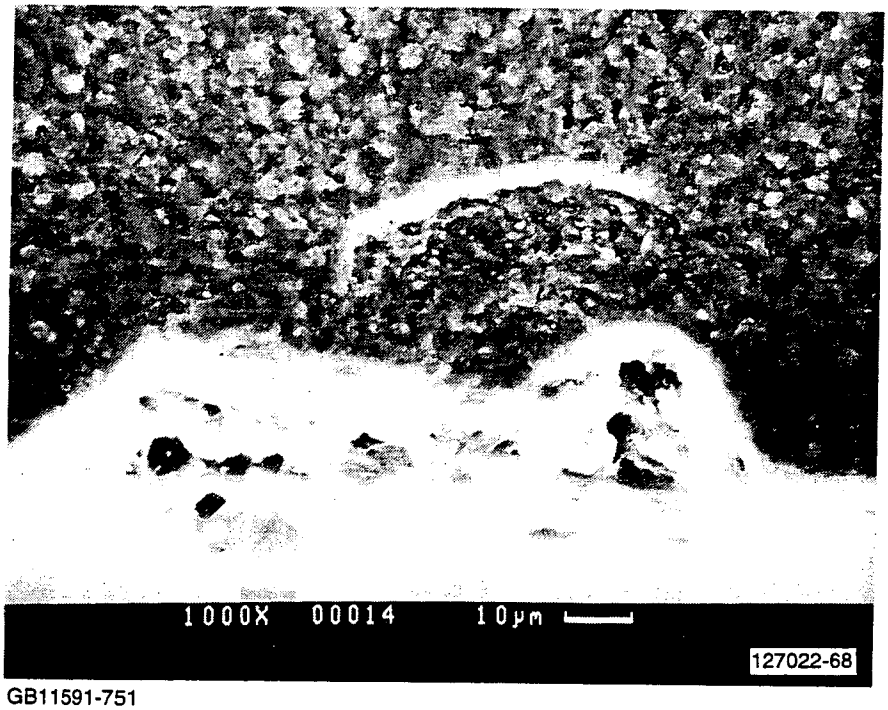

GB11591-751

Figure V-17(a). Failure Originated From Surface Pit Possibly Formed During Heat Treatment. Disk Burst Occurred At 82,800 rpm At Room Temperature.

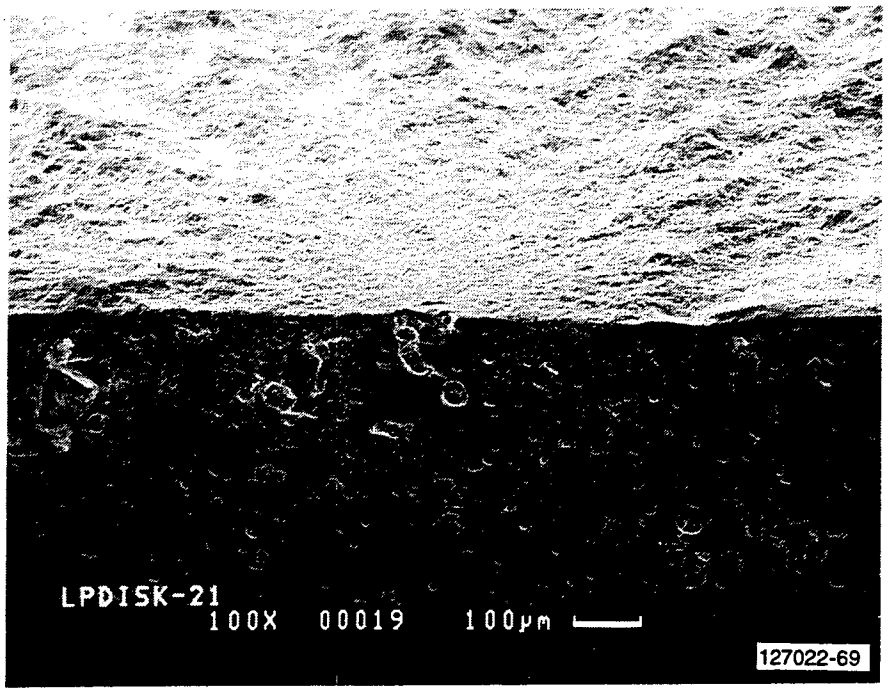

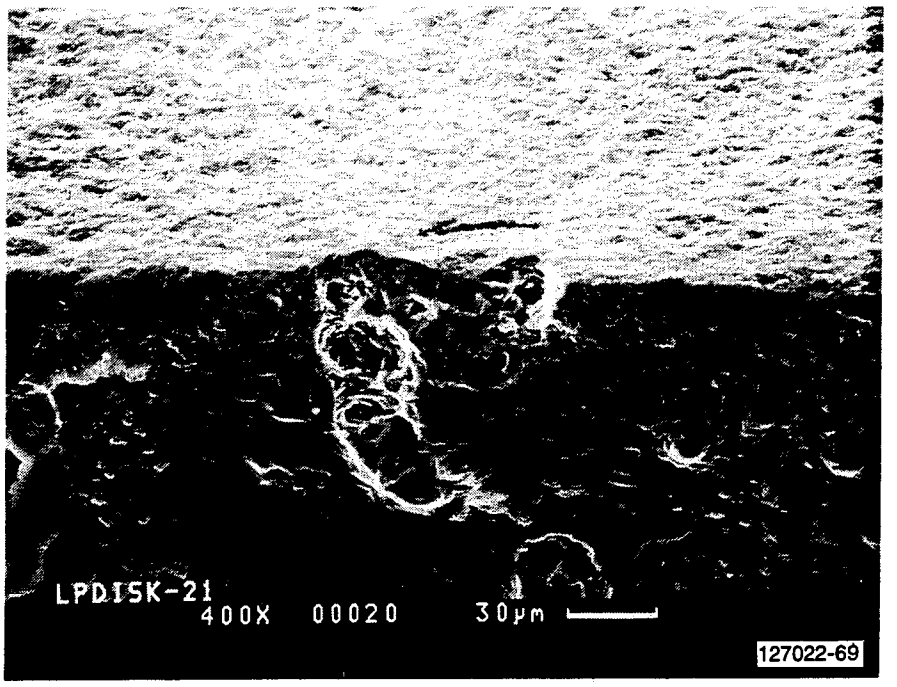

GB11591-752

Figure V-17(b). Arrows Indicate Surface Pit At Fracture Origin And Other Similar Pits.

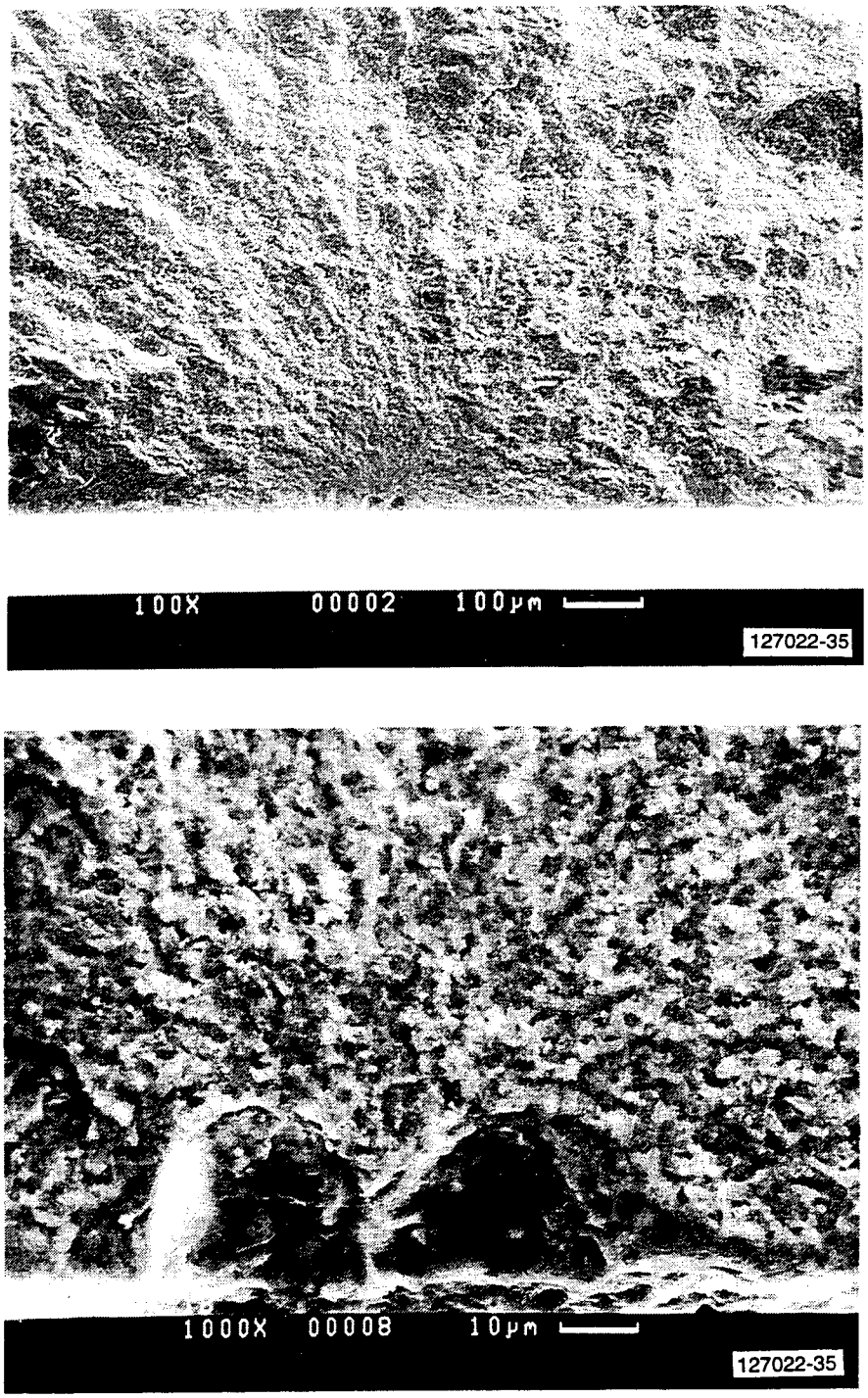

GB11591-753

Figure V-18(a). Failure Initiated From Surface Pits Possibly Formed During Heat Treatment.

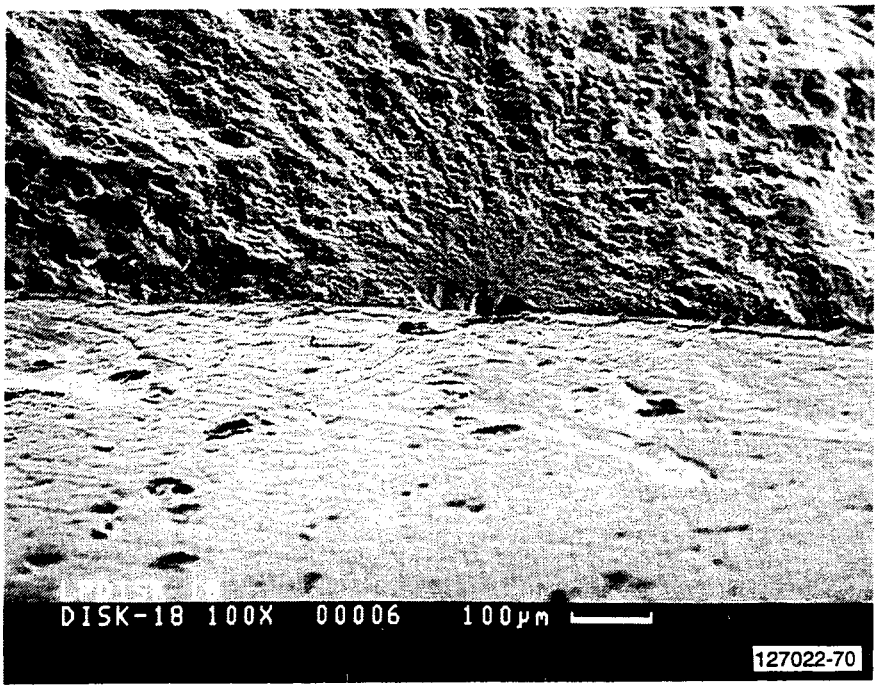

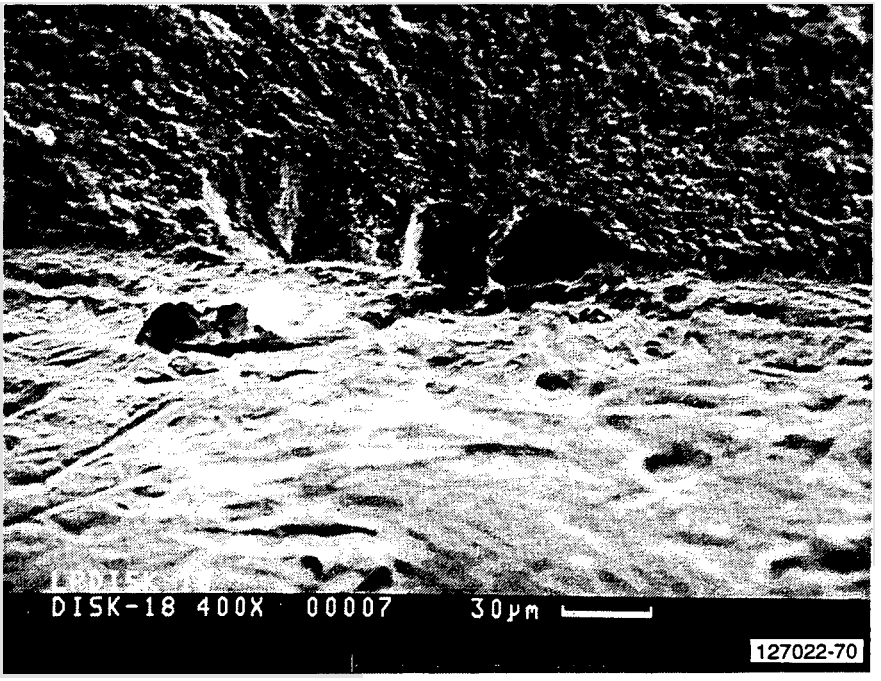

GB11591-754

Figure V-18(b). Tilting The Specimen Reveals Surface Condition Of The Spin Disk.

APPENDIX VI

DERIVATION OF STATISTICAL MODELS

(AlliedSignal Auxiliary Power and General Electric Corporate Research Center)

(70 pages)

This Appendix presents detailed derivations of the equations developed in this program for statistical analysis. The work was performed in collaboration with Dr. Curtis Johnson and Dr. William Tucker of the General Electric Corporate Research Center. Section 1 is a report written at AlliedSignal, and Sections 2 through 4 are sections written by Dr. Johnson and Dr. Tucker.

TABLE OF CONTENTS

TABLE OF CONTENTS

NOMENCLATURE

i , k	Subscripts specifying the ith, kth specimens, respectively
I_i	Multiaxial stress and stress gradient factor for the specimen -- a function of m , as defined by Evans/Lamon or Batdorf/Heinisch
I_c	Multiaxial stress and stress gradient factor for the component -- a function of m
m	Weibull modulus
R	Reliability
σ_i	Specimen fracture strength
σ_p	Component required design stress level for a probability of failure p
σ_o	Material strength constant, also known as the second Weibull parameter or the characteristic strength
V_i	Volume of the specimen
V_c	Volume of the component
A_i	Surface area of the specimen
A_c	Component surface area
Z	Component maximum stress level
p	Desired probability of failure for the component
n	Total number of specimens tested
r	Number of specimens failed for the given failure mode -- smaller than n
W	Likelihood Ratio statistics
$\chi_{1,\alpha}$,	Chi squared distribution with 1 degree of freedom and alpha probability, the level of confidence

SECTION 1 - MID-PROGRAM SUMMARY REPORT

This section of Appendix VI is an excerpt from AlliedSignal Auxiliary Power Report Number 32-3722. This report was written August, 22 1991 at the midpoint of this contract, as such it only included the development to that date and it outlined the goals that were then set. At some point those goals changed and some of them were not pursued, mainly the bias correction items outlined in section 5 of this appendix.

1.0 INTRODUCTION

An objective of the Oak Ridge Life Prediction Methodology for Ceramic Components of Advanced Heat Engines Project is to develop data analysis techniques for ceramic materials. Developed here are methods for the calculation of the Weibull parameters, their bias correction and confidence limits. This work also extends to the prediction of component reliability and the associated confidence level.

Maximum Likelihood methods are used over least squares methods to obtain the Weibull parameters because of their superior efficiency. Johnson and Tucker (ref 1) have shown that compared to Maximum Likelihood methods, least squares methods waste as much as 40 percent of the data available, hence the preference of maximum likelihood methods. Bootstrap and Likelihood Ratio methods are used to obtain confidence limits. Bias corrections are performed using Bootstrap methods.

An important contribution of this work is the development of techniques to combine multiple specimen data in the prediction of the Weibull parameters. The rationale behind pooling specimens of the same material, but of different shape, size and loading condition is that they are the same material and they must have common sets of Weibull parameters.

A computer code was written to implement these methods. Results from this code will be shown as examples as the material is presented. This code can generate, from a material data base, the set of Weibull parameters to be used in risk integration codes such as WESTAC and CARES.

This work was performed with the technical assistance of Dr. William Tucker and Dr. Curtis Johnson of the General Electric Company.

2.0 BACKGROUND

2.1 The Weibull Distribution

The Weibull distribution is an extreme value distribution of minima. It is commonly used to describe material strength. This distribution has found wide acceptability in reliability analysis as a model for time to failure of electronic and mechanical components and systems. The Weibull probability density function (PDF) as most commonly used in statistics is given by Equation [VI-1] and the cumulative density function (CDF) is given by equation [VI-2]. The cumulative density function is equivalent to the the probability of failure; hence,the probability of success is given by equation [VI-3].

$$f(\sigma_i) = m\sigma_O^{-1}\left(\frac{\sigma_i}{\sigma_o}\right)^{m-1} \exp-\left\{\left(\frac{\sigma_i}{\sigma_o}\right)^m\right\} \qquad \text{[VI-1]}$$

$$P_f = 1-\exp-\left\{\left(\frac{\sigma_i}{\sigma_o}\right)^m\right\} \qquad \text{[VI-2]}$$

$$P_s = \exp-\left\{\left(\frac{\sigma_i}{\sigma_o}\right)^m\right\}_- \qquad \text{[VI-3]}$$

In calculating the reliability of a system one must define the type of reliability system that is represented. A system can be a reliability-wise series system, a parallel system, or a combination of the two. A series system is one in which the failure of a system is obtained when any one of the components in the system fails, a parallel system is one in which all of the components must fail in order for the system to fail. In a series system, the reliability is calculated by computing the product of the reliability of each one of the components. In a parallel system, the reliability is computing by first calculating the unreliability which is the product of the probability of failure of the components in the system and then subtracting it from one. The statistical theory of brittle materials is based on the reliability-wise series system.

2.2 Weibull's Brittle Strength Theory

The statistical theory of brittle materials dates back to 1939, when W. Weibull (ref 2) published his first works on the subject. The approach used in the development is to assume that a ceramic part is made of many

small elements and that they behave as a reliability-wise series system. Weibull developed Equation [VI-4] for a uniaxial state of stress, this equation shows that the probability of failure of a component is a function of the size and of the stress of the component. Weibull also proposed equation [VI-5] in which the function $n(\sigma)$ is replaced by a power law. Batdorf and Crose (ref 3) and Evans (ref 4) later developed approaches for the statistical analysis under the multiaxial state of stress. Chao and Shetty (ref 5) proved by computation that the Batdorf and Crose and Evans theories gave identical predictions. Johnson and Tucker (ref 1), on the other hand, proved analytically that these two approaches were identical.

$$P_f = 1 - \exp\left\{-\int n(\sigma)dv\right\} \qquad \text{[VI-4]}$$

$$P_f = 1 - \exp\left\{-\int k\left(\frac{\sigma}{\sigma_o}\right)^m dv\right\} \qquad \text{[VI-5]}$$

After carrying out the integration in Equation [VI-5], it will yield an equation of the form of [VI-6] which shows the probability of failure to be a function of the component size, in this case volume, and of a factor I_i which is a function of the state of stress as derived by Batdorf and Crose or Evans. I_i is a function of the Weibull modulus m. Given that Equation [VI-6] represents the cumulative density function, Equation [VI-7] represents the probability density function and Equation [VI-8] the probability of survival or reliability.

$$P_f = 1 - \exp-\left\{V_i I_i\left(\frac{\sigma_i}{\sigma_o}\right)^m\right\} \qquad \text{[VI-6]}$$

$$f(\sigma_i) = mV_i I_i \sigma_O^{-1}\left(\frac{\sigma_i}{\sigma_o}\right)^{m-1} \exp-\left\{V_i I_i\left(\frac{\sigma_i}{\sigma_o}\right)^m\right\} \qquad \text{[VI-7]}$$

$$f(\sigma_i) = mV_i I_i \sigma_O^{-1}\left(\frac{\sigma_i}{\sigma_o}\right)^{m-1} \exp-\left\{V_i I_i\left(\frac{\sigma_i}{\sigma_o}\right)^m\right\} \qquad \text{[VI-8]}$$

3.0 PARAMETER ESTIMATION

This section describes the basic approach for parameter estimation for censored and uncensored data.

3.1 The Method Of Maximum Likelihood

The likelihood function of a sample is defined as the product of the probability density function of the distribution that represents the data, as shown by Equation [VI-9]. The likelihood function of the sample is a function of the unknown parameters of the governing distribution.

$$L(m,\sigma_o)=\prod_i f(\sigma_i,m,\sigma_o) \qquad \text{[VI-9]}$$

The maximum likelihood estimators of m and σ_o are values of m and σ_o that maximize the likelihood function; i.e., m and σ_o are the values that maximize the probability of occurrence of the sample results. If $\hat{m}$ and $\hat{\sigma}_o$ maximize $L(\hat{m},\hat{\sigma}_o)$, then $\hat{m}$ and $\hat{\sigma}_o$ also maximize the logarithm of the likelihood, $\ln\left[L(\hat{m},\hat{\sigma}_o)\right]$. In the case of the Weibull distribution, this transformation makes the derivation of $\hat{m}$ and $\hat{\sigma}_o$ much easier. The log likelihood for the Weibull distribution for a sample of size n would be:

$$l=\ln\left[L(m,\sigma_o)\right] \qquad \text{[VI-10]}$$

$$l=\sum_{i=1}^{n}\ln\left[f(\sigma_i,m,\sigma_o)\right] \qquad \text{[VI-11]}$$

$$l=\sum_{i=1}^{n}\ln\left[\frac{m}{\sigma_o}\left(\frac{\sigma_i}{\sigma_o}\right)^{m-1}\exp\left\{-\left(\frac{\sigma_i}{\sigma_o}\right)^{m}\right\}\right] \qquad \text{[VI-12]}$$

The maximum likelihood estimates can be obtained by taking the partial derivatives of the log likelihood with respect to m and σ_o and setting them equal to zero:

$$\frac{\partial l}{\partial m}=0,\ \frac{\partial l}{\partial \sigma_o}=0 \qquad \text{[VI-13]}$$

The solution of these equations are the maximum likelihood estimates and they must usually be solved by iterative methods.

3.2 Maximum Likelihood Estimates Of The Weibull Parameters

Johnson and Tucker (ref 1) categorize problems for the study of combined ceramic data into four different classes.

(1) Class I problems encompass specimens with uniform tensile stress and single specimen size.

(2) Class II problems encompass specimens with uniform tensile stress, but multiple specimen sizes.

(3) Class III problems encompass specimens with similar loading, but different specimen sizes. Similar loading refers to all the specimens being three-point bending, or four-point bending, or all tensile, etc.

(4) Class IV problems encompass specimens with different loading and different specimen sizes. Specimens can include an assortment of three-point bending, four-point bending, tensile, and any other arbitrary loading.

3.2.1 Uncensored Data (All Failures And Single Failure Mode)

Since Class IV problems embrace Classes I through III, the derivation of Weibull parameters for Class IV problems will therefore encompass Classes I through III. Equations [VI-6] through [VI-8] are the Weibull functions for the Class IV problems; these will be used in the subsequent derivations. Equation [VI-7] is repeated here for convenience.

$$f(\sigma_i) = mV_iI_i\sigma_O^{-1}\left(\frac{\sigma_i}{\sigma_o}\right)^{m-1} \exp-\left\{V_iI_i\left(\frac{\sigma_i}{\sigma_o}\right)^{m}\right\} \qquad \text{[VI-7]}$$

To compute the parameters of the distribution, we use the maximum likelihood procedure; for this we must formulate the problem using Equation [VI-10] where the log likelihood l is presented.

$$l = \sum \ln\left[f(\sigma_i)\right] \qquad \text{[VI-10]}$$

which yields:

$$l = \sum \ln(I_i) + \sum \ln(V_i) + \sum \ln(m) + \sum (m-1)\ln(\sigma_i) - \sum m \cdot \ln(\sigma_o) - \sum I_i V_i \left(\frac{\sigma_i}{\sigma_o}\right)^m \qquad \text{[VI-14]}$$

$$l = \sum \ln(I_i) + \sum \ln(V_i) + n \cdot \ln(m) + (m-1)\sum \ln(\sigma_i) - n\, m \ln(\sigma_o) - \sum I_i V_i \left(\frac{\sigma_i}{\sigma_o}\right)^m \qquad \text{[VI-15]}$$

Now the maximum likelihoods are obtained by maximizing [VI-15]. Taking the partials of l with respect to m and σ_o yields:

$$\frac{\partial l}{\partial m} = \sum \frac{I_i'}{I_i} + \frac{n}{m} + \sum \ln(\sigma_i) - n \cdot \ln(\sigma_o) - \sum I_i' V_i \left(\frac{\sigma_i}{\sigma_o}\right)^m - \sum I_i V_i \left(\frac{\sigma_i}{\sigma_o}\right)^m \ln\left(\frac{\sigma_i}{\sigma_o}\right) \qquad \text{[VI-16]}$$

and:

$$\frac{\partial l}{\partial \sigma_o} = -\frac{nm}{\sigma_o} - \sum I_i V_i \sigma_i^m (-m) \sigma_o^{-m-1} \qquad \text{[VI-17]}$$

$$\frac{\partial l}{\partial \sigma_o} = -\frac{nm}{\sigma_o} + \frac{m}{\sigma_o^{m+1}} \sum I_i V_i \sigma_i^m \qquad \text{[VI-18]}$$

and since:

$$\frac{\partial l}{\partial m} = \frac{\partial l}{\partial \sigma_o} = 0,$$

[VI-18] yields

$$\hat{\sigma}_o = \left[\frac{1}{n} \sum I_i V_i \sigma_i^{\hat{m}}\right]^{1/\hat{m}} \qquad \text{[VI-19]}$$

and substituting [VI-19] into [VI-16] yields:

$$0=\sum\frac{I_i'}{I_i}+\frac{n}{m}+\sum\ln(\sigma_i)-\frac{n}{m}\ln\left(\tfrac{1}{n}\sum I_iV_i\sigma_i^m\right)-\sum I_i'V_i\frac{\sigma_i^m}{\left[\tfrac{1}{n}\sum I_iV_i\sigma_i^m\right]}$$
$$-\sum I_iV_i\frac{\sigma_i^m}{\left[\tfrac{1}{n}\sum I_iV_i\sigma_i^m\right]}\left(\ln(\sigma_i)-\frac{1}{m}\ln\left(\tfrac{1}{n}\sum I_iV_i\,\sigma_i^m\right)\right) \qquad \text{[VI-20]}$$

Simplifying [VI-20]:

$$0=\sum\frac{I_i'}{I_i}\left(1-\frac{nI_iV_i\sigma_i^m}{\sum I_iV_i\sigma_i^m}\right)+\sum\ln(\sigma_i)\left(1-\frac{nI_iV_i\sigma_i^m}{\sum I_iV_i\sigma_i^m}\right)$$
$$+\frac{n}{m}\left(1-\ln\left(\frac{1}{n}\sum I_iV_i\sigma_i^m\right)\right)+\frac{n}{m}\frac{\sum I_iV_i\sigma_i^m\ln\left(\frac{1}{n}\sum I_iV\sigma_i^m\right)}{\sum I_iV_i\sigma_i^m} \qquad \text{[VI-21]}$$

and rearranging:

$$0=\sum\left(\frac{I_i'}{I_i}+\ln(\sigma_i)\right)\left(1-\frac{nI_iV_i\sigma_i^m}{\sum I_iV_i\sigma_i^m}\right)$$
$$+\frac{n}{m}\left(1-\ln\left(\frac{1}{n}\sum I_iV_i\sigma_i^m\right)+\frac{\sum I_iV_i\sigma_i^m\ln\left(\frac{1}{n}\sum I_iV_i\sigma_i^m\right)}{\sum I_iV_i\sigma_i^m}\right) \qquad \text{[VI-22]}$$

which finally yields:

$$0=\sum\left(\frac{I_i'}{I_i}+\ln(\sigma_i)\right)\left(1-\frac{nI_iV_i\sigma_i^m}{\sum I_iV_i\sigma_i^m}\right)+\frac{n}{m} \qquad \text{[VI-23]}$$

and:

$$\frac{1}{\hat{m}}=\frac{1}{n}\sum\left(\frac{I_i'}{I_i}+\ln(\sigma_i)\right)\left(\frac{nI_iV_i\sigma_i^m}{\sum I_iV_i\sigma_i^m}-1\right) \qquad \text{[VI-24]}$$

Hence the maximum likelihood estimates of m and σ_o are given by equations [VI-24] and [VI-19]. Equation [VI-24] has to be solved iteratively.

3.2.2 Censored Data (Suspended Or Multiple Failure Mode)

During a given testing program it is common to find that specimens, or components, fail in more than one failure mode. Whether this be for problems with the test itself or from inherent multiple failure modes of the specimens, it is essential to utilize all the data in order to extract all the information available from these tests to predict the behavior of the failure mode that is under investigation. In the case of ceramic materials, it is common to find strength failure locations at either the surface or internal to the specimen. It has also been observed that the strength distribution of these two failure locations exhibit two distinct strength levels, although both can be described by a Weibull distribution. In order to determine the best estimates of the Weibull parameters for these failure modes it is necessary to perform a censored data analysis. The approach taken in this analysis is the maximum likelihood method.

The likelihood function for censored data differs from the noncensored data in that the likelihood of the censored data contains the product of the PDF's of the noncensored data times the product of the CDF's of the censored data, as shown in Equation [VI-25]. For the log likelihood function this becomes the sum of the logs as shown in Equation [VI-26].

$$L = \prod_{i=1}^{r} f(\sigma_i) \bullet \prod_{j=r+1}^{n} P_s(\sigma_j) \qquad \text{[VI-25]}$$

$$l = \sum_{i=1}^{r} \ln\left[f(\sigma_i)\right] + \sum_{j=r+1}^{n} \ln\left[P_s(\sigma_j)\right] \qquad \text{[VI-26]}$$

$$l = \sum_{i=1}^{r} \ln\left[mV_iI_i\sigma_O^{-1}\left(\frac{\sigma_i}{\sigma_o}\right)^{m-1} \exp-\left\{V_iI_i\left(\frac{\sigma_i}{\sigma_o}\right)^{m}\right\}\right] + \sum_{j=r+1}^{n} \ln\left[\exp-\left\{V_jI_j\left(\frac{\sigma_j}{\sigma_o}\right)^{m}\right\}\right] \qquad \text{[VI-27]}$$

where: r is the number of failed units and n is the number of total units, and the number of censored units is the difference between n and r.

Equation [VI-27] yields:

$$l = \sum \ln(I_i) + \sum \ln(V_i) + \sum \ln(m) + \sum (m-1)\ln(\sigma_i) - \sum m \cdot \ln(\sigma_o) - \sum I_i V_i \left(\frac{\sigma_i}{\sigma_o}\right)^m - \sum I_j V_j \left(\frac{\sigma_j}{\sigma_o}\right)^m \quad \text{[VI-28]}$$

$$l = \sum \ln(I_i) + \sum \ln(V_i) + r \cdot \ln(m) + (m-1)\sum \ln(\sigma_i) - rm\ln(\sigma_o) - \sum I_i V_i \left(\frac{\sigma_i}{\sigma_o}\right)^m - \sum I_j V_j \left(\frac{\sigma_j}{\sigma_o}\right)^m \quad \text{[VI-29]}$$

The maximum likelihood estimates are obtained by maximizing Equation [VI-29]. Taking the partial derivatives of l with respect to σ_o and m yields:

$$\frac{\partial l}{\partial \sigma_o} = -\frac{rm}{\sigma_o} - \sum I_i V_i \sigma_i^m (-m)\sigma_o^{-m-1} - \sum I_j V_j \sigma_j^m (-m)\sigma_o^{-m-1} \quad \text{[VI-30]}$$

$$\frac{\partial l}{\partial \sigma_o} = -\frac{rm}{\sigma_o} + \frac{m}{\sigma_o^{m+1}} \sum I_i V_i \sigma_i^m + \frac{m}{\sigma_o^{m+1}} \sum I_j V_j \sigma_j^m \quad \text{[VI-31]}$$

and since:

$$\frac{\partial l}{\partial m} = \frac{\partial l}{\partial \sigma_o} = 0,$$

[VI-31] yields:

$$\hat{\sigma}_o = \left[\frac{1}{r}\sum_{k=1}^{n} I_k V_k \sigma_k^{\hat{m}}\right]^{1/\hat{m}} \quad \text{[VI-32]}$$

which is the solution for σ_o. The summation of k in [VI-9] is over all units. For the maximum likelihood estimate of m we must differentiate with respect to m as shown in Equation [VI-33]:

$$\frac{\partial l}{\partial m} = \sum \frac{I_i'}{I_i} + \frac{r}{m} + \sum \ln(\sigma_i) - r \cdot \ln(\sigma_o) - \sum I_i' V_i \left(\frac{\sigma_i}{\sigma_o}\right)^m - \sum I_i V_i \left(\frac{\sigma_i}{\sigma_o}\right)^m \ln\left(\frac{\sigma_i}{\sigma_o}\right) - \sum I_j' V_j \left(\frac{\sigma_j}{\sigma_o}\right)^m - \sum I_j V_j \left(\frac{\sigma_j}{\sigma_o}\right)^m \ln\left(\frac{\sigma_j}{\sigma_o}\right) \quad \text{[VI-33]}$$

Substituting [VI-32] into [VI-33] yields:

$$0=\sum\frac{I_i'}{I_i}+\frac{r}{m}+\sum\ln(\sigma_i)-\frac{r}{m}\ln\left(\tfrac{1}{r}\sum I_kV_k\sigma_k^m\right)-\sum I_i'V_i\frac{\sigma_i^m}{\left[\tfrac{1}{r}\sum I_kV_k\sigma_k^m\right]}$$
$$-\sum I_iV_i\frac{\sigma_i^m}{\left[\tfrac{1}{r}\sum I_kV_k\sigma_k^m\right]}\left(\ln(\sigma_i)-\frac{1}{m}\ln\left(\tfrac{1}{r}\sum I_kV_k\sigma_k^m\right)\right) \qquad \text{[VI-34]}$$
$$-\sum I_j'V_j\frac{\sigma_j^m}{\left[\tfrac{1}{r}\sum I_kV_k\sigma_k^m\right]}-\sum I_jV_j\frac{\sigma_j^m}{\left[\tfrac{1}{r}\sum I_kV_k\sigma_k^m\right]}\left(\ln(\sigma_j)-\frac{1}{m}\ln\left(\tfrac{1}{r}\sum I_kV_k\sigma_k^m\right)\right)$$

Rearranging and simplifying:

$$0=\sum\frac{I_i'}{I_i}+\frac{r}{m}+\sum\ln(\sigma_i)-\frac{r}{m}\ln\left(\tfrac{1}{r}\sum I_kV_k\sigma_k^m\right)-\frac{r}{\sum I_kV_k\sigma_k^m}\left[\sum I_i'V_i\sigma_i^m+\sum I_j'V_j\sigma_j^m\right]$$
$$-\frac{r}{\sum I_kV_k\sigma_k^m}\left[\sum I_iV_i\sigma_i^m\ln(\sigma_i)+\sum I_jV_j\sigma_j^m\ln(\sigma_j)\right] \qquad \text{[VI-35]}$$
$$+\frac{r}{\sum I_kV_k\sigma_k^m}\left[\sum I_iV_i\sigma_i^m\frac{1}{m}\ln\left(\left[\tfrac{1}{r}\sum I_kV_k\sigma_k^m\right]\right)+\sum I_jV_j\sigma_j^m\frac{1}{m}\ln\left(\left[\tfrac{1}{r}\sum I_kV_k\sigma_k^m\right]\right)\right]$$

and:

$$0=\sum\frac{I_i'}{I_i}+\frac{r}{m}+\sum\ln(\sigma_i)-\frac{r}{m}\ln\left(\tfrac{1}{r}\sum I_kV_k\sigma_k^m\right)-\frac{r}{\sum I_kV_k\sigma_k^m}\left[\sum I_k'V_k\sigma_k^m\right]$$
$$-\frac{r}{\sum I_kV_k\sigma_k^m}\left[\sum I_kV_k\sigma_k^m\ln(\sigma_k)\right]+\frac{r}{m}\ln\left(\tfrac{1}{r}\sum I_kV_k\sigma_k^m\right) \qquad \text{[VI-36]}$$

which finally yields:

$$\frac{1}{\hat{m}}=\frac{1}{\sum_{k=1}^{n}I_kV_k\sigma_k^m}\sum_{k=1}^{n}V_k\sigma_k^m\left[I_k'+I_k\ln(\sigma_k)\right]-\frac{1}{r}\sum_{i=1}^{r}\left[\frac{I_i'}{I_i}+\ln(\sigma_i)\right] \qquad \text{[VI-37]}$$

Equations [VI-32] and [VI-37] are used to estimate the Weibull parameters for censored and multifailure data. In the above equations the summation indices have the following ranges: i=1, r, j=r+1, n, k=1, n.

3.3 Reliability Estimates

Design evaluation is performed by computing the reliability of the component in question the higher the reliability the better the design. The reliability, or probability of success, of a component is computed using Equation [VI-8], as shown below:

$$P_s = \exp-\left\{V_i I_i \left(\frac{\sigma_i}{\sigma_o}\right)^m\right\} \qquad \text{[VI-8]}$$

The Weibull parameters, m and σ_o, are obtained from the statistical analysis of the specimen data. In the case of uncensored data, Equations [VI-19] and [VI-24] are used; in the case of censored or multifailure data, Equations [VI-32] and [VI-37] are used.

3.4 Design Stress Level Estimates σ_p

Preliminary component design dictates the knowledge of a target maximum stress level that will satisfy a required level of reliability with an acceptable confidence level. Such a stress level is referred to as the design stress level. The design stress level can be computed using equation [VI-6]; the derivation follows. Starting with Equation [VI-6] and setting the probability of failure equal to p yields equation [VI-38].

$$p = 1 - \exp\left\{-I_c V_c \left(\frac{\sigma_p}{\sigma_o}\right)^m\right\} \qquad \text{[VI-38]}$$

where:

p is the desired probability of failure.

σ_p is the stress level for the above probability of failure.

I_c is the component multiaxial stress factor.

V_c is the component size, surface, volume or length.

Solving for σ_p in [VI-38] yields Equations [VI-39] and [VI-40]:

$$\ln\left(\frac{1}{1-p}\right) = I_c V_c \left(\frac{\sigma_p}{\sigma_o}\right)^m \qquad \text{[VI-39]}$$

$$\sigma_p = \sigma_o \left\{\frac{1}{I_c V_c} \ln\left(\frac{1}{1-p}\right)\right\}^{1/m} \qquad \text{[VI-40]}$$

The Weibull parameters, m and σ_o, are obtained from the statistical analysis of the specimen data. In the case of uncensored data, Equations [VI-19] and [VI-24] are used; in the case of censored or multifailure data, Equations [VI-32] and [VI-37] are used.

4.0 CONFIDENCE LIMIT CALCULATION

In section 3 a method was outlined to predict the estimates of the Weibull parameters. It is observed that these are only best estimates of the parameters. It is also observed that reliability predictions, Equation [VI-8], use these estimates. Minor changes in the predictions of these estimates may produce significant errors in high reliability or low probability of failure predictions. The limited number of specimens that are usually available for testing preclude the prediction of the true parameters of the distribution, making it necessary to estimate confidence intervals that will contain the true parameter. Two approaches have been implemented to determine these confidence level intervals, the Bootstrap method and the Likelihood Ratio method. A description of these methods follows.

4.1 The Bootstrap Method

The Bootstrap method consists on gathering information about estimates of variability and uncertainty by evaluating the observed data set. Uncertainties on the estimates can arise from testing a finite number of specimens and from inefficiencies of the estimators. Bootstrap techniques can be parametric and non-parametric. The parametric technique uses the estimates for the assumed distribution to generate a new data set. This data set then produces new estimates for the distribution parameters of the experimental data. The non-parametric technique generates a new data set from the original data set, allowing for replacements. In both methods, a number of specimens similar to the original data set is used. This document describes only the parametric bootstrap approach. Bootstrap techniques are described by Efron and Tibshrani (ref 6).

The confidence limits are calculated by generating new data sets and their respective Weibull parameters a number of times that will accurately define the required confidence limits. For example, if the two-sided 95% confidence limit is required, the upper limit will be given by the 97.5 percentile of the generated Weibull parameters and the lower limit will be given by the 2.5 percentile. To define the 97.5 and the 2.5 percentiles 1000 data sets would be needed; when ordering the parameters in ascending order, the 25th value would yield the 2.5 percentile and the 975th value would yield the 97.5 percentile. Note that odd percentiles could be predicted with 100 data sets; i.e., the 96% confidence limit would be given by the 2nd and the 98th values of the parameters of the 100 data sets. The accuracy of these predictions would also depend on the number of data sets: the larger the set, the better the accuracy. The Bootstrap analysis for the characteristic value or first Weibull parameter is performed in a similar fashion.

4.2 The Likelihood Ratio Method

The Likelihood Ratio method involves the statistics of the log of the ratio of the likelihood function of two distributions. Cox and Oakes, Chapter 3.3, (ref 7), describe a method for the two-parameter Weibull distribution. The Likelihood Ratio method is based on the likelihood ratio statistic, Equation [VI-41].

$$W(m) = 2\left[l(\hat{m}, \hat{\sigma}_o) - l(m, \hat{\sigma}_{om})\right] \qquad \text{[VI-41]}$$

Where:

$l(\hat{m}, \hat{\sigma}_o)$ is the likelihood function given the maximum likelihood estimates of m and σ_o.
$l(m, \hat{\sigma}_{om})$ is the likelihood function given the maximum likelihood estimate of σ_o given m.

$W(m)$ has an approximate Chi-squared distribution with one degree of freedom, $\chi^2_{1,\alpha}$. To determine the $1-\alpha$ confidence limits one must compute the values of m for which Equation [VI-42] holds. Two solutions can be found to this equation: the upper confidence bound and the lower confidence bound.

$$m : W(m) \le \chi^2_{1,\alpha} \qquad \text{[VI-42]}$$

4.3 Confidence Limits For Single Failure Mode, All Specimens Fail

4.3.1 Confidence Limits By The Bootstrap Method

4.3.1.1 Confidence Limits For The First And Second Weibull Parameters

Given that the Bootstrap method relies heavily on evaluation, the process to calculate confidence intervals, the approach is better described in a step-by-step basis. The confidence limits of the Weibull parameters can be calculated simultaneously; both are presented in this section.

(a) The first step consists of estimating the Weibull parameters using the Maximum Likelihood method. The estimates are computed from Equations [VI-19] and [VI-24] (shown next for convenience; the equations were derived in Section 3.2.1).

$$\hat{\sigma}_o = \left[\tfrac{1}{n}\sum \hat{I}_i V_i \sigma_i^{\hat{m}}\right]^{\frac{1}{\hat{m}}} \qquad \text{[VI-19]}$$

$$\frac{1}{\hat{m}} = \frac{1}{n}\sum\left(\frac{I_i'}{I_i} + \ln(\sigma_i)\right)\left(\frac{n I_i V_i \sigma_i^m}{\sum I_i V_i \sigma_i^m} - 1\right) \qquad \text{[VI-24]}$$

(b) Second, choose a random number between zero and one, and pick this number to be a reliability value, R.

(c) Third, select a specimen type from the original data set, with its corresponding V_i and I_i . Using the above $\hat{m}$ and $\hat{\sigma}_o$ compute the fracture strength of this pseudo specimen, using Equation [VI-43], given that it has the reliability equivalent to the value of the random number chosen in (b).

$$\sigma_i = \hat{\sigma}_o\left(-\frac{\ell n(R_i)}{\hat{I}_i V_i}\right)^{1/\hat{m}} \qquad \text{[VI-43]}$$

(d) Repeat steps (b) and (c) for each specimen type and size a number of times equal to the number of specimens in the individual data set.

(e) Calculate the Weibull parameters for this newly generated data set using Equations [VI-44] and [VI-45] and save these values.

$$\tilde{\sigma}_o = \left[\tfrac{1}{n}\sum \tilde{I}_i V_i \sigma_i^{\tilde{m}}\right]^{\frac{1}{\tilde{m}}} \qquad \text{[VI-44]}$$

$$\frac{1}{\tilde{m}} = \frac{1}{n}\sum\left(\frac{I_i'}{I_i} + \ln(\sigma_i)\right)\left(\frac{n I_i V_i \sigma_i^m}{\sum I_i V_i \sigma_i^m} - 1\right) \qquad \text{[VI-45]}$$

(f) Repeat steps (b) through (e) a number of 1000 times.

(g) Sort the $\tilde{m}$ and $\tilde{\sigma}_o$ pair in ascending order for $\tilde{m}$ without losing the pair and also for $\tilde{\sigma}_o$ without losing the pair.

(h) To calculate the x confidence interval, pick the (100-x) (1000/2)(1/100) points from the upper and lower ends of the sorted values in (g); these define the limits. For example, if the 95 percent confidence interval is required, substitute the 95 for x to obtain 5, then multiply by the adjoining factor to get 25. Hence the 95 percent confidence interval is given by 25th point from the lowest and the 25th point from the top of the sorted values $\tilde{m}$ and $\tilde{\sigma}_o$ in (g).

4.3.1.2 Confidence Limits For The Design Stress Level

(a) The design stress level can be obtained from the Weibull parameters calculated in Equations [VI-44] and [VI-45] by using Equation [VI-46], where "p" is the desired probability of failure, V is the component volume, and $\tilde{I}$ is the component's multiaxial and stress gradient factor:

$$\sigma_p = \tilde{\sigma}_o \left[\frac{1}{\tilde{I}V} \ell n \left(\frac{1}{1-p} \right) \right]^{1/\tilde{m}} \qquad \text{[VI-46]}$$

(b) Given that we have a set of $\tilde{m}$ and $\tilde{\sigma}_o$ from Section 4.3.1.1, compute σ_p from [VI-46] for each one of these values and save them.

(c) Sort the σ_p and obtain the x confidence interval by picking the (100-x) 10/2 points from the upper and lower ends, using the same approach as in 4.3.1.1 (h).

4.3.1.3 Confidence Limits For The Reliability Prediction

(a) Similarly to σ_p, the reliability, R, has a functional relationship to σ_o and it is given by Equation [VI-47], where Z is the maximum stress level of the component, and $\tilde{I}$ and V are the component's multiaxial and stress gradient factor and volume, respectively.

$$R(Z) = \exp - \left[\tilde{I}V \left(\frac{Z}{\tilde{\sigma}_o} \right)^{\tilde{m}} \right] \qquad \text{[VI-47]}$$

(b) Given that we have $\tilde{m}$ and $\tilde{\sigma}_o$ from Section 4.3.1.1, we can substitute these values into [VI-47] to find a list of R's.

(c) Sort the R's and obtain the x confidence interval by picking the (100-x) 10/2 points from the upper and lower ends, using the same approach as in 4.3.1.1 (h).

4.3.2 Confidence Limits By The Likelihood Ratio Approach

4.3.2.1 Confidence Limits For The First And Second Weibull Parameters

As shown by Equation [VI-41] one must calculate a variety of log likelihoods to calculate the confidence limits on the Weibull parameters. For the case of the confidence limits on σ_o, it is necessary to compute the likelihood with a maximum likelihood of m given σ_o, and for the case of the confidence limit on m, it is necessary to compute the likelihood with a maximum likelihood of σ_o given m. Hence the equations needed are derived from Equation [VI-16] for m and from Equation [VI-19] for σ_o, yielding Equations [VI-48] and [VI-49].

$$\frac{1}{\hat{m}_{\sigma_o}} = \frac{1}{n}\left\{\sum \frac{I_i'}{I_i}\left(I_i V_i \left(\frac{\sigma_i}{\sigma_o}\right)^m - 1\right) + \sigma_o^{-m}\sum I_i V_i \sigma_i^m \ln\left(\frac{\sigma_i}{\sigma_o}\right)\right\} - \frac{1}{n}\sum \ln(\sigma_i) + \ln(\sigma_o) \qquad \text{[VI-48]}$$

$$\hat{\sigma}_{om} = \left[\tfrac{1}{n}\sum I_i V_i \sigma_i^m\right]^{\frac{1}{m}} \qquad \text{[VI-49]}$$

To compute the confidence limits of the parameters we must proceed to solve Equations [VI-50] and [VI-52]:

$$m : W(m) \le \chi^2_{1,\alpha} \qquad \text{[VI-50]}$$

where:

$$W(m) = 2\left[l(\hat{m}, \hat{\sigma}_o) - l(m, \hat{\sigma}_{om})\right] \qquad \text{[VI-51]}$$

$$\sigma_o : W(\sigma_o) \le \chi^2_{1,\alpha} \qquad \text{[VI-52]}$$

where:

$$W(\sigma_o) = 2\left[l(\hat{m}, \hat{\sigma}_o) - l(\hat{m}_{\sigma_o}, \sigma_o)\right] \qquad \text{[VI-53]}$$

4.3.2.2 Confidence Limits For The Design Stress Level

In order to calculate the design stress level for a given reliability and confidence level and for a given specimen size and stress state, we use the transformation in Equation [VI-54] with Equation [VI-19] to obtain

[VI-55], and by using the procedure described in Section 3.2.1, we derive equation [VI-56] by substituting [VI-54] into [VI-15] and differentiating:

$$\sigma_o = \sigma_p \left[\frac{1}{I_c V_c} \ln\left(\frac{1}{1-p}\right) \right]^{-\frac{1}{m}} \qquad \text{[VI-54]}$$

$$\hat{\sigma}_p = \left[\frac{1}{n I_c V_c} \ln\left(\frac{1}{1-p}\right) \sum I_i V_i \sigma_i^m \right]^{\frac{1}{m}} \qquad \text{[VI-55]}$$

$$\frac{1}{\hat{m}_{\sigma_p}} = \frac{1}{n} \sum \frac{I_i'}{I_i} \left[\frac{I_i V_i}{I_c V_c} \ln\left(\frac{1}{1-p}\right) \left(\frac{\sigma_i}{\sigma_p}\right)^m - 1 \right] + \frac{1}{n} \sum \frac{I_c'}{I_c} \left[1 + \frac{I_i V_i}{I_c V_c} \ln\left(\frac{1}{1-p}\right) \left(\frac{\sigma_i}{\sigma_p}\right)^m \right]$$
$$+ \frac{1}{n} \sum \frac{I_i V_i}{I_c V_c} \left(\frac{\sigma_i}{\sigma_p}\right)^m \ln\left(\frac{1}{1-p}\right) \ln\left(\frac{\sigma_i}{\sigma_p}\right) - \frac{1}{n} \sum \ln(\sigma_i) + \ln(\sigma_p) \qquad \text{[VI-56]}$$

The confidence limits are obtained by solving Equation [VI-57].

$$\sigma_p : W(\sigma_p) \le \chi^2_{1,\alpha} \qquad \text{[VI-57]}$$

where:

$$W(\sigma_p) = 2\left[l(\hat{m}, \hat{\sigma}_p) - l(\hat{m}_{\sigma_p}, \sigma_p) \right] \qquad \text{[VI-58]}$$

4.3.2.3 Confidence Limits For The Reliability, *R*

To calculate the confidence interval on the reliability, we use the change of variables in Equation [VI-59]. And given that the reliability of a component with a stress level Z, a volume V_c and a multiaxial and stress gradient factor I_c is given by [VI-60]:

$$\gamma = -\ln[R(Z)] \qquad \text{[VI-59]}$$

$$R(Z) = \exp - \left[I_c V_c \left(\frac{Z}{\sigma_o}\right)^m \right] \qquad \text{[VI-60]}$$

Equation [VI-60] becomes [VI-61], which after substituting in [VI-7] becomes [VI-62], and by applying the same process as in Section 3.2.1, we obtain Equations [VI-63] to [VI-72].

$$\sigma_o^m = \frac{I_c V_c Z^m}{\gamma} \quad \text{[VI-61]}$$

$$f(\sigma_i) = m\frac{I_i V_i}{I_c V_c Z}\gamma\left(\frac{\sigma_i}{Z}\right)^{m-1} \exp-\left\{\frac{I_i V_i}{I_c V_c}\gamma\left(\frac{\sigma_i}{Z}\right)^m\right\} \quad \text{[VI-62]}$$

$$l = \sum \ln\left[f(\sigma_i)\right] \quad \text{[VI-63]}$$

$$\sum \ln f(\sigma_i) = \sum \ln\left(m\frac{I_i V_i}{I_c V_c Z}\gamma\left(\frac{\sigma_i}{Z}\right)^{m-1} \exp-\left\{\frac{I_i V_i}{I_c V_c}\gamma\left(\frac{\sigma_i}{Z}\right)^m\right\}\right) \quad \text{[VI-64]}$$

$$\frac{\partial l}{\partial \gamma} = \sum \frac{1}{\gamma} - \sum \frac{I_i V_i}{I_c V_c}\left(\frac{\sigma_i}{Z}\right)^m \quad \text{[VI-65]}$$

$$0 = \frac{n}{\gamma} - \sum \frac{I_i V_i}{I_c V_c}\left(\frac{\sigma_i}{Z}\right)^m \quad \text{[VI-66]}$$

$$\frac{1}{\gamma} = \frac{1}{n}\sum \frac{I_i V_i}{I_c V_c}\left(\frac{\sigma_i}{Z}\right)^m \quad \text{[VI-67]}$$

$$\frac{1}{\gamma} = \frac{1}{n I_c V_c Z^m}\sum I_i V_i \sigma_i^m \quad \text{[VI-68]}$$

Now for the case of the Weibull slope:

$$\frac{\partial l}{\partial m} = \sum \frac{1}{m} + \sum \frac{I_i'}{I_i} - \sum \frac{I_c'}{I_c} + \sum \ln\left(\frac{\sigma_i}{Z}\right) - \sum \gamma \frac{V_i}{V_c}\frac{I_i' I_c\left(\frac{\sigma_i}{Z}\right)^m - I_i I_c'\left(\frac{\sigma_i}{Z}\right)^m + I_i I_c\left(\frac{\sigma_i}{Z}\right)^m \ln\left(\frac{\sigma_i}{Z}\right)}{I_c^2} \quad \text{[VI-69]}$$

$$0=\frac{n}{m}+\sum\left(\frac{I_i'}{I_i}-\frac{I_c'}{I_c}\right)+\sum\ln\left(\frac{\sigma_i}{Z}\right)-\sum\gamma\frac{V_i}{V_c}\frac{I_i'}{I_c}\left(\frac{\sigma_i}{Z}\right)^m$$
$$+\sum\gamma\frac{V_i}{V_c}\frac{I_i}{I_c}\frac{I_c'}{I_c}\left(\frac{\sigma_i}{Z}\right)^m-\sum\gamma\frac{V_i}{V_c}\frac{I_i}{I_c}\left(\frac{\sigma_i}{Z}\right)^m\ln\left(\frac{\sigma_i}{Z}\right) \quad \text{[VI-70]}$$

$$\frac{1}{m_\gamma}=\frac{1}{n}\sum\frac{I_i'}{I_i}\left[\gamma\frac{V_i}{V_c}\frac{I_i}{I_c}\left(\frac{\sigma_i}{Z}\right)^m-1\right]+\frac{1}{n}\sum\frac{I_c'}{I_c}\left[1-\gamma\frac{V_i}{V_c}\frac{I_i}{I_c}\left(\frac{\sigma_i}{Z}\right)^m\right]$$
$$+\sum\gamma\frac{V_i}{V_c}\frac{I_i}{I_c}\left(\frac{\sigma_i}{Z}\right)^m\ln\left(\frac{\sigma_i}{Z}\right)-\frac{1}{n}\sum\ln(\sigma_i)+\ln(Z) \quad \text{[VI-71]}$$

The confidence limits are obtained by solving Equation [VI-72]:

$$\gamma: W(\gamma)\le\chi^2_{1,\alpha} \quad \text{[VI-72]}$$

where:

$$W(\gamma)=2\left[l(\hat{m},\hat{\gamma})-l(\hat{m}_\gamma,\gamma)\right] \quad \text{[VI-73]}$$

4.4 Confidence Limit Calculation For Censored Data

4.4.1 Confidence Limits By The Bootstrap Approach

This section describes the Bootstrap method to define the confidence interval for censored data given that the censored data belongs to additional failure modes. The approach is described for two failure modes, but from this description it can easily be extended to any number of concurrent failure modes. This approach does not apply for a single failure mode with censored data, because one does not know what specimen to assign the censoring to. Approaches will be investigated later on in the program to determine if the Bootstrap method is possible for a single failure mode.

4.4.1.1 Confidence Limits For The First And Second Weibull Parameters

As in Section 4.3.1, a reevaluation of the data is performed to determine the confidence intervals of the Weibull parameters for as many failure modes as there are present. The methods are again better described in a step-by-step basis.

(a) The first step consists of estimating the Weibull parameters using the Maximum Likelihood method. The estimates are computed from Equations [VI-32] and [VI-37], derived in Section 3.2.1. Equations [VI-32] and [VI-37] are presented here for convenience:

$$\hat{\sigma}_o = \left[\frac{1}{r}\sum_{k=1}^{n} I_k V_k \sigma_k^{\hat{m}}\right]^{1/\hat{m}} \qquad \text{[VI-32]}$$

$$\frac{1}{\hat{m}} = \frac{1}{\sum_{k=1}^{n} I_k V_k \sigma_k^m}\sum_{k=1}^{n} V_k \sigma_k^m \left[I_k' + I_k \ln(\sigma_k)\right] - \frac{1}{r}\sum_{i=1}^{r}\left[\frac{I_i'}{I_i} + \ln(\sigma_i)\right] \qquad \text{[VI-37]}$$

From these equations, calculate the Weibull parameters for all of the failure modes found in the data.

(b) Second, choose a random number between zero and one, and pick this number to be a reliability value, R, and assign this reliability to failure mode 1.

(c) Third, select a specimen type from the original data set, with its corresponding V_i and I_i . Using the above $\hat{m}$ and $\hat{\sigma}_o$, compute the fracture strength of this pseudo specimen, using Equation [VI-74], given that it has the reliability equivalent to the value of the random number obtained above.

$$\sigma_i = \hat{\sigma}_o\left(-\frac{\ell n(R_i)}{\hat{I}_i V_i}\right)^{1/\hat{m}} \qquad \text{[VI-74]}$$

(d) Repeat steps (b) and (c), this time for failure mode 2. Keep the specimen type and size used for failure mode 1 and calculate σ_i for failure mode 2.

(e) Compare the value of σ_i for failure modes 1 and 2. If σ_i for failure mode 1 is smaller than σ_i for failure mode 2, then this will represent a failure for this failure mode; if not, the σ_i for failure mode 2 will represent a censored specimen for failure mode 1.

(f) Repeat steps (a) through (e) for each specimen type and size a number of times equal to the number of specimens in the individual data set.

(g) Calculate the Weibull parameters for this newly generated data set using Equations [VI-75] and [VI-76] and save these values. Calculate $\tilde{m}$ and $\tilde{\sigma}_o$ for the second failure mode at the same time.

$$\tilde{\sigma}_o = \left[\frac{1}{r}\sum_{k=1}^{n} I_k V_k \sigma_k^{\tilde{m}}\right]^{1/\tilde{m}} \qquad \text{[VI-75]}$$

$$\frac{1}{\tilde{m}} = \frac{1}{\sum_{k=1}^{n} I_k V_k \sigma_k^m}\sum_{k=1}^{n} V_k \sigma_k^m \left[I_k' + I_k \ln(\sigma_k)\right] - \frac{1}{r}\sum_{i=1}^{r}\left[\frac{I_i'}{I_i} + \ln(\sigma_i)\right] \qquad \text{[VI-76]}$$

(h) Repeat steps (b) through (g) a number of 1000 times.

(i) Sort the $\tilde{m}$ and $\tilde{\sigma}_o$ pair in ascending order for $\tilde{m}$ without losing the pair and also for $\tilde{\sigma}_o$ without losing the pair, for both failure modes.

(j) To calculate the x confidence interval, pick the (100-x) (1000/2)(1/100) points from the upper and lower ends; these define the limits. For example, if the 95 percent confidence interval is desired, substitute the 95 for x to obtain 5, then multiply by the adjoining factor to get 25. Hence the 95 percent confidence interval is given by the 25th point from the lowest and the 25th point from the top.

4.4.1.2 Confidence Limits For The Design Stress Level

(a) The design stress level can be obtained from the Weibull parameters calculated in Equations [VI-75] and [VI-76] by using Equation [VI-78], where p is the desired probability of failure, V is the component volume and $\tilde{I}$ belongs to the component.

$$R(\sigma_p) = \exp -\left[\tilde{I}_1 V_1 \left(\frac{\sigma_p}{\tilde{\sigma}_{o1}}\right)^{\tilde{m}_1} + \tilde{I}_2 V_2 \left(\frac{\sigma_p}{\tilde{\sigma}_{o2}}\right)^{\tilde{m}_2}\right] \qquad \text{[VI-77]}$$

(b) Equation [VI-77] has to be solved iteratively for σ_p for the given reliability and two sets of Weibull parameters.

(c) Given that we have the sets of $\tilde{m}$ and $\tilde{\sigma}_o$ from Section 4.4.1.1, compute σ_p from [VI-75] for each one of these values and save them.

(d) Sort the σ_p and obtain the x confidence interval by picking the (100-x) 10/2 points from the upper and lower ends, using the same approach as in 4.4.1.1 (j).

4.4.1.3

(a) Similarly to σ_p, the reliability, R, has a functional relationship to σ_o, given by Equation [VI-78], where Z is the maximum stress level of the component, and $\tilde{I}$ and V are the component multiaxial and stress gradient factor and volume, respectively.

$$R(Z) = \exp-\left[\tilde{I}_1 V_1 \left(\frac{Z}{\tilde{\sigma}_{o1}}\right)^{\tilde{m}_1} + \tilde{I}_2 V_2 \left(\frac{Z}{\tilde{\sigma}_{o2}}\right)^{\tilde{m}_2}\right] \qquad \text{[VI-78]}$$

(b) Given that we have $\tilde{m}$ and $\tilde{\sigma}_o$ from Section 4.4.1.1 and for both failure modes, we can substitute these values into [VI-78] to find a list of R's.

(c) Sort the R's and obtain the x confidence interval by picking the (100-x) 10/2 points from the upper and lower ends, using the same approach as in 4.4.1.1 (j).

4.4.2 Confidence Limits By The Likelihood Ratio Approach

4.4.2.1 Confidence Limits For The First And Second Weibull Parameter

As shown by Equation [VI-41] one must calculate a variety of log likelihoods to calculate the confidence intervals on the Weibull parameters. For the case of the confidence limits on σ_o, it is necessary to compute the likelihood with a maximum likelihood of m given σ_o and for the case of the confidence limit on m, it is necessary to compute the likelihood with a maximum likelihood of σ_o given m. Hence the equations needed are derived from Equation [VI-29] for m and from Equation [VI-32] for σ_o, yielding equations [VI-79] and [VI-80]:

$$\hat{\sigma}_{om} = \left[\frac{1}{r}\Sigma I_k V_k \sigma_k^m\right]^{1/m} \qquad \text{[VI-79]}$$

$$\frac{1}{\hat{m}_{\sigma_o}} = \frac{1}{r}\left\{\sum_{k=1}^{n}\left[I_k' V_k\left(\frac{\sigma_k}{\sigma_o}\right)^{\hat{m}_{\sigma_o}} + I_k V_k\left(\frac{\sigma_k}{\sigma_o}\right)^{\hat{m}_{\sigma_o}} \ln\left(\frac{\sigma_k}{\sigma_o}\right)\right]\right\} + \ln(\sigma_o) - \frac{1}{r}\left\{\sum_{i=1}^{r}\left[\frac{I_i'}{I_i} + \ln(\sigma_i)\right]\right\} \qquad \text{[VI-80]}$$

To compute the confidence limits of the parameters we must proceed to solve Equations [VI-81] and [VI-83]:

$$m : W(m) \le \chi^2_{1,\alpha} \qquad \text{[VI-81]}$$

where:

$$W(m) = 2\left[l(\hat{m}, \hat{\sigma}_o) - l(m, \hat{\sigma}_{om})\right] \qquad \text{[VI-82]}$$

$$\sigma_o : W(\sigma_o) \le \chi^2_{1,\alpha} \qquad \text{[VI-83]}$$

where:

$$W(\sigma_o) = 2\left[l(\hat{m}, \hat{\sigma}_o) - l(\hat{m}_{\sigma_o}, \sigma_o)\right] \qquad \text{[VI-84]}$$

4.4.2.2 Confidence Limits For The Design Stress Level

In order to calculate the design stress level for a given reliability and confidence level and for a given specimen size and stress state, we use the transformation in Equation [VI-85] with Equation [VI-32] to obtain [VI-86], and by using the procedure described in Section 3.2.1, we derive Equation [VI-90] by substituting [VI-85] into [VI-29] and differentiating as shown by Equations [VI-87] through [VI-89].

$$\sigma_o = \sigma_p\left[\frac{1}{I_c V_c}\ln\left(\frac{1}{1-p}\right)\right]^{\frac{1}{m}} \qquad \text{[VI-85]}$$

$$\hat{\sigma}_p = \left[\frac{1}{r I_c V_c}\ln\left(\frac{1}{1-p}\right)\sum_{k=1}^{n} I_k V_k \sigma_k^{\hat{m}}\right]^{\frac{1}{\hat{m}}} \qquad \text{[VI-86]}$$

$$l = \sum_{i=1}^{r}\ln\left[f(\sigma_i)\right] + \sum_{j=r+1}^{n}\ln\left[P_s(\sigma_j)\right] \qquad \text{[VI-87]}$$

$$l=\sum_{i=1}^{r}\ln\left[m\frac{I_iV_i}{I_cV_c}\sigma_p^{-1}\left(\frac{\sigma_i}{\sigma_p}\right)^{m-1}\ln\left(\frac{1}{1-p}\right)\right]-\sum_{i=1}^{r}\left[\frac{I_iV_i}{I_cV_c}\left(\frac{\sigma_i}{\sigma_p}\right)^{m}\ln\left(\frac{1}{1-p}\right)\right]$$
$$-\sum_{j=r+1}^{n}\left[\frac{I_jV_j}{I_cV_c}\left(\frac{\sigma_j}{\sigma_p}\right)^{m}\ln\left(\frac{1}{1-p}\right)\right] \quad \text{[VI-88]}$$

$$l=\sum_{i=1}^{r}\ln\left[m\frac{I_iV_i}{I_cV_c}\sigma_p^{-1}\left(\frac{\sigma_i}{\sigma_p}\right)^{m-1}\ln\left(\frac{1}{1-p}\right)\right]-\sum_{k=1}^{n}\left[\frac{I_kV_k}{I_cV_c}\left(\frac{\sigma_k}{\sigma_p}\right)^{m}\ln\left(\frac{1}{1-p}\right)\right] \quad \text{[VI-89]}$$

$$\frac{1}{\hat{m}_{\sigma_p}}=\frac{1}{r}\sum_{i=1}^{r}\left[\frac{I_c'}{I_c}-\frac{I_i'}{I_i}\right]-\frac{1}{r}\sum_{i=1}^{r}\ln(\sigma_i)+\ln(\sigma_p)$$
$$+\frac{1}{r}\sum_{k=1}^{n}\left\{\ln\left(\frac{1}{1-p}\right)\frac{V_k}{V_c}\left(\frac{\sigma_k}{\sigma_p}\right)^{m}\left[\frac{I_k'}{I_c}-\frac{I_k}{I_c}\frac{I_c'}{I_c}+\frac{I_k}{I_c}\ln\left(\frac{\sigma_k}{\sigma_p}\right)\right]\right\} \quad \text{[VI-90]}$$

The confidence limits are obtained by applying solving Equation [VI-91]:

$$\sigma_p : W(\sigma_p)\le\chi^2_{1,\alpha} \quad \text{[VI-91]}$$

where:
$$W(m)=2\left[l(\hat{m},\hat{\sigma}_p)-l(m,\hat{\sigma}_{pm})\right] \quad \text{[VI-92]}$$

4.4.2.3 Confidence Limits For The Reliability, *R*

To calculate the confidence interval on the reliability, we use the change of variables in [VI-93]. And given that the reliability of a component with a stress level Z, a volume V_c and a multiaxial and stress gradient factor I_c is given by [VI-94]:

$$\gamma=-\ln[R(Z)] \quad \text{[VI-93]}$$

$$R(Z)=\exp-\left[I_cV_c\left(\frac{Z}{\sigma_o}\right)^{m}\right] \quad \text{[VI-94]}$$

Equation [VI-94] becomes [VI-94], which after substituting into [VI-3] becomes [VI-96] and into [VI-7] becomes [VI-97]. After substituting Equations [VI-96] and [VI-97] into the log likelihood function, Equation [VI-98], and applying the same process described in Section 3.2.1, yields Equations [VI-99] to [VI-107].

$$\sigma_o^m = \frac{I_c V_c Z^m}{\gamma} \qquad \text{[VI-95]}$$

$$P_s(\sigma_k) = \exp - \left\{ \frac{V_k I_k}{V_c I_c} \gamma \left(\frac{\sigma_k}{Z} \right)^m \right\} \qquad \text{[VI-96]}$$

$$f(\sigma_i) = m \frac{I_i V_i}{I_c V_c Z} \gamma \left(\frac{\sigma_i}{Z} \right)^{m-1} \exp - \left\{ \frac{I_i V_i}{I_c V_c} \gamma \left(\frac{\sigma_i}{Z} \right)^m \right\} \qquad \text{[VI-97]}$$

$$l = \sum_{i=1}^{r} \ln \left[f(\sigma_i) \right] + \sum_{j=r+1}^{n} \ln \left[P_s(\sigma_j) \right] \qquad \text{[VI-98]}$$

$$l = \sum_{i=1}^{r} \ln \left[m \frac{I_i V_i}{I_c V_c Z} \gamma \left(\frac{\sigma_i}{Z} \right)^{m-1} \exp - \left\{ \frac{I_i V_i}{I_c V_c} \gamma \left(\frac{\sigma_i}{Z} \right)^m \right\} \right] + \sum_{j=r+1}^{n} \ln \left[\exp - \left\{ \frac{V_j I_j}{V_c I_c} \gamma \left(\frac{\sigma_j}{Z} \right)^m \right\} \right] \qquad \text{[VI-99]}$$

$$l = r \left[\ln(m) + \ln(\gamma) - \ln(I_c) - \ln(V_c) - m \ln(Z) \right] + \sum_{i=1}^{r} \ln(I_i) + \sum_{i=1}^{r} \ln(V_i) + (m-1) \sum_{i=1}^{r} \ln(\sigma_i) - \sum_{k=1}^{n} \frac{V_k I_k}{V_c I_c} \gamma \left(\frac{\sigma_k}{Z} \right)^m \qquad \text{[VI-100]}$$

The maximization of [VI-99] with respect to γ and m yields:

$$\frac{\partial l}{\partial \gamma} = \sum_{i=1}^{r} \frac{1}{\gamma} - \sum_{k=1}^{n} \frac{I_k V_k}{I_c V_c} \left(\frac{\sigma_k}{Z} \right)^m \qquad \text{[VI-101]}$$

$$0 = \frac{r}{\gamma} - \sum_{k=1}^{n} \frac{I_k V_k}{I_c V_c} \left(\frac{\sigma_k}{Z} \right)^m \qquad \text{[VI-102]}$$

$$\frac{1}{\gamma} = \frac{1}{r} \sum_{k=1}^{n} \frac{I_k V_k}{I_c V_c} \left(\frac{\sigma_k}{Z} \right)^m \qquad \text{[VI-103]}$$

$$\frac{1}{\hat{\gamma}} = \frac{1}{r I_c V_c Z^{\hat{m}}} \sum_{k=1}^{n} I_k V_k \sigma_k^{\hat{m}} \qquad \text{[VI-104]}$$

Now for the case of the Weibull slope:

$$\frac{\partial l}{\partial m} = \sum_{i=1}^{r} \frac{1}{m} + \sum_{i=1}^{r} \frac{I_i'}{I_i} - \sum_{i=1}^{r} \frac{I_c'}{I_c} + \sum_{i=1}^{r} \ln\left(\frac{\sigma_i}{Z} \right) - \sum_{k=1}^{n} \gamma \frac{V_i}{V_c} \frac{I_i' I_c \left(\frac{\sigma_i}{Z} \right)^m - I_i I_c' \left(\frac{\sigma_i}{Z} \right)^m + I_i I_c \left(\frac{\sigma_i}{Z} \right)^m \ln\left(\frac{\sigma_i}{Z} \right)}{I_c^2} \qquad \text{[VI-105]}$$

$$\begin{aligned} 0 = {} & \frac{r}{m} + \sum_{i=1}^{r} \left(\frac{I_i'}{I_i} - \frac{I_c'}{I_c} \right) + \sum_{i=1}^{r} \ln\left(\frac{\sigma_i}{Z} \right) - \sum_{k=1}^{n} \gamma \frac{V_k}{V_c} \frac{I_k'}{I_c} \left(\frac{\sigma_k}{Z} \right)^m \\ & + \sum_{k=1}^{n} \gamma \frac{V_k}{V_c} \frac{I_k}{I_c} \frac{I_c'}{I_c} \left(\frac{\sigma_k}{Z} \right)^m - \sum_{k=1}^{n} \gamma \frac{V_k}{V_c} \frac{I_k}{I_c} \left(\frac{\sigma_k}{Z} \right)^m \ln\left(\frac{\sigma_k}{Z} \right) \end{aligned} \qquad \text{[VI-106]}$$

$$\begin{aligned} \frac{1}{\hat{m}_\gamma} = {} & \frac{1}{r} \sum_{i=1}^{r} \left(\frac{I_c'}{I_c} - \frac{I_i'}{I_i} \right) - \frac{1}{r} \sum_{i=1}^{r} \ln(\sigma_i) + \ln(Z) \\ & + \frac{1}{r} \sum_{k=1}^{n} \gamma \frac{V_k}{V_c} \left(\frac{\sigma_k}{Z} \right)^{\hat{m}_\gamma} \left[\frac{I_k'}{I_c} - \frac{I_k}{I_c} \frac{I_c'}{I_c} + \frac{I_k}{I_c} \ln\left(\frac{\sigma_k}{Z} \right) \right] \end{aligned} \qquad \text{[VI-107]}$$

The above yields the needed equations for the calculation of the confidence limits on γ. The confidence limits are obtained by solving Equation [VI-108] .

$$\gamma : W(\gamma) \le \chi^2_{1,\alpha} \qquad \text{[VI-108]}$$

$$W(\gamma) = 2\left[l(\hat{m}, \hat{\gamma}) - l(\hat{m}_\gamma, \gamma) \right] \qquad \text{[VI-109]}$$

5.0 BIAS CORRECTION FOR PARAMETER ESTIMATES

Bias is the systematic error or deviation of the expected value of a statistical estimate from the quantity it estimates. The amount of the bias depends on the efficiency of the estimators. The estimator used in this work is the maximum likelihood estimate procedure. These estimators have been proven (ref 6) to have less bias when compared to estimators such as the least squares method. The following section presents bias correction procedures using bootstrap methods for the Weibull parameters, reliability and design stress levels. A likelihood approach is under development, but such approach is not ready yet, and depending on the success of the formulation, it will be reported in the future.

The Bootstrap method consists of gathering information about estimates of variability and uncertainty by evaluating the observed data set. Uncertainties on the estimates can arise from testing a finite number of specimens and from inefficiencies of the estimators. Bootstrap techniques can be parametric and non-parametric. The parametric technique uses the estimates for the assumed distribution to generate a new data set; this data set then produces new estimates for the distribution parameters of the experimental data. The non-parametric technique generates a new data set from the original data set, allowing for replacements. In both methods, the number of specimens used is equal to the number of specimens in the original data set. The parametric approach is the only approach used in this document.

The bootstrap evaluations used to compute confidence limits of m and σ_o contain information about the amount of bias present in $\hat{m}$ and $\hat{\sigma}_o$. The information stems from the fact that the bootstrapped values $\tilde{m}$ and $\tilde{\sigma}_o$ were generated with the known $\hat{m}$ and $\hat{\sigma}_o$. And if the median values of $\tilde{m}$ and $\tilde{\sigma}_o$ do not coincide with the $\hat{m}$ and $\hat{\sigma}_o$, these values provide a measure of the bias produced by the estimator. This bias can be measured by using invariants of the distribution. For the case of the Weibull modulus, the ratio of the estimated m to the true m is an invariant, as shown in Equation [VI-110]. This implies that Equation [VI-111] is also true.

$$C_P = \frac{\hat{m}}{m_{U,P}} \qquad \text{[VI-110]}$$

$$C_P = \frac{\tilde{m}_{B,P}}{\hat{m}} \qquad \text{[VI-111]}$$

Equation [VI-112] shows the invariant of the Weibull characteristic strength.

$$D_P = \hat{m} \ln\left(\frac{\hat{\sigma}_o}{\sigma_o}\right) \quad \text{[VI-112]}$$

From Equation [VI-112] it follows that Equation [VI-113] must also hold.

$$D_P = \tilde{m}_{B,P} \ln\left(\frac{\tilde{\sigma}_{o\,B,P}}{\hat{\sigma}_o}\right) \quad \text{[VI-113]}$$

5.1 Bias Correction For The Weibull Parameters

5.1.1 Bias Correction By The Bootstrap Approach

(a) One must start by performing the bootstrap reevaluations of the data.

(b) Perform the bootstrap simulation 1000 times, or as many as required to produce accurate estimates of the values corresponding to the desired probability. We are currently using 99 for savings in computation time.

(c) To perform the bias correction on the Weibull slope select the median, $\tilde{m}_{B,50}$, value of the estimated values from the bootstrap simulation and use it in Equation [VI-114], derived from equating Equations [VI-110] and [VI-111].

$$m_{U,50} = \hat{m}\left(\frac{\hat{m}}{\tilde{m}_{B,50}}\right) \quad \text{[VI-114]}$$

where:

$\hat{m}$ = the estimated m from the original data set

$m_{U,50}$ = the true median m

$\tilde{m}_{B,50}$ = the median bootstrapped m

(d) To perform the bias correction on the second Weibull parameter, σ_o, select the median $\tilde{m}_{B,50}$ value and the median $\tilde{\sigma}_{o\,B,P}$ value from the bootstrap simulation and use them in Equation [VI-115] that was derived from equating Equations [VI-112] and [VI-113].

$$\sigma_{oU,50} = \hat{\sigma}_o \left(\frac{\hat{\sigma}_o}{\tilde{\sigma}_{oB,50}} \right)^{\frac{\tilde{m}_{B,50}}{\hat{m}}} \qquad \text{[VI-115]}$$

5.1.2 Bias Correction By The Likelihood Method

This work is in progress and will be published when completed.

5.2 Bias Correction For The Design Stress Level

5.2.1 Bias Correction By The Bootstrap Approach

Calculate σ_{pU} using the unbiased Weibull parameters calculated above into the following equation:

$$\sigma_{pU} = \sigma_{oU,50} \left[\frac{1}{I_U V} \ln \left(\frac{1}{1-p} \right) \right]^{1/m_{U,50}} \qquad \text{[VI-116]}$$

where I_U is calculated using the unbiased estimates. This, σ_{pU}, is the unbiased prediction for the design stress level.

5.2.2 Bias Correction By The Likelihood Ratio Approach

This work is in progress and will be published when completed.

5.3 Bias Correction For The Reliability

5.3.1 Bias Correction By The Bootstrap Approach

Calculate the unbiased reliability by using the unbiased estimators in Equation [VI-117]:

$$R(Z) = \exp - \left[I_U V \left(\frac{Z}{\sigma_{oU,50}} \right)^{m_{U,50}} \right] \qquad \text{[VI-117]}$$

5.3.2 Bias Correction By The Likelihood Ratio Approach

This work is in progress and will be published when completed.

5.4 Bias Correction For The Confidence Limits

5.4.1 Bias Correction By The Bootstrap Approach

Confidence limit bias corrections can be performed using Equations [VI-114] and [VI-115] in which the value of the probability is changed from 50 to the desired confidence level, for example:

$$m_{U,99} = \hat{m}\left(\frac{\hat{m}}{\tilde{m}_{B,99}}\right) \qquad \text{[VI-118]}$$

$$\sigma_{oU,99} = \hat{\sigma}_o\left(\frac{\hat{\sigma}_o}{\tilde{\sigma}_{oB,99}}\right)^{\frac{\tilde{m}_{B,99}}{\hat{m}}} \qquad \text{[VI-119]}$$

Equations [VI-118] and [VI-119] provide the unbiased confidence limits for the Weibull parameters.

The unbiased confidence limits for the design stress level and the reliability are in the development process, they will be reported on when completed.

5.4.2 Bias Correction By The Likelihood Approach

This method is under development and will be reported on later.

6.0 PROGRAMMING LOGIC

The following is a description of the steps and the equations to use in the calculation of the variables and confidence limits described in the previous sections. The equations will be referred to by their equation number in the previous sections, but with the appropriate change of variables. Described are the Maximum Likelihood method, the Likelihood Ratio method and the Bootstrap method.

6.1 Maximum Likelihood Method Estimates of the Weibull Parameters

(a) Calculate the MLE (maximum likelihood estimate) of m by using Equation [VI-24] and solving for m using an iterative scheme.

$$\frac{1}{\hat{m}} = \frac{1}{n}\sum\left(\frac{I_i'}{I_i} + \ln(\sigma_i)\right)\left(\frac{nI_iV_i\sigma_i^m}{\sum I_iV_i\sigma_i^m} - 1\right) \qquad \text{[VI-24]}$$

(b) Calculate the MLE of σ_o by using [VI-19] and the MLE of m obtained from the solution of [VI-24]:

$$\hat{\sigma}_o = \left[\frac{1}{n}\sum I_iV_i\sigma_i^{\hat{m}}\right]^{1/\hat{m}} \qquad \text{[VI-19]}$$

6.2 Likelihood Ratio Method

The logic is presented for uncensored data analysis; for censored data analysis or multimodal failure, interchange the equations with the equations for the multimodal analysis presented in section 4.4.

6.2.1 Confidence Limits for the First Weibull Parameter

(a) Compute the log likelihood of the Weibull probability density function (PDF) with the MLE of m and σ_o using [VI-7] and [VI-10]:

$$f(\sigma_i) = mV_iI_i\sigma_O^{-1}\left(\frac{\sigma_i}{\sigma_o}\right)^{m-1}\exp-\left\{V_iI_i\left(\frac{\sigma_i}{\sigma_o}\right)^m\right\} \qquad \text{[VI-7]}$$

$$l = \sum \ln\left[f(\sigma_i)\right] \qquad \text{[VI-10]}$$

(b) Compute the MLE of σ_o given m using [VI-19]:

$$\hat{\sigma}_o = \left[\frac{1}{n}\sum I_i V_i \sigma_i^{\hat{m}}\right]^{1/\hat{m}} \qquad \text{[VI-19]}$$

(c) Compute the log likelihood of the Weibull PDF with the chosen m and respective MLE of σ_o with [VI-7] and [VI-10] above.

(d) Iteratively solve for the solution of [VI-50] subject to [VI-51]; this equation has two solutions: the upper and lower confidence limits. The solution gives the limits of m:

$$m : W(m) \le \chi^2_{1,\alpha} \qquad \text{[VI-50]}$$

$$W(m) = 2\left[l(\hat{m}, \hat{\sigma}_o) - l(m, \hat{\sigma}_{om})\right] \qquad \text{[VI-51]}$$

6.2.2 Confidence Limits On σ_o, The Weibull Characteristic Strength

(a) Repeat step 6.2.1(a)

(b) Compute the MLE of m given σ_o using [VI-48]:

$$\frac{1}{\hat{m}_{\sigma_o}} = \frac{1}{n}\left\{\sum \frac{I_i'}{I_i}\left(I_i V_i \left(\frac{\sigma_i}{\sigma_o}\right)^m - 1\right) + \sigma_o^{-m}\sum I_i V_i \sigma_i^m \ln\left(\frac{\sigma_i}{\sigma_o}\right)\right\} - \frac{1}{n}\sum \ln(\sigma_i) + \ln(\sigma_o) \qquad \text{[VI-48]}$$

(c) Compute the log likelihood of the Weibull PDF with the chosen σ_o and respective MLE of m using [VI-7] and [VI-10] from 6.2.1(a)

(d) Iteratively solve for the solution of [VI-52] subject to [VI-53]; this equation has two solutions: the upper and lower confidence limits. The solution gives the limits of σ_o:

$$\sigma_o : W(\sigma_o) \le \chi^2_{1,\alpha} \qquad \text{[VI-52]}$$

$$W(\sigma_o) = 2\left[l(\hat{m},\hat{\sigma}_o) - l(\hat{m}_{\sigma_o},\sigma_o)\right] \quad \text{[VI-53]}$$

6.2.3 Confidence Limits On σ_p, The Design Stress Level

It is often the case that there is a need to design a component to a desired reliability and confidence level. This section addresses this case, and computes the maximum stress level which will satisfy the requirements.

(a) Use Equation [VI-54] and substitute it for σ_o in [VI-7] and obtain [VI-41]:

$$\sigma_o = \sigma_p\left[\frac{1}{I_c V_c}\ln\left(\frac{1}{1-p}\right)\right]^{-\frac{1}{m}} \quad \text{[VI-54]}$$

$$f(\sigma_i) = m\frac{I_i V_i}{I_c V_c}\sigma_p^{-1}\ln\left(\frac{1}{1-p}\right)\left(\frac{\sigma_i}{\sigma_p}\right)^{m-1}\exp-\left\{\frac{I_i V_i}{I_c V_c}\ln\left(\frac{1}{1-p}\right)\left(\frac{\sigma_i}{\sigma_p}\right)^{m}\right\} \quad \text{[VI-120]}$$

(b) Using [VI-120], compute the log likelihood, Equation [VI-10], of the Weibull PDF using m and σ_p where m is the MLE from [VI-24] and σ_p is obtained from [VI-54] or [VI-55] where σ_o is obtained from [VI-19].

$$l = \sum \ln\left[f(\sigma_i)\right] \quad \text{[VI-10]}$$

$$\hat{\sigma}_o = \left[\frac{1}{n}\sum I_i V_i \sigma_i^{\hat{m}}\right]^{1/\hat{m}} \quad \text{[VI-19]}$$

$$\hat{\sigma}_p = \left[\frac{1}{nI_c V_c}\ln\left(\frac{1}{1-p}\right)\sum I_i V_i \sigma_i^{m}\right]^{\frac{1}{m}} \quad \text{[VI-55]}$$

(c) Calculate the MLE of m given σ_p using Equation [VI-56]:

$$\frac{1}{\hat{m}_{\sigma_p}} = \frac{1}{n}\sum \frac{I_i'}{I_i}\left[\frac{I_i V_i}{I_c V_c}\ln\left(\frac{1}{1-p}\right)\left(\frac{\sigma_i}{\sigma_p}\right)^m - 1\right] + \frac{1}{n}\sum \frac{I_c'}{I_c}\left[1 + \frac{I_i V_i}{I_c V_c}\ln\left(\frac{1}{1-p}\right)\left(\frac{\sigma_i}{\sigma_p}\right)^m\right]$$
$$+ \frac{1}{n}\sum \frac{I_i V_i}{I_c V_c}\left(\frac{\sigma_i}{\sigma_p}\right)^m \ln\left(\frac{1}{1-p}\right)\ln\left(\frac{\sigma_i}{\sigma_p}\right) - \frac{1}{n}\sum \ln(\sigma_i) + \ln(\sigma_p) \qquad \text{[VI-56]}$$

(d) Calculate the log likelihood of the Weibull PDF with MLE of m given σ_p

(e) Iteratively solve for the solution of [VI-57] subject to [VI-58]. Solve for the lower limit and this value will give the design stress level, σ_p,for the desired reliability and confidence level.

$$\sigma_p : W(\sigma_p) \le \chi^2_{1,\alpha} \qquad \text{[VI-57]}$$

$$W(\sigma_p) = 2\left[l(\hat{m}, \hat{\sigma}_p) - l(\hat{m}_{\sigma_p}, \sigma_p)\right] \qquad \text{[VI-58]}$$

6.2.4 Limits On The Reliability

It is often the case to design a component to satisfy a variety of design constraints; in turn, the design configuration yields a stress level and stress distribution and multiaxial state of stress that cannot be changed. For this case, a reliability estimate of the design has to be computed. It is also the case that confidence limits on this reliability may be desired. This section addresses the calculation of the reliability and the confidence limits on the reliability. The reliability, R, of the component is given by Equation [VI-60] and this will usually be computed with a program such as WESTAC or CARES. The confidence limits of the reliability are computed as follows:

$$R(Z) = \exp -\left[I_c V_c \left(\frac{Z}{\sigma_o}\right)^m\right] \qquad \text{[VI-60]}$$

(a) Compute the MLE of m given g by using equation [VI-71]:

$$\frac{1}{m_\gamma}=\frac{1}{n}\sum\frac{I_i'}{I_i}\left[\gamma\frac{V_i}{V_c}\frac{I_i}{I_c}\left(\frac{\sigma_i}{Z}\right)^m-1\right]+\frac{1}{n}\sum\frac{I_c'}{I_c}\left[1+\gamma\frac{V_i}{V_c}\frac{I_i}{I_c}\left(\frac{\sigma_i}{Z}\right)^m\right]$$
$$-\sum\gamma\frac{V_i}{V_c}\frac{I_i}{I_c}\left(\frac{\sigma_i}{Z}\right)^m\ln\left(\frac{\sigma_i}{Z}\right)-\frac{1}{n}\sum\ln(\sigma_i)+\ln(Z) \qquad \text{[VI-71]}$$

(b) Compute the MLE of g using Equation [VI-68]:

$$\frac{1}{\hat{\gamma}}=\frac{1}{nI_cV_cZ^m}\sum I_iV_i\sigma_i^m \qquad \text{[VI-68]}$$

(c) Compute the log likelihood of the Weibull PDF , equation [VI-10], using the MLE of m and g in Equation [VI-62]. The MLE of m is given by [VI-24] and the MLE of g is given by [VI-68]:

$$f(\sigma_i)=m\frac{I_iV_i}{I_cV_cZ}\gamma\left(\frac{\sigma_i}{Z}\right)^{m-1}\exp-\left\{\frac{I_iV_i}{I_cV_c}\gamma\left(\frac{\sigma_i}{Z}\right)^m\right\} \qquad \text{[VI-62]}$$

(d) Compute the log likelihood of the Weibull PDF, using equation [VI-10], with the MLE of m given g , Equation [VI-41].

(e) Iteratively solve for the solution of [VI-72] subject to [VI-73]; this equation has two solutions: the upper and lower confidence limits. The solution gives the limits of g, hence the reliability, Equation [VI-121].

$$\gamma: W(\gamma)\le\chi^2_{1,\alpha} \qquad \text{[VI-72]}$$

$$W(\gamma)=2\left[l(\hat{m},\hat{\gamma})-l(\hat{m}_\gamma,\gamma)\right] \qquad \text{[VI-73]}$$

$$R(Z)=e^{-\gamma} \qquad \text{[VI-121]}$$

6.3 The Bootstrap Method

The following description is a repetition of the description of Section 4.3.1, Confidence Limits for Single Failure Mode, and is given as an example of how to approach the logic for the Bootstrap method. For a description of censored data, refer to Section 4.4.1.

6.3.1 Confidence Limits For The First And Second Weibull Parameters

Given that the Bootstrap method relies heavily on evaluation, the process to calculate confidence intervals, the approach is better described in a step-by-step basis. The confidence limits of the Weibull parameters can be calculated simultaneously; both are presented in this section.

(a) The first step consists of estimating the Weibull parameters using the Maximum Likelihood method. The estimates are computed from Equations [VI-19] and [VI-24] (shown next for convenience; they were derived in Section 3.2.1).

$$\hat{\sigma}_o = \left[\frac{1}{n}\sum \hat{I}_i V_i \sigma_i^{\hat{m}}\right]^{\frac{1}{\hat{m}}} \qquad \text{[VI-19]}$$

$$\frac{1}{\hat{m}} = \frac{1}{n}\sum\left(\frac{I_i'}{I_i} + \ln(\sigma_i)\right)\left(\frac{nI_iV_i\sigma_i^m}{\sum I_iV_i\sigma_i^m} - 1\right) \qquad \text{[VI-24]}$$

(b) Second, choose a random number between zero and one, and pick this number to be a reliability value, R.

(c) Third, select a specimen type from the original data set, with its corresponding V_i and I_i . Using the above $\hat{m}$ and $\hat{\sigma}_o$, compute the fracture strength of this pseudo specimen, using Equation [VI-43], given that it has the reliability equivalent to the value of the random number chosen in step (b).

$$\sigma_i = \hat{\sigma}_o\left(-\frac{\ell n(R_i)}{\hat{I}_i V_i}\right)^{1/\hat{m}} \qquad \text{[VI-43]}$$

(d) Repeat steps (b) and (c) for each specimen type and size a number of times equal to the number of specimens in the individual data set.

(e) Calculate the Weibull parameters for this newly generated data set using Equations [VI-44] and [VI-45] and save these values.

$$\tilde{\sigma}_o = \left[\frac{1}{n}\sum \tilde{I}_i V_i \sigma_i^{\tilde{m}}\right]^{\frac{1}{\tilde{m}}} \qquad \text{[VI-44]}$$

$$\frac{1}{\tilde{m}} = \frac{1}{n}\sum\left(\frac{I_i'}{I_i} + \ln(\sigma_i)\right)\left(\frac{nI_iV_i\sigma_i^m}{\sum I_iV_i\sigma_i^m} - 1\right) \qquad \text{[VI-45]}$$

(f) Repeat steps (b) through (e) a number of 1000 times.

(g) Sort the $\tilde{m}$ and $\tilde{\sigma}_o$ pair in ascending order for $\tilde{m}$ without losing the pair and also for $\tilde{\sigma}_o$ without losing the pair.

(h) To calculate the x confidence interval, pick the (100-x) (1000/2)(1/100) points from the upper and lower ends of the sorted values in (g); these define the limits. For example, if the 95 percent confidence interval is required, substitute the 95 for x to obtain 5, then multiply by the adjoining factor to get 25. Hence the 95 percent confidence interval is given by the 25th point from the lowest and the 25th point from the top of the sorted values $\tilde{m}$ and $\tilde{\sigma}_o$ in step (g).

6.3.2 Confidence Limits For The Design Stress Level

(a) The design stress level can be obtained from the Weibull parameters calculated in Equations [VI-44] and [VI-45] by using Equation [VI-46], where "p" is the desired probability of failure, V is the component volume and $\tilde{I}$ is the component's multiaxial and stress gradient factor:

$$\sigma_p = \tilde{\sigma}_o\left[\frac{1}{\tilde{I}V}\ell n\left(\frac{1}{1-p}\right)\right]^{1/\tilde{m}} \qquad \text{[VI-46]}$$

(b) Given that we have a set of $\tilde{m}$ and $\tilde{\sigma}_o$ from section 6.3.1, compute σ_p from [VI-46] for each one of these values and save them.

(c) Sort the σ_p and obtain the x confidence interval by picking the (100-x) 10/2 points from the upper and lower ends, using the same approach as in 6.3.1(h).

6.3.3 Confidence Limits For The Reliability

(a) Similarly to σ_p, the reliability, R, has a functional relationship to σ_o given by Equation [VI-47], where Z is the maximum stress level of the component, and $\tilde{I}$ and V are the component's multiaxial and stress gradient factor and volume, respectively:

$$R(Z) = \exp-\left[\tilde{I}V\left(\frac{Z}{\tilde{\sigma}_o}\right)^{\tilde{m}}\right] \qquad \text{[VI-47]}$$

(b) Given that we have $\tilde{m}$ and $\tilde{\sigma}_o$ from section 6.3.1, we can substitute these values into [VI-47] to find a list of R's.

(c) Sort the R's and obtain the x confidence interval by picking the (100-x) 10/2 points from the upper and lower ends, using the same approach as in 6.3.1(h).

REFERENCES - SECTION 1

(1) C.A. Johnson,and W.T. Tucker, "Advanced Statistical Concepts of Fracture in Brittle Materials," Final Report for Phase II, to be published. *Ceramic Technology for Advanced Heat Engines Project of the Advanced Materials Development Program*, Contract DE-AC05-840R21400 with Martin Marrietta Energy Systems, Inc., WBS Subelement 2.3.1.3.

(2) W. Weibull, "A Statistical Theory of the Strength of Materials," *Royal Swedish Academy of Eng. Sci. Proc.*, 151, 1-45, 1939.

(3) S.B. Batdorf and J.G. Crose, "A Statistical Theory for the Fracture of Brittle Structures Subjected to Nonuniform Polyaxial Stresses," *Journal of Applied Mechanics*, 41, 459-464, 1974.

(4) A.G. Evans, "A General Approach for the Statistical Analysis of Multiaxial Fracture," *Journal of the American Ceramic Society*,61, 7-8, 302-308, 1978.

(5) L. Chao and D.K. Shetty, "Equivalence of Physically Based Statistical Fracture Theories for Reliability Analysis of Ceramics in Multiaxial Loading," *J. AM. Ceram. Soc.*, 73, 7, 1917-1921, 1990.

(6) B. Efron and R. Tibshirani, "Bootstrap Methods for Standard Errors, Confidence Intervals, and Other Measures of Statistical Accuracy," *Statistical Science*, Vol. I, 54-57, 1986.

(7) D.R. Cox and D. Oakes, Analysis of Survival Data, Chapman and Hall, New York, 1984.

SECTION 2 - BOOTSTRAP TECHNIQUES FOR CONFIDENCE AND TOLERANCE BOUNDS

Dr. C.A. Johnson
General Electric Corporate Research and Development Center
Schenectady, NY 12301

(5 pages)

BOOTSTRAP TECHNIQUES FOR CONFIDENCE AND TOLERANCE BOUNDS

C.A. Johnson
General Electric Corporate Research and Development
Schenectady, NY 12301

As the term implies, bootstrap methods for determining confidence and tolerance bounds "pull themselves up by their own bootstraps." That is, they gather information about variability and uncertainty in estimates by evaluating only the data available in the observed data set. A good review of bootstrap techniques and their basis can be found in a paper by Efron (1). The techniques are readily applied to a variety of distributions, but to our knowledge, have not been applied to the Weibull distribution with size-scaling prior to the work described herein. The work has been carried out at GE Corporate Research and Development under a DOE/ORNL subcontract entitled "Advanced Statistical Concepts of Fracture in Brittle Materials"; contract number 86X-00223C; as part of ORNL's Ceramics Technology for Advanced Heat Engines project.

Bootstrap techniques characterize a combination of the uncertainty in estimates that arises from random sampling error (error due to testing less than an infinite number of test specimens) as well as any additional uncertainty from inefficiencies of the estimator in utilizing all the information contained in the data set (some estimators are known to be more efficient than others). The technique can be used with any type of estimator including maximum likelihood, linear regression, moments methods, etc. Bootstrap methods are able to characterize the confidence bounds for any "quantity" that an estimator is capable of estimating. For estimators in the Weibull size-scaling problem, these estimated quantities typically include the two Weibull parameters, the fracture strength of a component of interest at any quantile of interest, and/or the probability of failure of that component at a stress level of interest.

Bootstrap approaches are based on "resampling techniques" where the experimental data set is resampled and reevaluated numerous times. The resampling process is therefore a type of numerical simulation. Parametric and non-parametric bootstrap techniques differ only in the method in which the original data is resampled to generate the many simulated data sets. In both cases, the simulated specimens are generally chosen such that each simulated data set has the same number of observations within each specimen geometry as the original experimental data set.

In non-parametric bootstrapping, no assumption of the form of the strength distribution is made prior to generation of the simulated data sets. The simulated data is created by randomly choosing strengths from the original data "with replacements." That is, after a strength is chosen from the list of experimental strengths, it will still be available to be chosen again within that same data set. Therefore, each simulated data set is virtually guaranteed to have some repeat observations.

In parametric bootstrapping, an estimator for an assumed distribution is used to estimate the distribution parameters that best describe the experimental data. Simulated strength data is then generated by randomly choosing simulated specimens from the infinite population of specimens that are consistent with those distribution parameters. This random sampling of simulated specimens also involves the use of a random number generator. For each specimen to be simulated, a random number is chosen within the interval from zero to one. The Weibull distribution function is solved for the fracture strength and the random number is substituted as the probability of failure for that specimen. All other parameters such as Weibull modulus, sigma zero and specimen size/geometry are either known or assumed, therefore the strength of that simulated specimen is fully defined.

In both parametric and non-parametric bootstrapping, each of the simulated data sets is analyzed using a suitable estimator. (In parametric bootstrapping, it is most rational to use the same estimator

that was used to analyze the experimental data.) The variability in estimates from the numerous simulated data sets reflects the intrinsic variability of the estimator in analyzing data similar to the original experimental data set. The results can then be used with the experimental data set to state confidence bounds on estimates of distribution parameters and tolerance bounds on estimates of strengths.

The parametric bootstrap will be further described and demonstrated by example using fracture data from 137 specimens of sintered beta silicon carbide. The data set consists of three different specimen sizes (Mil Std 1942 MR specimens A, B and C) tested in two different testing geometries (three and four-point bending) for a total of six different combinations of specimen size and testing configuration. Each group contains approximately 18 specimens with the exception of the four-point B group that contains 48 specimens. Further details of specimen preparation and testing procedures can be found in the semi-annual reports of the ORNL Ceramic Technology Program.

The estimator that will be used in this discussion is a maximum likelihood estimator with the capability of combining data from multiple specimen sizes and geometries. This estimator was developed within GE's Advanced Statistics contract and is described in detail in semi-annual reports of that contract. When used with data such as the silicon carbide, the estimator uses three types of information contained in the data set: strength variability within each of the six subgroups; the dependence of the average strength on the physical size of the specimens (specimen size A versus B versus C); and the dependence of the average strength on the loading geometry (3-point versus 4-point bending). The estimator allows size-scaling to be carried out using volume, surface area or edge length. Fractography of the silicon carbide revealed that surface-related flaws accounted for most of the failures. Therefore, all size-scaling of this data will be carried out using surface area.

Figures 1-4 will be used to demonstrate the parametric bootstrap using maximum likelihood for analysis of the silicon carbide data. The four figures are similar in format; log of fracture stress is plotted versus log of stressed area (effective area). In each figure the observed fracture strengths are displayed with identifying symbols for the six subgroups. Although the parametric bootstrap can be used to calculate confidence bounds on many different estimates, this discussion will primarily describe confidence bounds on the 0.05 quantile of strength.

The analysis begins by using the maximum likelihood estimator to determine the two Weibull parameters that best describe the overall set of 137 observed fracture strengths. In this case, maximum likelihood yields a Weibull modulus of 14.22 and sigma zero of 433.1 MPa meter$^{(2/m)}$. (The strange units of sigma zero are necessary to account for the area term in the exponential of the Weibull distribution function.) The Weibull parameters can be used to position lines of constant probability of failure on plots such as Figure 1. Included on Figure 1 are the predicted strength versus component size for two quantiles (two probabilities of failure). The upper line is for the median strength (0.5 quantile), while the lower line is the predicted strength at which five percent of the components would be expected to fail (0.05 quantile). Although only two quantiles are drawn in Figure 1, there are, of course, a whole family of parallel lines that represent all possible quantile behaviors.

Figure 1 can be used to derive the "best estimate" of the stress at which five percent of a given component should fail, but there is no information to indicate the degree of uncertainty in that estimate. The bootstrap simulation is one means of providing a quantitative indication of the degree of uncertainty. As described earlier, the parametric bootstrap uses the estimated m and sigma zero to simulate many new data sets. For a moment, we will concentrate on one of these simulated data sets, say the very first set to be generated. This simulated data set contains 137 strengths from six different sub-groups corresponding to the six actual specimen sizes and geometries. If the original data set is compared with this first simulated set, it would be obvious that they are not identical in a one-for-one relationship. On the other hand, it would be easy to recognize close similarities in the two groups. If

the Weibull model that was used in generating the simulated data is a valid assumption, then many characteristics of the two groups will be similar. For instance, the average strength of the simulated 4-point B strengths should "tend" to be the same as the average of 4-point B's in the real data. There is no requirement that the two averages be identical, but they should differ only by statistical sampling error. Similar statements can be made about much more complex summaries of the data such as the Weibull modulus and the estimated strength of a component at a quantile of interest.

If the maximum likelihood estimator used on the original data is also used to analyze the first set of simulated data, the resulting m and sigma zero would be similar to (but not exactly equal to) the values of 14.22 and 433.1 that were used in generating the simulated data. The new parameters define the position of a new 0.05 quantile line on Figure 1. Because of the slightly different parameters, one would expect this new line to be slightly different in slope and position relative to the original line. Figure 2 is such a plot and includes the resulting 0.05 quantile lines for 10 simulated data sets. The original 0.5 and 0.05 quantile lines are drawn as bold lines, while the ten examples of 0.05 quantiles from the parametric simulation are drawn as lighter weight lines. (Occasional coincidences of multiple simulated lines appear to make additional bold lines.) The degree of scatter in these ten simulated lines is a coarse measure of the uncertainty in the position of the 0.05 quantile. The closer the agreement of the ten lines, the less the uncertainty.

Rather than ten simulated data sets, the full parametric bootstrap typically involves analysis of 1000 simulated data sets. Display of 1000 quantile lines would be very confusing and difficult to use; therefore the results are summarized and displayed differently. For a given stressed area, say 100 square mm, the predicted strength of the 0.05 quantile is calculated for each of the 1000 combinations of m and sigma zero. These strengths are then ordered from smallest to largest. The resulting list reflects the frequency that statistical sampling error will indicate any given strength. The 95 percent confidence interval on the estimate of this 0.05 quantile behavior is then defined as the interval of strengths from the 2.5 percentile to the 97.5 percentile positions on the list of 1000 strengths. Therefore the confidence interval on the 0.05 quantile strength of a component with 100 square mm of effective area would be roughly the interval from the strength of the 25th to the strength of the 975th position on the list of ordered strengths. This evaluation has been carried out for the silicon carbide data and the results are included on Figure 3. The two hyperbolic shaped lines that bound the 0.05 quantile straight line are the 95 percent confidence intervals on the 0.05 quantile. The earlier example of 100 square mm defined the positions of the upper and lower curves at that stressed area. A similar evaluation (using the same list of m's and sigma zero's) was performed for several other stressed areas to define smooth, continuous curves for the upper and lower bounds. (50 stressed areas are typically evaluated on plots of this type.)

It is interesting to note that the confidence interval on the 0.05 quantile of Figure 3 is smallest in the region of 300-350 MPa and expands at both higher and lower stresses. The position of this "pinch point" is the region of stresses and effective areas where there is the least uncertainty due to statistical sampling error. The pinch point is always positioned at the stress level corresponding to the "middle" of the experimentally measured strengths (log average of the strengths, I believe). Therefore, it can be seen on Figure 3 that the pinch point will move to progressively smaller stressed areas as one considers progressively smaller quantile behaviors. Since the shape of the hyperbolic curves is largely independent of the quantile being considered, it can also be stated that the confidence interval for a given sized component will progressively increase as one considers progressively smaller quantile behaviors.

The above discussion concentrated on confidence bounds for strength estimates. With that background, confidence bounds on parameters such as the Weibull modulus can be easily described. After the 1000 simulations are completed, the m's are simply ordered from smallest to largest and

treated very much as the ordered strengths described above. The 95 percent bounds on m are then defined as the interval between the 2.5 percentile and the 97.5 percentile positions of this ordered list. The 95 percent confidence interval on the Weibull modulus for the silicon carbide data is included on Figure 3 in parentheses next to the Weibull modulus. This interval is 13.05 to 15.79.

When bootstrap simulation techniques are used to determine bounds, the endpoints of intervals are subject to some random fluctuations related to the number of iterations in the simulation. Therefore if the same group of silicon carbide specimens were analyzed again but with a different "seed" for the bootstrap's random number generator, the resulting confidence interval on m will be slightly different.

Confidence and tolerance intervals are often quoted at the 95 percent level, but it should be mentioned that other intervals, of course, can be useful. Determination of other intervals is carried out in a manner parallel to earlier descriptions. If the 80 percent interval is of interest, then the ordered list of 1000 m's (or strengths, etc.) is quoted at the 10 percentile and 90 percentile positions.

The bootstrapping technique is computationally intensive, but it offers the potential of estimating confidence and tolerance on a variety of very complex problems, even beyond Class IV problems of combined data (such as those involving multiple flaw populations, multiaxial stresses, strength degradation due to slow crack growth, etc). Unlike likelihood ratio and likelihood integration techniques, the bootstrap technique does not require the existence of a likelihood estimator. If any estimator can be designed to estimate all the adjustable parameters of a given model, then the bootstrapping technique will be capable of estimating confidence bounds on all the parameters and tolerance bounds on estimated strengths. (It should be pointed out that the better the quality and efficiency of the estimator, the smaller the width of the bounds.) In addition, bootstrap techniques offer opportunities to correct for "bias" (the tendency of an estimator to give consistently high or consistently low estimates relative to the true value), and to estimate the "goodness-of-fit" of the data relative to the assumed model of size-scaled, two-parameter Weibull.

As with most estimators, the linear regression and maximum likelihood estimators for the Weibull model have the property of yielding offset or "biased" estimates. Strength estimates are particularly prone to large bias errors, especially if the strength is being estimated for a specimen or component with a much larger (or smaller) effective size than the test specimens. This large bias after size extrapolation can generally be traced to bias in the estimate of m. Of course, a small error in m will lead to progressively larger errors in predicted strength as one extrapolates farther and farther from the effective size of the test specimen data. Although not normally utilized, bootstrap simulations contain information about the magnitude of bias introduced by the estimator. The degree of bias in the silicon carbide fracture data can be judged by comparing Figure 4 where all estimates (parameters, strengths and bounds) have been corrected for bias, with Figure 3 where no corrections have been made. This comparison reveals very little bias present in any of the estimates. It has been found in most data sets that have been analyzed to date that the maximum likelihood estimator for combined data yields only small to moderate bias. This is in contrast to linear regression estimators that can have much larger biases. Nevertheless, smaller data sets are more prone to large bias errors, and the degree of bias in a new combination of specimen sizes and geometries cannot be predicted in advance; therefore, it is recommended that bias correction be a standard part of a bootstrap analysis. Details of how bias is corrected within a bootstrap simulation have been described within the reports of our ORNL statistics contract. Further details can be provided when desired.

Finally, it should be emphasized that bootstrap techniques are only capable of estimating uncertainty in estimates due to random sampling error and inefficiency of the estimator in utilization of information. Neither bootstrap nor likelihood methods are capable of estimating the uncertainty that arises from failure of the "model". Therefore, for instance, if the model assumes a single distribution

of strength controlling volume flaws, but the material actually contains a second distribution of surface flaws that are also active, then estimates are subject to errors that are not represented in the quoted bounds. In addition, it can be shown that the errors from such model failures can be virtually unbounded (arbitrary large errors). The unbounded nature of such model errors increases the importance of goodness-of-fit tests that can provide a more quantitative measure of the validity of the assumed model.

REFERENCES

1. B. Efron, "Bootstrap Methods: Another Look at the Jackknife," *The Annals of Statistics*, 7, No. 1, 1-26, 1979.

SECTION 3 - LIKELIHOOD RATIO METHODS FOR CERAMIC LIFE PREDICTION

Dr. W.T. Tucker
General Electric Corporate Research and Development Center
Schenectady, NY 12301

(6 pages)

LIKELIHOOD RATIO METHODS FOR CERAMIC LIFE PREDICTION

W. T. Tucker
General Electric Corporate Research and Development
Schenectady, NY 12301

1. Introduction

The objective of this brief report is to review the use of likelihood ratio methods for obtaining confidence/tolerance bounds. These bounds are part of the the statistical and probabilistic methods needed to fulfill the ORNL Ceramic Life Prediction Program requirements for the development of a methodology for use in design and application of brittle materials.

The report will give an introduction to the likelihood ratio method in Section 2 and a full development of the procedure as applied to Weibull strengths in Section 3. Summary comments, covering bias issues, will be given in Section 4. Recent developments, by the author, on the effects of multiaxial stress states to the statistical fracture problem carried out under Subcontract No. 86X-00223C (GE ORNL contract, with Dr. Curtis Johnson, on the Ceramic Technology for Advanced Heat Engines Program) are important in the development of the statistical procedures outlined in GAPD memorandum Ref. 1. These will also be reviewed in Section 3.

2. The Likelihood Ratio Procedure

We follow closely the development given by Cox and Oakes (Ref. 2) in Chapter 3.3 as applied to the two parameter, (m,σ_0), Weibull distribution. Denote the log likelihood by $l(m,\sigma_0)$ (a general formulation will be given in the next Section). The likelihood ratio method is based on the direct use of the likelihood ratio statistic

$$W(\sigma_0) = 2[l(\hat{m},\hat{\sigma}_0) - l(\hat{m}_{\sigma_0},\sigma_0)], \tag{1}$$

where $(\hat{m},\hat{\sigma}_0)$ is the joint maximum likelihood estimate of (m,σ_0) and $\hat{m}_{\sigma_0}$ is the maximum likelihood estimate of m conditional on σ_0 (i.e., taking σ_0 fixed). The function $l(\hat{m}_{\sigma_0},\sigma_0)$ of σ_0 is sometimes called the profile log likelihood for σ_0. Under the null hypothesis that σ_0 is the true or actual value of the inherent strength, $W(\sigma_0)$ has, approximately, a chi-squared distribution with $p_{\sigma_0} = dim(\sigma_0)$ (= 1) degrees of freedom. Inverting the test, yields a corresponding 1-α confidence region as

$$\{\sigma_0 : W(\sigma_0) \le \chi^2_{p_{\sigma_0},\alpha}\}, \tag{2}$$

where $\chi^2_{p_{\sigma_0},\alpha}$ is the upper α point of the chi-squared distribution with p degrees of freedom. The procedure of inverting a statistical test to obtain a confidence region is common practice: The set of all σ_0 values that satisfy the acceptance criterion, i.e, would not result in a decision of rejection if that particular value had been the null value, are associated with a test statistic value that has probability of 1-α under the prescribed null hypothesis. But this just defines a 1-α confidence region. Thus in order to obtain a 1-α confidence region on σ_0 we must find those σ_0 values that satisfy (2).

If the asymptotic distribution were exact, then

$$E[W(\sigma_0);\sigma_0] = p_{\sigma_0}.$$

Sometimes it is possible to find an expansion such that

$$E[W(\sigma_0);\sigma_0] = p_{\sigma_0}\left[1+\frac{c}{n}+o(\frac{1}{n})\right]. \quad (3)$$

Then $(1+c/n)$ is called a Bartlett correction factor and improved properties are obtained by replacing W by $W' = W/(1+c/n)$ in (1) and (2). Frequently c must be estimated to carry out this bias correction procedure. But, as pointed out by Cox and Oakes, it is rarely feasible to carry out such calculations in the presence of censoring. Also increased complexity of a problem diminishes the ability to determine c so as make bias corrections via (3).

3. The Likelihood Ratio Procedure Applied To Weibull Strengths

We suppose that the cumulative strength distribution for a test specimen observation is given by

$$F_i(x_i) = 1 - \exp\{-k_i V_i (x_i/\sigma_0)^m\}, \quad (4)$$

where $F_i(x_i)$ is the probability that the tested strength is less than or equal x_i; $k_i = k_i(m)$ is the size factor, a known function of m only; V_i is the size of the ith specimen; m is the Weibull modulus (shape factor); and σ_0 is the inherent strength (scale factor). The equivalent size usually accounts for only loading geometry in standard Weibull developments. However, it can be shown that multiaxial failure criteria also produce an equivalent size factor that is only a function of m. This result follows from the equivalence of the two principle methods for treating multiaxial stress states, Batdorf and Heinisch (Ref. 3) and Lamon and Evans (Ref. 4), as shown under the ORNL contract referenced in the Introduction. This equivalence has broad reaching implications. For example, as Curt points out, one can use CARES to generate k as a function of m. (This, of course, assumes that CARES has been properly implemented.) Finally, we assume that measurement error in the strength observations is negligible. Then (4) gives the complete distribution of interest.

Of some importance are quantiles for a component, i.e., the strength for the component, of a size and loading geometry generally differing from that of a test specimen(s), for which the probability of failure has a predetermined value, say, p. We denote this strength by σ_p $(0 < p < 1)$. In practice p is generally chosen to be "small," for example, 0.05 or 0.01. It is well known that with mild conditions the maximum likelihood estimator (MLE) of a function of a parameter(s) is the function of the MLE('s). For example, if $\hat{\theta}$ is the MLE of θ, then the MLE of $f(\theta)$ is $f(\hat{\theta})$. This fact is commonly used to estimate σ_p; see for example Nelson (Ref. 5). However, since we also want to determine various kinds of confidence limits via the likelihood ratio method, we shall follow the somewhat different course of redefining σ_0 into σ_p. Thus let σ_p be such that

$$p = 1 - \exp\{-kV(\sigma_p/\sigma_0)^m\}, \quad (5)$$

where k and V are associated with the component of interest. Then solving for σ_0 yields

$$\sigma_0 = \sigma_p\left[\frac{1}{kV}\ln(1/1-p)\right]^{-1/m}, \quad (6)$$

and substituting (6) into (4) yields

$$F_i(x_i) = 1 - \exp\{-r_i R_i \ln(1/1-p)(x_i/\sigma_p)^m\}, \quad (7)$$

where $r_i = k_i/k$ and $R_i = V_i/V$. Now (7) has the two unknown parameters m and σ_p and relates the component situation to the test situation. For example, the parameter σ_p is the pth quantile at size V associated with the component, appearing in the strength distribution of x_i for the ith specimen. We note in (7) that r_i is a (known) function of m and also R_i is known; m and σ_p must be estimated by taking data, x_i. To this end, we employ (7) in the remaining developments.

3.1 MLE's for m and σ_p

Differentiating (7) we obtain the density for the ith observation as

$$f_i(x_i) = r_i R_i \ln(1/1\text{-}p) m (x_i^{m-1}/\sigma_p^m) \exp\{-r_i R_i \ln(1/1\text{-}p)(x_i/\sigma_p)^m\}. \tag{8}$$

Thus the (log) likelihood is

$$\begin{aligned} l &= \sum \ln f_i(x_i) \\ &= \sum \ln r_i(m) + \sum \ln(R_i \ln(1/1\text{-}p)) + n \ln m + (m\text{-}1)\sum \ln x_i - nm \ln \sigma_p \\ &\qquad - \ln(1/1\text{-}p)\sum r_i(m) R_i (x_i/\sigma_p)^m, \end{aligned} \tag{9}$$

where the summation, $\sum$, is over all observations, i.e., 1 to n. (We are not considering censoring in (9).) Now the MLE's are obtained by finding $(\hat{m},\hat{\sigma}_0)$ such that (9) is maximized. Necessary conditions are that the partial derivatives of (9) with respect to m and σ_0 are zero. If $r(m)$ is a constant function of m, then it can be shown that these conditions are sufficient and the resulting solution unique. This is not true in a general context and may not be generally true for (9). However, in our investigations to date, we have not experienced trouble in finding the MLE's by this method; we return to this issue shortly. Taking the partial of (9) with respect to m yields

$$\begin{aligned} \partial l/\partial m = \sum r_i'(m)/r_i(m) + n/m + \sum \ln x_i - n \ln \sigma_p - \ln(1/1\text{-}p)\sum \Big[& r_i'(m) R_i (x_i/\sigma_p)^m \\ & + r_i(m) R_i (x_i/\sigma_p)^m \ln(x_i/\sigma_p) \Big], \end{aligned} \tag{10}$$

and with respect to σ_p yields

$$\partial l/\partial \sigma_p = -nm/\sigma_p - \ln(1/1\text{-}p)\sum r_i R_i x_i^m m (\sigma_p)^{-(m-1)}(-1/\sigma_p^2), \tag{11}$$

where the $'$ denotes differentiation with respect to m. Solving (11) for $\hat{\sigma}_p$ yields

$$\begin{aligned} \hat{\sigma}_p &= \left[\ln(1/1\text{-}p)\sum r_i(\hat{m}) R_i x_i^{\hat{m}}/n\right]^{1/\hat{m}} \\ &= \left[\ln(1/1\text{-}p)\sum \hat{r}_i R_i x_i^{\hat{m}}/n\right]^{1/\hat{m}}. \end{aligned} \tag{12}$$

Equation (12) can be used directly to determine $\hat{\sigma}_p$, if $\hat{m}$ can be obtained. This can be done by substituting (12) into (10) and then solving for $\hat{m}$. The result is

$$0 = \sum \hat{r}_i'/\hat{r}_i + n/\hat{m} + \sum \ln x_i - n\left[\sum \hat{r}_i R_i x_i^{\hat{m}} (\hat{r}_i'/\hat{r}_i + \ln x_i)/\sum \hat{r}_i R_i x_i^{\hat{m}}\right], \tag{13}$$

where the $\hat{}$'s on the r's indicates that m has been replaced by $\hat{m}$. Equation (13) must be solved iteratively for $\hat{m}$, starting from an initial value of $\hat{m}$.

In (13) divide by n and rearrange to obtain

$$1/\hat{m} = \sum \hat{r}_i R_i x_i^{\hat{m}} \ln x_i / \sum \hat{r}_i R_i x_i^{\hat{m}} - (1/n)\sum \ln x_i - (1/n)\sum \hat{r}_i'/\hat{r}_i \left[n \hat{r}_i R_i x_i^{\hat{m}} / \sum \hat{r}_i R_i x_i^{\hat{m}} - 1\right] \tag{14}$$

as the solution for $\hat{m}$. Now the left hand side of (14) is unbounded at $\hat{m} = 0$ and is monotonically decreasing as $\hat{m}$ increases. Thus, if the right hand side acts reasonably, then there will be a unique solution for $\hat{m}$. Suppose that r is a constant; this occurs when the specimens and component all have the same loading geometry in the standard Weibull setting. (I conjecture that this is also true for shear sensitive failure criteria.) Then the last term on the right hand side of (14) vanishes and the first becomes

$$\sum R_i x_i^{\hat{m}} \ln x_i / \sum R_i x_i^{\hat{m}}. \tag{15}$$

As $\hat{m}$ approaches infinity, (15) approaches $\ln x_M$ where x_M is the maximum x_i and the right hand side of (14) approaches $\ln x_M - \sum \ln x_i / n$ (> 0). Also it is straightforward, but tedious, to show that the derivative of (15) with respect to $\hat{m}$ is nonnegative. Thus the derivative of the right hand side of (14) is nonnegative when r is constant. These results imply that in this situation (14) has a unique solution.

This same approach can be employed to show that in general the left hand side of (14) is eventually less than the right hand side as $\hat{m}$ increases. Thus (14) has at least one solution. In general we assume that the test specimens are chosen so that for a for a fixed $\hat{m}$, $\sum \hat{r}_i R_i x_i^{\hat{m}} / n$ approaches a limit with probability one. Then for a fixed $\hat{m}$ as n approaches infinity, the last term on the right hand side of (14) approaches zero with probability one and is thus statistically negligible. Moreover the first term on the right hand side of (14) acts similarly to (15) so that with increasing probability a unique solution exists. In any event, as we have indicated we have not experienced problems in obtaining solutions for $\hat{m}$ via (13) for non-limiting n. In practice we employ a secant method with a check to avoid obtaining nonpositive $\hat{m}$. To allow for a fixed starting point for the secant method and to aid in round-off problems the data are relocated and rescaled so as to approximately have a σ_0 and a m of one. After the estimation is complete, a transform back to the original units is made.

3.2 Likelihood Ratio Confidence Limits for σ_p

In order to obtain confidence limits on σ_p, (2) must be solved with σ_0 replaced by σ_p. This requires evaluating $l(\hat{m},\hat{\sigma}_p)$ and $l(\hat{m}_{\sigma_p},\sigma_p)$. We have indicated how to obtain $\hat{m}$ and $\hat{\sigma}_p$. Now take σ_p fixed so as to determine $\hat{m}_{\sigma_p}$. Inspection of (10) reveals that the solution is

$$0 = \sum \hat{r}_i' / \hat{r}_i + n / \hat{m}_{\sigma_p} + \sum \ln x_i - n \ln \sigma_p - \ln(1/1\text{-}p) \sum \left[\hat{r}_i R_i (x_i/\sigma_p)^{\hat{m}_{\sigma_p}} \{ \hat{r}_i' / \hat{r}_i + \ln(x_i/\sigma_p) \} \right], \tag{16}$$

where the $\hat{}$'s on the r's indicates that m_{σ_p} has been replaced by $\hat{m}_{\sigma_p}$. Equation (16) is solved in the same manner as is (13). Having solved (13) and (12) for $\hat{m}$ and $\hat{\sigma}_p$, respectively, we repeatedly solve (16) in an iterative procedure to find the boundary values of σ_p such that

$$\{\sigma_p : W(\sigma_p) \le \chi^2_{p_{\sigma_p},\alpha}\}, \tag{2*}$$

is met, i.e., we replace σ_0 by σ_p in (1) and (2) via the change in density from (4) to (7) to carry out the likelihood ratio procedure to obtain confidence limits on σ_p. This requires

$$\begin{aligned} \hat{l} - \hat{l}_{\sigma_p} &= l(\hat{m},\hat{\sigma}_p) - l(\hat{m}_{\sigma_p},\sigma_p) \\ &= \sum \ln r_i(\hat{m}) / r_i(\hat{m}_{\sigma_p}) + n \ln \hat{m} / \hat{m}_{\sigma_p} + (\hat{m} - \hat{m}_{\sigma_p}) \sum \ln x_i - n\hat{m} \ln \hat{\sigma}_p + n\hat{m}_{\sigma_p} \ln \sigma_p \\ &\quad - \ln(1/1\text{-}p) \sum \left[r_i(\hat{m}) R_i (x_i/\hat{\sigma}_p)^{\hat{m}} - r_i(\hat{m}_{\sigma_p}) R_i (x_i/\sigma_p)^{\hat{m}_{\sigma_p}} \right]. \end{aligned} \tag{17}$$

We note that the only unknown in (17) is σ_p and the boundary values for σ_p from (2*) are given by

$$\hat{l} - \hat{l}_{\sigma_p} - \chi^2_{p_{\sigma_p},\alpha}/2 = 0. \tag{18}$$

Now $\hat{l} - \hat{l}_{\sigma_p}$ is more or less parabolic in shape with a maximum at $\hat{\sigma}_p$. Thus (18) has two solutions on either side of $\hat{\sigma}_p$. A secant method is also employed (in the iterative procedure indicated with (16)) to solve for each zero of (18). In the case of the root to the left of $\hat{\sigma}_p$ a check is made to avoid obtaining nonpositive σ_p, while in the case of the root to the right of $\hat{\sigma}_p$ a check is made to avoid a value of σ_p less than or equal $\hat{\sigma}_p$. Also the confidence limit boundaries are determined in the transformed state employed in the estimation of m, σ_p, and m_{σ_p} and then transformed back to the original units.

4. Summary

We have given a description of how to apply the likelihood ratio method to obtain confidence limits for Weibull strengths. The method is intuitive in that confidence limits are obtained by inverting the likelihood ratio test procedure. Both the MLE's and the confidence limits are obtained via procedures that, loosely speaking, maximize the probability of obtaining the observed sample. It is obvious how to alter the procedure given in Section (3.2) in order to obtain confidence limits on m. However, if one desires confidence limits via the likelihood ratio method for a reliability, then a reparameterization similar to that of (5) to (7) must be carried out. This results in a cumulative distribution of

$$F_i(x_i) = 1 - \exp\{-r_i R_i \gamma (x_i/z)^m\}, \tag{19}$$

where $\gamma = \gamma(z)$ is such that the reliability at strength z is

$$R(z) = e^{-\gamma}. \tag{20}$$

Thus γ is defined such that

$$\gamma = \ln(1/R(z)) \tag{21}$$

with

$$R(z) = \exp\{-kV(z/\sigma_0)^m\}. \tag{22}$$

Solving (22) for σ_0, as in (6), yields

$$\sigma_0 = z(\gamma/kV)^{-1/m},$$

which substituted into (4) gives (19). The procedures of Sections (3.1) and (3.2) are then carried out with (19) as the distribution in order to obtain confidence limits on $R(z)$ by ultimately employing (21). Thus the likelihood ratio method is very flexible and can be employed to obtain various kinds of confidence limits. The trick is to make a suitable change of variables for the parameter(s) of interest.

Unfortunately, the likelihood ratio method has one drawback: The limits so obtained are, in general, biased. As we have indicated it is well known that the likelihood ratio method produces biased limits and much theoretical work has gone into determining corrections for bias (the Bartlett correction mentioned earlier, cf Ref. 6). Limited work on the ORNL contract indicates that the likelihood ratio and parametric bootstrap methods give confidence limits that practically agree. This is consistent with the general knowledge base for bootstrap methods. It is also possible to correct the bootstrap limits for bias. Indeed this is a central issue in the study of bootstrap methods for determining confidence limits. At this point, a method has been developed on the ORNL contract for correcting the bias in the parametric bootstrap confidence limits. However, a general study has not yet been carried out that compares all the methods of bias correction with an aim of determining, if possible, a preferred way of obtaining "unbiased" confidence limits. One could envisage correcting bootstrap confidence limits via Bartlett corrections, on the one hand, or, at another extreme, correcting likelihood ratio confidence limits via bootstrap means. At this time I do not know the best way to proceed.

REFERENCES

1. J. Cuccio and A. Peralta (1990), "Subject: Trip Report to GE Corporate Research and Development," *Memorandum, MCD:AP:0001:090690,* GAPD, Phoenix.
2. D.R. Cox and D. Oakes (1984), *Analysis of Survival Data,* Chapman and Hall, New York.
3. S.B. Batdorf and H.L. Heinisch (1978), "Weakest Link Theory Reformulated for Arbitrary Fracture Criterion," *J. Am. Ceram. Soc.,* **61,** 7-8, 355-58.

4. J. Lamon and A.G. Evans (1983), "Statistical Analysis of Bending Strengths for Brittle Solids: A Multiaxial Fracture Problem," *J. Am. Ceram. Soc.*, 66, 3, 177-82.

5. Nelson, W. (1982), *Applied Life Data Analysis*, John Wiley & Sons, New York.

6. O.E. Barndorff-Nielson and D.R. Cox (1984), "Bartlett Adjustments to the Likelihood Ratio Statistic and the Distribution of the Maximum Likelihood Estimator," *J. R. Statist. Soc., B*, 46, 483-95.

AlliedSignal
AEROSPACE

SECTION 4 - LIKELIHOOD RATIO METHODS FOR CERAMIC LIFE PREDICTION - MULTIMODE PROCEDURES

Dr. W.T. Tucker
General Electric Corporate Research and Development Center
Schenectady, NY 12301

(11 pages)

LIKELIHOOD RATIO METHODS FOR CERAMIC LIFE PREDICTION-MULTIMODE PROCEDURES

W. T. Tucker
General Electric Corporate Research and Development
Schenectady, NY 12301

5. Introduction

This report is a continuation of an earlier report submitted to Garrett titled "LIKELIHOOD RATIO METHODS FOR CERAMIC LIFE PREDICTION." The purpose of this report is to extend the single mode methods developed in the earlier report to cover as many as three different competing failure modes. The procedure will give a justification and generalize the methods put forth by Alonso Peralta in the report, "STATISTICAL METHODS DEVELOPMENT SUMMARY REPORT," Ref. 7. This report should be considered as an extension of the first report. As such, the section, equation, and reference numbering will be continued from the first report. Also see the first report for general background information (Sections 1, 2, and 3). Our updated setup and notation (also employed by Peralta) will be used in this report. Thus the development will cover multiaxial stress states, as well. For example, (4) becomes

$$F_j(x_i) = 1 - \exp\{-I_{ji}V_{ji}(x_i/\sigma_{0j})^{m_j}\}, \tag{23}$$

where $I_{ji} = I_{ji}(m)$ is the multiaxial size factor, a known function of only m that takes into account the failure criterion and stress state, the j subscript refers to the jth competing (concurrent) failure mode, the i subscript refers to the ith specimen observation, and the other terms are as in (4). For a definition and development of I see Ref. 8.

The main purpose of this report is to give a quick introduction and problem setup, and act as a forum to exchange ideas on the multimode problem. The remainder of this report is as follows. Section 6 will cover the development of a general likelihood function for the situation in which the failure mode has been determined for each observation. This likelihood can then be used to implement the likelihood ratio procedure. Moreover, it may be possible to generalize this likelihood to cover the situation in which the failure mode has not been determined for all observations. Section 7 will give the setup for determining confidence bounds on a quantile and a reliability. Hopefully, much of the programming employed in the current implementation can also be used for the general multimode situation. The report closes with a brief summary in Section 8.

6. A General Likelihood Function

From (23) the survival probability for mode j to exceed a strength x_i is

$$\begin{aligned} S_j(x_i) &= 1 - F_j(x_i) \\ &= \exp\{-I_{ji}V_{ji}(x_i/\sigma_{0j})^{m_j}\}. \end{aligned} \tag{24}$$

Also the probability density for strength x_i for failure mode j is

$$\begin{aligned} f_j(x_i) &= dF_j(x_i)/dx_i \\ &= \exp\{-I_{ji}V_{ji}(x_i/\sigma_{0j})^{m_j}\}I_{ji}V_{ji}m_j(x_i)^{m_j-1}/(\sigma_{0j})^{m_j}. \end{aligned} \tag{25}$$

The probability that the ith specimen yields a strength observation less than or equal to x_i is given by

$$F(x_i) = 1 - S_1(x_i)S_2(x_i)S_3(x_i) \tag{26}$$

with the assumption that the failure modes act independently of each other and the specimen is tested to failure. The derivative of (26) yields the strength density

$$f(x_i) = f_1(x_i)S_2(x_i)S_3(x_i) + S_1(x_i)f_2(x_i)S_3(x_i) + S_1(x_i)S_2(x_i)f_3(x_i) \tag{27}$$

where the density for an individual failure mode strength comes from (25) and an individual failure mode survival probability is given by (24). From (27) it follows that the joint probability density of a specimen failing from the first mode *and* at strength x_i is

$$g_1(x_i) = f_1(x_i)S_2(x_i)S_3(x_i). \tag{28}$$

Similar expressions hold for modes 2 and 3. Since (27) must integrate to unity and the failure modes are independent of each other, the event of failure by any one of the three is mutually exclusive of any of the others. And all three events are exhaustive. Thus the likelihood for an observed strength and observed failure mode is given by either g_1, or g_2, or g_3.

Let

$$\delta_{ji} = \begin{cases} 1, & \text{if the ith specimen fails from mode j} \\ 0, & \text{otherwise,} \end{cases} \tag{29}$$

and suppose that

$$\delta_{1i} + \delta_{2i} + \delta_{3i} = 1. \tag{30}$$

Then the likelihood for the observed strength x_i and observed failure mode is

$$\begin{aligned} L_i &= [f_1(x_i)S_2(x_i)S_3(x_i)]^{\delta_{1i}}[S_1(x_i)f_2(x_i)S_3(x_i)]^{\delta_{2i}}[S_1(x_i)S_2(x_i)f_3(x_i)]^{\delta_{3i}} \\ &= [f_1(x_i)^{\delta_{1i}}S_1(x_i)^{\delta_{2i}}S_1(x_i)^{\delta_{3i}}][S_2(x_i)^{\delta_{1i}}f_2(x_i)^{\delta_{2i}}S_2(x_i)^{\delta_{3i}}][S_3(x_i)^{\delta_{1i}}S_3(x_i)^{\delta_{2i}}f_3(x_i)^{\delta_{3i}}] \end{aligned} \tag{31}$$

from (28), the similar expressions for g_2 and g_3, and the definitions of (29) and (30). For future reference, note that the bracketed terms in the last line of (31) each only involve failure mode 1, or failure mode 2, or failure mode 3. The log likelihood is by definition the logarithm of the likelihood of the complete data set, which under independence is the product of the L_i. This yields

$$\begin{aligned} l &= \sum_{i=1}^{n} \ln L_i \\ &= \sum_{i=1}^{n} \left(\ln[f_1(x_i)^{\delta_{1i}}S_1(x_i)^{\delta_{2i}}S_1(x_i)^{\delta_{3i}}] + \ln[S_2(x_i)^{\delta_{1i}}f_2(x_i)^{\delta_{2i}}S_2(x_i)^{\delta_{3i}}] + \ln[S_3(x_i)^{\delta_{1i}}S_3(x_i)^{\delta_{2i}}f_3(x_i)^{\delta_{3i}}] \right) \end{aligned} \tag{32}$$

as the log likelihood of the observed strengths and failure modes for the complete data set.

The maximum likelihood solution for the six parameters (m_j, σ_{0j}, j = 1,2,3) is given by maximizing (32) as the six parameter values range over the positive half space of possible values. Since the bracketed terms of (32) only involve a single mode, the maximum of (32) is obtained by maximizing individually each of the summed bracketed terms. But, due to the nature of the δ_{ji}, i.e., within a bracket one and only one of the δ_{ji} is unity and the others are zero, the maximization of an individual sum of brackets is obtained from a censored data analysis. Thus (32) justifies the use of the method put forth in Ref. 7 and insures that that procedure gives a MLE solution.

7. Confidence Limits in the Multimode Case

Among other things, Ref. 7 develops the use of the likelihood ratio method to obtain confidence limits for a single failure mode, based on Sections 1, 2, and 3 of this report. This Section will develop

a general method to obtain confidence limits employing the likelihood ratio method using (32), covering the multimode situation. While the ML point estimates can be obtained from (32) acting as if only a particular failure mode were present, this is not generally true when obtaining confidence limits. Clearly an exception is in obtaining confidence limits for any of the distribution parameters, (m_j, σ_{0j}, j = 1,2,3), since the three sums of brackets in (32) act in an independent manner vis-a-vis the pairs of distribution parameters. In this case the methods of Ref. 7 directly apply.

7.1 Confidence Limits for σ_p

The more general methodology is similar in setup to that covered by (1), (2), (2*), and (17). Beyond the distribution parameters, the other major parameters of interest are the pth quantile, σ_p, and the reliability, $R(z)$, at a given strength, z. The resulting procedure is very similar for obtaining confidence limits on both σ_p and $R(z)$. The development will thus be carried through for σ_p and the results stated for $R(z)$. To this end let

$$S_j(\sigma_{p_c}) = \exp\{-I_{jc}V_{jc}(\sigma_p/\sigma_{0j})^{m_j}\}, \tag{33}$$

where the c subscript denotes a component and the other terms are as defined previously. Then, in view of (26), setting

$$p = 1 - S_1(\sigma_{p_c})S_2(\sigma_{p_c})S_3(\sigma_{p_c}) \tag{34}$$

defines σ_p. Rearranging and taking the natural logarithm of (34), and employing (33) yields

$$\ln\left\{\frac{1}{1-p}\right\} = I_{1c}V_{1c}(\sigma_p/\sigma_{01})^{m_1} + I_{2c}V_{2c}(\sigma_p/\sigma_{02})^{m_2} + I_{3c}V_{3c}(\sigma_p/\sigma_{03})^{m_3}. \tag{35}$$

For given (m_j, σ_{0j}, j = 1,2,3), (35) implicitly defines σ_p. Since (35) is monotone increasing in σ_p and in the limit unbounded, there is a unique σ_p for each value of p. Thus (35) can be employed to obtain the ML point estimate of σ_p given ($\hat{m}_j$, $\hat{\sigma}_{0j}$, j = 1,2,3).

Equation (35) could be solved for, say, σ_{01}, in terms of σ_p, and σ_{02} and σ_{03}, in order to determine confidence limits for σ_p. Substituting the result into (32) and following the procedure of Section 3.2 would give a method for determining confidence limits on σ_p, and indeed this was the method that was followed in the single failure mode case (where there would be no σ_{02} or σ_{03}). However, in the multimode situation this procedure would loose the symmetry of (35). And it is not clear which parameter should be eliminated; the choice of σ_{01} was arbitrary. Loss of symmetry and arbitrariness in the choice of which parameter to eliminate could lead to difficulties in obtaining a solution if there is a large imbalance in the number of observations occurring for each of the failure modes--a situation very likely to happen in practice. It is well known from practical applications of optimization theory that elimination by substitution can have convergence difficulties in situations of imbalance, etc. (see, for example, Ref. 9). Moreover, in obtaining confidence limits by the likelihood ratio method, σ_p would be fixed and the MLE's obtained for the remaining parameters. Thus the likelihood ratio method also requires that an optimization be carried out with σ_p constrained to various values. The procedure put forth herein, hopefully, avoids the difficulties associated with elimination and substitution, and its resulting optimization under constraints.

In developing a procedure, first consider the elimination and substitution approach. Following the method of (2*), the confidence limits on σ_p would be determined by those

$$\{\sigma_p : W(\sigma_p) \le \chi^2_{\phi_{\sigma_p},\alpha}\}, \tag{36}$$

where

$$W(\sigma_p) = 2[l(\hat{m}_1,\hat{m}_2,\hat{m}_3,\hat{\sigma}_p,\hat{\sigma}_{02},\hat{\sigma}_{03}) - l(\hat{m}_{1\sigma_p},\hat{m}_{2\sigma_p},\hat{m}_{3\sigma_p},\sigma_p,\hat{\sigma}_{02\sigma_p}\hat{\sigma}_{03\sigma_p})], \quad (37)$$

l is given by (32) with the substitution of σ_p for σ_{01} solved from (35), and the σ_p subscript denotes that the appropriate MLE's are determined with the given value of σ_p. Denote the first log likelihood term in (37) by $\hat{l}(\hat{\sigma}_p)$ and the second by $\hat{l}(\sigma_p)$. Also denote (32) evaluated at the MLE's, $(\hat{m}_j, \hat{\sigma}_{0j}$, $j = 1,2,3)$, by $\hat{l}$. It is straightforward to show that $\hat{l}(\hat{\sigma}_p)$ equals $\hat{l}$. Thus, only the evaluation of $\hat{l}(\sigma_p)$ requires further computation; this is a constrained optimization problem.

The constrained optimization problem, the fact that $\hat{l}(\hat{\sigma}_p)$ equals $\hat{l}$, and the fact that a MLE of a function of parameters is the function of the MLE's are interconnected and strongly related. This latter property of MLE's is called the invariance property of MLE's. The invariance property clearly shows the relationship and we begin there. Let θ denote the k-dimensional parameter space of the distribution (k is six in the present situation). Suppose a MLE of $\tau(\theta) = (\tau_1(\theta), \ldots, \tau_r(\theta))$, where $1 \le r \le k$, is desired. Let T denote the range of possible values of $\tau(.)$; T is r-dimensional. (Just considering σ_p makes r one; r would be six in the context of (37).) Define $M = M(\tau) = M(\tau; x_1, \ldots, x_n) = \sup_{\{\theta:\tau(\theta)=\tau\}} L(\theta; x_1, \ldots, x_n)$. (In the present situation L is the likelihood given by the product of the L_i.) $M(.)$ is called the likelihood function induced by the transformation, $\tau(.)$. The invariance property states that a MLE of $\tau(\theta)$ is $\tau(\hat{\theta})$, where $\hat{\theta}$ denotes a vector of MLE's of the (initial) k parameters. The proof follows from the inequality/equalities: $M(\tau; x_1, \ldots, x_n) = \sup_{\{\theta:\tau(\theta)=\tau\}} L(\theta; x_1, \ldots, x_n) \le \sup_{\theta \in \Theta} L(\theta; x_1, \ldots, x_n) = L(\hat{\theta}; x_1, \ldots, x_n) = \sup_{\{\theta:\tau(\theta)=\tau(\hat{\theta})\}} L(\theta; x_1, \ldots, x_n) = M(\tau(\hat{\theta}); x_1, \ldots, x_n)$. The inequality follows from the fact that the supremum over a subset of θ values must be less than or equal to the supremum over all θ values. The first equality that follows the inequality comes from the definition of a MLE. The second is important and comes about since the supremum is taken over those θ values that result in a τ value of $\tau(\hat{\theta})$. Clearly this set of θ values must include $\hat{\theta}$, and since a supremum over a subset cannot be greater than the supremum over the complete set equality follows. The final equality comes from the definition of M (as does the equality before the inequality). The proof of the invariance follows that given by Mood, Graybill, and Boes (Ref. 10).

The invariance property of MLE's produces the fact that a MLE of a function of parameters is the function of the MLE's, while the equalities that follow the inequality in the proof show that $\hat{l}(\hat{\sigma}_p)$ equals $\hat{l}$. In this latter context the transformation is 6-dimensional and maps $(m_1, m_2, m_3, \sigma_{01}, \sigma_{02}, \sigma_{03})$ into $(m_1, m_2, m_3, \sigma_p, \sigma_{02}, \sigma_{03})$, where σ_p is implicitly defined by (35). Actually in this case the mapping is one-to-one and onto, since (35) uniquely defines σ_p and the other relationships in the mapping are identities. This implies that for each value of θ there is a unique value of τ, and conversely. Thus if the MLE of $(m_1, m_2, m_3, \sigma_{01}, \sigma_{02}, \sigma_{03})$ is unique, then so is the MLE of $(m_1, m_2, m_3, \sigma_p, \sigma_{02}, \sigma_{03})$. We make the assumption that the censored analyses produce a unique MLE for any particular failure mode (see also the discussion in Section 3.2). This implies that there is a unique MLE for σ_p. To investigate the constrained optimization, consider the second log likelihood term in (37) and take σ_p fixed. Then $\hat{l}(\sigma_p)$ gives an optimum value for the log likelihood constrained so that (35) holds. Let Θ^* denote the space of θ values such that (35) holds for the given σ_p, $\hat{\theta}^*$ denote a MLE over Θ^*, $\{\theta:\tau(\theta)=\tau\}^*$ denote the set of θ values that result in a $\tau(\theta)$ value of τ for the transformation of $(m_1, m_2, m_3, \sigma_{01}, \sigma_{02}, \sigma_{03})$ into $(m_1, m_2, m_3, \sigma_p, \sigma_{02}, \sigma_{03})$ with given σ_p, and M^* denote the MLE in the constrained, transformed space. For this setup the invariance property also holds (as a straightforward corollary to the proof). This implies that the three equalities after the inequality hold. But $\sup_{\theta \in \Theta^*}$ defines a constrained optimization problem and $\sup_{\{\theta:\tau(\theta)=\tau(\hat{\theta}^*)\}^*}$ defines an optimization via elimination and substitution (which also has an optimum equal to M^*). Thus the constrained MLE can be obtained from a constrained optimization or by elimination and substitution as $\hat{l}(\sigma_p)$; the two values of l are equal. Moreover, since the 6-dimensional mapping is one-to-one and onto the resulting MLE's are unique to each other and equal. If the censored analyses produce unique MLE's then the constrained MLE's will also be unique. Therefore the optimum associated with $\hat{l}(\sigma_p)$ can be obtained

as follows. Let p be given. Since $\hat{l}(\sigma_p)$ must be obtained for various values of σ_p in order to meet (36), σ_p can be taken as fixed at the next step of the procedure. Then carry out

$$\text{Maximize} \quad l \tag{38}$$

$$s.t.\ \ln\left(\frac{1}{1-p}\right) = I_{1c}V_{1c}(\sigma_p/\sigma_{01})^{m_1} + I_{2c}V_{2c}(\sigma_p/\sigma_{02})^{m_2} + I_{3c}V_{3c}(\sigma_p/\sigma_{03})^{m_3} \tag{39}$$

with fixed σ_p.

The fact that σ_p is fixed in (39) allows a further change of variable to be made that simplifies the problem. Define

$$\gamma_{1p} = I_{1c}V_{1c}(\sigma_p/\sigma_{01})^{m_1}, \tag{40}$$

$$\gamma_{2p} = I_{2c}V_{2c}(\sigma_p/\sigma_{02})^{m_2}, \tag{41}$$

and

$$\gamma_{3p} = I_{3c}V_{3c}(\sigma_p/\sigma_{03})^{m_3}. \tag{42}$$

With σ_p known and $(m_j,\ j = 1,2,3)$ taken as given, (40), (41), and (42) define a unique mapping of $(\sigma_{0j},\ j = 1,2,3)$ to $(\gamma_{jp},\ j = 1,2,3)$. Then the 6-dimensional mapping of $(m_1,m_2,m_3,\sigma_{01},\sigma_{02},\sigma_{03})$ into $(m_1,m_2,m_3,\gamma_{1p},\gamma_{2p},\gamma_{3p})$ is also one-to-one and onto. The above arguments show that the optimization problem

$$\text{Maximize} \quad l \tag{43}$$

$$s.t.\ \ln\left(\frac{1}{1-p}\right) = \gamma_{1p} + \gamma_{2p} + \gamma_{3p} \tag{44}$$

with fixed σ_p and working in $(m_1,m_2,m_3,\gamma_{1p},\gamma_{2p},\gamma_{3p})$ is equivalent to the problem of (38) and (39) working in $(m_1,m_2,m_3,\sigma_{01},\sigma_{02},\sigma_{03})$. At this stage a transformation is made by solving (40), (41), and (42) for σ_{01}, σ_{02}, and σ_{03} and thereby substituting the γ's into (24), (25), and ultimately (31) and (32). The log likelihood that results is

$$l = \sum_{i=1}^{n}\left(\ln[f_1(x_i)^{\delta_{1i}}S_1(x_i)^{\delta_{2i}}S_1(x_i)^{\delta_{3i}}] + \ln[S_2(x_i)^{\delta_{1i}}f_2(x_i)^{\delta_{2i}}S_2(x_i)^{\delta_{3i}}] + \ln[S_3(x_i)^{\delta_{1i}}S_3(x_i)^{\delta_{2i}}f_3(x_i)^{\delta_{3i}}]\right), \tag{45}$$

where

$$S_j(x_i) = \exp\{-r_{ji}R_{ji}\gamma_{jp}(x_i/\sigma_p)^{m_j}\}, \tag{46}$$

and

$$f_j(x_i) = \exp\{-r_{ji}R_{ji}\gamma_{jp}(x_i/\sigma_p)^{m_j}\}r_{ji}R_{ji}\gamma_{jp}m_j(x_i)^{m_j-1}/(\sigma_p)^{m_j}, \tag{47}$$

with $r_{ji} = I_{ji}/I_{jc}$ and $R_{ji} = V_{ji}/V_{jc}$. In view of (45), and (46) and (47) it is clear that the optimization of l separates into the maximization of three terms. Thus the general methodology of Ref. 7 is applicable to the optimization of (45). However, the procedure must be carried out with the constraint (44). Note in the setup of (45)-(47) that σ_p explicitly appears and the unknowns over which the maximization takes place are $(m_1,m_2,m_3,\gamma_{1p},\gamma_{2p},\gamma_{3p})$. Thus the optimization given by (43) and (44) preserves the symmetry of (32) and the individual censored data analysis approach.

The maximization of (45) subject to (44) is central to solving (36). Thus an efficient solution method must be determined. Moreover, there are advantages to having the constraint in the linear form of (44). In the setup of (43) and (44) Fletcher (Ref. 11) discusses general methods of solution. However, the method we propose will employ as much of the methodology as developed in Ref. 7 as

possible, and be based on the use of Lagrange multipliers. The use of Lagrange multipliers has a well developed theory and established practice. And the methods of Ref. 7 are very efficient. The procedure will be based on results in Chapters 10 and 13 of Luenberger (Ref. 12) and Whittle (Ref. 9), Chapters 2 and 3. In order to apply the Lagrange method, the Lagrangian must be set up. For (43) and (44) this is

$$L = l + \lambda(\gamma - \gamma_{1p} - \gamma_{2p} - \gamma_{3p}) \tag{48}$$

where L denotes the Lagrangian, λ is the Lagrange multiplier (for an excellent derivation and interpretation see Ref. 9), and $\gamma = \ln(1/(1-p))$. The objective of Lagrangian methods is to replace the optimization problem of (43) with the constraint (44) by the optimization of (48) in an unconstrained manner, but with the additional parameter λ. A number of procedures for doing this have been developed. Ref. 11 discusses some of these and a general methodology called sequential quadratic programming (SQR) has also evolved. SQR methods are studied in Chapter 14 of Ref. 12 and by Stoer (Ref. 13). Thus, if for any reason the procedure proposed herein does not work, there are a number of well established, more general methods that can be employed to carry out either the optimization of (43) and (44), or (48).

Ref. 9, Chapter 2, studies stationary points of L in the context of the weak Lagrangian principle and the strong Lagrangian principle in terms of a supporting hyperplane to the set of possible values of the constraint and l. Also background information on constrained maximization and Lagrange methods is given in Chapter 2. It is clear that stationarity is important in obtaining an optimum to (48), since the partial of (48) with respect to λ set equal to zero forces the constraint to hold. However, we will be primarily concerned with the strong Lagrangian principle, since it leads to the dual programming problem that will be the basis of the proposed method. The strong principle stated in terms of (48), when valid, asserts that $l - \lambda(\gamma_{1p} + \gamma_{2p} + \gamma_{3p})$ is maximal in Θ at a solution to (43) and (44). Here Θ denotes the possible values of $\theta = (m_1, m_2, m_3, \gamma_{1p}, \gamma_{2p}, \gamma_{3p})$.

Theorem (3.3) in Chapter 3 of Ref. 9 states (in the present context) that $\min_\lambda \max_{\theta \in \Theta} L$ is an upper bound to l evaluated at the solution of (43) and (44). The dual solution based on this would be carried out as follows. Pick λ, then maximize (48) over all $\theta \in \Theta$; a method to do this based on the procedures of Ref. 7 will be discussed shortly. Iterate on λ to find the minimum value of $\max_{\theta \in \Theta} L$. The solution of this procedure will solve $\min_\lambda \max_{\theta \in \Theta} L$ with equality to the solution of (43) and (44) if and only if the strong Lagrangian principle holds. We assume that for a given value of σ_p the censored data analyses associated with (45) have a (unique) solution. As will be shown, this implies that a solution to $\min_\lambda \max_{\theta \in \Theta} L$ exists. Now fix λ at this solution, designated by λ^*, and denote the corresponding value of θ by θ^*. Then $L^* = l(\theta^*) + \lambda^*(\gamma - \gamma_{1p}^* - \gamma_{2p}^* - \gamma_{3p}^*) \rightarrow l(\theta^*) - \lambda^*(\gamma_{1p}^* + \gamma_{2p}^* + \gamma_{3p}^*)$, since λ^* is fixed and γ is constant. This implies that a value of λ, λ^* has been found that maximizes $l(\theta^*) - \lambda^*(\gamma_{1p}^* + \gamma_{2p}^* + \gamma_{3p}^*)$ with θ^* in Θ. As shown by Theorem 3.1, if this θ^* value meets (44), then it solves (43) and (44).

Consider now a means to solve $\max_{\theta \in \Theta} L$ for a given λ. Taking the partial of L with respect to γ_{jp}, and employing (46) and (47), yields

$$\frac{\partial L}{\partial \gamma_{jp}} = -\sum_{i=1}^{n} r_{ji} R_{ji}(x_i/\sigma_p)^{m_j} + \frac{n_j}{\gamma_{jp}} - \lambda, \tag{49}$$

where n_j is the number of uncensored observations on failure mode j. Setting (49) to zero and solving for γ_{jp} yields

$$\gamma_{jp} = \frac{n_j}{\sum_{i=1}^{n} r_{ji} R_{ji} (x_i/\sigma_p)^{m_j} + \lambda}. \tag{50}$$

These solutions are substituted into the partial of L with respect to m_j set to zero, as is done in Ref. 7 in equations [30] to [33] for an individual failure mode. This procedure can be followed since each bracketed term in (45) contains only the parameters of one particular failure mode, (48) is being solved in an unconstrained manner, and the constraint as it appears in the right hand side of (48) does not involve any m_j. Thus individual censored analyses can be made in solving $\max_{\theta \in \Theta} L$. The first step is to obtain the partial of L with respect to m_j, which employing (46) and (47) is

$$\frac{\partial L}{\partial m_j} = -\sum_{i=1}^{n} R_{ji} \gamma_{jp} (x_i/\sigma_p)^{m_j} [r_{ji} \ln(x_i/\sigma_p) + r_{ji}'] + \sum_{i=1}^{n_j} [\frac{r_{ji}'}{r_{ji}} + \ln(x_i)] + \frac{n_j}{m_j} - n_j \ln(\sigma_p), \tag{51}$$

where the summation to n_j is over the failed (uncensored) observations for the jth failure mode and the summation to n is over all observations. Substituting (50) into (51) and rearranging yields for the jth failure mode

$$\frac{1}{m_j} = \frac{1}{(\sum_{i=1}^{n} r_{ji} R_{ji} (x_i/\sigma_p)^{m_j} + \lambda)} \sum_{i=1}^{n} R_{ji} (x_i/\sigma_p)^{m_j} [r_{ji} \ln(x_i/\sigma_p) + r_{ji}'] - \frac{1}{n_j} \sum_{i=1}^{n_j} [\frac{r_{ji}'}{r_{ji}} + \ln(x_i)] + \ln(\sigma_p), \tag{52}$$

where the $'$ indicates differentiation with respect to m_j. This shows how each failure mode can censor the others.

If (52) is useful, a solution must exist for $\lambda \geq 0$. To show this, consider the matrix of second partials of L with respect to γ_{jp} and m_j. Inspection of (49) and (51) reveals, since all terms in λ drop out, that the result is just the Hessian (matrix of second partials) of an unconstrained problem given by (43) with l defined by (45). Now we assume that the censored analyses result in a unique MLE for $(m_j, \sigma_{0j}, j = 1,2,3)$. Since l defined by (45) has derivatives of all orders, l is very well behaved and it is reasonable to further assume that a unique maximum value exists for (45) for any value of σ_p sufficiently close to $\hat{\sigma}_p$. This implies that the Hessian of l from (45) is negative definite. Thus for any given σ_p, by application of the Implicit Function Theorem, (49) and (51) when set to zero have a solution in a neighborhood of any λ value such that the resulting values of $(m_j, \gamma_{jp}, j = 1,2,3)$ keep the Hessian of l negative definite. Moreover, when λ equals zero, all terms in (52) that involve σ_p cancel and (52) reduces to [33] of Ref. 7 with I_{jc} and V_{jc} equal to one, which gives a solution to the original unconstrained problem. Thus for λ in a neighborhood of zero (50) and (52) have a solution. It is clear that the partial of L with respect to λ set to zero imposes the constraint of (44). Thus if the necessary conditions that L have an optimum are met (its first partials equaling zero), then $\min_{\lambda} \max_{\theta \in \Theta} L$ has a solution which meets the constraints and hence gives a θ^* that solves (43) and (44). In this situation, a line search on λ starting at $\lambda = 0$ can be made in order to solve $\min_{\lambda} \max_{\theta \in \Theta} L$ and obtain the dual solution. Then a check that the resulting θ^* meets (44) can be made to verify the procedure.

We have shown if unique MLE's of (45) exist in a neighborhood of $\hat{\sigma}_p$ and (48) has an extremum that the solution to the dual problem gives a solution to (43) and (44). If a solution to (45) is taken as given, one is still faced with the situation of when (48) has an extremum. If the strong Lagrangian principle holds then (48) would have an extremum. Strong, global sufficiency conditions that the strong principle hold are given by Whittle in Section 3.6. These conditions are equivalent to the convex duality conditions given by Luenberger in Chapter 13. These convexity conditions ensure that a solution is unique and is the global solution, but are difficult to verify and very constraining. It would

be pleasing if sufficiency conditions could be related to the assumption that (43) and (44) have a solution. Second-order necessary and sufficient conditions that (43) and (44) have a local solution are given by Luenberger (Ref. 12) in Chapter 10. Part of these conditions imply the existence of a λ such that (50) and (52) are met. Moreover, Luenberger also gives a local duality theory in Chapter 13. Under the local theory, the critical assumption that Luenberger makes is that the Hessian of the Lagrangian evaluated at the solution point is negative definite (Luenberger assumes positive definite, but note that he sets up the optimization as a minimization problem). In the present problem, due to the nature of (44), this local assumption reduces to the assumption that the Hessian of l from (45) is negative definite. This is just the assumption we have made. Thus the assumptions that (43) and (44) have a solution, and the Hessian of l is negative definite (for σ_p values sufficiently close to $\hat{\sigma}_p$) imply that Luenberger's local duality assumptions are met. As an aside, these conditions contain the necessary and sufficient conditions that the problem have a maximum, i.e., that (43) with l given by (45) hold under (44). But importantly when the local duality assumptions are met Luenberger shows that $\min_{\lambda}\max_{\theta\in\Theta} \mathrm{L}$ has a solution that is equivalent through duality to that of (43) and (44). Thus θ^* will be a solution to (43) and (44).

7.2 Confidence Limits for $R(z)$

In obtaining confidence limits for $R(z)$, z is taken as given. Then by definition

$$R(z) = S_1(z_{R_c})S_2(z_{R_c})S_3(z_{R_c}) \tag{53}$$

where

$$S_j(z_{R_c}) = \exp\{-I_{jc}V_{jc}(z/\sigma_{0j})^{m_j}\}, \tag{54}$$

with j = 1,2,3, and all terms, except z, are defined as in (33).

Similar to (36), the confidence limits on $R(z)$ would be determined by those

$$\{R(z): W(R(z)) \le \chi^2_{p_{R(z)},\alpha}\}, \tag{55}$$

where

$$W(R(z)) = 2[l(\hat{m}_1,\hat{m}_2,\hat{m}_3,R(\hat{z}),\hat{\sigma}_{02},\hat{\sigma}_{03}) - l(\hat{m}_{1R(z)},\hat{m}_{2R(z)},\hat{m}_{3R(z)},R(z),\hat{\sigma}_{02R(z)}\hat{\sigma}_{03R(z)})], \tag{56}$$

l is given by (32) with the substitution of $R(z)$ for σ_{01} solved from (53), and the $R(z)$ subscript denotes that the appropriate MLE's are determined with the given value of $R(z)$.

The substitution and elimination optimization problem given by the right hand log likelihood in (56) is replaced by an equivalent constrained optimization problem:

$$\text{Maximize} \quad l \tag{57}$$

$$s.t.\ \ln\left[\frac{1}{R(z)}\right] = I_{1c}V_{1c}(z/\sigma_{01})^{m_1} + I_{2c}V_{2c}(z/\sigma_{02})^{m_2} + I_{3c}V_{3c}(z/\sigma_{03})^{m_3} \tag{58}$$

with fixed $R(z)$. The constraint given by (58) follows from manipulation of (53). Also at this stage l is given by (32). Now make the change of variables

$$\gamma_{1z} = I_{1c}V_{1c}(z/\sigma_{01})^{m_1}, \tag{59}$$

$$\gamma_{2z} = I_{2c}V_{2c}(z/\sigma_{02})^{m_2}, \tag{60}$$

and

$$\gamma_{3z} = I_{3c}V_{3c}(z/\sigma_{03})^{m_3}. \tag{61}$$

With z known and (m_j, j = 1,2,3) taken as given, (59), (60), and (61) define a unique mapping of (σ_{0j}, j = 1,2,3) to (γ_{jz}, j = 1,2,3). Then the 6-dimensional mapping of $(m_1,m_2,m_3,\sigma_{01},\sigma_{02},\sigma_{03})$ into $(m_1,m_2,m_3,\gamma_{1z},\gamma_{2z},\gamma_{3z})$ is also one-to-one and onto. As was the case for σ_p, a transformation is made by solving (59), (60), and (61) for the respective σ_{0j}'s and thereby substituting the γ's into (57) and (58). Also set $\gamma = \ln\left\{1/R(z)\right\}$. The resulting constrained optimization problem is then

$$\text{Maximize} \quad l \tag{62}$$

$$s.t.\ \gamma = \gamma_{1z} + \gamma_{2z} + \gamma_{3z} \tag{63}$$

with fixed γ. The resulting log likelihood is given by (45) in conjunction with (46) and (47), where now γ_{jp} is replaced by γ_{jz} for j = 1,2,3, and σ_p is replaced by z. Note that this results in only a simple change of notation so that The Lagrangian is still given by (48) and the method of solution based on (49)-(52) is applicable here.

8. Summary

In summary assume that unique MLE's of (45) exist in a neighborhood of $\hat{\sigma}_p$, and (43) and (44) have a solution. This implies that $\min_\lambda \max_{\theta\in\Theta}$ L has a solution that is equivalent through duality to that of (43) and (44), and thus (50) and (52) are met. Then (48) is optimized and the strong Lagrangian principle holds. Conversely, assume that unique MLE's of (45) exist in a neighborhood of $\hat{\sigma}_p$, and (48) is optimized. This implies that λ^* maximizes $l(\theta^*)-\lambda^*(\gamma^*_{1p}+\gamma^*_{2p}+\gamma^*_{3p})$ with θ^* in Θ and such that θ^* meets (44). Thus θ^* solves (43) and (44), the strong Lagrangian principle holds, and $\min_\lambda \max_{\theta\in\Theta}$ L has a solution that meets (44). Moreover, with only the assumption that unique MLE's of (45) exist in a neighborhood of $\hat{\sigma}_p$ it follows that $\min_\lambda \max_{\theta\in\Theta}$ L has a solution. If (44) is not met then (48) is not optimized and there is no solution to (43) *and* (44). Thus the check to verify that θ^* meets (44) completes the procedure.

The procedure for σ_p in outline is: Given p,

i. Obtain the MLE's ($\hat{m}_j$, $\hat{\sigma}_{0j}$, j = 1,2,3) via the procedures of Ref. 7 by carrying out the individual censored analyses associated with (32),

ii. Evaluate $l(\hat{m}_1,\hat{m}_2,\hat{m}_3,\hat{\sigma}_p,\hat{\sigma}_{02},\hat{\sigma}_{03}) = l(\hat{m}_1,\hat{m}_2,\hat{m}_3,\hat{\sigma}_{01},\hat{\sigma}_{02},\hat{\sigma}_{03})$,

iii. Solve (35) by iteration for $\hat{\sigma}_p$,

iv. For a given σ_p, solve $\min_\lambda \max_{\theta\in\Theta}$ L by a line search on λ through solving $\max_{\theta\in\Theta}$ L for a given λ via (50) and (52),

v. Make a check to insure that θ^* meets (44) and is the solution for the given σ_p,

vi. Evaluate $l(\hat{m}_{1\sigma_p},\hat{m}_{2\sigma_p},\hat{m}_{3\sigma_p},\sigma_p,\hat{\sigma}_{02\sigma_p}\hat{\sigma}_{03\sigma_p})$ from the value of (43) at the solution,

vii. Finally, solve (36) on σ_p via (37) to obtain the boundary points for the confidence bounds associated with $\hat{\sigma}_p$.

The procedure for $R(z)$ in outline is: Given z,

a. Obtain the MLE's ($\hat{m}_j$, $\hat{\sigma}_{0j}$, j = 1,2,3) via the procedures of Ref. 7 by carrying out the individual censored analyses associated with (32),

b. Evaluate $l(\hat{m}_1,\hat{m}_2,\hat{m}_3,\hat{R(z)},\hat{\sigma}_{02},\hat{\sigma}_{03}) = l(\hat{m}_1,\hat{m}_2,\hat{m}_3,\hat{\sigma}_{01},\hat{\sigma}_{02},\hat{\sigma}_{03})$,

c. Solve (53) directly for $\hat{R(z)}$ by employing the MLE's: $(\hat{m}_1,\hat{m}_2,\hat{m}_3,\hat{\sigma}_{01},\hat{\sigma}_{02},\hat{\sigma}_{03})$,

d. For a given γ, i.e., given $R(z)$, solve $\min_{\lambda}\max_{\theta\in\Theta} L$ by a line search on λ through solving $\max_{\theta\in\Theta} L$ for a given λ via (50) and (52), where $\theta = (m_1, m_2, m_3, \gamma_{1z}, \gamma_{2z}, \gamma_{3z})$,

e. Make a check to insure that θ^* (the solution from (d)) meets (63) and is the solution for the given $R(z)$,

f. Evaluate $l(\hat{m}_{1R(z)}, \hat{m}_{2R(z)}, \hat{m}_{3R(z)}, R(z), \hat{\sigma}_{02R(z)}\hat{\sigma}_{03R(z)})$ from the value of (62) at the solution,

g. Finally, solve (55) on $R(z)$ via (56) to obtain the boundary points for the confidence bounds associated with $\hat{R}(z)$.

Note that the two methods of solution are essentially the same. The inner optimization loops defined by (iv) and (v) for σ_p and defined by (d) and (e) for $R(z)$ are the same. The real difference in the two procedures is how the constraint is employed. In solving for σ_p, the value of the constraint is held constant at $\ln(1/(1-p))$, while the value of the constraint, $\ln(1/R(z))$, varies in obtaining the solution for $R(z)$. Also the right hand side of the constraint is handled differently in the two approaches. In solving for σ_p, the iteration value of σ_p varies, while in iterating for $R(z)$ the value of z is held constant. This is a very symmetric exchange between the two methods--it should be studied further. Of course, if confidence limits on more than one quantile are desired, p would vary, but this constitutes a completely new problem. Similar comments apply in obtaining confidence limits for reliabilities for more than one strength, z.

REFERENCES

7. Alonso Peralta, "Statistical Methods Development Summary Report," Report No. 32-3722, AlliedSignal Aerospace Company, Garrett Auxiliary Power Division, Phoenix, 1991.

8. W.T. Tucker and C.A. Johnson, "Multiaxial Equivalent of Stressed Volume", Life Prediction Methodology for Ceramic Material, ASTM STP 1201. C.R. Brinkman, S.F. Duffy (eds), pp. 263-279, American Society for Testing and Materials (ASTM), 1993.

9. Peter Whittle, *Optimization under Constraints*, John Wiley & Sons, New York, 1971.

10. A.M. Mood, F.A. Graybill, and D.C. Boes, *Introduction to the Theory of Statistics*, 3rd Ed., McGraw-Hill Book Company, New York, 1974.

11. R. Fletcher, *Practical Methods of Optimization*, 2nd Ed., John Wiley & Sons, New York, 1987.

12. D.G. Luenberger, *Linear and Nonlinear Programming*, 2nd Ed., Addison-Wesley Publishing Company, Reading, Massachusetts, 1984.

13. J. Stoer, "Principles of Sequential Quadratic Programming Methods for Solving Nonlinear Programs," *NATO ASI Series*, F15, Computational Mathematical Programming, Ed. K. Schittkowski, Springer-Verlag, Berlin, 1985.

APPENDIX VII

WEIBULL STRENGTH PLOTS FOR FAST FRACTURE TEST SPECIMENS

(32 pages)

WEIBULL STRENGTH PLOTS FOR FAST FRACTURE SPECIMENS

Weibull strength plots for all flexure and tensile fast fracture data are provided in this Appendix. The median estimates of the reliability lines were calculated with the maximum likelihood. Confidence intervals were calculated with the bootstrap technique. Both methods are described in section 5.2. Interpretation of these data and parameters are provided in section 5.3.2.

Weibull plots are included for each data set listed in Table VII-1. Each failure mode is plotted separately. Failures not from the mode being plotted were censored. These plots have two estimates of the median reliability line; a solid line calculated from maximum likelihood, and a dashed line, which is the median reliability value at each stress calculated from 1000 bootstrap simulations. The bootstrap simulations were generated from the maximum likelihood parameter estimates used to plot the solid line. Therefore, the difference between the solid and dashed median lines indicates the bias associated with the bootstrap simulations.

TABLE VII-1. WEIBULL STRENGTH PARAMETER ESTIMATES AND 95 PERCENT CONFIDENCE BOUNDS FOR INDIVIDUAL AND POOLED DATA SETS

			Surface							Volume							Chamfer						
Specimen	Temp.	Total No.	No.	σ_0	-	+	m	-	+	No.	σ_0	-	+	m	-	+	No.	σ_0	-	+	m	-	+
Mil-A	70	60	10	126.2	114.3	134.3	25.7	16	38	1	27.5	0	81.6	4.1	0.26	15.7	49	140.9	136.2	145.9	8.46	6.87	10.82
Mil-B	70	60	17	119.2	107.4	128.3	12.2	8.24	16.7	5	49.3	18.8	1000	6.62	2.77	12.5	38	168.4	159.2	182.9	5.89	4.42	7.6
Mil-B	1800	30	23	78.3	67.9	87.1	8.07	5.97	10.4	0							7	158.4	139.7	222.8	6.47	3.33	10.38
Mil-B	2100	30	23	75	67.6	80.7	12.5	9.09	16.26	1	713	27.2	1000	23.2	4.25	58.4	6	119.4	110.9	148	11.6	5.66	19
Mil-B	2200	30	24	86	81.5	89.3	28.8	20.7	38.2	1	60	0	68.2	15.7	1.05	54.4	5	107.7	103.9	120.5	27.2	12	48.7
Mil-B	2300	30	22	80.1	73.7	84.8	17.5	12.5	23.2	0							7	109	105.5	118	21.5	11.8	33.4
Mil-B	2400	28	18	77.2	71	81.5	20.6	13.7	29	1	73.4	27.4	76.1	40	4.7	109.9	9	97.8	96	101.8	31.7	18.5	48.2
Mil-B	2500	29	21	78.3	82.5	85.4	33.1	23.2	45	4	59	33.5	66.3	21.7	7.81	43.6	4	100.2	96.5	115.4	25.8	9.6	50.7
Size-E	70	100	50	103.6	99.6	107.5	8.06	6.47	9.82	15	67.4	56.7	76.8	7.98	5.23	11.29	35	210.5	179.8	269.7	4.34	3.2	5.67
Tensile	70	7	1	120.1	87.5	1E+05	4.71	0.344	16.5	1	48.7	14.8	8770	3.58	0.24	12.9	4	Button head					
Tensile	70	93	24	118.4	112.8	126.2	7.6	5.52	9.98	68	63.2	56.6	69.1	7.97	6.63	9.4	1	Surface inclusion					
Tensile	70	100	25	118.7	113.1	126.5	7.69	5.6	10.1	69	62.9	56.5	68.8	7.89	6.58	9.32							
Tensile	2100	5	0							5	56.9	39.4	59.4	16.1	7.18	28.5							
Tensile	2200	20	1	96.6	78.9	26000	7.53	0.67	21.4	18	38.7	30	46	7.45	5.13	10.11	1						
Combined																							
Tensile		125	26	119.2	113.9	127	7.75	5.94	10.8	92	63.2	58.2	69.6	7.97	6.96	9.57							
ALL 70F		320	42	116.5	112.8	121.1	9.74	8.24	11.6	90	64.9	60.2	70.5	8.26	7.2	9.86							
70 to 2200F		405	89	116.7	113	120.6	9.99	8.78	11.63	114	65.7	61.4	70.9	8.45	7.45	9.85							

The methods described in section 5.2 allowed plotting of the data and lines to any arbitrary size. Standard sizes were selected (length, area, and volume) that would put the data near the center of the plots for the diverse number of specimens sizes. The use of a standard size results in the center of the data not always being plotted near the 50-percent failure probability, which results in an unconventional appearance compared with more conventional, non-size-scaled Weibull plots.

The 95-percent confidence bounds are plotted in each figure. These were generated from 1000 simulations, using the bootstrap technique described in section 5.2.4. The likelihood ratio technique was not used for calculating confidence intervals, because it is not sufficiently advanced to handle pooled strength data from multiple temperatures.

The data were plotted using a re-ranking technique, described in section 5.2.3, to adjust the ranks for the censored data. This plotting technique provides some physical evidence of the quality of the maximum likelihood estimated line relative to the data. However, since these rank positions calculated in the plotting technique are not used in the maximum likelihood line estimates some discrepancy is expected between the plotted data and predicted lines. This can be more pronounced with small sample sizes.

The objective of the pooled data analyses was to obtain a large combined set of data for confirmatory specimen predictions. Weibull plots for the pooled data set used for confirmatory specimen predictions are shown in Figures VII-1, and VII-2. The approach used to decide which groups of specimens should be pooled is described in section 5.3.2.

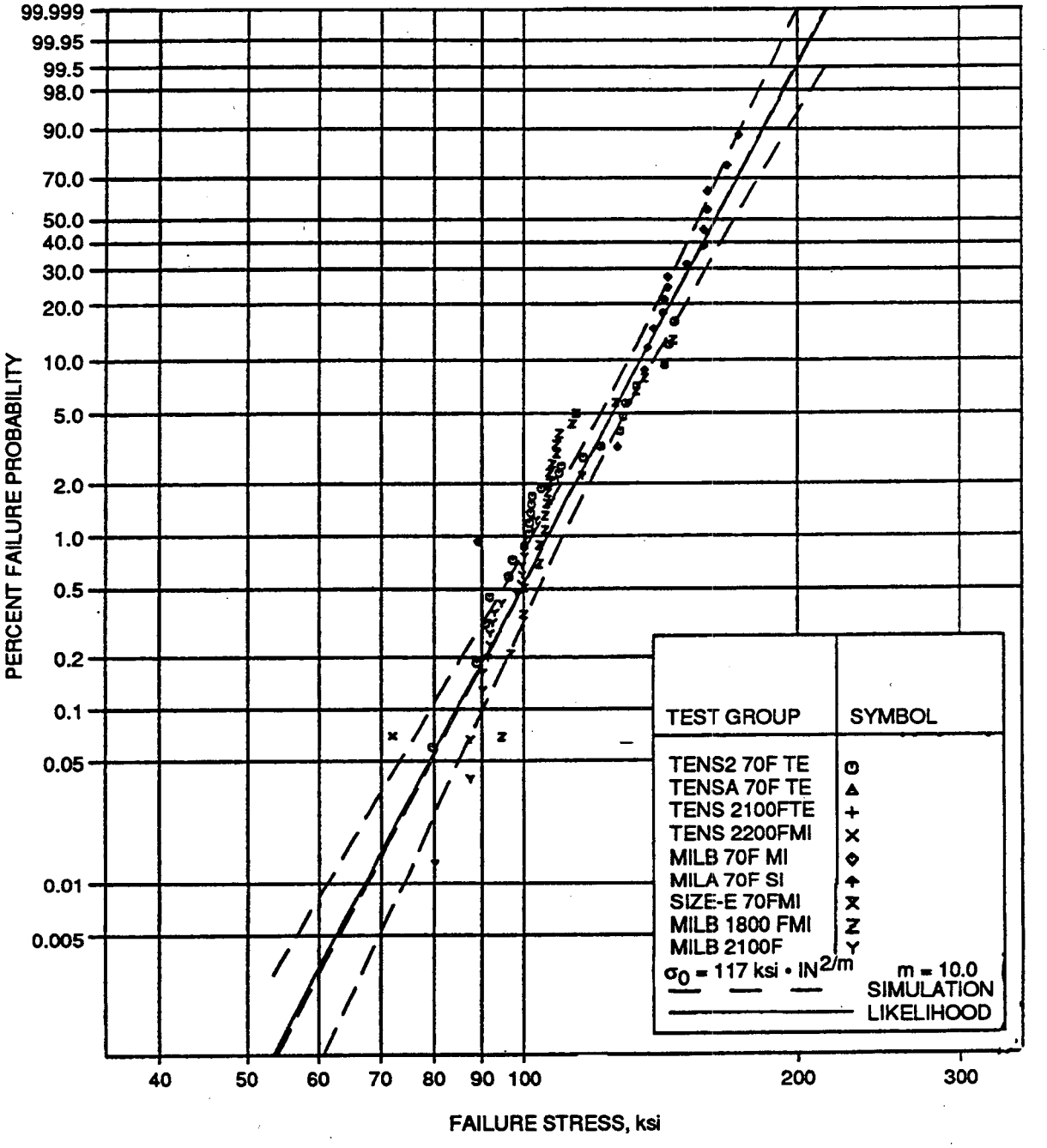

GC11591-778

Figure VII-1. Surface Strength Estimated From Nine Pooled Sets Of Specimen Data. These Parameter Estimates Were Used For Predicting Confirmatory Specimen Failure Probabilities.

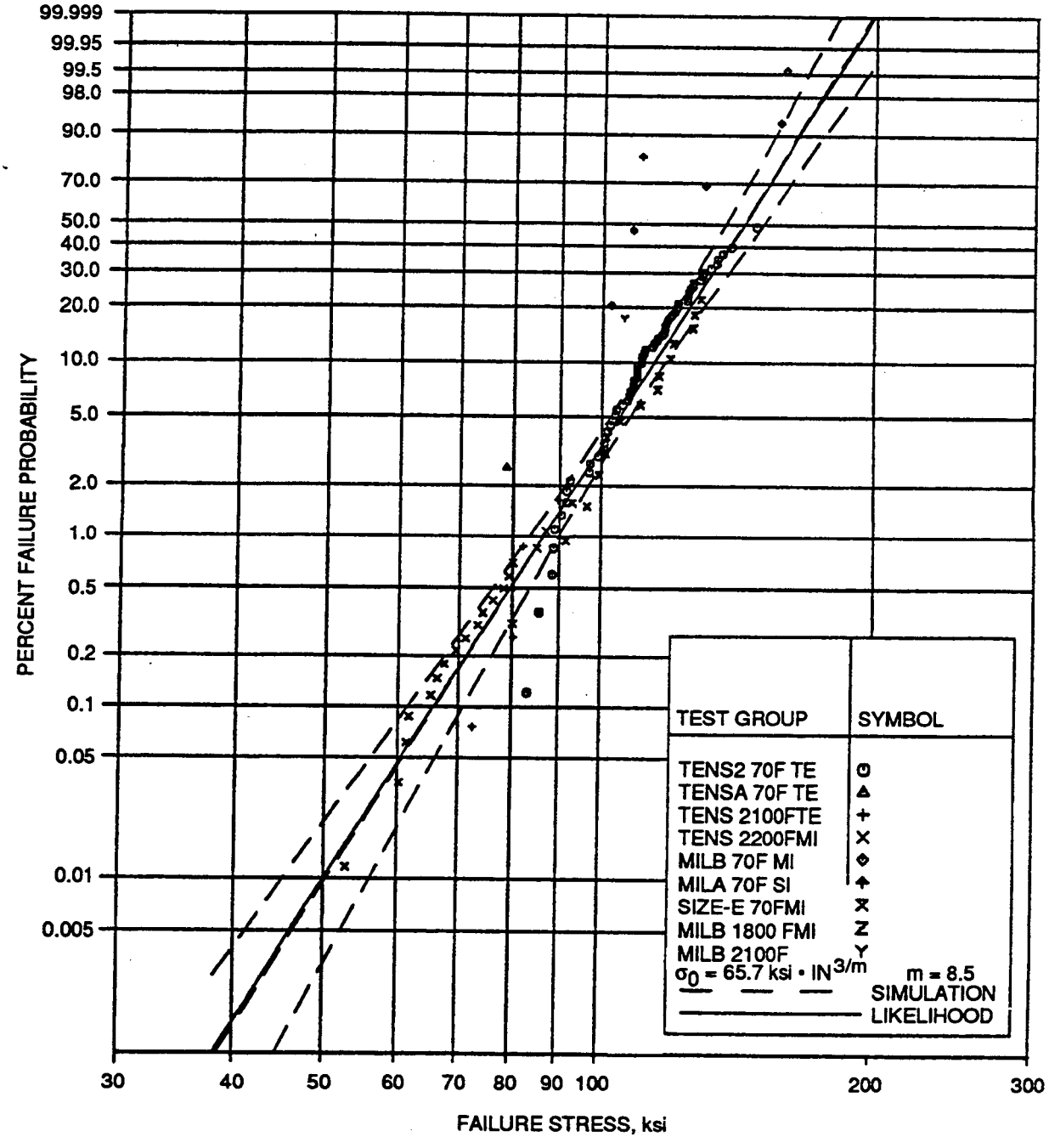

Figure VII-2. Volume Strength Estimated From Nine Pooled Sets Of Specimen Data. These Parameter Estimates Were Used For Predicting Confirmatory Specimen Failure Probabilities.

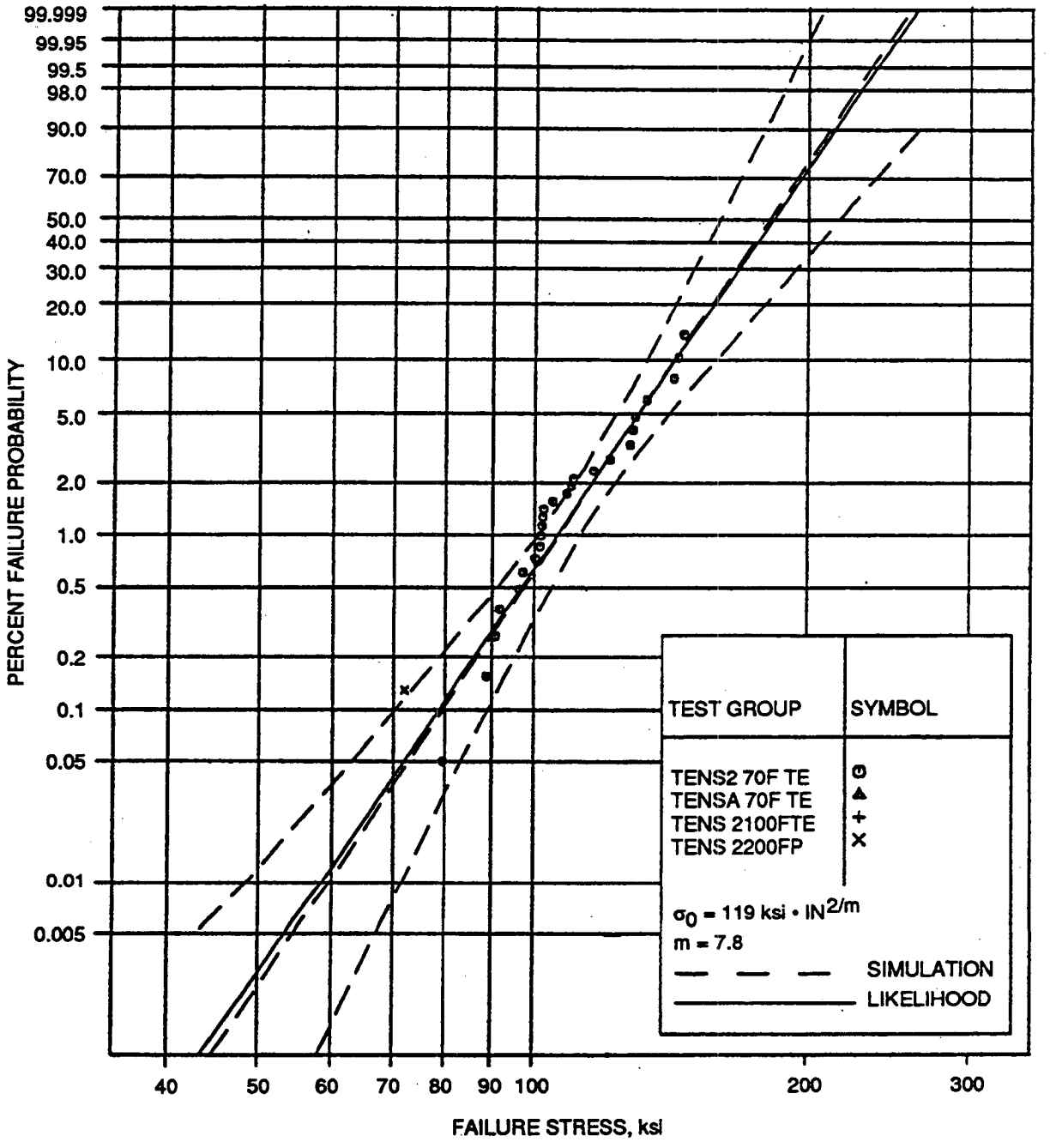

Figure VII-3. Surface Strength Estimated From Four Pooled Sets Of Tensile Specimen Data Tested At Three Temperatures.

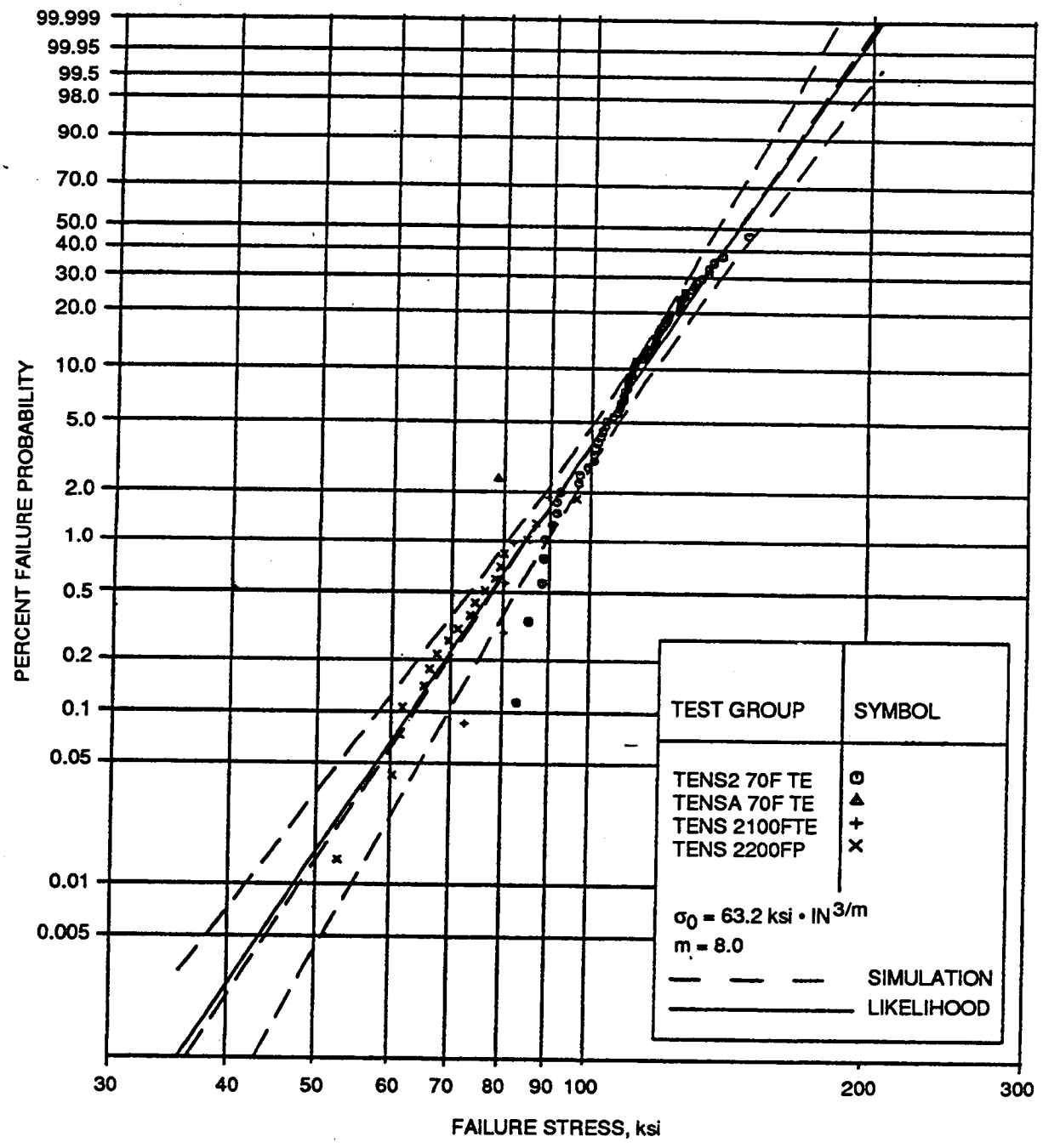

Figure VII-4. Volume Strength Estimated From Four Pooled Sets Of Tensile Specimen Data Tested At Three Temperatures.

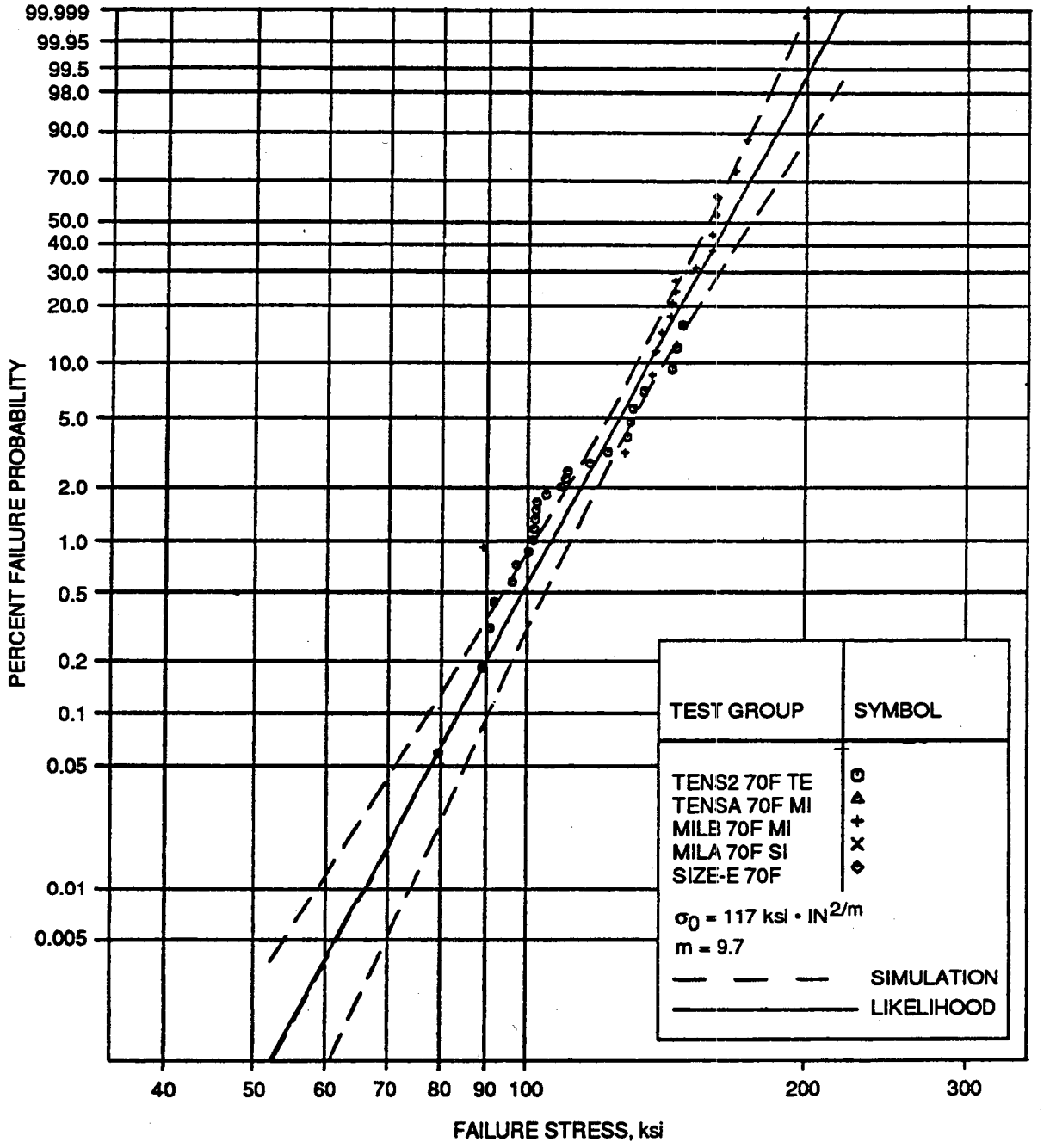

Figure VII-5. Surface Strength Estimated From Room Temperature Strength Data. Data From Four Types Of Specimens Are Pooled.

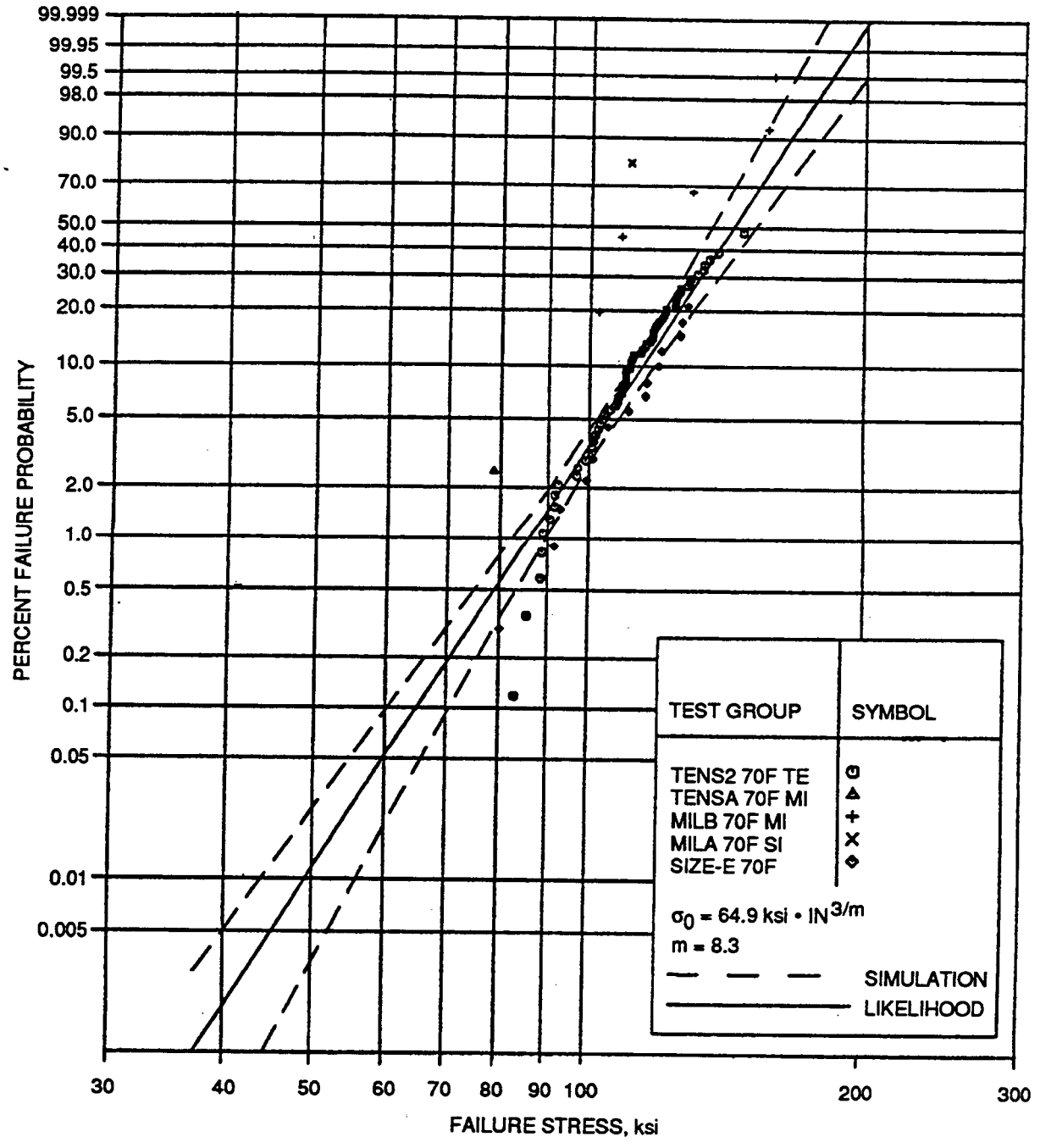

Figure VII-6. Volume Strength Estimated From Room Temperature Strength Data. Data From Four Types Of Specimens Are Pooled.

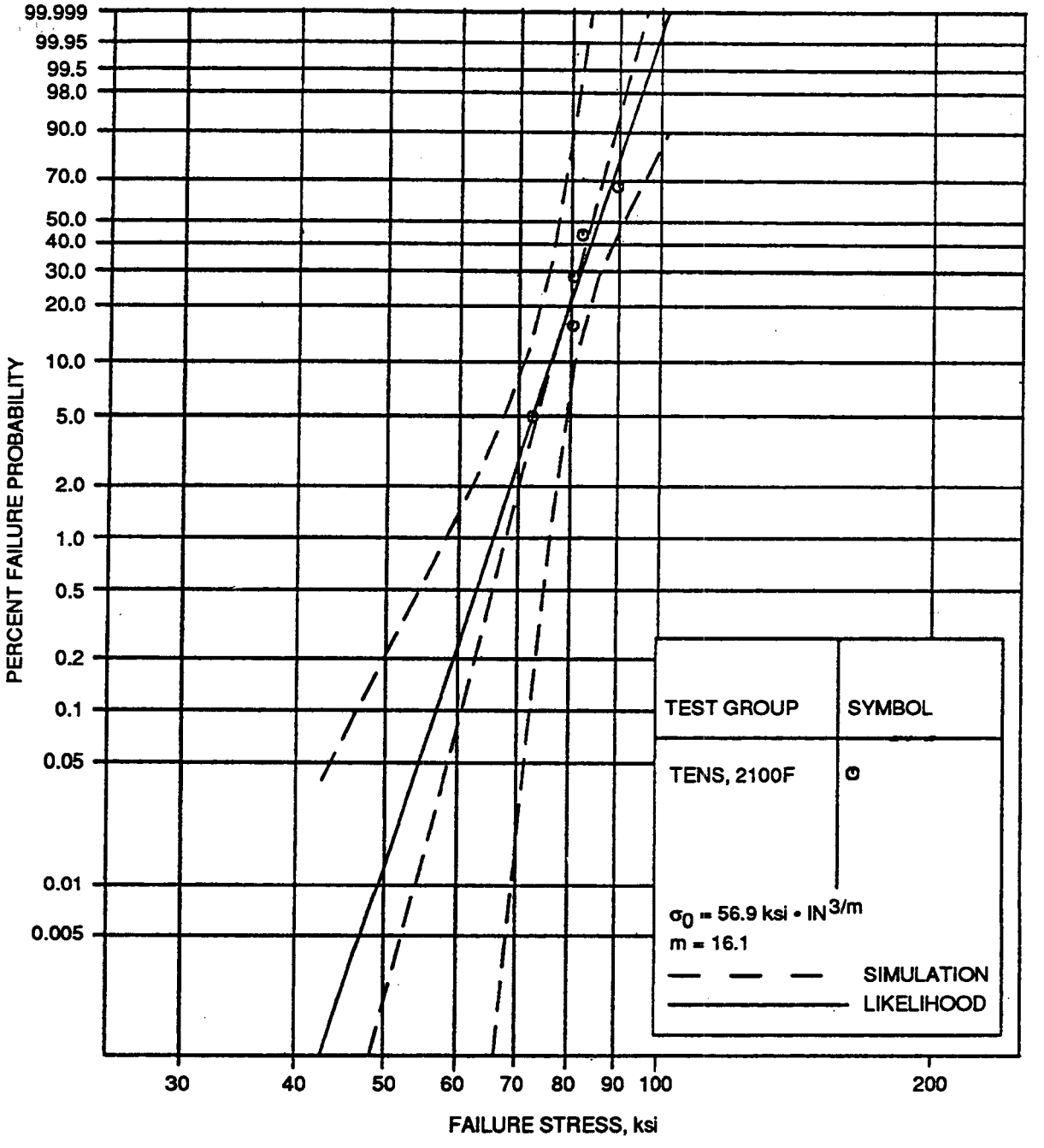

Figure VII-7. Volume Strength Estimated From 2100F Tensile Data.

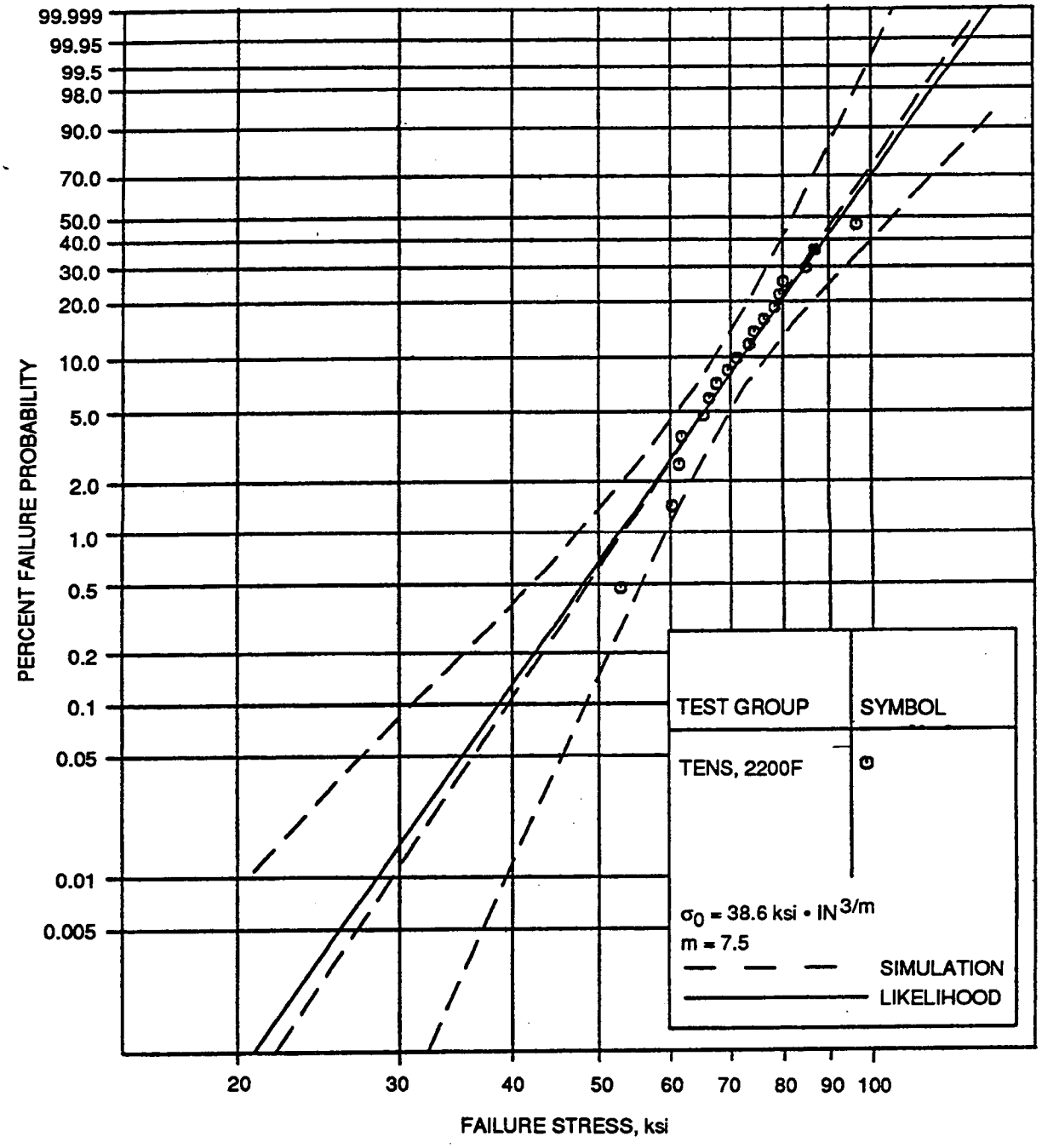

Figure VII-8. Volume Strength Estimated From 2200F Tensile Data.

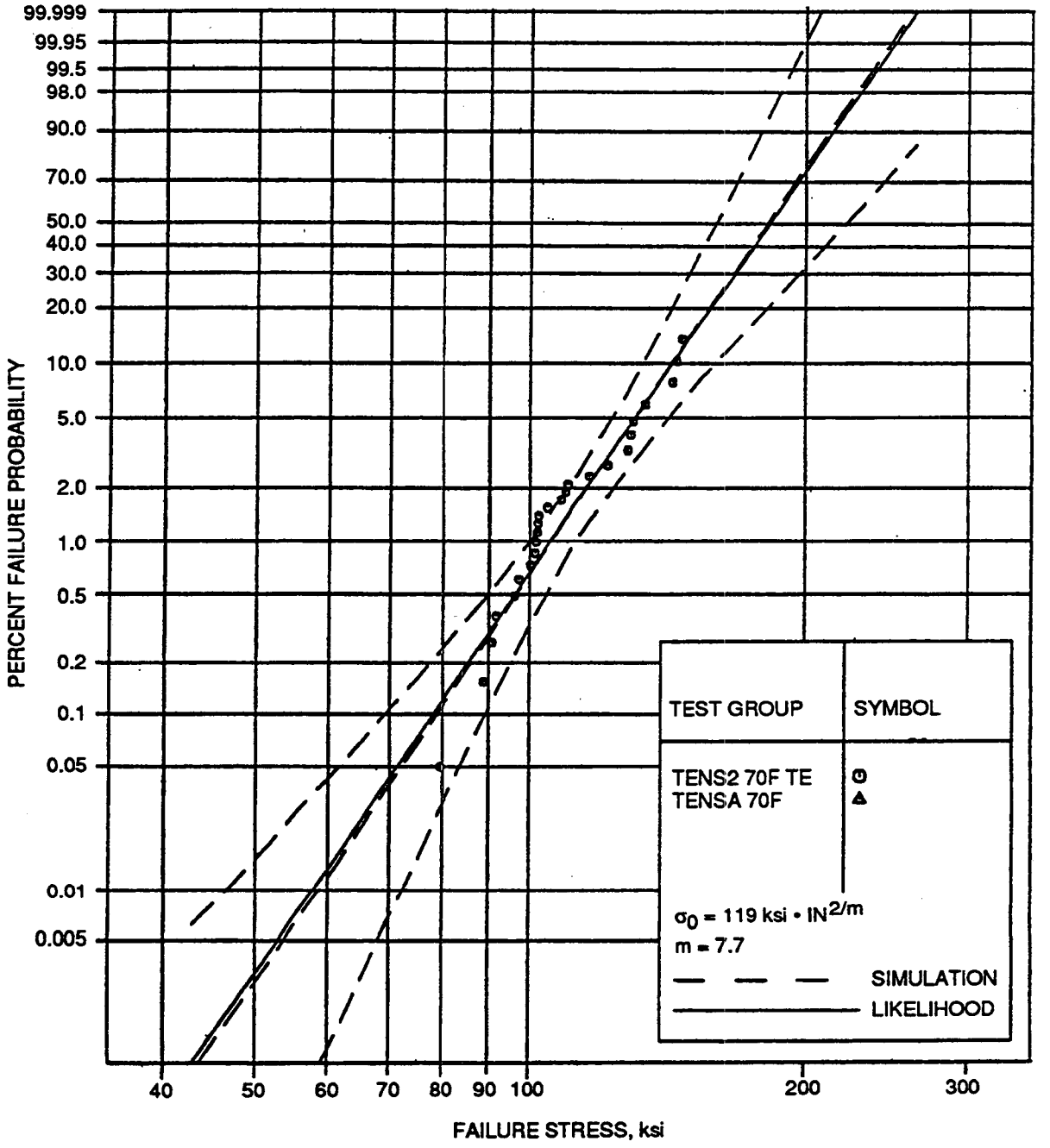

Figure VII-9. Surface Strength Estimated From Room Temperature Tensile Data.

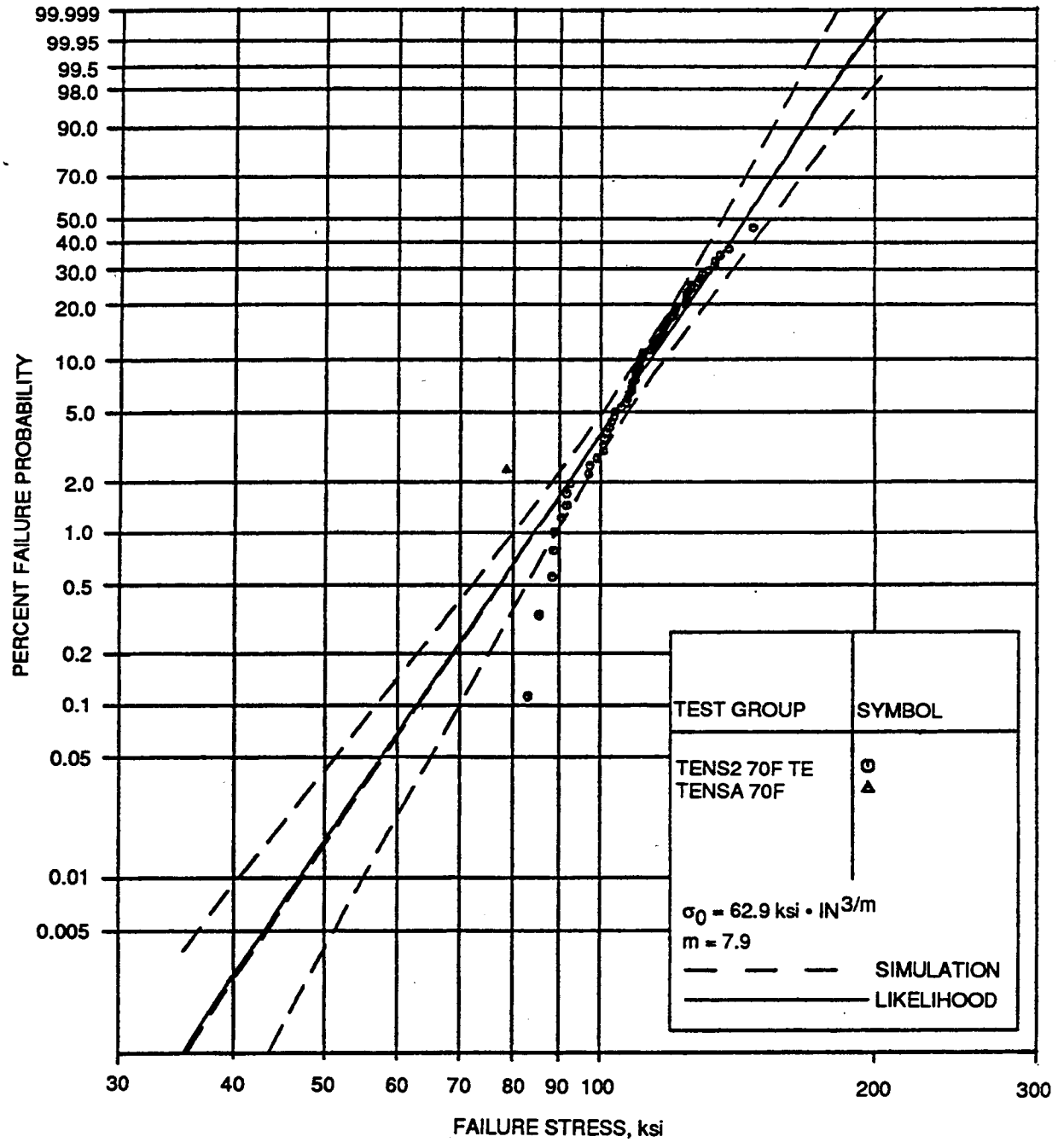

Figure VII-10. Volume Strength Estimated From Room Temperature Tensile Data.

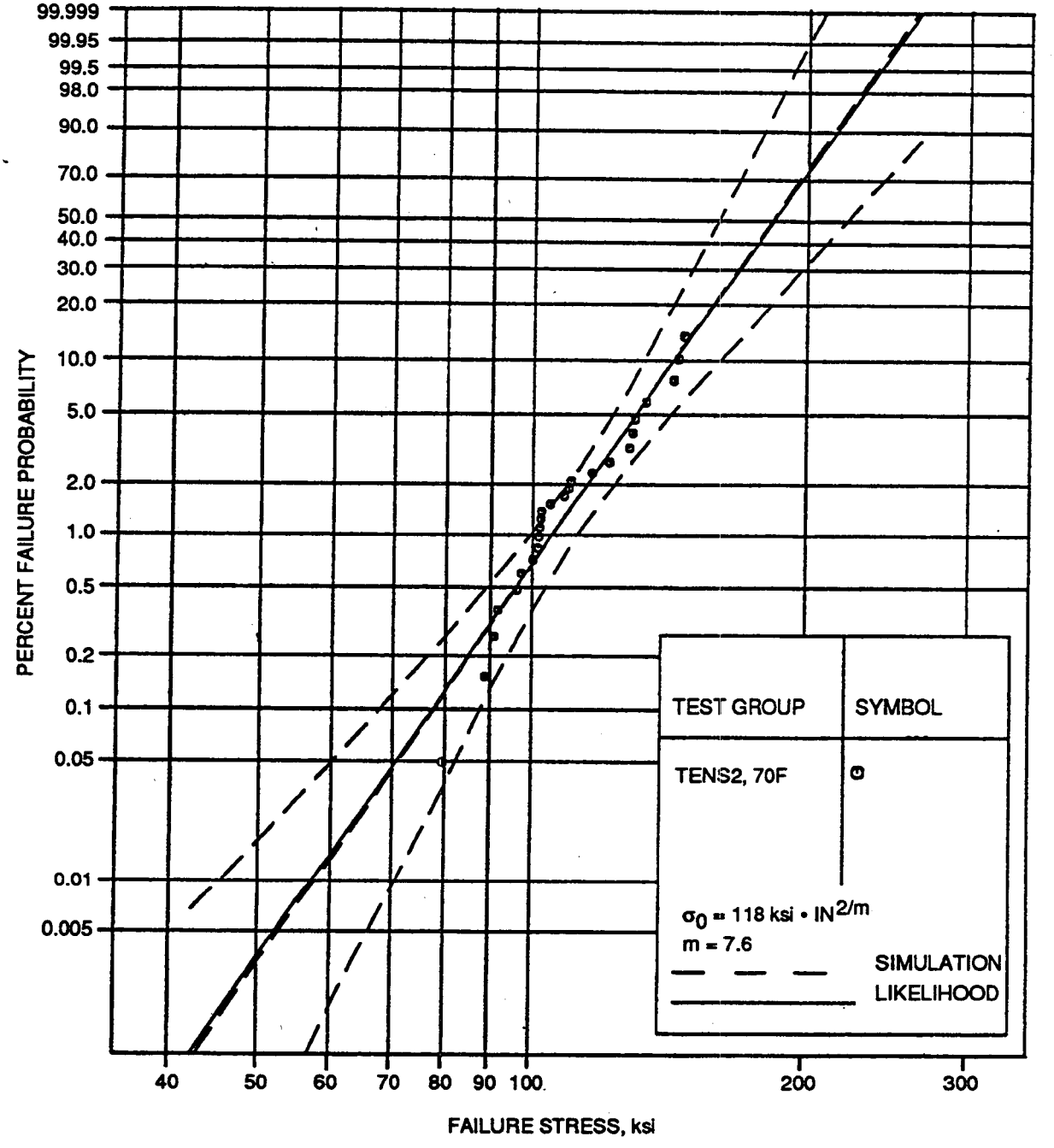

Figure VII-11. Surface Strength Estimated From Room Temperature Tensile Tests Run With Copper Collets.

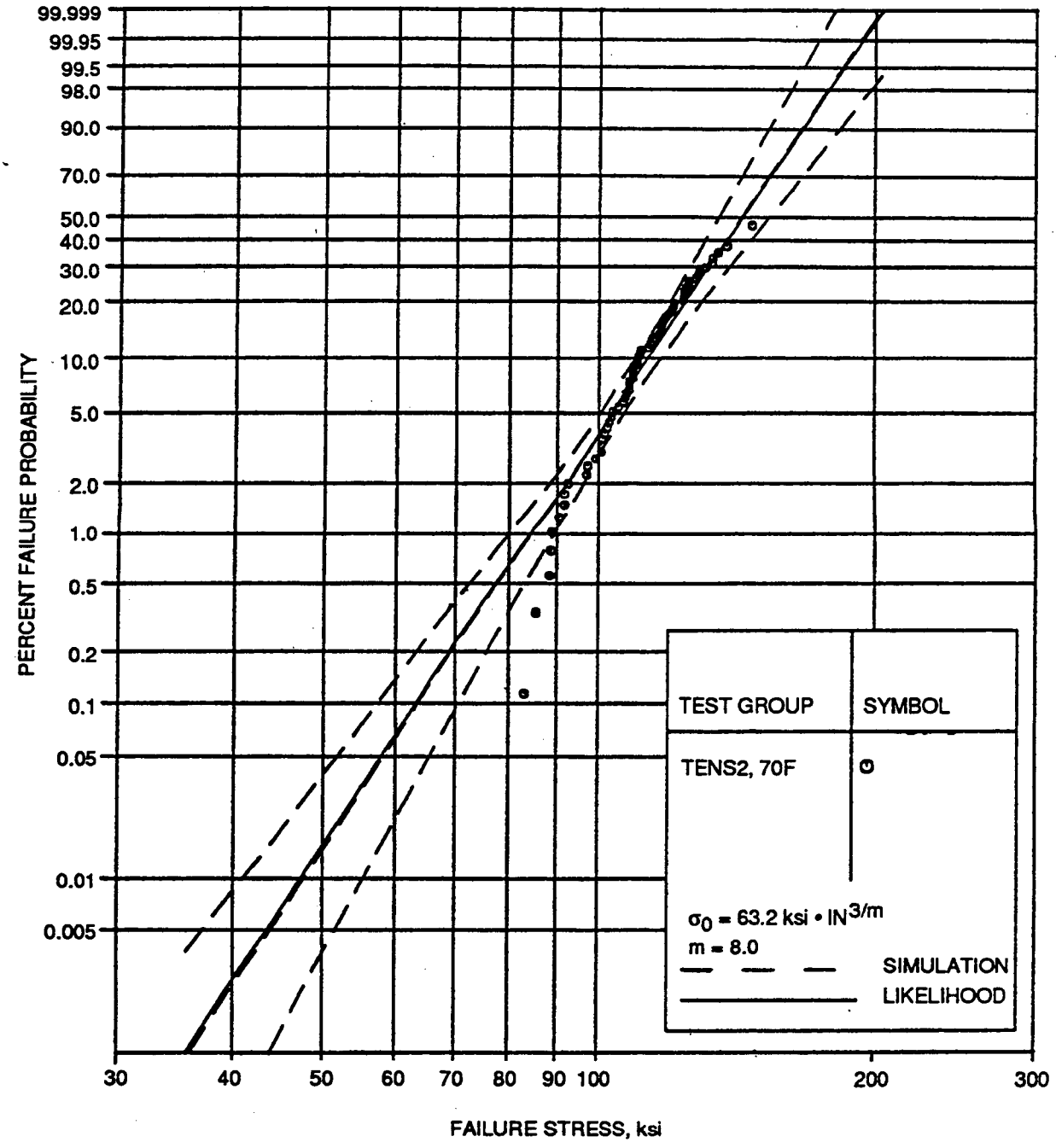

Figure VII-12. Volume Strength Estimated From Room Temperature Tensile Tests Run With Copper Collets.

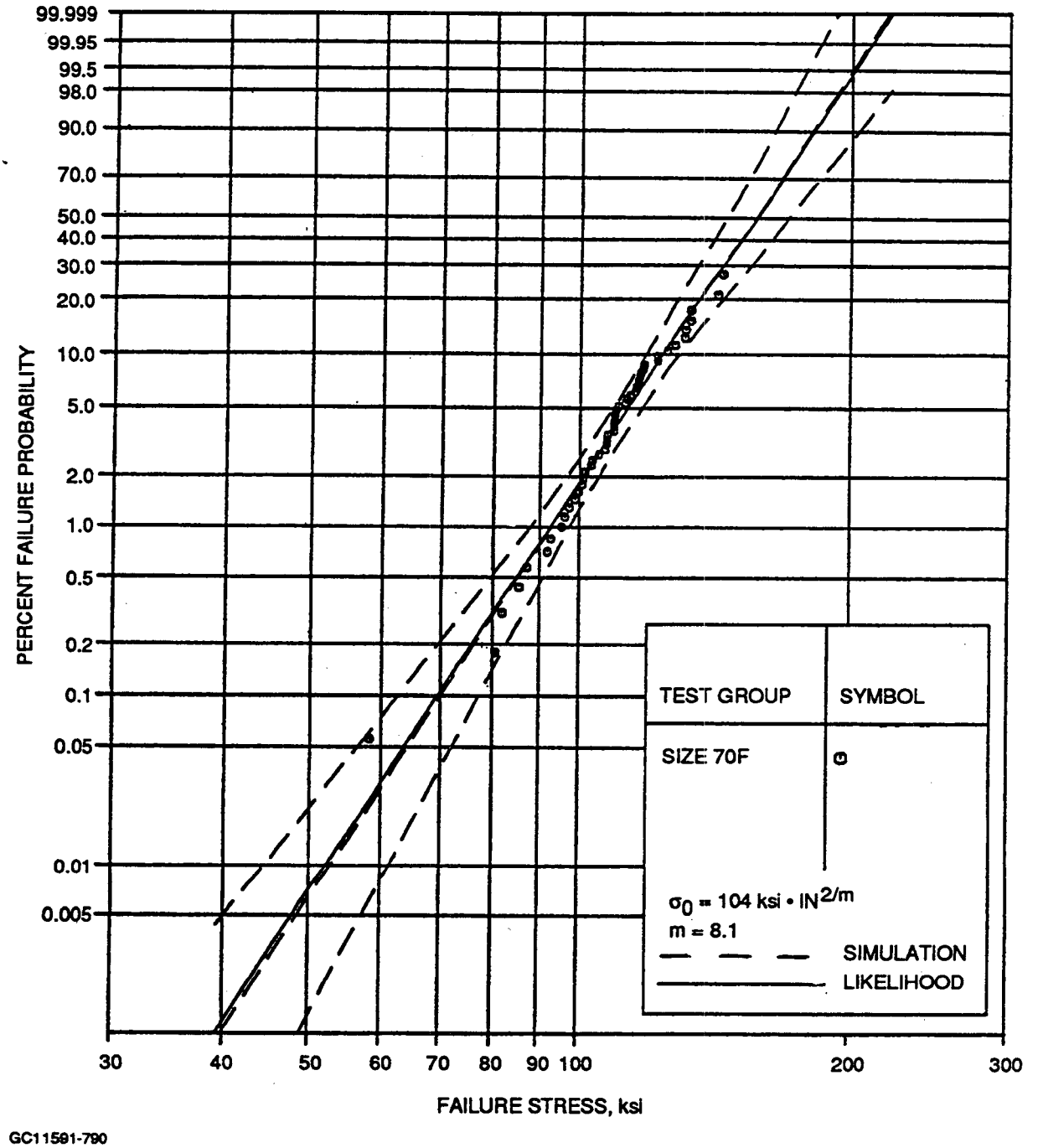

Figure VII-13. Surface Strength Estimated From Size-E Flexure Specimens Tested At Room Temperature.

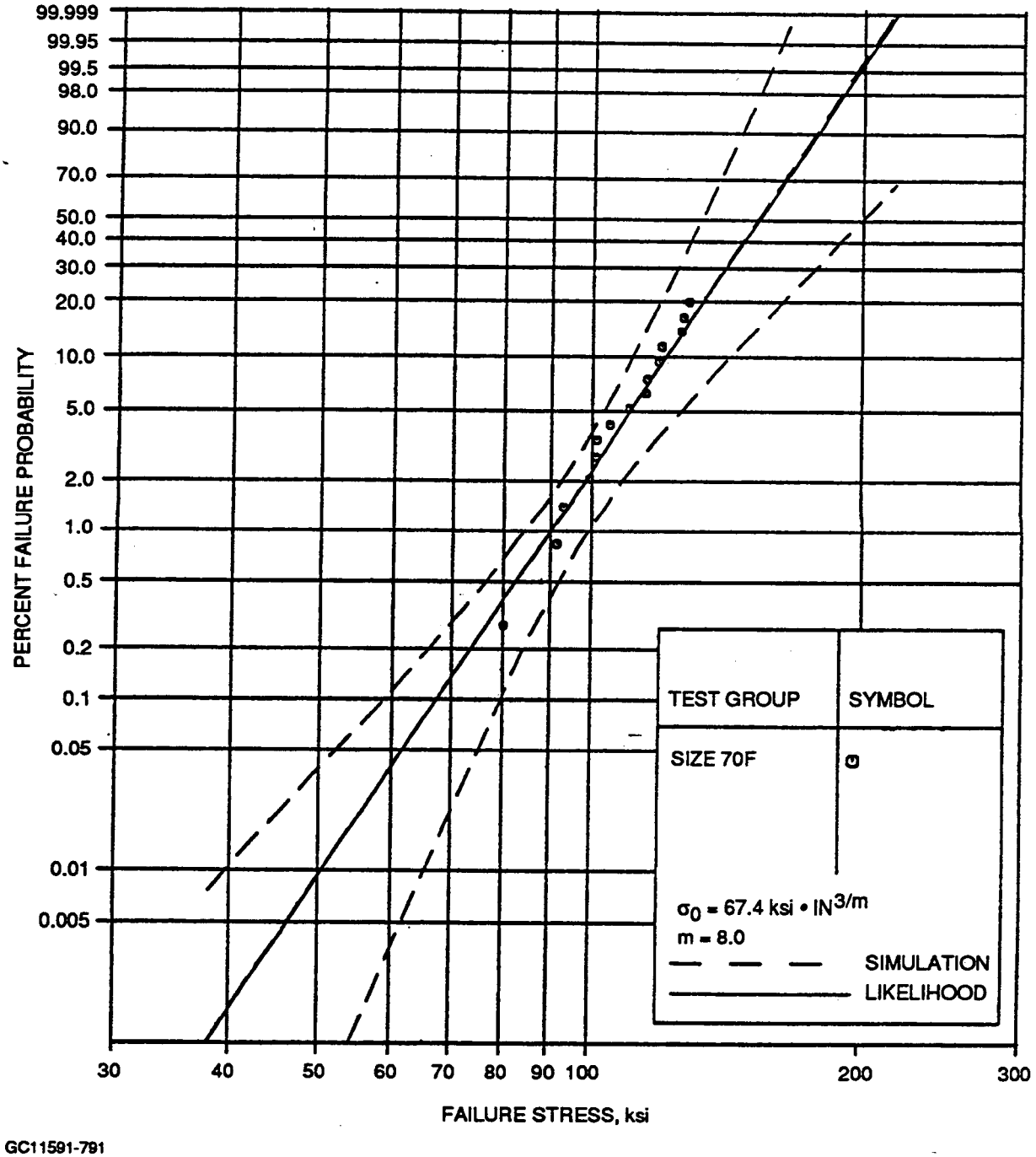

Figure VII-14. Volume Strength Estimated From Size-E Flexure Specimens Tested At Room Temperature.

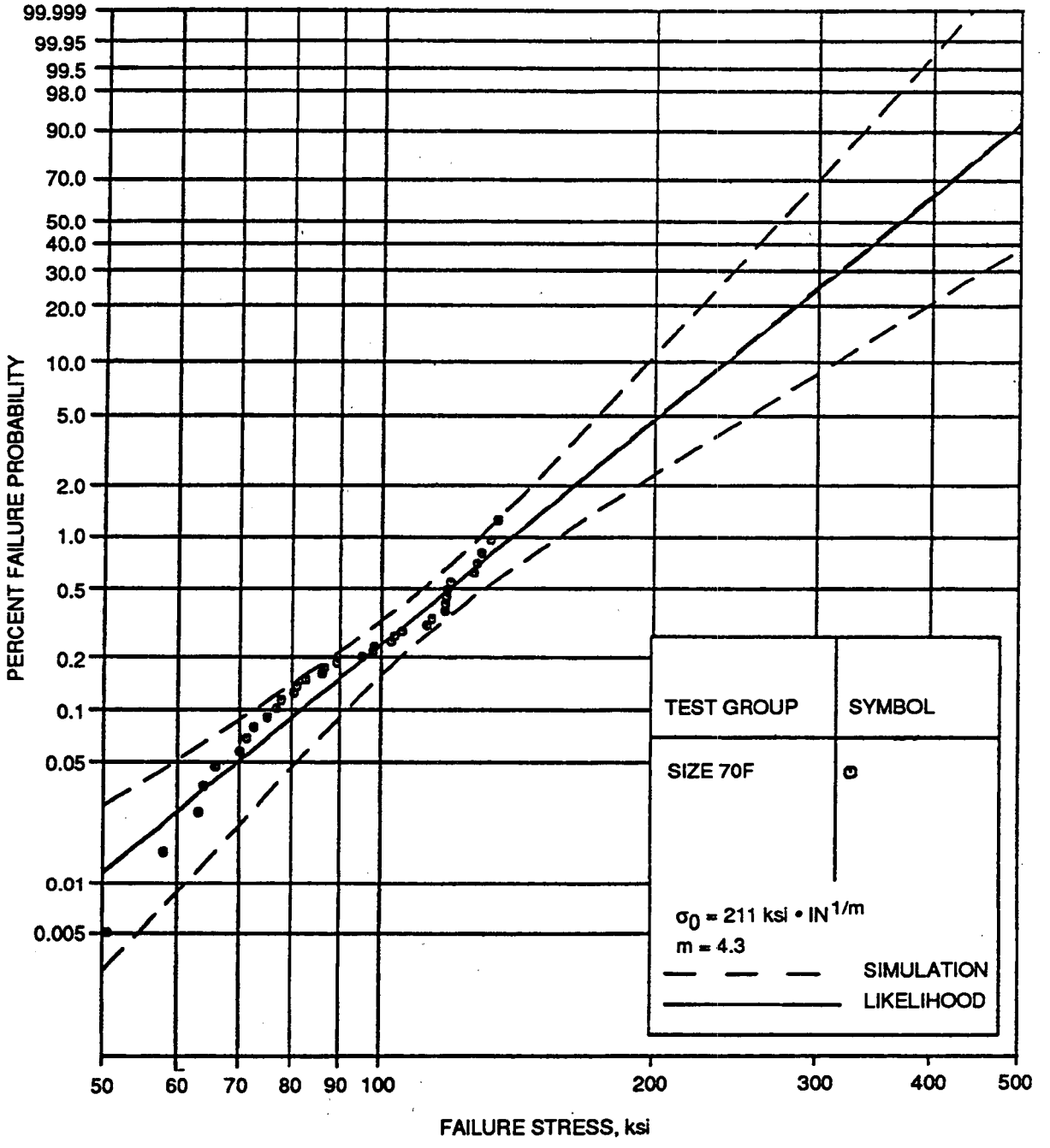

Figure VII-15. Chamfer Strength Estimated From Size-E Flexure Specimens Tested At Room Temperature.

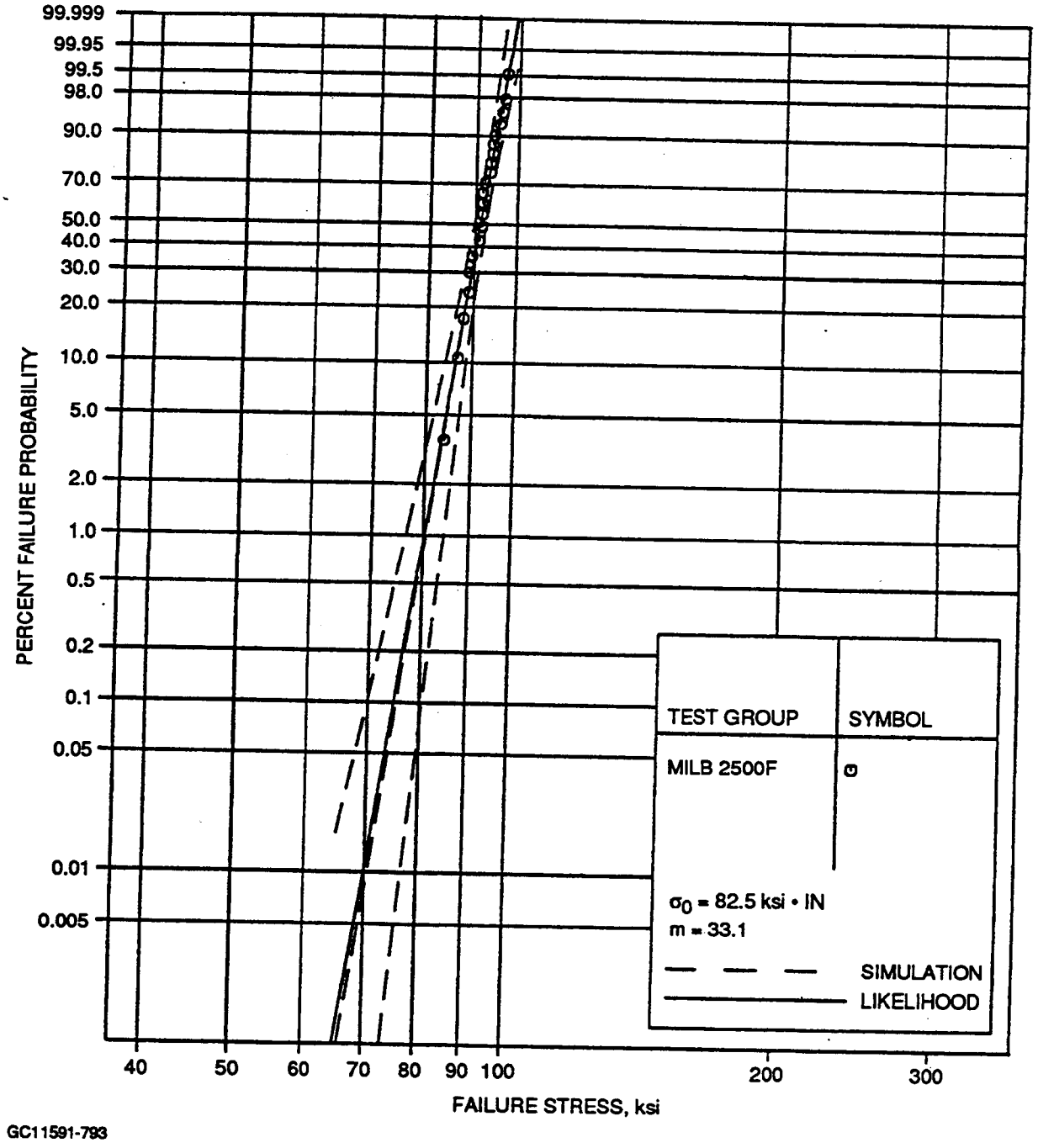

Figure VII-16. Surface Strength Estimated From MIL-B Flexure Specimens Tested At 2500F.

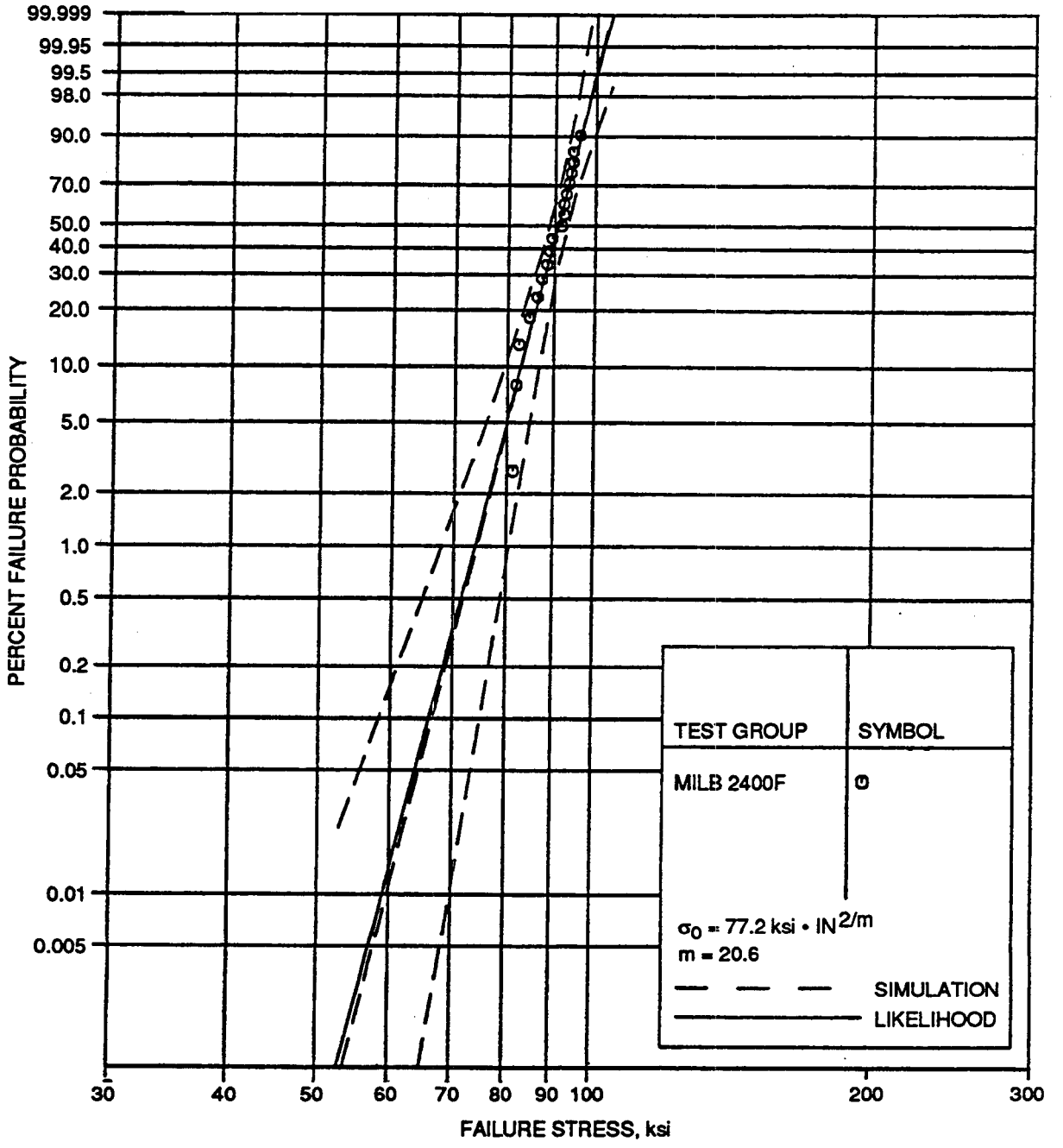

Figure VII-17. Surface Strength Estimated From MIL-B Flexure Specimens Tested At 2400F.

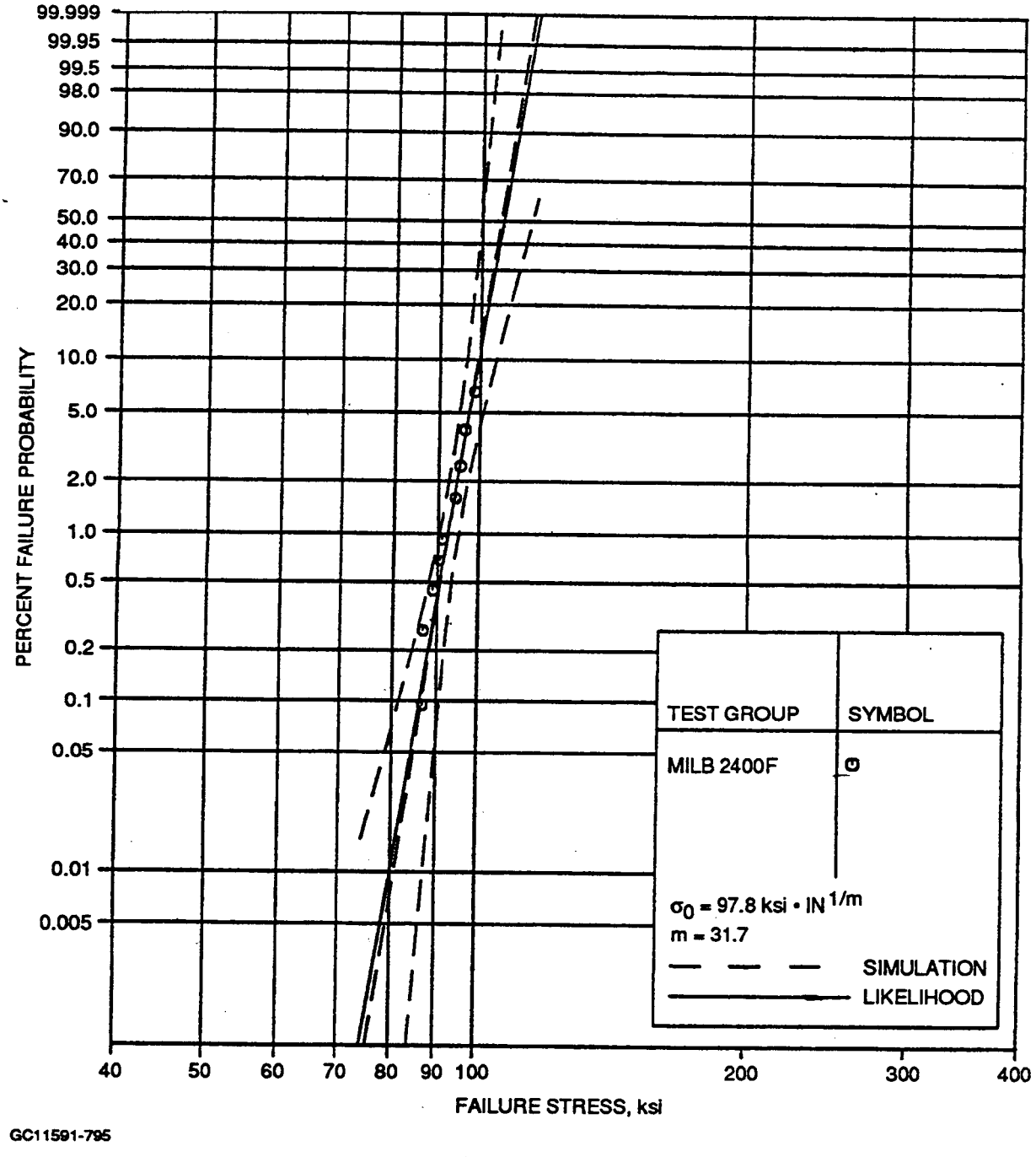

Figure VII-18. Chamfer Strength Estimated From MIL-B Flexure Specimens Tested At 2400F.

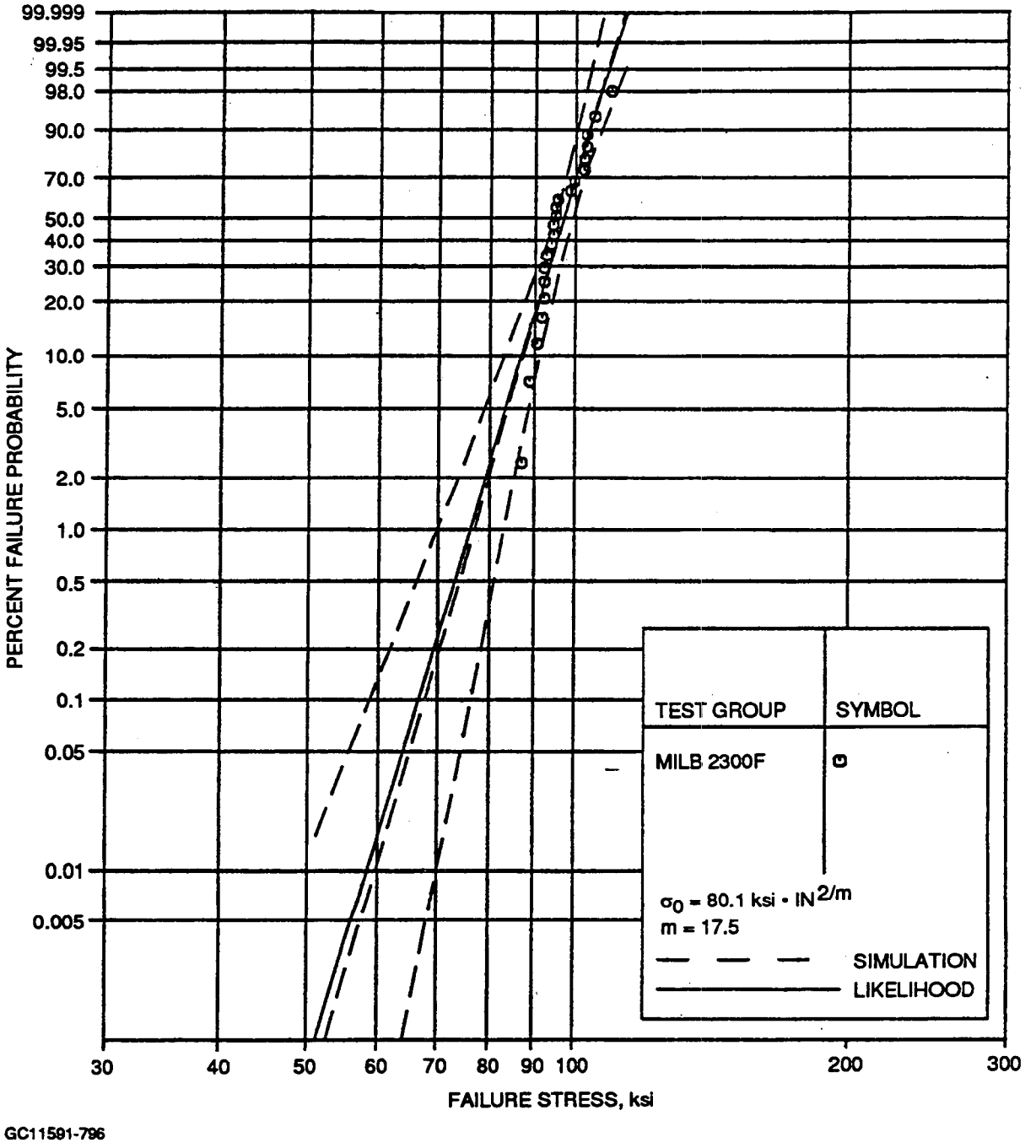

Figure VII-19. Surface Strength Estimated From MIL-B Flexure Specimens Tested At 2300F.

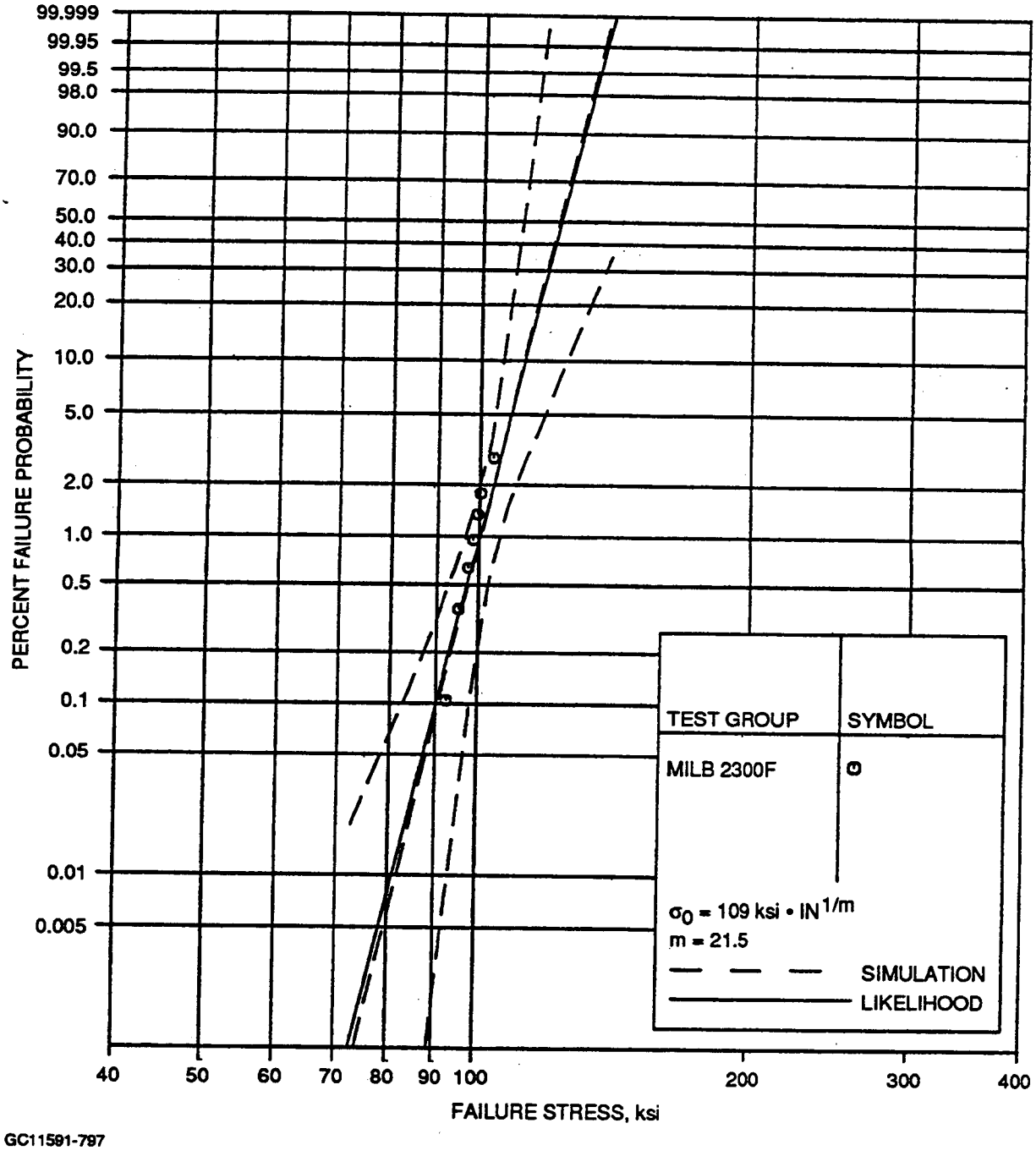

Figure VII-20. Chamfer Strength Estimated From MIL-B Flexure Specimens Tested At 2300F.

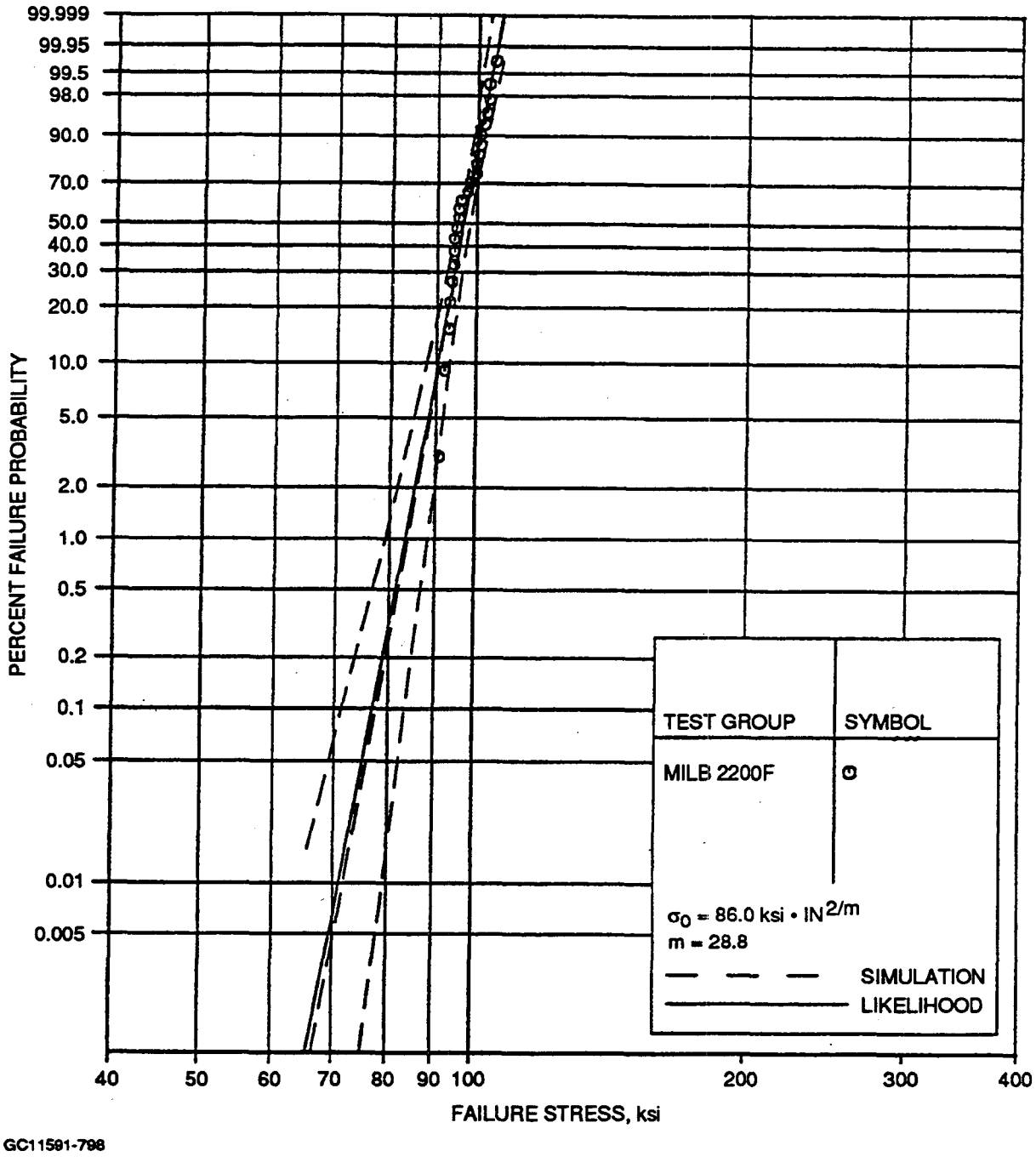

Figure VII-21. Surface Strength Estimated From MIL-B Flexure Specimens Tested At 2200F.

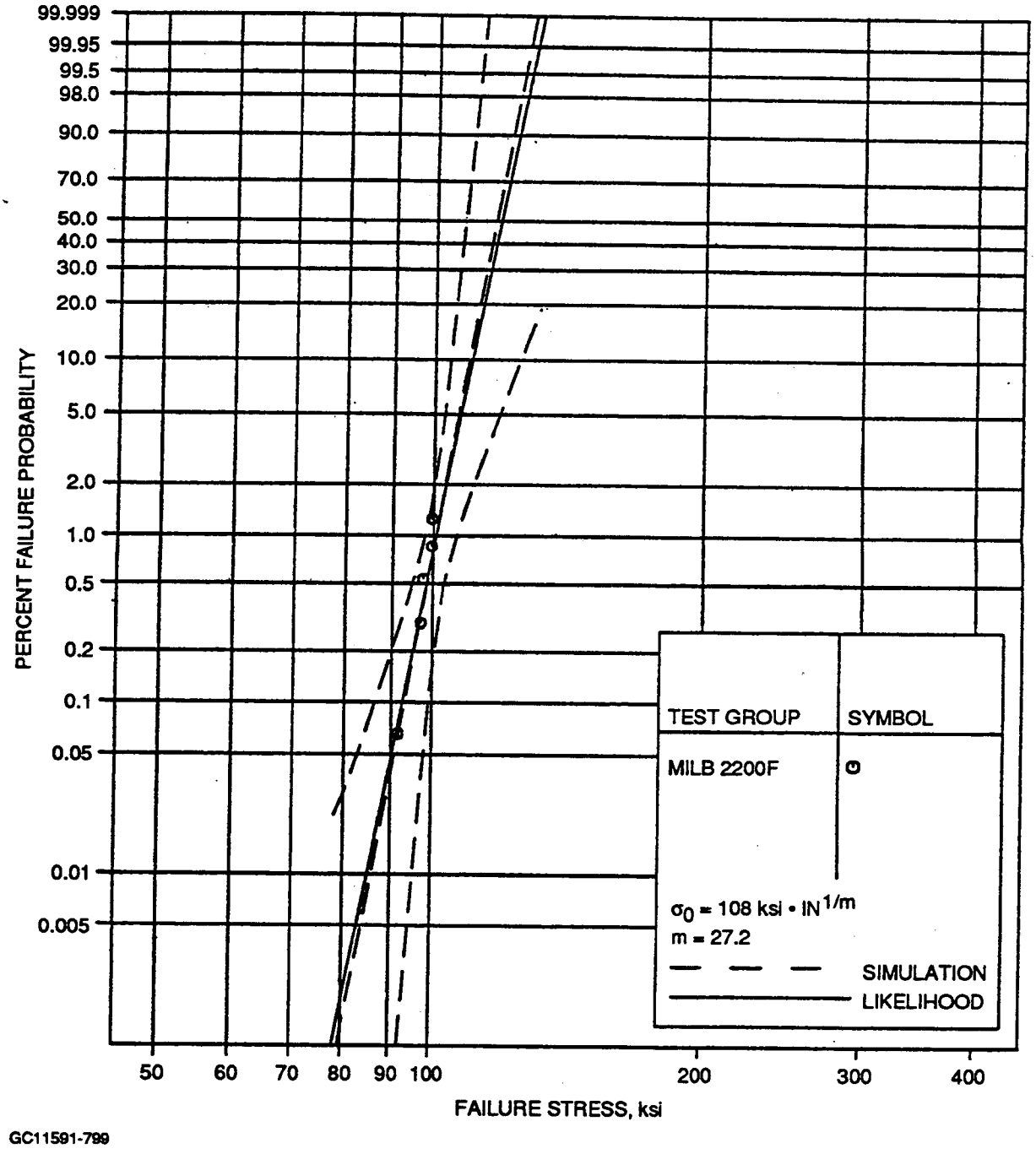

Figure VII-22. Chamfer Strength Estimated From MIL-B Flexure Specimens Tested At 2200F.

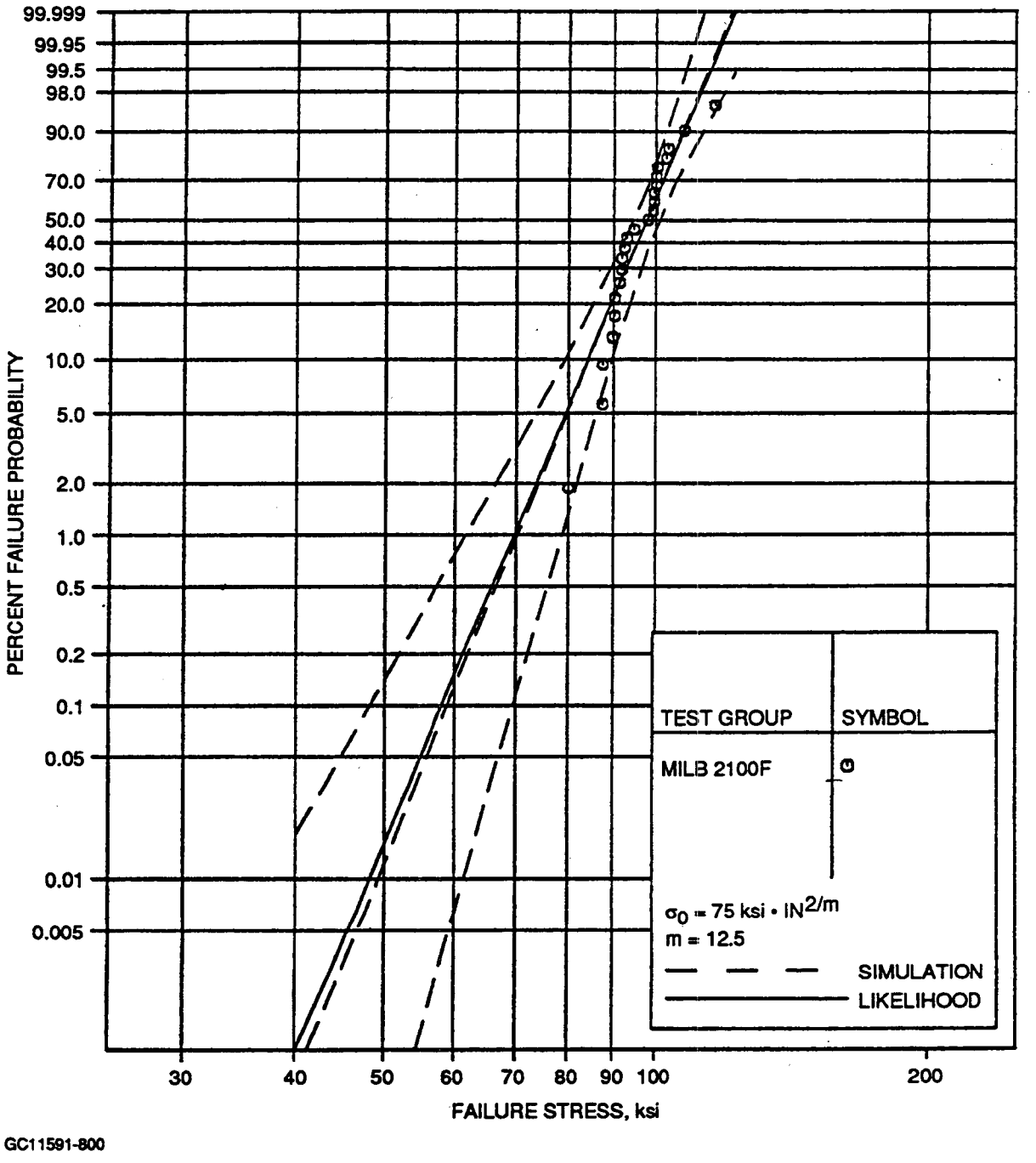

Figure VII-23. Surface Strength Estimated From MIL-B Flexure Specimens Tested At 2100F.

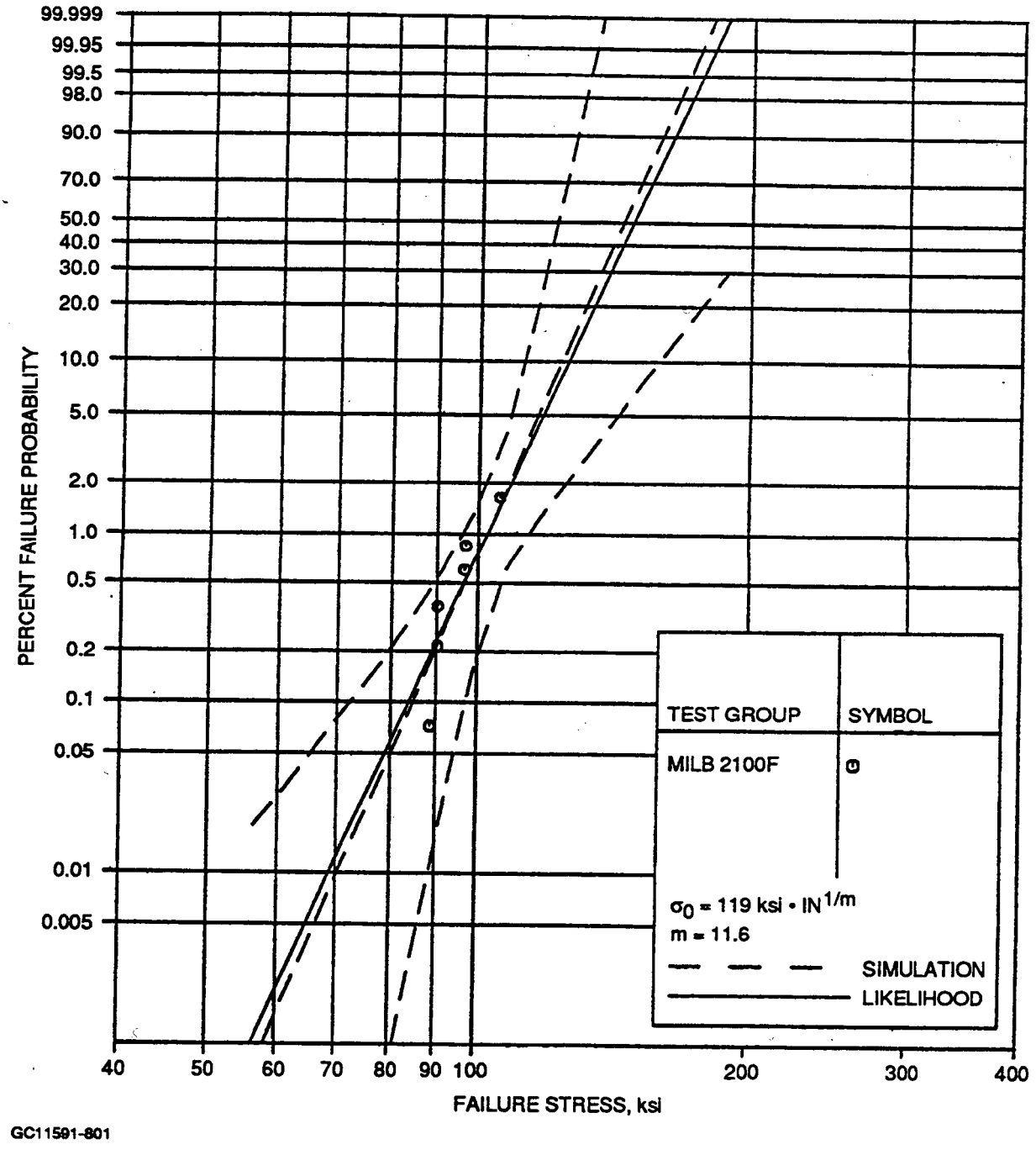

Figure VII-24. Chamfer Strength Estimated From MIL-B Flexure Specimens Tested At 2100F.

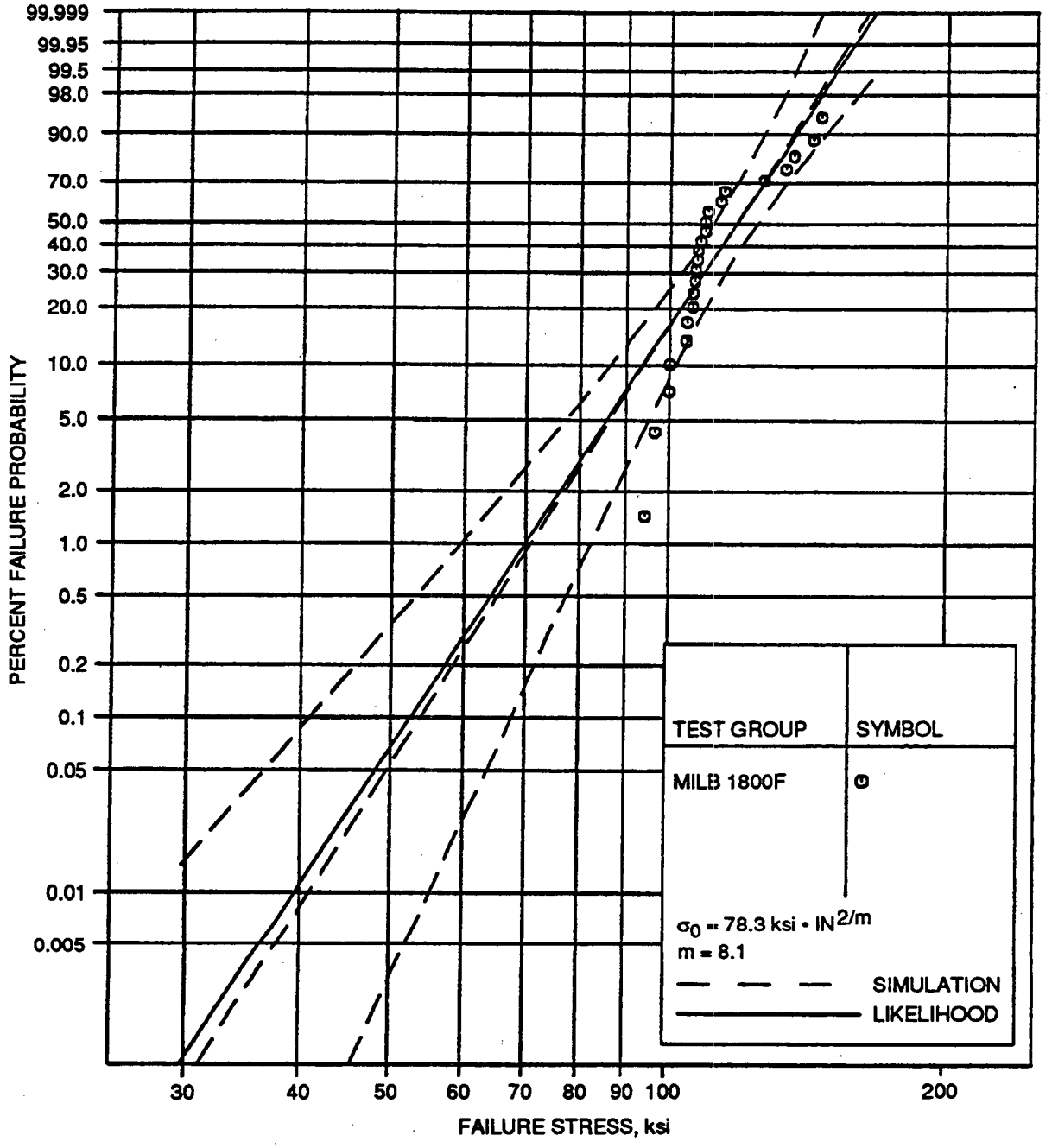

Figure VII-25. Surface Strength Estimated From MIL-B Flexure Specimens Tested At 1800F.

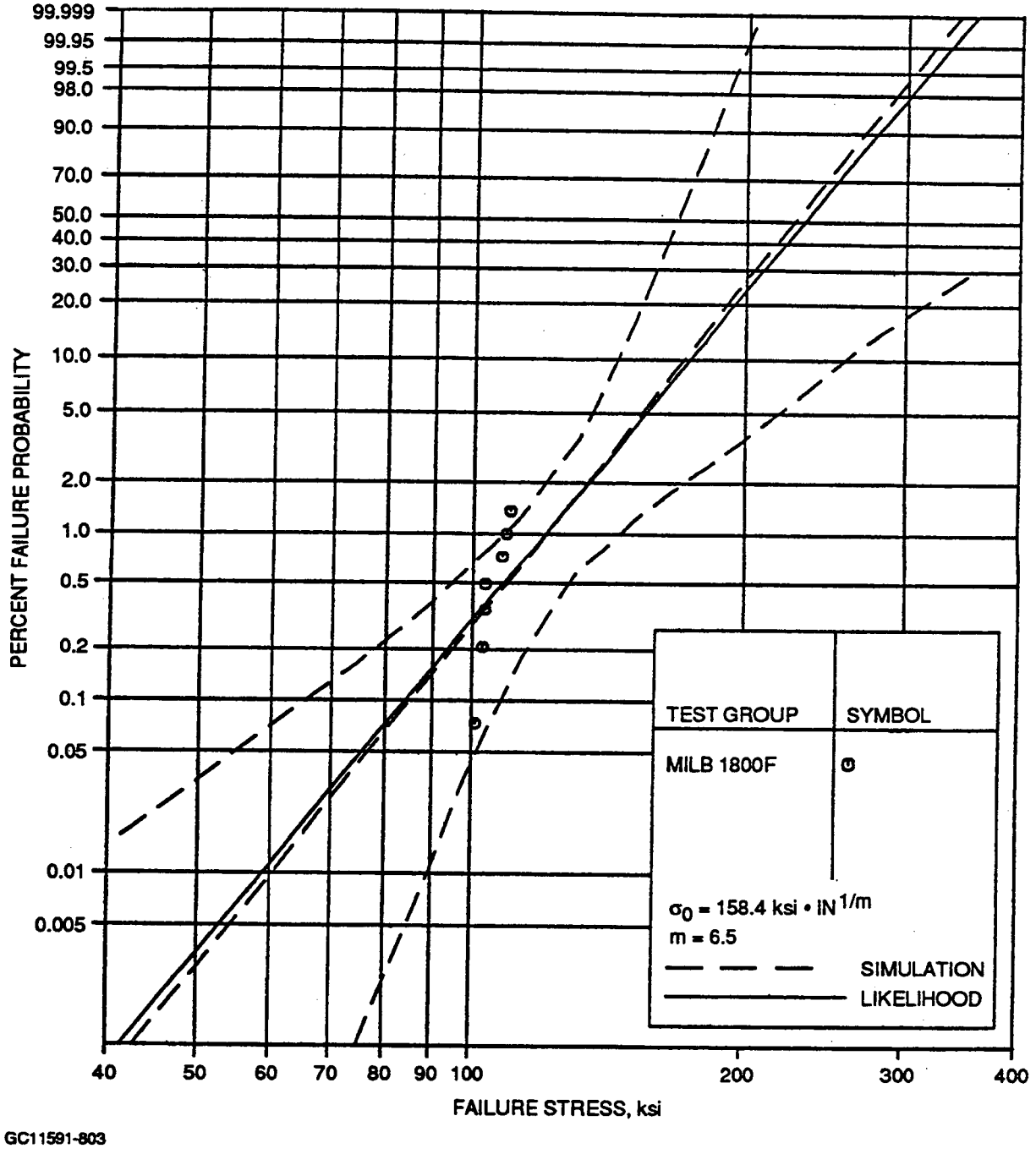

Figure VII-26. Chamfer Strength Estimated From MIL-B Flexure Specimens Tested At 1800F.

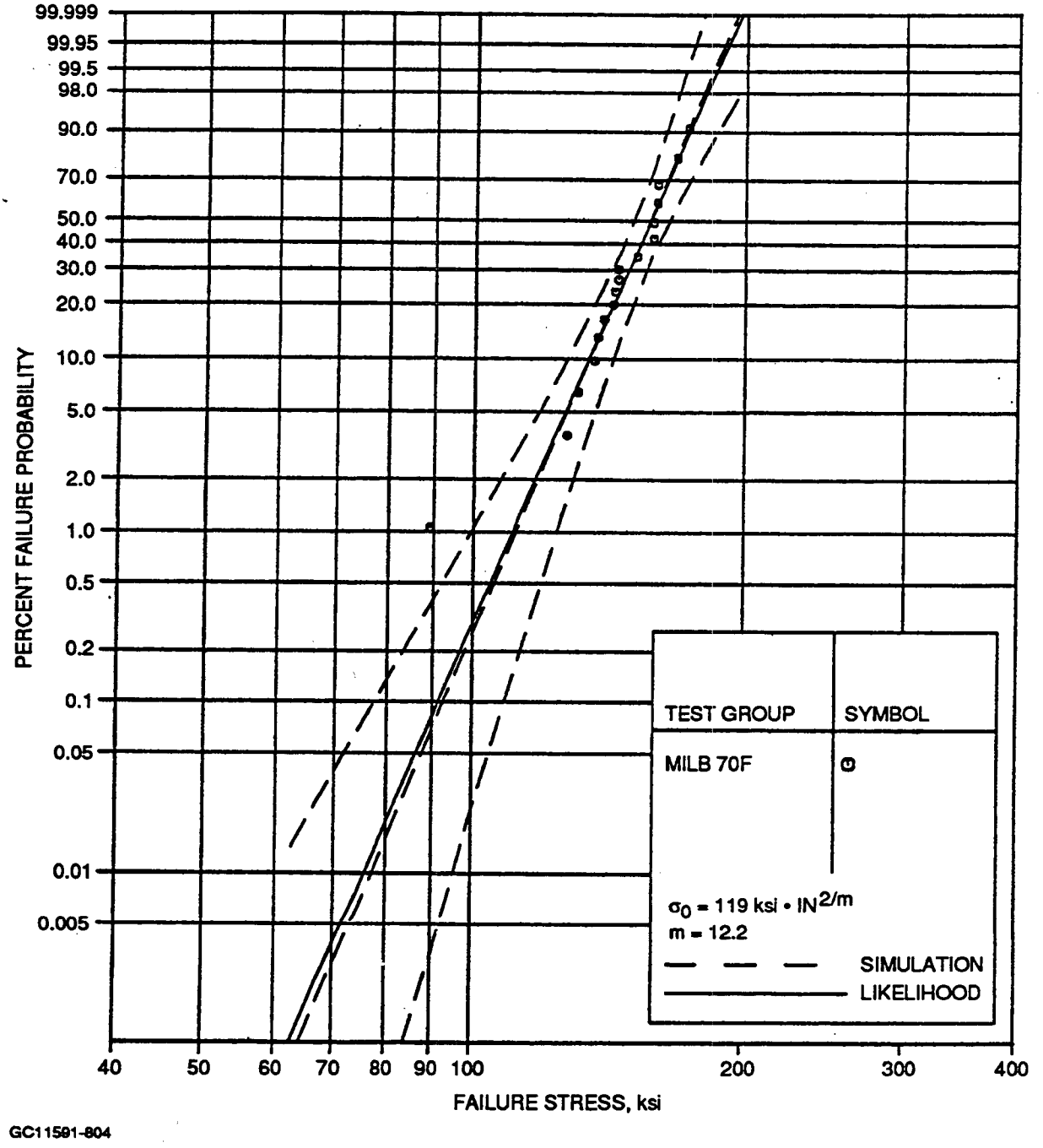

Figure VII-27. Surface Strength Estimated From MIL-B Flexure Specimens Tested At Room Temperature.

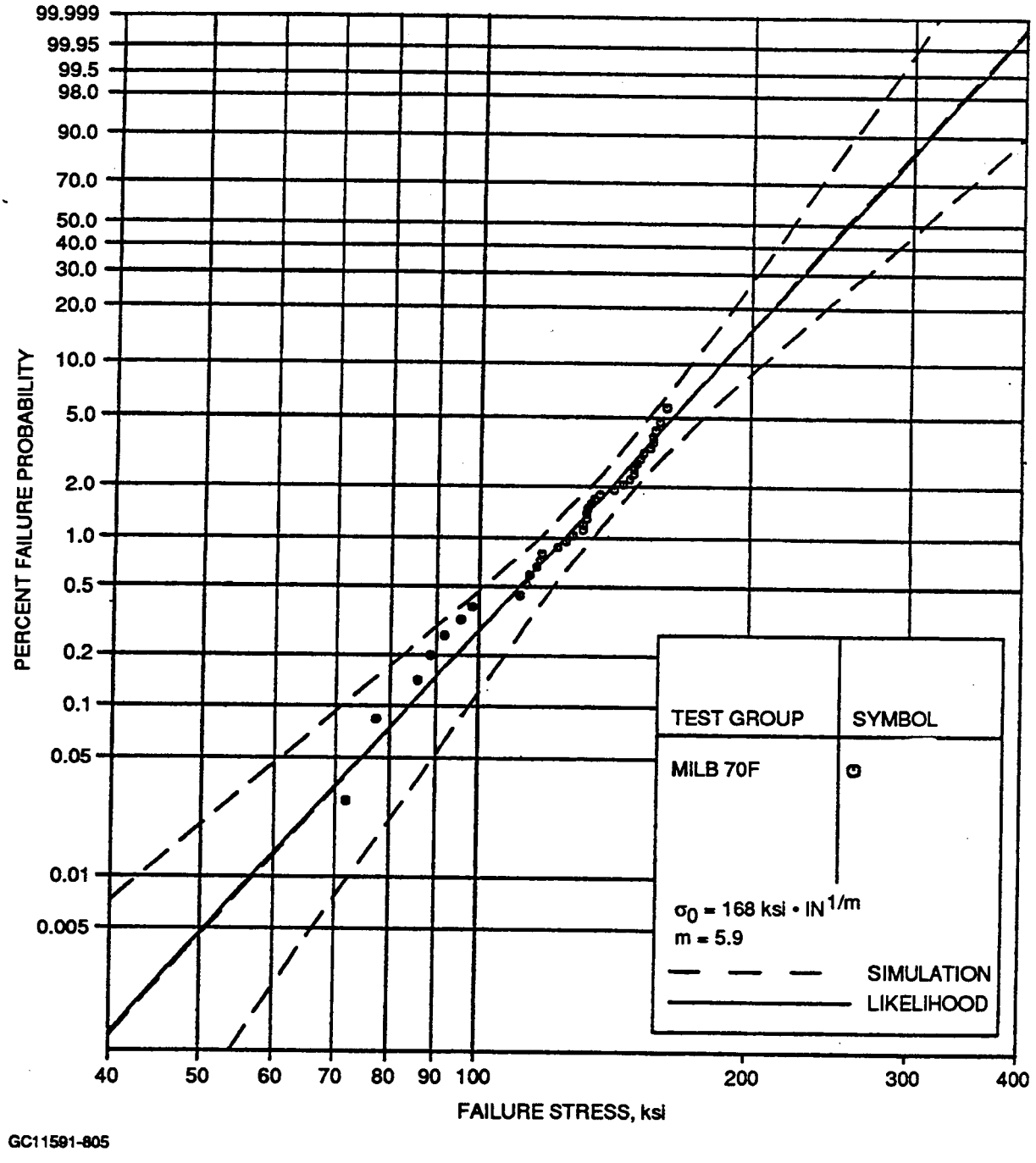

Figure VII-28. Chamfer Strength Estimated From MIL-B Flexure Specimens Tested At Room Temperature.

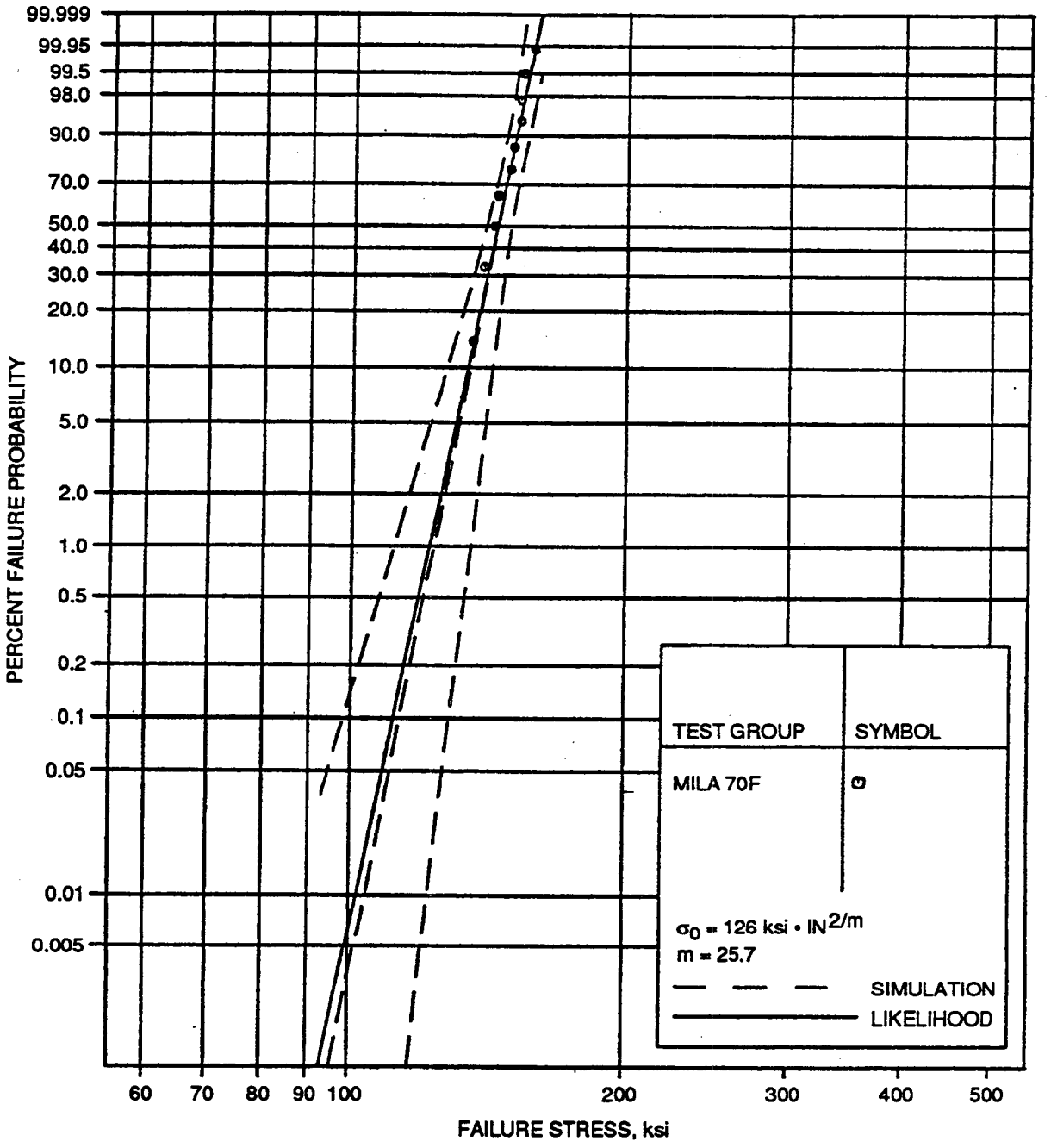

Figure VII-29. Surface Strength Estimated From MIL-A Flexure Specimens Tested At Room Temperature.

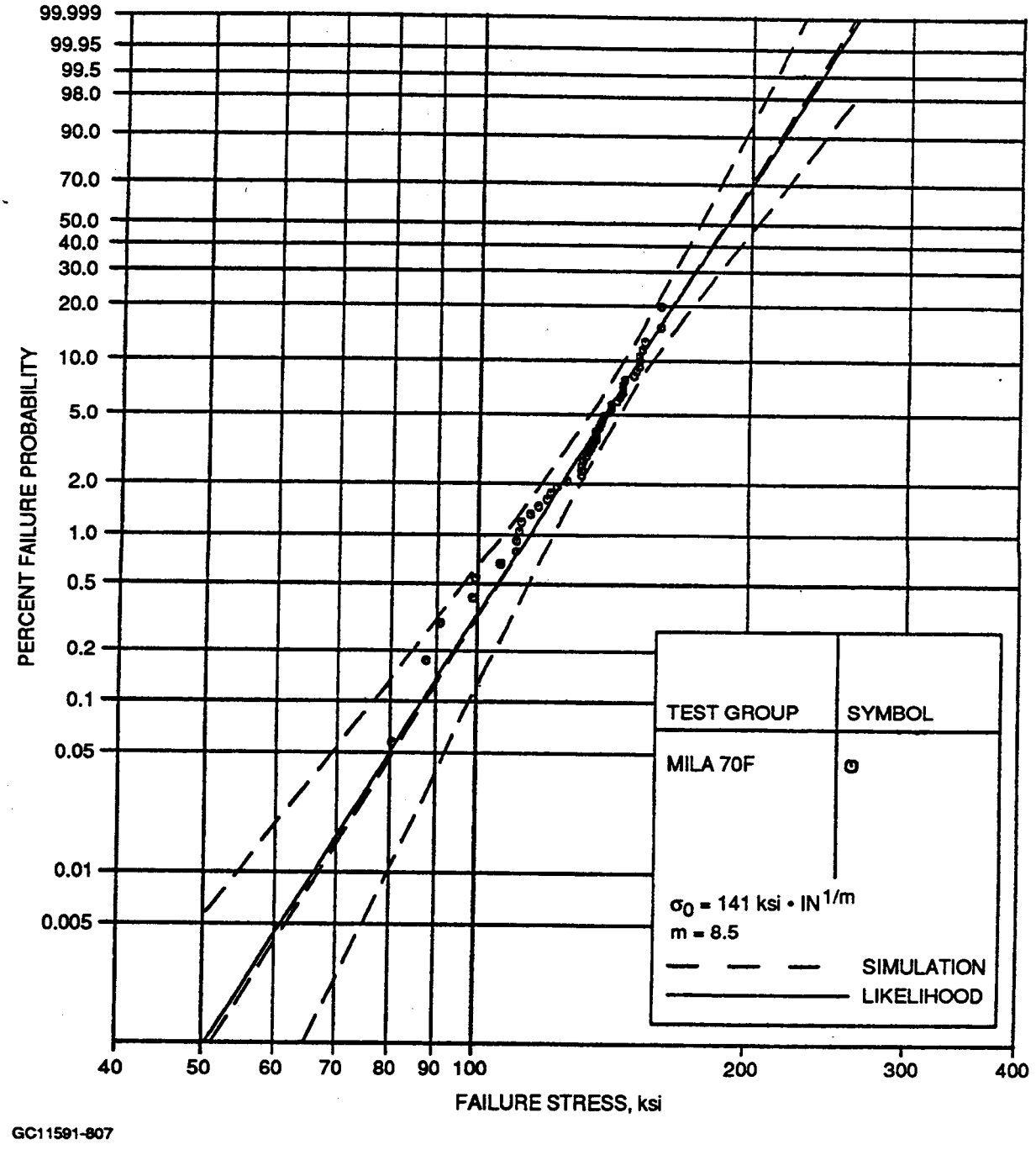

Figure VII-30. Chamfer Strength Estimated From MIL-A Flexure Specimens Tested At Room Temperature.

APPENDIX VIII

SIZE FUNCTIONS

(40 pages)

APPENDIX VIII
SIZE FUNCTIONS

VIII-1 Introduction

In section 5.2.2, the multiaxial and stress gradient factor (I) was introduced; I follows the definition by Tucker and Johnson (ref 1) after their proof of equivalence of the Lamons and Evans (ref 2)and Batdorf and Heinisch (ref 3) multiaxial fracture theories. A generalization of the multiaxial and stress gradient factor is made to surface and edge failure modes. The I factor is a complicated integral whose solution depends on the state of stress of the component in question and on the failure theory under consideration; it is defined in such a way that it is a function of the first Weibull parameter, m, only. Closed-form solutions to this integral are few. The opportunity is taken here to present some closed-form solutions, and to define the multiaxial and stress gradient factor for those specimens used in the CERAMIC code. Presented are also the I factors for the specimens that were used in this program and that had to be computed numerically using the integration code ERICA, developed in this program. ERICA is a probability integration code similar to CARES (ref 4). The finite element meshes used to compute the specimen stress distributions and I factors are also presented.

Three kinds of multiaxial and stress gradient factors were introduced earlier: volume (internal), area (surface), and corner (edge). These embrace all possible types of I factors: one, two, and three dimensions, respectively. The definition and evaluation of the following integrals, Equations [VIII-1] and [VIII-2], at this point makes the following presentation clearer and more concise. These equations appear repeatedly in the evaluation of the multiaxial and stress gradient factor. Figure VIII-1 presents the results graphically and Table VIII-1 presents them numerically. In the following equations, $\delta = m - Int(m)$, which means that $0 \le \delta < 1$.

$$\Theta = \int_0^{\frac{\pi}{2}} \cos^{2\delta}(\theta) d\theta \qquad \text{[VIII-1]}$$

$$\Phi = \int_0^{\frac{\pi}{2}} \cos^{1+2\delta}(\theta) d\theta \qquad \text{[VIII-2]}$$

The equations that are to be integrated to calculate the multiaxial and stress gradient factor are as follows:

Volume failure mode:
$$I_V = \frac{1}{4\pi V} \iiint_V \int_{-\frac{\pi}{2}}^{\frac{\pi}{2}} \int_0^{2\pi} \frac{\sigma_E^m(x,y,z,\phi,\psi)}{\sigma_{\max}^m} \cos\phi \, d\phi \, d\psi \, dV \qquad \text{[VIII-3]}$$

Area failure mode:
$$I_A = \frac{1}{2\pi A} \iint_A \int_0^{2\pi} \frac{\sigma_E^m(x,y,\theta)}{\sigma_{\max}^m} d\theta \, dA \qquad \text{[VIII-4]}$$

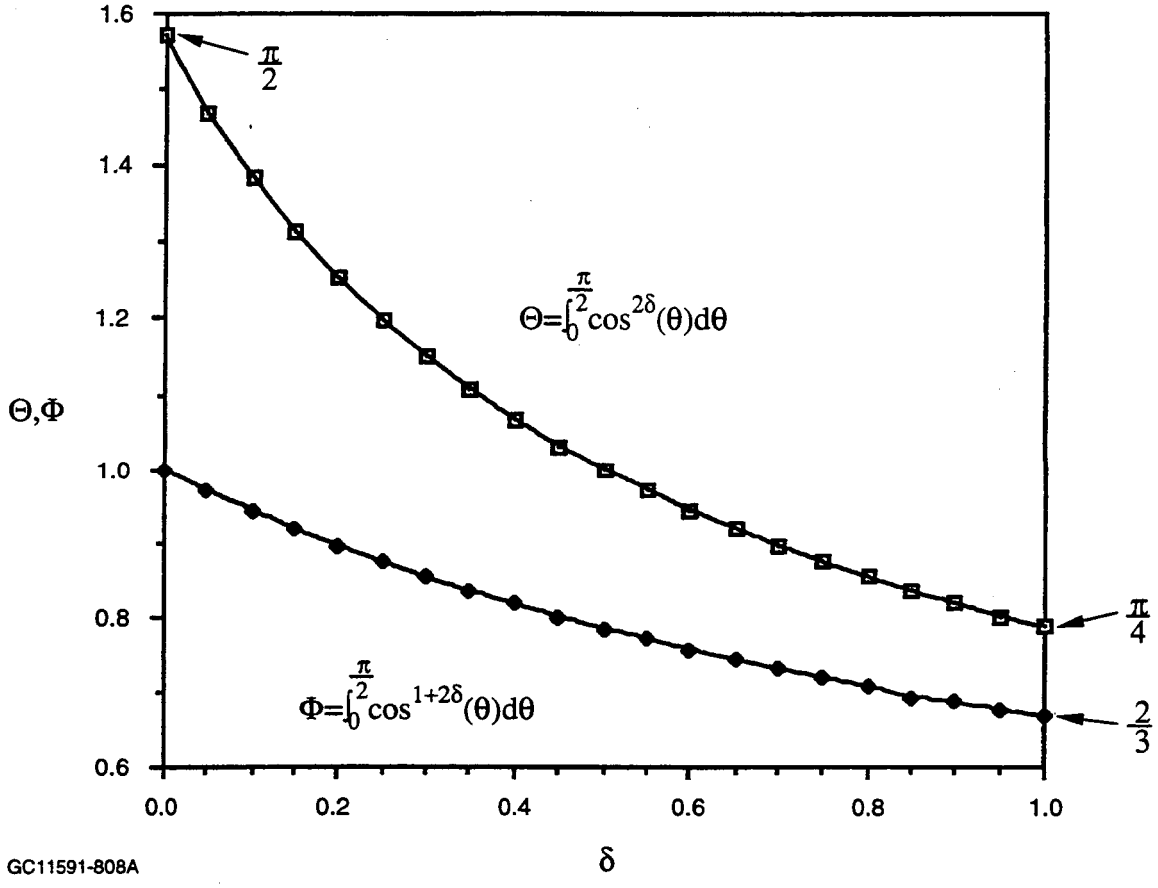

Figure VIII-1. Graphical Representation For The Values Of Θ And Φ, Integration Values Used In Calculation Of The Multiaxial And Stress Gradient Factor.

TABLE VIII-1. TABULAR REPRESENTATION FOR THE VALUES OF Θ AND Φ, INTEGRATION VALUES USED IN CALCULATION OF THE MULTIAXIAL AND STRESS GRADIENT FACTOR

δ	Θ	Φ
0.00	1.571	1.000
0.05	1.470	0.971
0.10	1.386	0.944
0.15	1.315	0.919
0.20	1.252	0.896
0.25	1.198	0.874
0.30	1.149	0.854
0.35	1.106	0.835
0.40	1.067	0.818
0.45	1.032	0.801
0.50	1.000	0.785
0.55	0.971	0.771
0.60	0.944	0.757
0.65	0.919	0.743
0.70	0.896	0.731
0.75	0.874	0.719
0.80	0.854	0.707
0.85	0.835	0.693
0.90	0.818	0.686
0.95	0.801	0.676
1.00	0.7853982	0.66666667

Corner failure mode:

$$I_C = \frac{1}{L}\int_L \frac{\sigma_E^m}{\sigma_{\max}^m} dL \qquad \text{[VIII-5]}$$

Based on the coordinate systems shown in Figure VIII-2, the spatial integration for the volume is the surface of a unit sphere and for the area is a unit circle. Notice that the corner failure mode has no spatial integration. The corner failure mode is a one-dimensional entity; hence, its spatial integration is a point. Since a point has no dimension(s), there is no spatial integration for the corner failure mode.

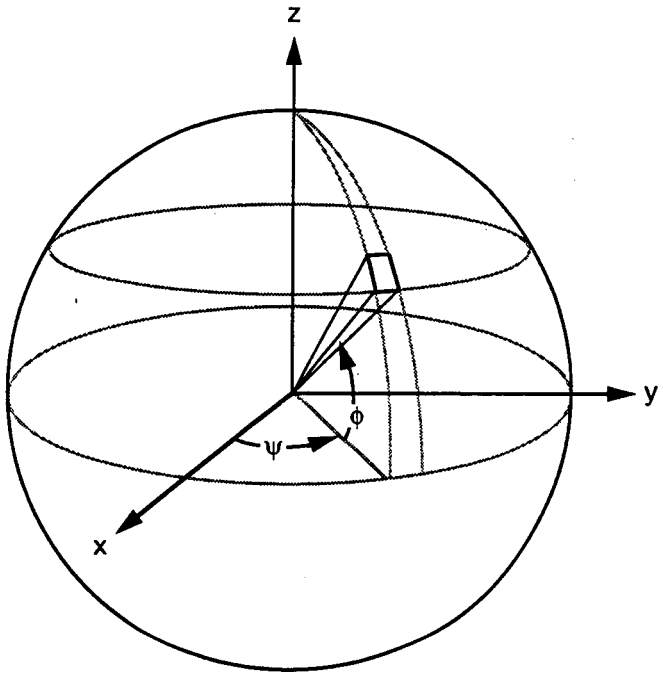

A) VOLUME FAILURE MODE

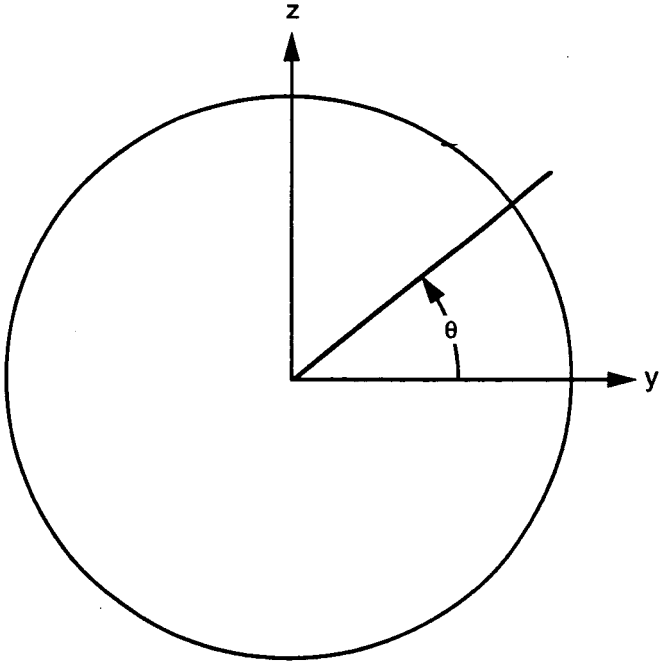

B) SURFACE FAILURE MODE

GC11591-809

Figure VIII-2. Coordinate Systems For Spatial Integration. (a) Volume Failure Mode; (b) Surface Failure Mode.

The following equations have been derived for the normal stress criterion. The effective stress is defined as shown in equations [VIII-6], [VIII-7] and [VIII-8]:

For volume failure mode: $$\sigma_E = \sigma_1 \ell_1^2 + \sigma_2 \ell_2^2 + \sigma_3 \ell_3^2 \qquad \text{[VIII-6]}$$

Where: $\ell_1 = \cos\phi \cos\psi$

$\ell_2 = \cos\phi \sin\psi$

$\ell_3 = \sin\phi$

$\sigma_1, \sigma_2, \sigma_3$ = the maximum principal stresses.

For surface failure mode: $$\sigma_E = \sigma_1 \ell_1^2 + \sigma_2 \ell_2^2 \qquad \text{[VIII-7]}$$

Where: $\ell_1 = \cos\theta$

$\ell_2 = \sin\theta$

And for corner failure mode: $$\sigma_E = \sigma_N \qquad \text{[VIII-8]}$$

Where: σ_N= the stress along the axis of the edge.

It is important to notice the values for which the multiaxial and stress gradient factors are equal to unity. The volume I factor is unity under a uniform equitriaxial state of stress; the area I factor is unity under a uniform equibiaxial state of stress; and finally, the corner I factor is unity under a uniform uniaxial state of stress. The I factors are summarized in the following sections.

VIII-2 Closed-Form Solutions For The Multiaxial And Stress Gradient Factor

Volume failure mode:

(a) Uniform equitriaxial state of stress:

$$I_V(m) = 1 \qquad \text{[VIII-9]}$$

(b) Uniform equibiaxial state of stress:

$$I_V(m) = \int_0^{\frac{\pi}{2}} \cos^{1+2\delta}(\theta) d\theta \cdot \prod_{i=1}^{Int(m)} \frac{2(i+\delta)}{2(i+\delta)+1} \qquad \text{[VIII-10]}$$

(c) Uniform uniaxial state of stress:

$$I_V(m) = \frac{2}{\pi} \cdot \frac{1}{2m+1} \cdot \int_0^{\frac{\pi}{2}} \cos^{1+2\delta}(\theta) d\theta \cdot \int_0^{\frac{\pi}{2}} \cos^{2\delta}(\theta) d\theta \qquad \text{[VIII-11]}$$

(d) Beam in pure bending:

$$I_V(m) = \frac{1}{\pi(m+1)} \cdot \frac{1}{2m+1} \cdot \int_0^{\frac{\pi}{2}} \cos^{1+2\delta}(\theta) d\theta \cdot \int_0^{\frac{\pi}{2}} \cos^{2\delta}(\theta) d\theta \qquad \text{[VIII-12]}$$

Area failure mode:

(a) Uniform biaxial state of stress:

$$I_A(m) = 1 \qquad \text{[VIII-13]}$$

(b) Uniform uniaxial state of stress:

$$I_A(m) = \frac{2}{\pi} \int_0^{\frac{\pi}{2}} \cos^{2\delta}(\theta) d\theta \cdot \prod_{i=1}^{Int(m)} \frac{2(i+\delta)-1}{2(i+\delta)} \qquad \text{[VIII-14]}$$

(c) Beam in pure bending, sides of beam included:

$$I_A(m) = \frac{1}{\pi(m+1)} \cdot \left[\frac{mw}{w+t}+1\right] \cdot \int_0^{\frac{\pi}{2}} \cos^{2\delta}(\theta) d\theta \cdot \prod_{i=1}^{Int(m)} \frac{2(i+\delta)-1}{2(i+\delta)} \qquad \text{[VIII-15]}$$

Corner failure mode:

(a) Uniform uniaxial state of stress:

$$I_c(m) = 1 \qquad \text{[VIII-16]}$$

(b) Pure bending:

$$I_c(m) = \frac{1}{2} \qquad \text{[VIII-17]}$$

(c) Beam four-point bending, where a is the inner span and b the outer span:

$$I_c(m) = \frac{(\%m+1)}{2(m+1)} \qquad \text{[VIII-18]}$$

VIII-3 Multiaxial And Stress Gradient Factor For The Specimen Types Included In CERAMIC

The list of specimens included in CERAMIC is shown in Table VIII-2; only a few of those have closed-form solutions for the I factor. A short description of the specimens and their multiaxial and stress gradient factor follows:

TABLE VIII-2. LIST OF SPECIMENS INCLUDED IN CERAMIC AND THEIR DESCRIPTION

CERAMIC Specimen Name	Specimen Description
BEND	Three- or four-point bend bar
TCIRC	Uniform cylindrical cross section tensile specimen
TRECT	Uniform rectangular cross section tensile specimen
ABEND	Anisotropic BEND specimen
SPECIAL i	Specimen with no closed-form solution for I
ORNLTENS	Oak Ridge NL buttonhead tensile specimen

- **BEND Specimen:** This is a beam with rectangular cross section; it may be loaded in three- or four-point bending. The stress solution is assumed to obey beam theory; hence, it neglects the stress concentrations resulting from the load points. The loads are assumed to be symmetric about the midspan. In the inner span, the specimen is in a pure bending state of stress; while in the outer span, it has a combination of bending and shear loading. The calculation of the effective stress for the normal stress criterion is trivial, but the spatial integration is not, and a closed-form solution is not readily available. Hence, an approximation is made here, in which the effective stress is assumed to be the same as the bending stress, neglecting the shear stresses in the calculation of the I factor. The multiaxial and stress gradient factors are as follows:

  (a) Volume failure mode:

$$I_V(m) = \frac{(\%m+1)}{\pi(m+1)^2} \cdot \frac{1}{2m+1} \cdot \int_0^{\frac{\pi}{2}} \cos^{1+2\delta}(\theta) d\theta \cdot \int_0^{\frac{\pi}{2}} \cos^{2\delta}(\theta) d\theta \qquad \text{[VIII-19]}$$

  (b) Surface failure mode:

$$I_A(m) = \frac{(\%m+1)}{\pi(m+1)^2} \cdot \left[\frac{mw}{w+t}+1\right] \cdot \int_0^{\frac{\pi}{2}} \cos^{2\delta}(\theta) d\theta \cdot \prod_{i=1}^{Int(m)} \frac{2(i+\delta)-1}{2(i+\delta)} \qquad \text{[VIII-20]}$$

  (c) Corner failure mode: the same as Equation [VIII-18]

- **TCIRC Specimen:** This is a bar specimen with circular cross section. The specimen is in a uniform uniaxial state of stress; hence, its multiaxial and stress gradient factors are given by Equation [VIII-11] for the volume and Equation [VIII-14] for the surface. Since this specimen has no corners, its corner I is zero.

- **TRECT Specimen:** This is a bar specimen with rectangular cross section. This specimen is also in a uniaxial state of stress; hence, its multiaxial and stress gradient factors are the same as for the TCIRC specimen, except that its corner I is unity, Equation [VIII-16].

- **ABEND Specimen:** This is an anisotropic BEND specimen; an anisotropic specimen is one that has its surface flaws aligned in a single orientation (e.g., surface machined specimens). The volume failure mode is assumed to be isotropic (i.e., random orientation of flaws). Its volume and the corner I factors are the same as for the BEND specimen, Equation [VIII-19]. The surface failure mode for this

specimen does not include the side surfaces; it only includes the surface that is in tension. The surface failure mode I factor is given by:

$$I_A(m) = \frac{\cos^{2m}(\theta_o)}{\pi}\left[\frac{\%m+1}{m+1}\right] \qquad \text{[VIII-21]}$$

- **SPECIAL i Specimen:** This specimen type was included in CERAMIC to allow the program to use the information provided in the full specimen or to analyze component data. The multiaxial and stress gradient factors for these specimens do not have closed-form solutions, and must be calculated using the integration code ERICA.

- **ORNLTENS Specimen:** This is the buttonhead tensile specimen design by ORNL. This specimen does not have a closed-form solution for the I factor, but it was deemed necessary to include it as an option in the CERAMIC code because it is a specimen commonly used in ceramic testing today. The specimen I factor was calculated using ERICA.

VIII-4. Multiaxial Stress Gradient Factors For The Specimens Used In This Program

The multiaxial and stress gradient factors for the specimens used in this program are shown in Tables VIII-3 through VIII-11, and Figures VIII-3 through VIII-13. With this information, the physical size of the specimens and components is presented. The product of the multiaxial and stress gradient factor and the physical size is called the equivalent size. The equivalent size of a specimen or component can be used to decide on the most effective method or specimen to be used for developing material property data bases.

VIII-5. Finite Element Models Used In The Calculation Of Stresses And Multiaxial And Stress Gradient Factors For The Specimens Used In This Program

The finite element analysis was performed with the ANSYS finite element code. The results are presented in Figures VIII-14 through VIII-23.

TABLE VIII-3. TABULAR SUMMARY OF THE MULTIAXIAL AND STRESS GRADIENT FACTOR FOR THE BEND SPECIMENS USED IN THIS PROGRAM.

Note that the "volume" and "edge" factors are the same for all of these specimens, and since the MIL-B and MIL-A specimens have the same cross sectional dimension ratio, the "surface" factors are the same.

WEIBULL SLOPE \SIZE=>	VOLUME	EDGE	SIZE-E SURFACE 10.7 IN^2	MIL-B SURFACE 0.868 IN^2	MIL-A SURFACE 0.341 IN^2	MIL-B ANISOTROPIC SURFACE 0 deg 0.186 IN ^2	MIL-B ANISOTROPIC SURFACE 45 deg 0.186 IN^2
1	6.2500E-02	3.7500E-01	1.2442E-01	1.4720E-01	1.4720E-01	2.3873E-01	1.1937E-01
2	2.2200E-02	3.3300E-01	6.8925E-02	8.9175E-02	8.9175E-02	2.1221E-01	5.3052E-02
3	1.1100E-02	3.1200E-01	4.8372E-02	6.6169E-02	6.6169E-02	1.9894E-01	2.4868E-02
4	6.6000E-03	3.0000E-01	3.7872E-02	5.3819E-02	5.3819E-02	1.9099E-01	1.1937E-02
5	4.4000E-03	2.9100E-01	3.1528E-02	4.6063E-02	4.6063E-02	1.8568E-01	5.8025E-03
6	3.1000E-03	2.8500E-01	2.7278E-02	4.0703E-02	4.0703E-02	1.8189E-01	2.8421E-03
7	2.3000E-03	2.8100E-01	2.4226E-02	3.6753E-02	3.6753E-02	1.7905E-01	1.3988E-03
8	1.8000E-03	2.7700E-01	2.1922E-02	3.3705E-02	3.3705E-02	1.7684E-01	6.9078E-04
9	1.4000E-03	2.7500E-01	2.0116E-02	3.1270E-02	3.1270E-02	1.7507E-01	3.4193E-04
10	1.1806E-03	2.7273E-01	1.8658E-02	2.9273E-02	2.9273E-02	1.7362E-01	1.6955E-04
11	9.8128E-04	2.7083E-01	1.7454E-02	2.7600E-02	2.7600E-02	1.7242E-01	8.4188E-05
12	8.2840E-04	2.6923E-01	1.6441E-02	2.6174E-02	2.6174E-02	1.7140E-01	4.1845E-05
13	7.0862E-04	2.6786E-01	1.5574E-02	2.4941E-02	2.4941E-02	1.7052E-01	2.0816E-05
14	6.1303E-04	2.6667E-01	1.4823E-02	2.3862E-02	2.3862E-02	1.6977E-01	1.0362E-05
15	5.3553E-04	2.6563E-01	1.4166E-02	2.2908E-02	2.2908E-02	1.6910E-01	5.1606E-06
16	4.7185E-04	2.6471E-01	1.3584E-02	2.2056E-02	2.2056E-02	1.6852E-01	2.5714E-06
17	4.1887E-04	2.6389E-01	1.3065E-02	2.1291E-02	2.1291E-02	1.6800E-01	1.2817E-06
18	3.7434E-04	2.6316E-01	1.2598E-02	2.0599E-02	2.0599E-02	1.6753E-01	6.3908E-07
19	3.3654E-04	2.6250E-01	1.2176E-02	1.9968E-02	1.9968E-02	1.6711E-01	3.1874E-07
20	3.0419E-04	2.6190E-01	1.1793E-02	1.9392E-02	1.9392E-02	1.6673E-01	1.5901E-07
21	2.7628E-04	2.6136E-01	1.1441E-02	1.8861E-02	1.8861E-02	1.6639E-01	7.9341E-08
22	2.5205E-04	2.6087E-01	1.1119E-02	1.8371E-02	1.8371E-02	1.6607E-01	3.9595E-08
23	2.3087E-04	2.6042E-01	1.0821E-02	1.7917E-02	1.7917E-02	1.6579E-01	1.9763E-08
24	2.1224E-04	2.6000E-01	1.0545E-02	1.7494E-02	1.7494E-02	1.6552E-01	9.8658E-09
25	1.9579E-04	2.5962E-01	1.0289E-02	1.7099E-02	1.7099E-02	1.6528E-01	4.9256E-09
30	1.3647E-04	2.5806E-01	9.2335E-03	1.5459E-02	1.5459E-02	1.6429E-01	1.5301E-10
35	1.0053E-04	2.5694E-01	8.4429E-03	1.4211E-02	1.4211E-02	1.6358E-01	4.7607E-12
40	7.7115E-05	2.5610E-01	7.8232E-03	1.3222E-02	1.3222E-02	1.6304E-01	1.4828E-13
50	4.9486E-05	2.5490E-01	6.9037E-03	1.1737E-02	1.1737E-02	1.6228E-01	1.4413E-16
60	3.4426E-05	2.5410E-01	6.2450E-03	1.0659E-02	1.0659E-02	1.6176E-01	1.4031E-19
75	2.2071E-05	2.5329E-01	5.5344E-03	9.4848E-03	9.4848E-03	1.6125E-01	4.2682E-24
100	1.2437E-05	2.5248E-01	4.7483E-03	8.1711E-03	8.1711E-03	1.6073E-01	1.2679E-31

SPECIMEN SIZES
MIL-A V=0.0073 IN^3 E=3.15 IN
MIL-B V=0.029 IN^3 E=6.3 IN
SIZE-E V=1.26 IN^3 E=20 IN

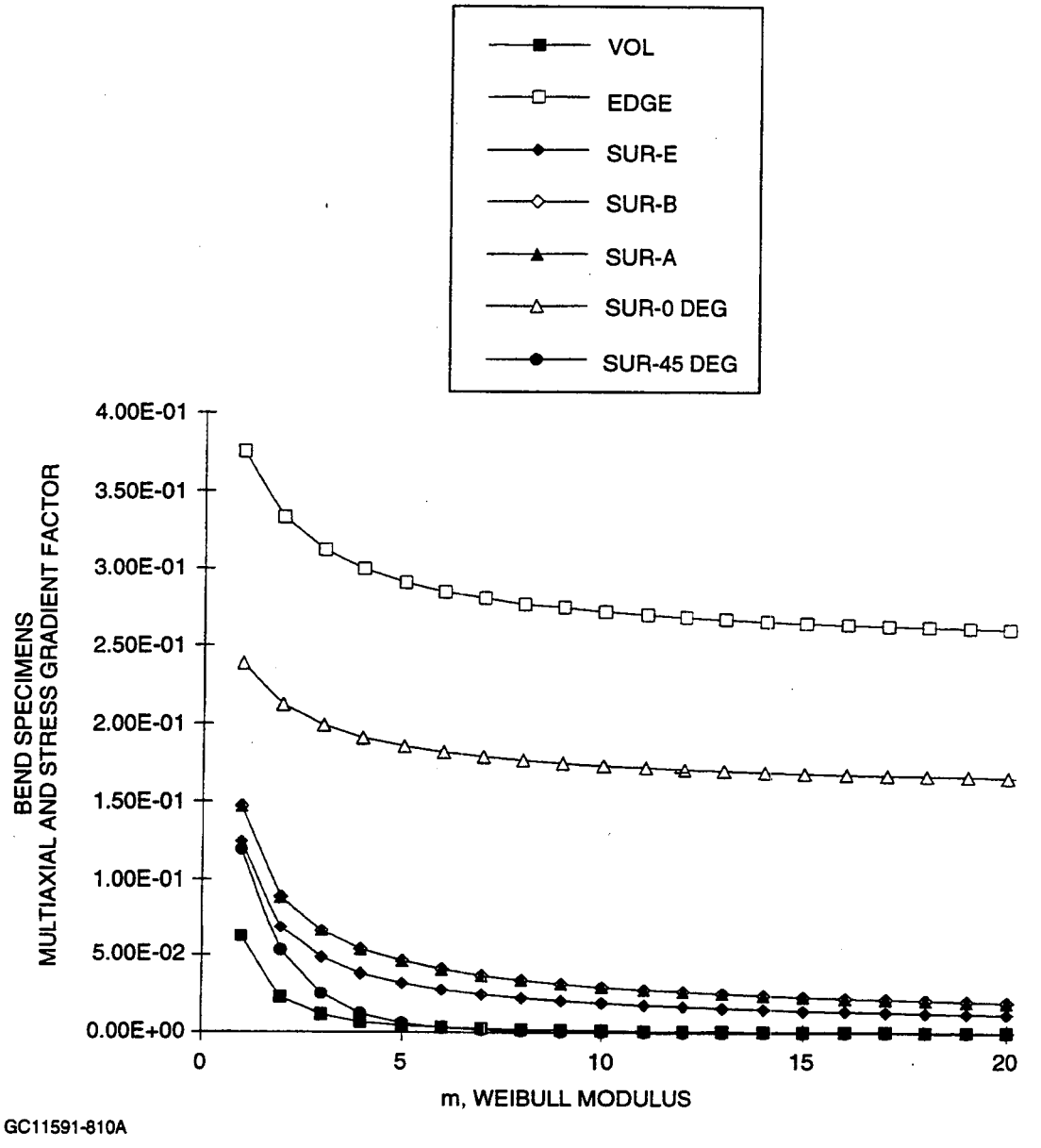

Figure VIII-3. Graphical Presentation Of The Data In Table VIII-3.

TABLE VIII-4. TABULAR SUMMARY FOR THE MULTIAXIAL AND STRESS GRADIENT FACTOR FOR THE SPIN DISK

Note the small effect the thermal gradient has on the spin disks that combine the speed and thermal gradient, relative to the speed-only disks; all of these for the low Weibull modulus cases. Based on this observation, the decision was made to use just the speed-only factor in the analyses.

	VOLUME FAILURE MODE				SURFACE FAILURE MODE			
WEIBULL SLOPE	SPEED ONLY	THERMAL S ONLY	THERMALS+ 67000 RPM	THERMALS+ 93000 RPM	SPEED ONLY	THERMALS ONLY	THERMALS + 67000 RPM	THERMALS + 93000 RPM
0.1	9.0038E-01	3.1353E-01	8.9909E-01	8.9934E-01	9.3956E-01	5.4196E-01	9.3943E-01	9.4015E-01
0.2	8.2293E-01				8.8565E-01			
0.3	7.5642E-01	1.3800E-01	7.5350E-01	7.5488E-01	8.3671E-01	2.1400E-01	8.3516E-01	8.3703E-01
0.4	6.9870E-01				7.9208E-01			
0.5	6.4814E-01	6.4381E-02	6.4401E-01	6.4598E-01	7.5122E-01	9.3846E-02	7.4805E-01	7.5082E-01
1	4.6756E-01	1.1689E-02	4.6169E-01	4.6448E-01	5.8953E-01	1.7402E-02	5.8285E-01	5.8709E-01
2	2.8267E-01	7.6500E-04	2.7589E-01	2.7911E-01	3.9099E-01	2.3930E-03	3.8098E-01	3.8632E-01
3	1.9043E-01				2.7450E-01			
4	1.3650E-01	3.1000E-05	1.3046E-01	1.3330E-01	1.9935E-01	6.4700E-04	1.8943E-01	1.9443E-01
5	1.0191E-01	1.2000E-05	9.6468E-02	9.9021E-02	1.4807E-01	4.7200E-04	1.3912E-01	1.4360E-01
6	7.8339E-02	6.0000E-06	7.3481E-02	7.5753E-02	1.1176E-01	3.7200E-04	1.0388E-01	1.0780E-01
7	6.1566E-02	4.0000E-06	5.7244E-02	5.9259E-02	8.5372E-02	3.0700E-04	7.8526E-02	8.1926E-02
8	4.9235E-02	2.0000E-06	4.5396E-02	4.7180E-02	6.5815E-02	2.6600E-04	5.9927E-02	6.2841E-02
9	3.9937E-02				5.1107E-02			
10	3.2780E-02	1.0000E-06	2.9749E-02	3.1149E-02	3.9919E-02	2.0400E-04	3.5648E-02	3.7749E-02
12	2.2733E-02				2.4688E-02			
14	1.6260E-02	4.0000E-07	1.4344E-02	1.5219E-02	1.5481E-02	1.4200E-04	1.3338E-02	1.4379E-02
16	1.1920E-02				9.8081E-03			
18	8.9176E-03				6.2637E-03			
20	6.7868E-03	3.0000E-08	5.7800E-03	6.2320E-03	4.0257E-03	9.7000E-05	3.3100E-03	3.6500E-03
22	5.2420E-03				2.6009E-03			
24	4.1014E-03				1.6878E-03			
26	3.2457E-03				1.0993E-03			
28	2.5947E-03				7.1832E-04			
30	2.0933E-03	1.0000E-07	1.7060E-03	1.8760E-03	4.7070E-04	6.4000E-05	3.6400E-04	4.1300E-04
25	3.6436E-03				1.3615E-03			
40	7.9853E-04				5.8756E-05			
45	5.2067E-04				2.1086E-05			
50	3.4923E-04				7.6277E-06			

Volume=15.29 IN^3 Surface= 50.20 IN^2

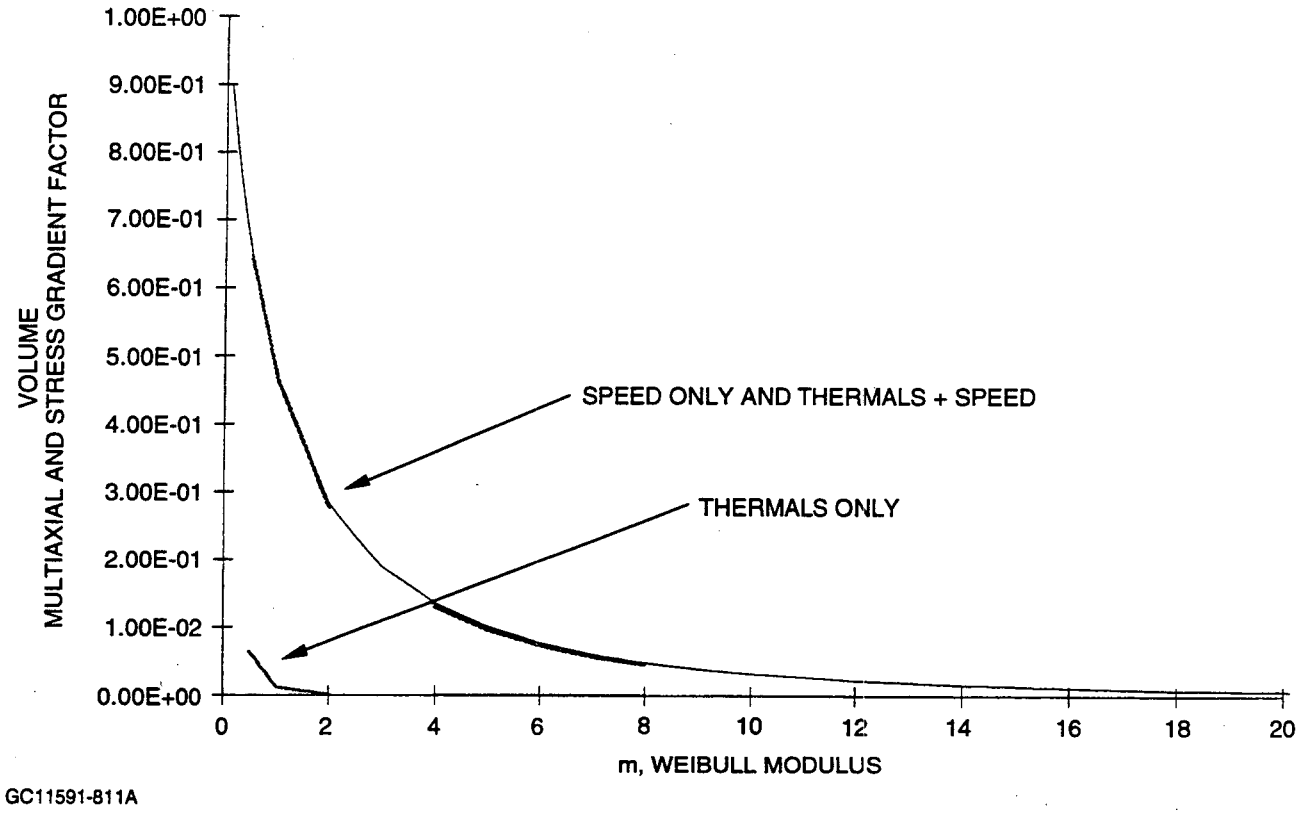

Figure VIII-4. Graphical Presentation Of The Volume Data In Table VIII-4.

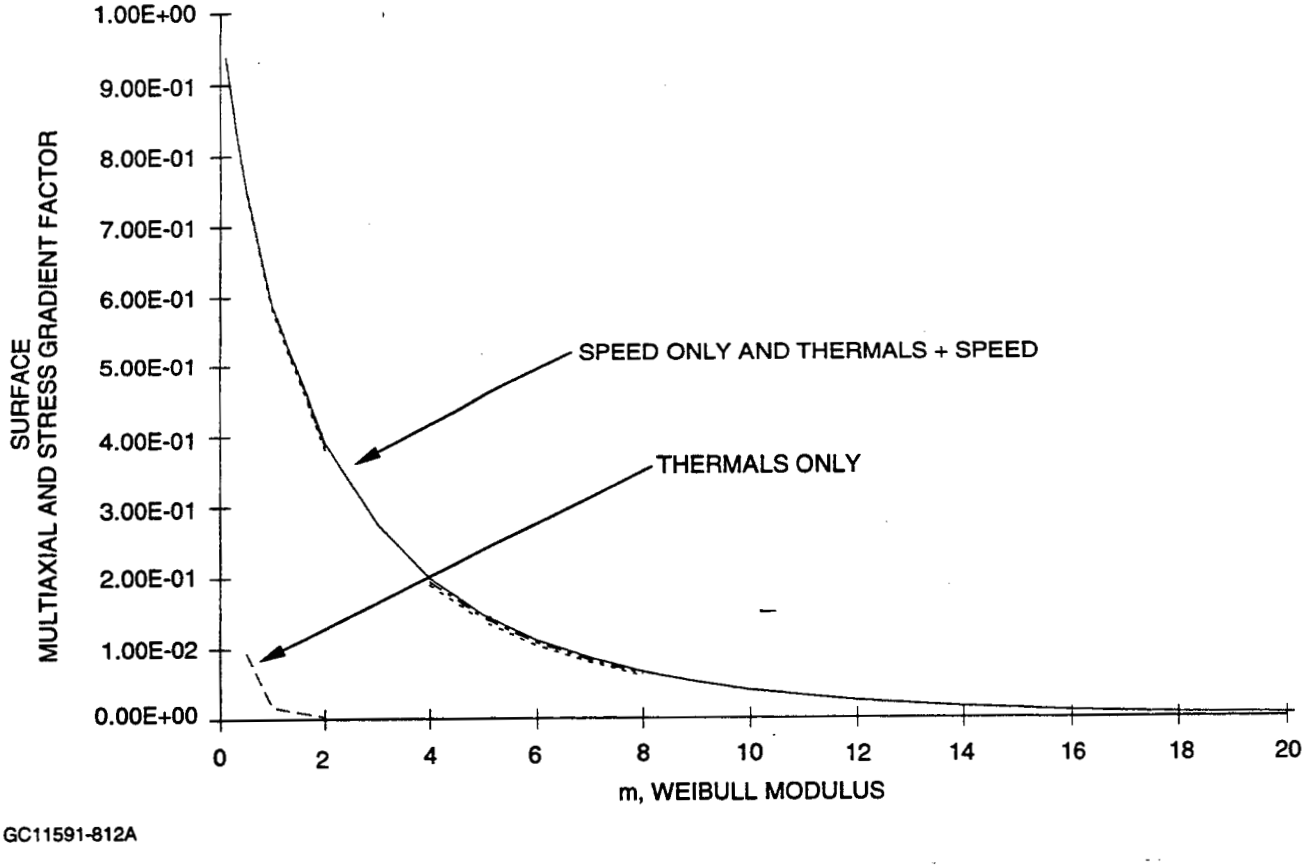

Figure VIII-5. Graphical Presentation Of The Surface Data In Table VIII-4.

TABLE VIII-5. TABULAR SUMMARY OF THE ISOTROPIC MULTIAXIAL AND STRESS GRADIENT FACTOR FOR THE PLATE BENDING SPECIMENS

WEIBULL SLOPE \SIZE=>	VOLUME 0.387 IN^3	SURFACE 6.2 IN^2	EDGE 12.48 IN
0.1	3.82E-01	4.53E-01	0.4569
0.2	3.13E-01	4.24E-01	0.4174
0.3	2.60E-01	3.98E-01	0.3814
0.4	2.19E-01	3.75E-01	0.3485
0.5	1.86E-01	3.54E-01	0.3185
1	9.24E-02	2.76E-01	0.2028
2	3.33E-02	1.86E-01	0.0823
3	1.58E-02	1.38E-01	0.03338
4	8.83E-03	1.08E-01	1.35E-02
5	5.44E-03	8.79E-02	5.49E-03
7	2.52E-03	5.57E-02	9.04E-04
9	1.37E-03	4.23E-02	1.49E-04
11	8.25E-04	3.35E-02	2.45E-05
15	3.61E-04	2.27E-02	6.63E-07
20	1.56E-04	1.53E-02	7.28E-09
25	7.60E-05	1.10E-02	8.00E-11
30	3.97E-05	8.21E-03	8.79E-13
40	1.24E-05	4.99E-03	1.06E-16
100	6.11E-08	8.08E-04	3.28E-40
200	6.26E-11	2.01E-04	2.15E-79

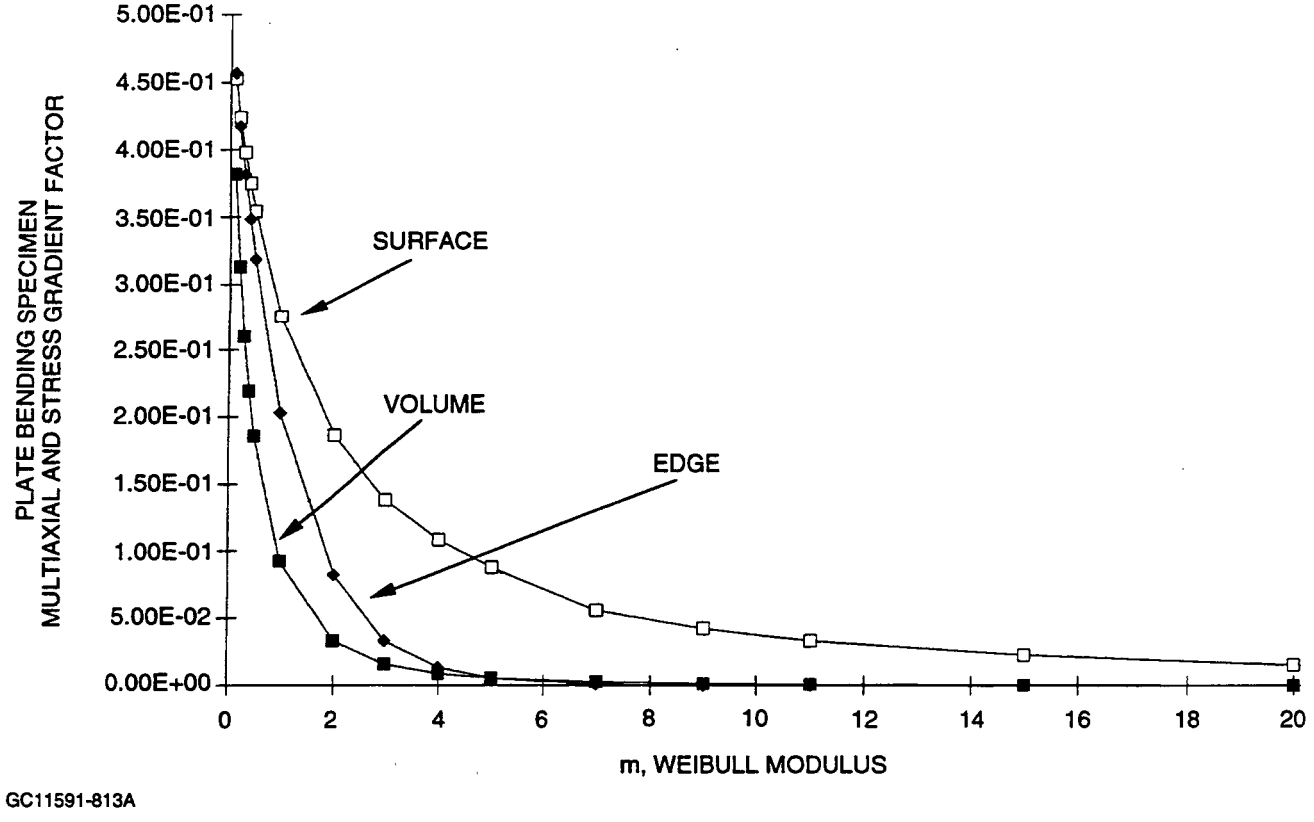

Figure VIII-6. Graphical Representation For The Data In Table VIII-5.

TABLE VIII-6. TABULAR SUMMARY OF THE MULTIAXIAL AND STRESS GRADIENT FACTOR FOR THE ORNL TENSILE SPECIMENS. THE ANISOTROPIC FORMULATION ASSUMES A SECONDARY FLAW NORMAL TO THE MACHINING DIRECTION

WEIBULL MODULUS	VOLUME FAILURE MODE	SURFACE FAILURE MODE	SURFACE FAILURE MODE
		Isotropic Formulation	Anisotropic Formulation
0.1	7.38E-01	8.01E-01	2.92E-01
0.2	5.78E-01	6.68E-01	2.68E-01
0.3	4.63E-01	5.66E-01	2.47E-01
0.4	3.76E-01	4.87E-01	2.28E-01
0.5	3.10E-01	4.24E-01	2.12E-01
1	1.39E-01	2.42E-01	1.54E-01
2	4.76E-02	1.20E-01	1.02E-01
3	2.53E-02	8.19E-02	8.32E-02
4	1.70E-02	6.46E-02	7.51E-02
6	1.02E-02	4.79E-02	6.74E-02
8	7.23E-03	3.90E-02	6.32E-02
10	5.52E-03	3.33E-02	6.01E-02
15	3.34E-03	2.47E-02	5.44E-02
20	2.31E-03	1.98E-02	5.02E-02
30	1.33E-03	1.41E-02	4.37E-02
99	1.64E-04	3.53E-03	1.98E-02
200	2.38E-05	9.61E-04	7.66E-03
500	4.20E-07	1.55E-04	1.95E-03

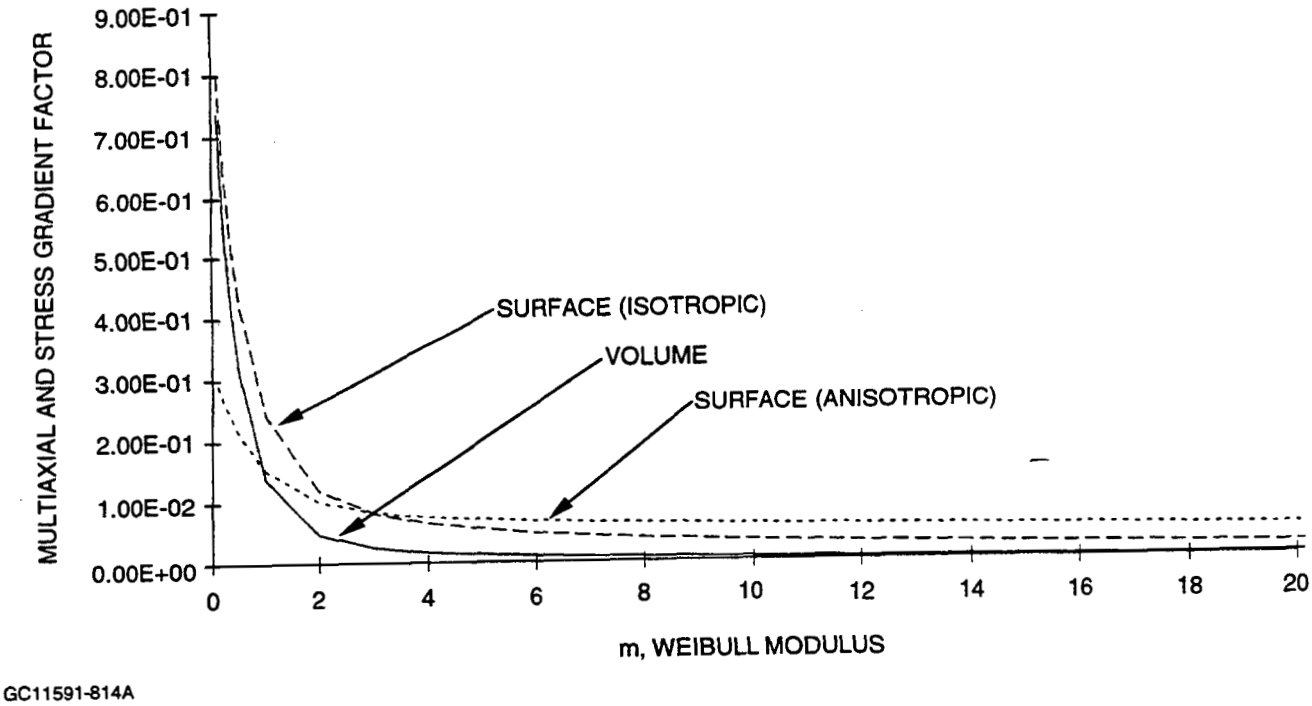

GC11591-814A

Figure VIII-7. Graphical Representation For The Data In Table VIII-6.

TABLE VIII-7. TABULAR SUMMARY OF THE ISOTROPIC MULTIAXIAL AND STRESS GRADIENT FACTOR FOR THE TENSION-TORSION SPECIMEN FOR A LOADING FACTOR OF 0.5 (TENSILE/MAX SHEAR STRESS)

WEIBULL SLOPE	VOLUME FAILURE MODE	SURFACE FAILURE MODE
0.1	4.05E-01	6.23E-01
0.2	2.68E-01	4.78E-01
0.3	1.83E-01	3.78E-01
0.4	1.27E-01	3.07E-01
0.5	9.12E-02	2.56E-01
1	2.40E-02	1.35E-01
2	5.79E-03	7.70E-02
3	2.85E-03	5.89E-02
4	1.73E-03	4.91E-02
6	8.41E-04	3.81E-02
8	4.92E-04	3.17E-02
10	3.21E-04	2.75E-02
15	1.44E-04	2.11E-02
20	7.95E-05	1.73E-02
30	3.34E-05	1.29E-02
99	1.86E-06	4.13E-03

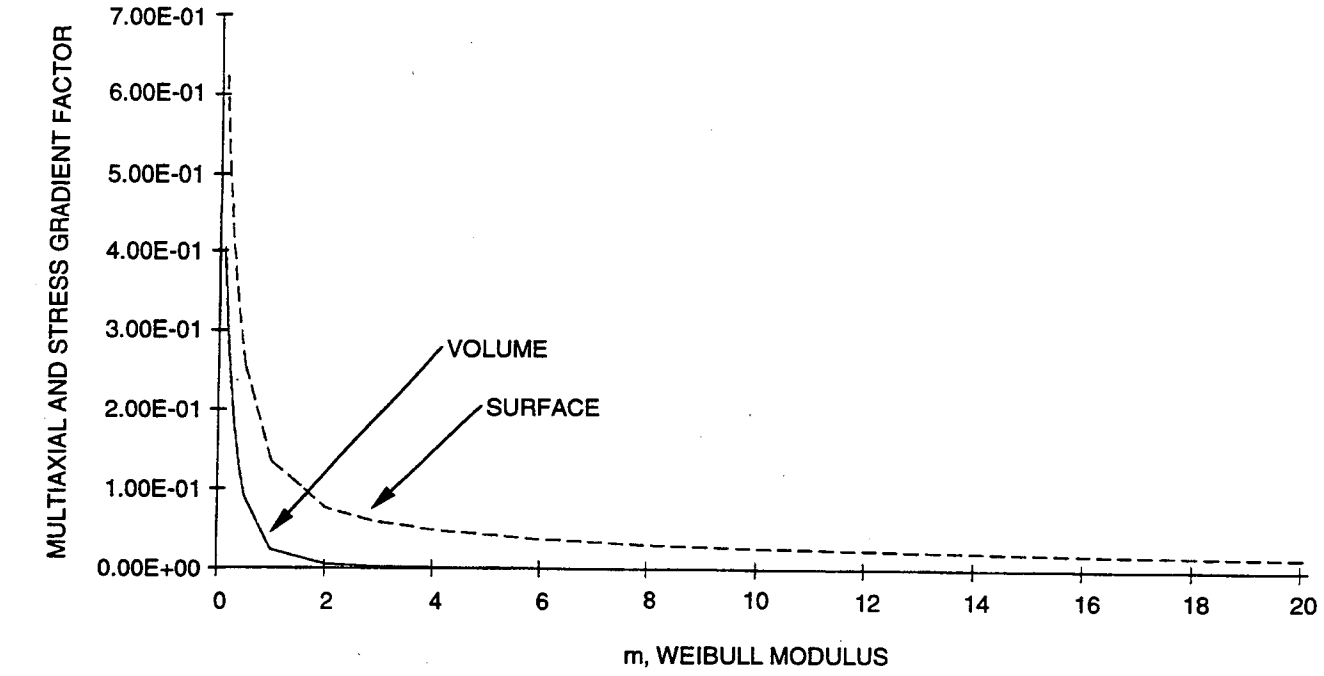

Figure VIII-8. Graphical Representation For The Data In Table VIII-7.

TABLE VIII-8. TABULAR SUMMARY OF THE ISOTROPIC MULTIAXIAL AND STRESS GRADIENT FACTOR FOR THE TENSION-TORSION SPECIMEN FOR A LOADING FACTOR OF 0.29 (TENSILE/MAX SHEAR STRESS)

WEIBULL SLOPE	VOLUME FAILURE MODE	SURFACE FAILURE MODE
0.1	3.64E-01	6.18E-01
0.2	2.35E-01	4.69E-01
0.3	1.57E-01	3.67E-01
0.4	1.08E-01	2.96E-01
0.5	7.60E-02	2.45E-01
1	1.94E-02	1.28E-01
2	4.85E-03	7.34E-02
3	2.42E-03	5.62E-02
4	1.48E-03	4.69E-02
6	7.18E-04	3.64E-02
8	4.21E-04	3.05E-02
10	2.75E-04	2.65E-02
15	1.24E-04	2.04E-02
20	6.88E-05	1.69E-02
30	2.92E-05	1.27E-02
99	1.73E-06	4.35E-03

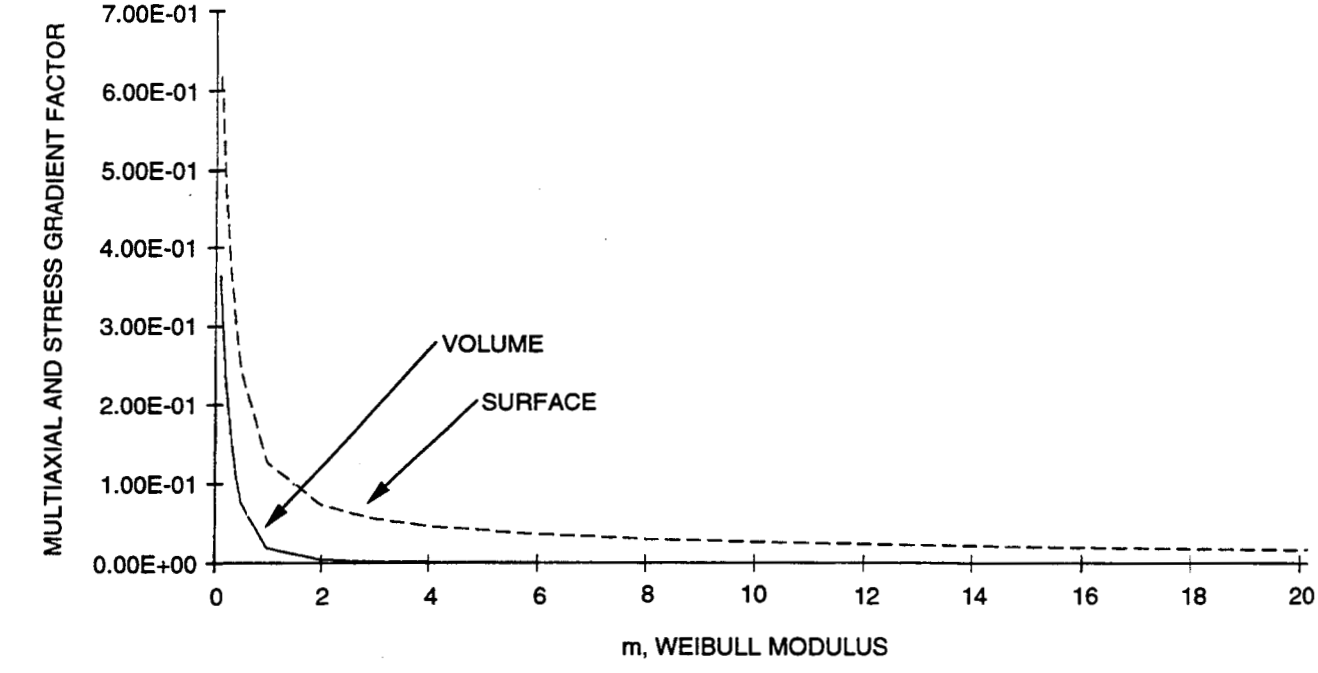

Figure VIII-9. Graphical Representation For The Data In Table VIII-8.

TABLE VIII-9. TABULAR SUMMARY OF THE ISOTROPIC MULTIAXIAL AND STRESS GRADIENT FACTOR FOR THE TENSION-TORSION SPECIMEN FOR A LOADING FACTOR OF 0.13 (TENSILE/MAX SHEAR STRESS)

WEIBULL SLOPE	VOLUME FAILURE MODE	SURFACE FAILURE MODE
0.1	3.23E-01	6.09E-01
0.2	2.03E-01	4.56E-01
0.3	1.33E-01	3.54E-01
0.4	8.94E-02	2.83E-01
0.5	6.23E-02	2.33E-01
1	1.58E-02	1.21E-01
2	4.20E-03	7.00E-02
3	2.13E-03	5.38E-02
4	1.31E-03	4.50E-02
6	6.37E-04	3.51E-02
8	3.74E-04	2.94E-02
10	2.45E-04	2.57E-02
15	1.11E-04	1.99E-02
20	6.18E-05	1.65E-02
30	2.64E-05	1.26E-02
99	1.67E-06	4.59E-03

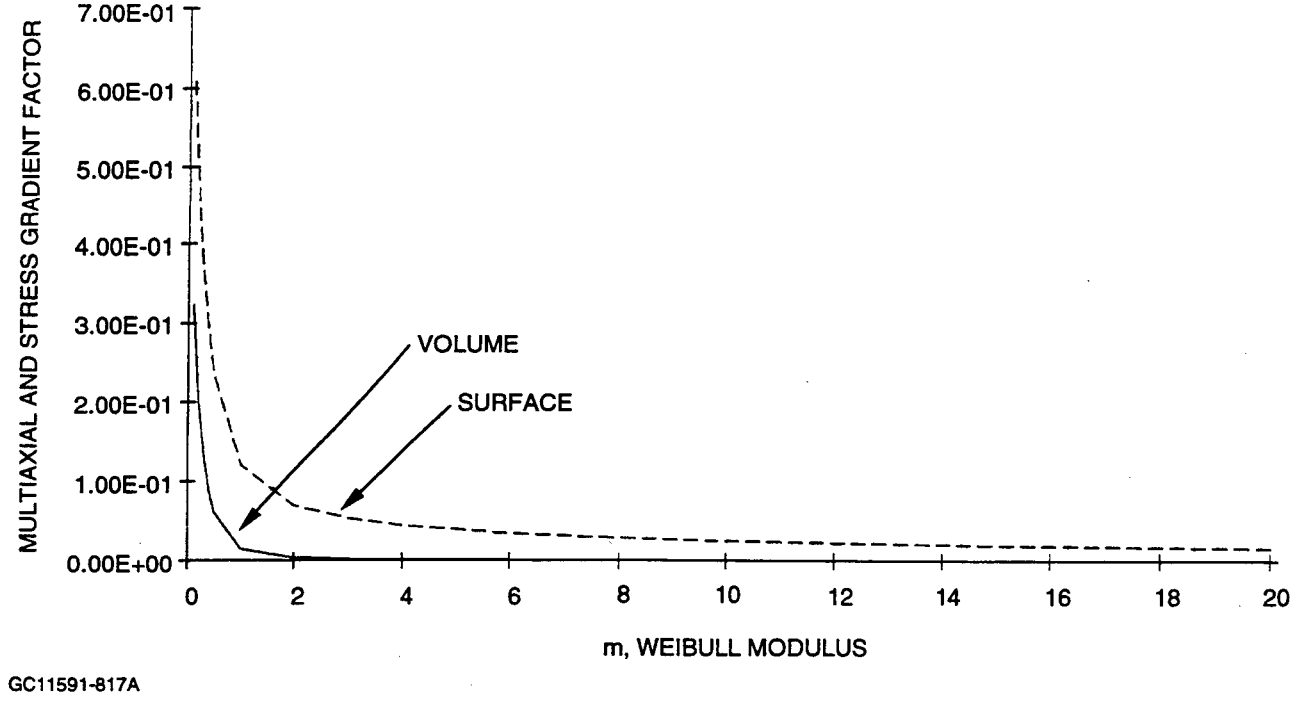

Figure VIII-10. Graphical Representation For The Data In Table VIII-9.

TABLE VIII-10. TABULAR SUMMARY OF THE ISOTROPIC MULTIAXIAL AND STRESS GRADIENT FACTOR FOR THE TENSION-TORSION SPECIMEN IN PURE TORSION

WEIBULL SLOPE	VOLUME FAILURE MODE	SURFACE FAILUR MODE
0.1	2.88E-01	5.92E-01
0.2	1.76E-01	4.34E-01
0.3	1.12E-01	3.33E-01
0.4	7.41E-02	2.64E-01
0.5	5.11E-02	2.17E-01
1	1.32E-02	1.13E-01
2	3.74E-03	6.69E-02
3	1.92E-03	5.18E-02
4	1.18E-03	4.34E-02
6	5.77E-04	3.40E-02
8	3.40E-04	2.86E-02
10	2.23E-04	2.50E-02
15	1.01E-04	1.95E-02
20	5.67E-05	1.62E-02
30	2.45E-05	1.24E-02
99	1.64E-06	4.75E-03

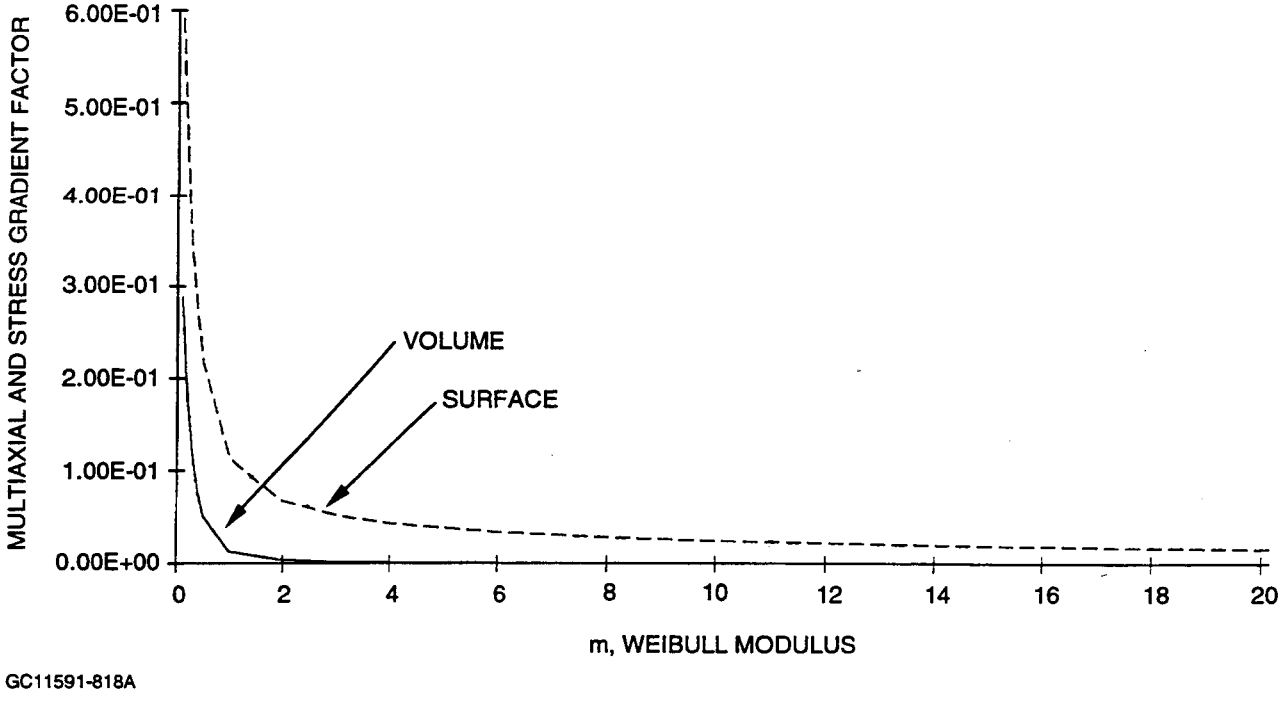

Figure VIII-11. Graphical Representation For The Data In Table VIII-10.

TABLE VIII-11. TABULAR SUMMARY OF THE MULTIAXIAL AND STRESS GRADIENT FACTORS FOR THE NOTCHED SPECIMENS. THE SURFACE FACTOR IS CALCULATED ASSUMING AN ANISOTROPIC FLAW POPULATION IN THE TRANSVERSE DIRECTION. THE AREA IS THAT IN THE NOTCH REGION ONLY

	SURFACE FAILURE		VOLUME FAILURE	
MODULUS	SHALLOW NOTCH	DEEP NOTCH	SHALLOW NOTCH	DEEP NOTCH
(SIZE)	3.736 in^2	8.426 in^2	0.667 in^3	0.966 in^3
0.5	1.33E-01	1.10E-01	2.43E-01	1.80E-01
1	5.63E-02	4.06E-02	8.45E-02	4.49E-02
3	3.18E-03	1.99E-03	5.08E-03	4.94E-04
5	1.34E-03	1.05E-03	8.20E-04	3.08E-05
7	1.13E-03	8.80E-04	1.78E-04	8.56E-06
8	1.06E-03	8.24E-04	8.72E-05	5.63E-06
9	1.01E-03	7.78E-04	4.39E-05	3.98E-06
10	9.68E-04	7.39E-04	2.27E-05	2.95E-06
11	9.29E-04	7.05E-04	1.21E-05	2.27E-06
12	8.95E-04	6.76E-04	6.65E-06	1.80E-06
13	8.64E-04	6.50E-04	3.83E-06	1.46E-06
14	8.37E-04	6.26E-04	2.32E-06	1.20E-06
15	8.13E-04	6.05E-04	1.50E-06	1.01E-06
16	7.90E-04	5.86E-04	1.03E-06	8.54E-07
18	7.51E-04	5.53E-04	5.88E-07	6.33E-07
20	7.18E-04	5.25E-04	4.00E-07	4.85E-07
25	6.53E-04	4.70E-04	2.15E-07	2.77E-07
30	6.05E-04	4.29E-04	1.36E-07	1.74E-07
40	5.37E-04	3.71E-04	6.46E-08	8.13E-08
50	4.92E-04	3.32E-04	3.45E-08	4.30E-08

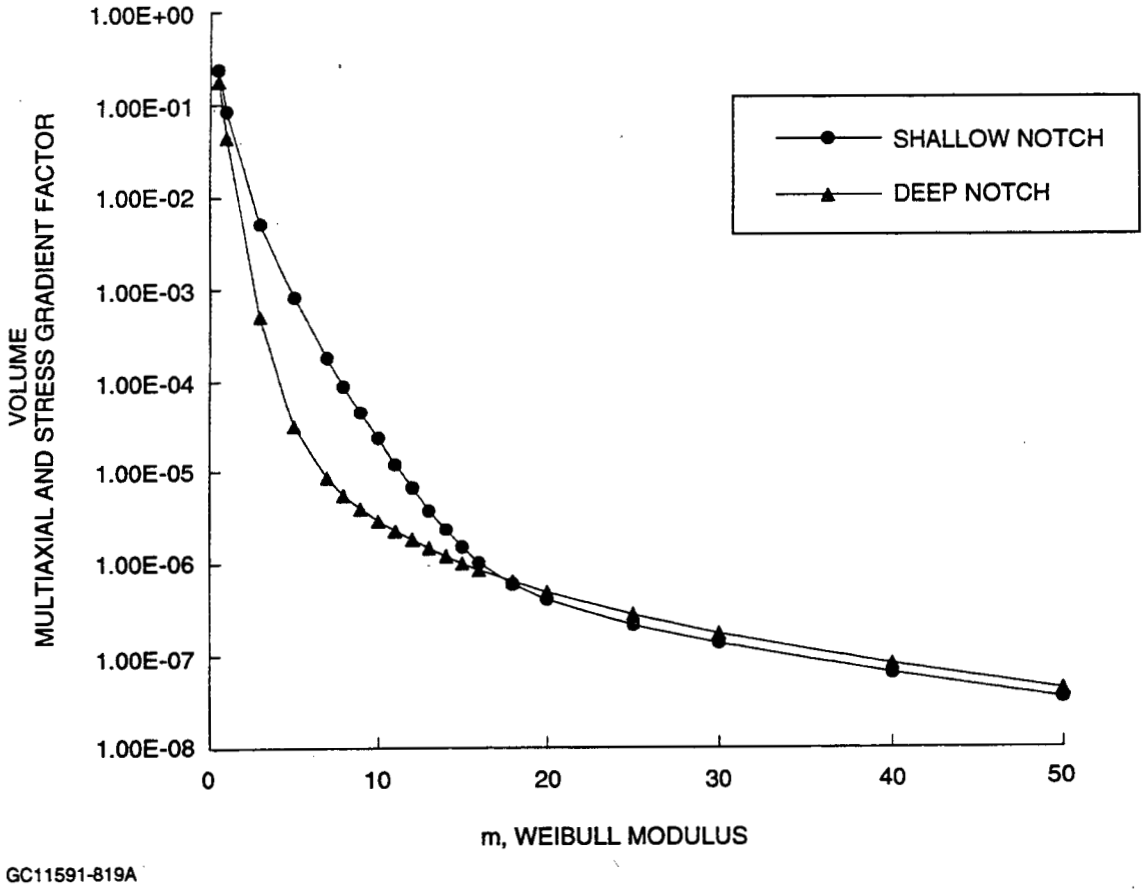

Figure VIII-12. Graphical Representation Of The Data In Table VIII-11.

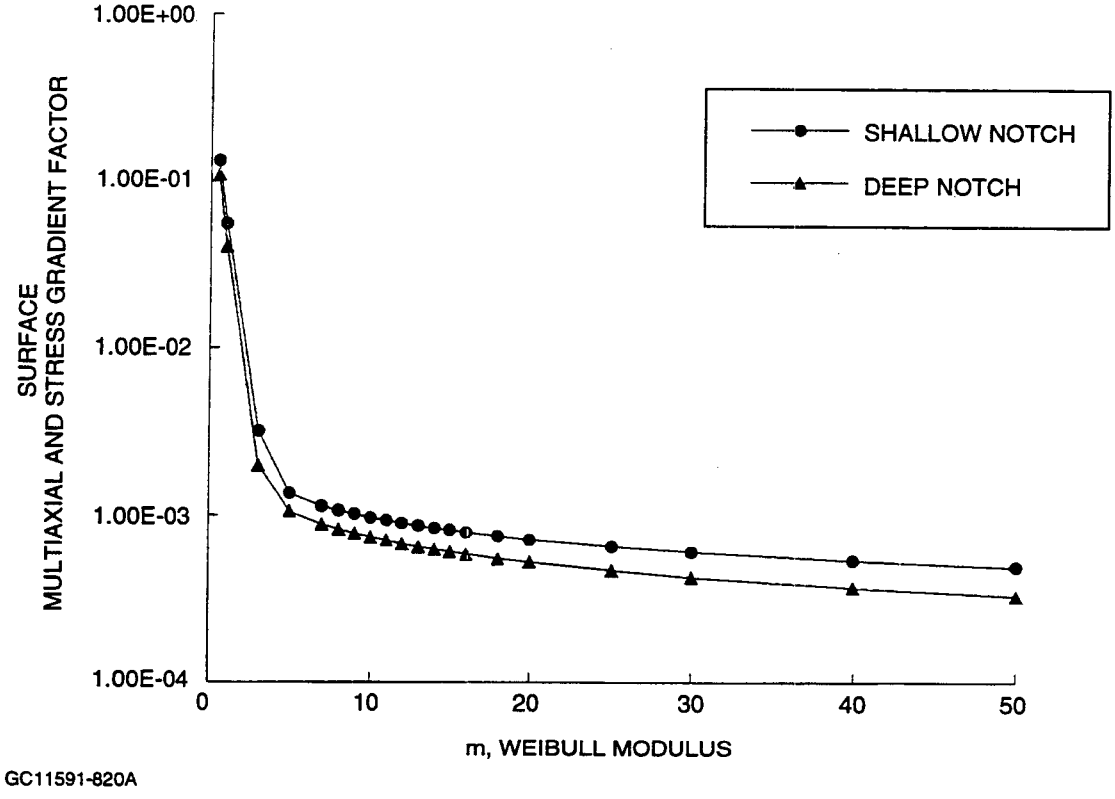

Figure VIII-13. Graphical Representation Of The Data In Table VIII-11.

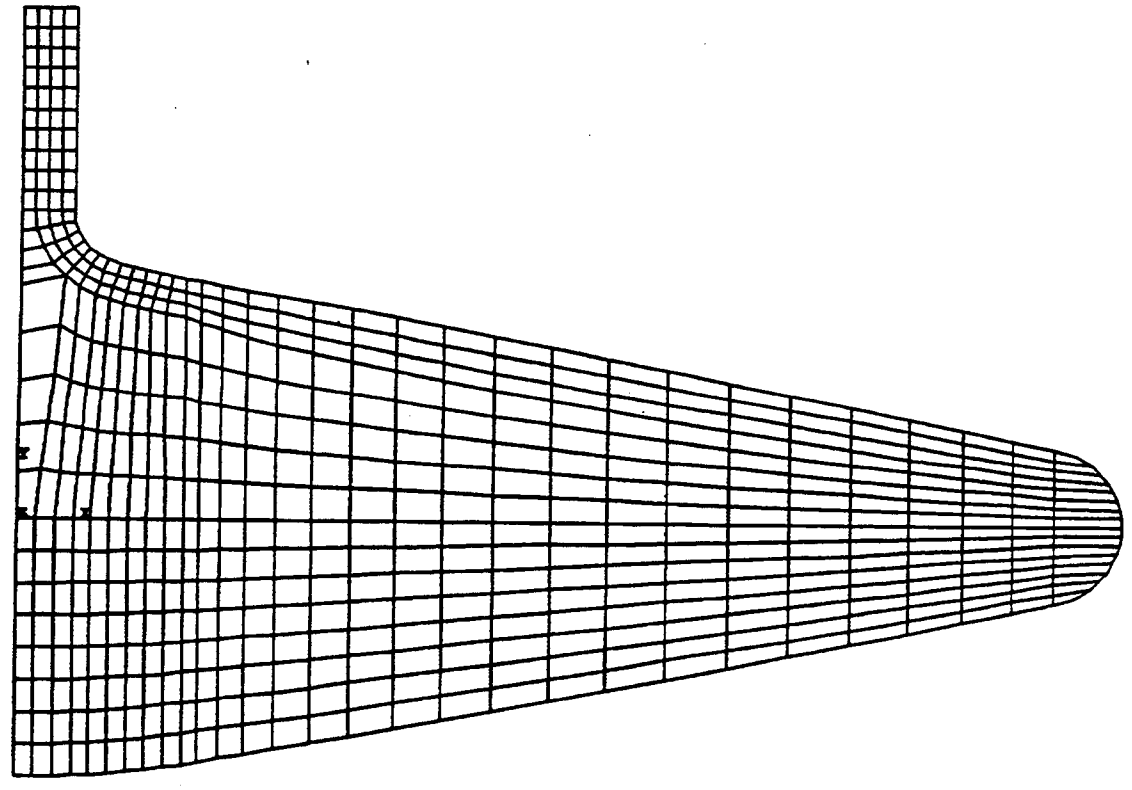

GC11591-821

Figure VIII-14. Finite Element Model For The Spin Disk. The Stress Distribution Is Given In Section 5.4.3.

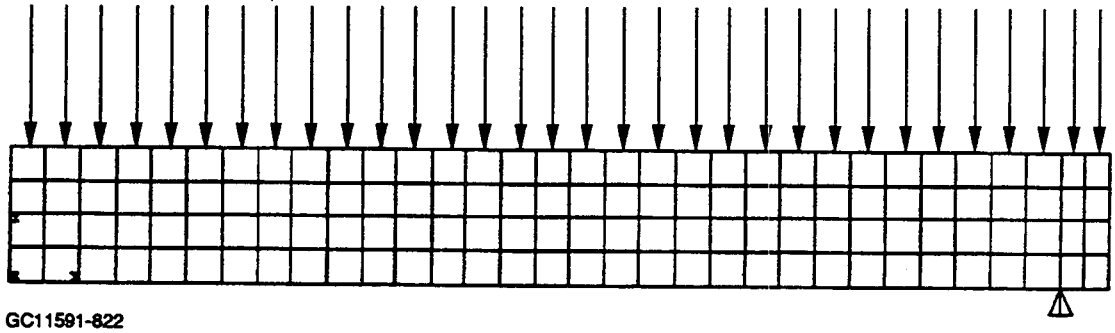

Figure VIII-15. Finite Element Model For The Plate Bending Specimen. The Boundary Conditions Used For This Specimen Are Also Presented.

A = 152.808
B = 1080
C = 2007
D = 2934
E = 3861
F = 4788
G = 5715
H = 6643
MX = 7106

GC11591-823

Figure VIII-16. Maximum Principal Stress Distribution For The Plate Bending Specimen.

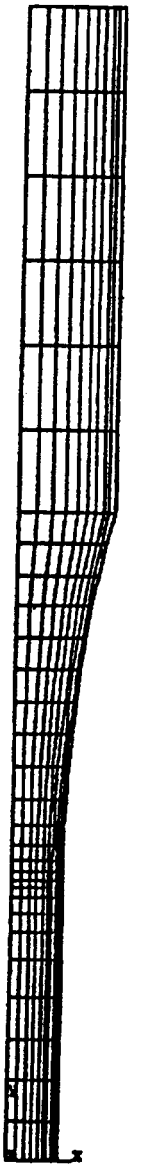

GC11591-824

Figure VIII-17. Finite Element Model For The ORNL Tensile Specimen (Buttonhead Not Modeled) Load Applied Via Distributed Pressure At The Top Of The Specimen.

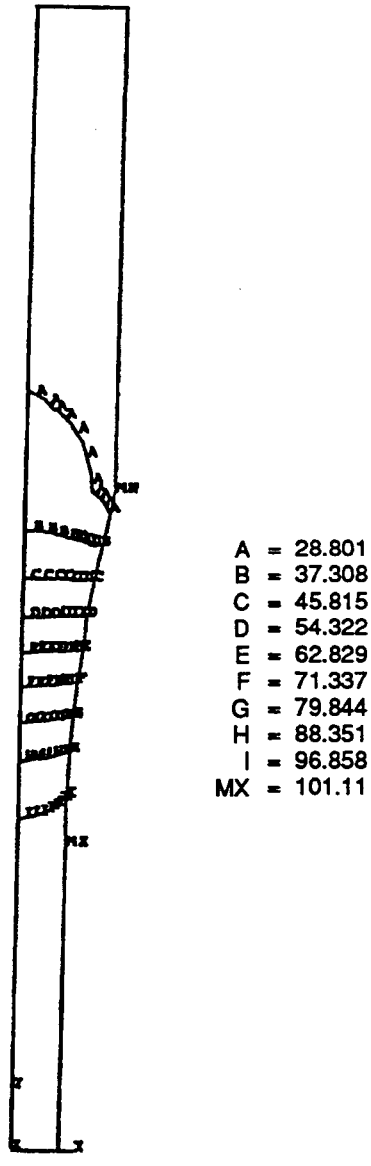

Figure VIII-18. Maximum Principal Stress Distribution In The ORNL Tensile Specimen. Average Maximum Principal Stress In The Gage Section = 100.

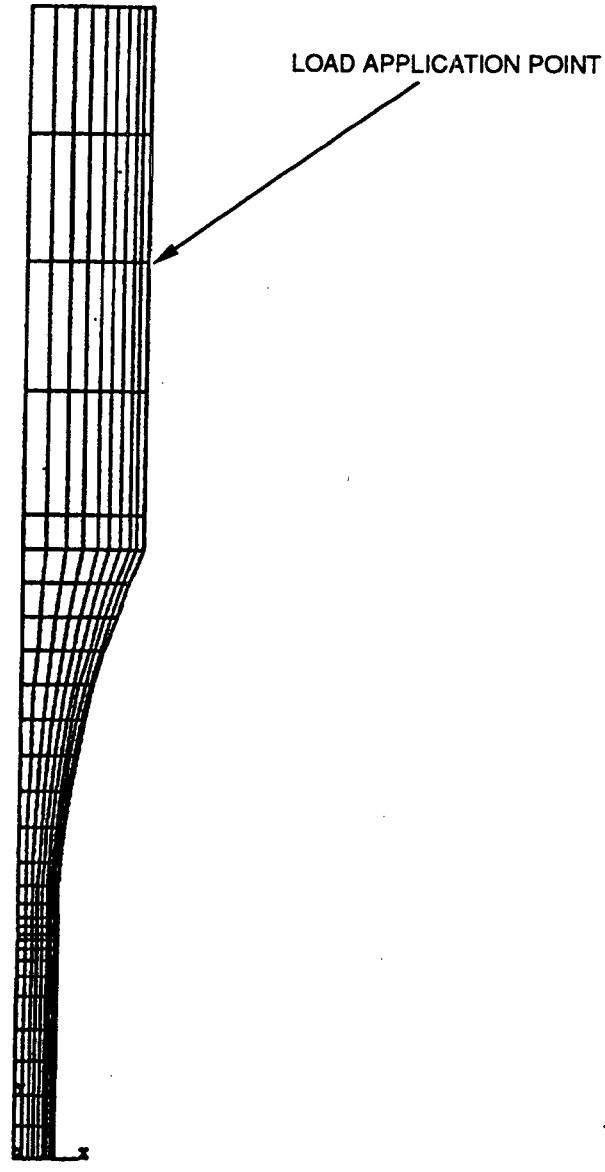

Figure VIII-19. Finite Element Model For The Tension-Torsion Specimens. Tensile Load And Torque Applied Via Concentrated Loads At Locations Indicated.

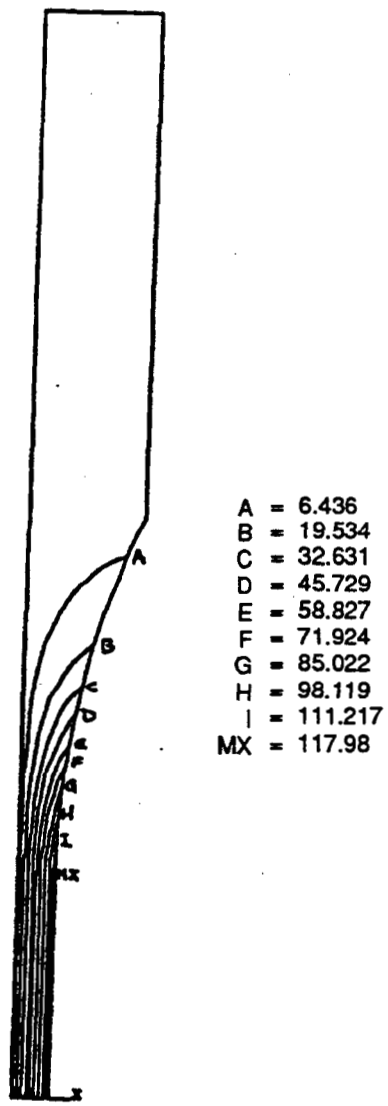

Figure VIII-20. Maximum Principal Stress Distribution In Specimen 9 At Failure. Specimen Was Loaded In Pure Torsion.

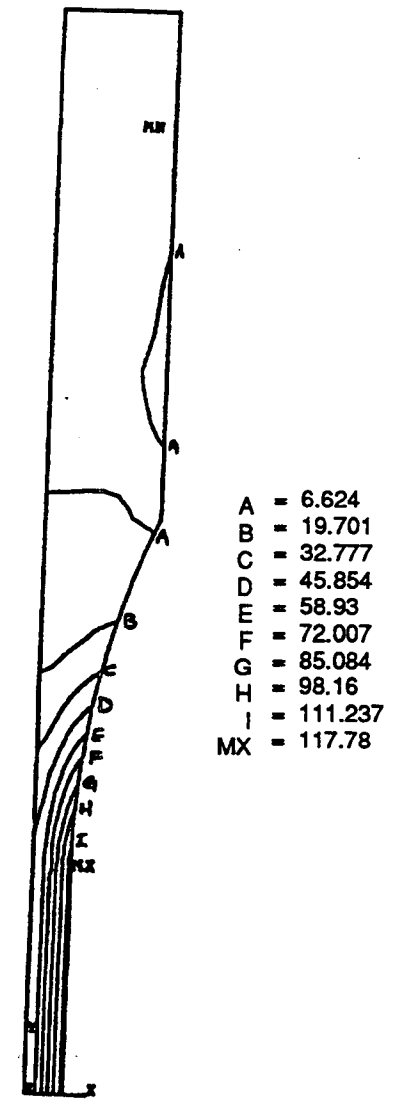

Figure VIII-21. **Maximum Principal Stress Distribution In Specimen 15 At Failure. Specimen Was Loaded In Axial Tension And Torsion, Nominal Tensile Stress To Shear Stress Ratio = 0.5 At Gage Section Surface.**

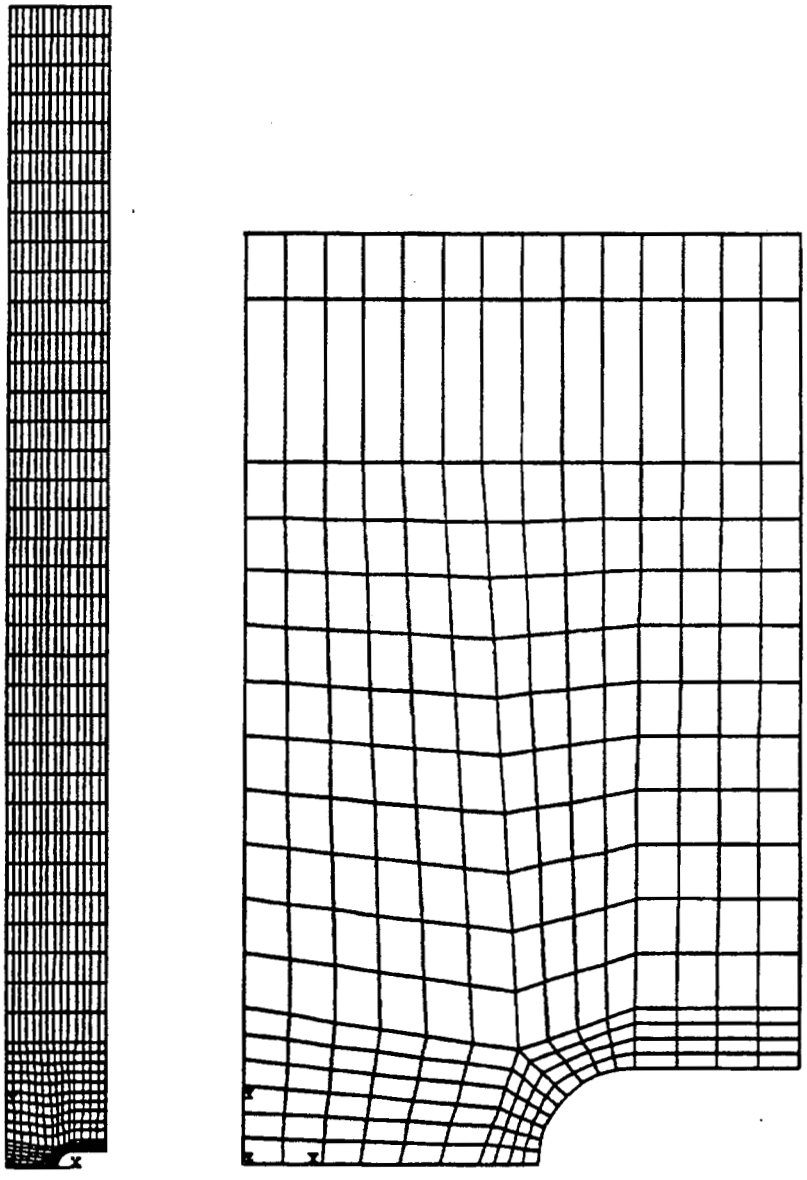

Figure VIII-22. Finite Element Model For The Deep Notch Tensile Specimen (Stress Distributions Are Shown In Section 5.4.1.1).

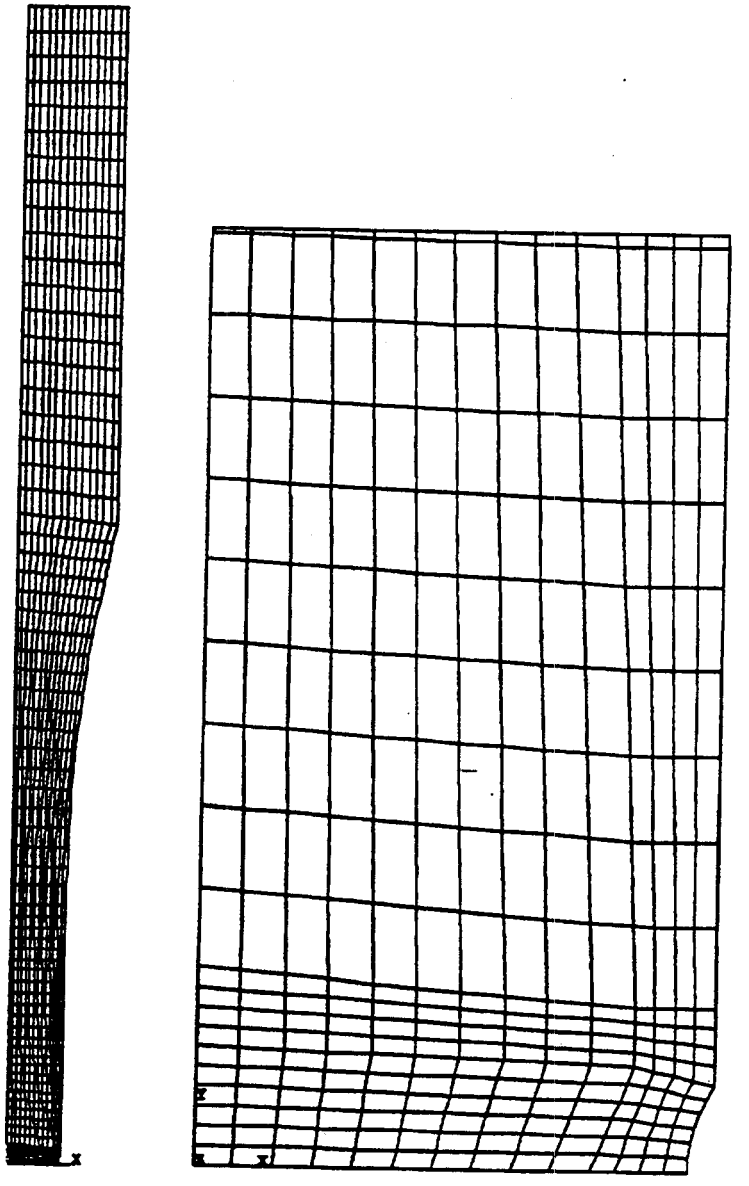

Figure VIII-23. Finite Element Model For The Shallow Notch Tensile Specimen (Stress Distributions Are Shown In Section 5.4.1.1).

REFERENCES - APPENDIX VIII

(VIII-1) Tucker, W.T., and Johnson, C.A., "The Multiaxial Equivalent of Stresses Volume," Life Prediction Methodologies and Data for Ceramic Materials. ASTM Stp 1201, C.R. Brinkman, and S.F. Duffy, Eds., American Society for Testing and Materials, Philadelphia, 1993.

(VIII-2) Lamon, J., and Evans, A.G., "Statistical Analysis of Bending Strengths for Brittle Solids: A Multiaxial Fracture Problem," J. Am. Ceram. Soc., 66, 3, 177-182, 1983.

(VIII-3) Batdorf, S.B., and Heinisch, H.L., " Weakest Link Theory Reformulated for Arbitrary Fracture Criterion," J. Am. Ceram. Soc., 61, 7-8, 355-358, 1978.

(VIII-4) Nemeth, N.N., Manderscheid, J.M., and Gyekenyesi, J.P., "Ceramic Analysis and Reliability Evaluation of Structures (CARES): Users and Programmers Manual," NASA TP 2916, August 1990.

INTERNAL DISTRIBUTION

Central Research Library (2)
Document Reference Section
Laboratory Records Department (2)
Laboratory Records, ORNL RC
ORNL Patent Section
M&C Records Office (3)
C. R. Brinkman
S. A. David
M. K. Ferber
D. R. Johnson (5)
M. A. Karnitz
K. C. Liu
R. W. McClung
V. J. Tennery
S. G. Winslow

EXTERNAL DISTRIBUTION

James H. Adair
University of Florida
Materials Science & Engineering
317 MAE Bldg.
Gainesville, FL 32611-2066

Mufit Akinc
Iowa State University
322 Spedding Hall
Ames, IA 50011

Norman C. Anderson
Ceradyne, Inc.
Ceramic-to-Metal Division
3169 Redhill Avenue
Costa Mesa, CA 92626

Frank Armatis
3M Company
Building 60-1N-01
St. Paul, MN 55144-1000

Everett B. Arnold
Detroit Diesel Corporation
Mechanical Systems Technology
13400 Outer Drive West
Detroit, MI 48239-4001

Dennis Assanis
University of Illinois
Dept. of Mechanical Engineering
1206 W. Green Street
Urbana, IL 61801

John M. Bailey
Consultant
Caterpillar, Inc.
P.O. Box 1875
Peoria, IL 61656-1875

B. P. Bandyopadhyay
ELID Team
Wako Campus
2-1 Hirosawa Wako-shi
Saitama 351-01
JAPAN

David L. Baty
Babcock & Wilcox - LRC
P.O. Box 11165
Lynchburg, VA 24506-1165

M. Brad Beardsley
Caterpillar Inc.
Technical Center Bldg. E
P.O. Box 1875
Peoria, IL 61656-1875

Larry D. Bentsen
BFGoodrich Company
R&D Center
9921 Brecksville Road
Brecksville, OH 44141

Tom Bernecki
Northwestern University
1801 Maple Avenue
Evanston, IL 60201-3135

Bruce Boardman
Deere and Company Technical Ctr.
3300 River Drive
Moline, IL 61265

Steven C. Boyce
Air Force Office of Scientific Research
AFOSR/NA Bldg. 410
Bolling AFB, DC 20332-6448

P. Brehm (5)
AlliedSignal Engines
2739 E. Washington Street
P.O. Box 52180
Phoenix, AZ 85072-2180

Sherman D. Brown
University of Illinois
Materials Science and Engineering
105 South Goodwin Avenue
Urbana, IL 61801

Roger Cannon
Rutgers University
P.O. Box 909
Piscataway, NJ 08855-0909

David Carruthers
Kyocera Industrial Ceramics Company
P.O. Box 2279
Vancouver, WA 98668-2279

James D. Cawley
Case Western Reserve University
Materials Science & Engineering
Cleveland, OH 44106

Nam S. Chang
Chrysler Corporation
12000 Chrysler Drive
Highland Park, MI 48288-0001

Gary M. Crosbie
Ford Motor Company
20000 Rotunda Drive
MD-2313, SRL Building
Dearborn, MI 48121-2053

J. C. Cuccio (5)
AlliedSignal Engines
2739 E. Washington Street
P.O. Box 52180, MS:1302-2Q
Phoenix, AZ 85072-2180

Bill Durako
Sundstrand Aviation Operations
P.O. Box 7002
Rockford, IL 61125-7002

J. J. Eberhardt
U.S. Department of Energy
Office of Transportation Matrl's
CE-34, Forrestal Building
Washington, DC 20585

H. T. Fang (5)
AlliedSignal Engines
2739 E. Washington Street
P.O. Box 52180
Phoenix, AZ 85072-2180

J. P. Gallagher
University of Dayton Research Institute
300 College Park, JPC-250
Dayton, OH 45469-0120

Stephen T. Gonczy
Allied Signal Research
P.O. Box 5016
Des Plaines, IL 60017

Robert J. Gottschall
U.S. Department of Energy
ER-131, MS:G-236
Washington, DC 20585

Thomas J. Gross
U.S. Department of Energy
Transportation Technologies
CE-30, Forrestal Building
Washington, DC 20585

John P. Gyekenyesi
NASA Lewis Research Center
21000 Brookpark Road, MS:6-1
Cleveland, OH 44135

J. Hartman (5)
AlliedSignal Engines
2739 E. Washington Street
P.O. Box 52180
Phoenix, AZ 85072-2180

Thomas P. Herbell
NASA Lewis Research Center
21000 Brookpark Road, MS:49-3
Cleveland, OH 44135

Osama Jadaan
U. of Wisconsin-Platteville
1 University Plaza
Platteville, WI 53818

Curtis A. Johnson
General Electric Company
P.O. Box 8
Schenectady, NY 12301

Martha R. Kass
U.S. Department of Energy
Oak Ridge Operations
Building 4500N, MS:6269
Oak Ridge, TN 37831-6269

Pramod K. Khandelwal
General Motors Corporation
Allison Gas Turbine Division
P.O. Box 420, MS:W05
Indianapolis, IN 46206

James W. McCauley
Alfred University
Binns-Merrill Hall
Alfred, NY 14802

W. Meade (5)
AlliedSignal Engines
2739 E. Washington Street
P.O. Box 52180
Phoenix, AZ 85072-2180

M. N. Menon (5)
AlliedSignal Engines
2739 E. Washington Street
P.O. Box 52180
Phoenix, AZ 85072-2180

Ken Michaels
Chrysler Motors Corporation
P.O. Box 1118, CIMS:418-17-09
Detroit, MI 48288

A. Peralta (5)
AlliedSignal Engines
2739 E. Washington Street
P.O. Box 52180
Phoenix, AZ 85072-2180

John J. Petrovic
Los Alamos National Laboratory
Group MST-4, MS:G771
Los Alamos, NM 87545

George Quinn
NIST
Ceramics Division, Bldg. 223
Gaithersburg, MD 20899

Maxine L. Savitz
AlliedSignal, Inc.
Ceramic Components
P.O. Box 2960, MS:T21
Torrance, CA 90509-2960

Robert B. Schulz
U.S. Department of Energy
Office of Transportation Matrls.
CE-34, Forrestal Building
Washington, DC 20585

Dinesh K. Shetty
University of Utah
Materials Science and
Engineering
Salt Lake City, UT 84112

Jay R. Smyth
AlliedSignal Engines
111 S. 34th Street, MS:503-412
Phoenix, AZ 85034

J. Z. Song (5)
AlliedSignal Engines
2739 E. Washington Street
P.O. Box 52180
Phoenix, AZ 85072-2180

T. Strangman (5)
AlliedSignal Engines
2739 E. Washington Street
P.O. Box 52180
Phoenix, AZ 85072-2180

Thomas N. Strom
NASA Lewis Research Center
21000 Brookpark Road, MS:86-6
Cleveland, OH 44135

Janet Wade (5)
AlliedSignal Engines
P.O. Box 52180, MS:1303-2
Phoenix, AZ 85072-2180

Thomas J. Whalen
Ford Motor Company
SRL Bldg., Mail Drop 2313
P.O. Box 2053
Dearborn, MI 48121-2053

Sheldon M. Wiederhorn
NIST
Building 223, Room A329
Gaithersburg, MD 20899

J. M. Wimmer (5)
Supervisor
AlliedSignal Engines
2739 E. Washington Street
P.O. Box 52180, MS:1302-2P
Phoenix, AZ 85072-2180

D. C. Wu (5)
AlliedSignal Engines
2739 E. Washington Street
P.O. Box 52180
Phoenix, AZ 85072-2180

Department of Energy
Oak Ridge Operations Office
Asst. Manager for Energy
Research and Development
P.O. Box 2001
Oak Ridge, TN 37831-8600

Department of Energy
Office of Scientific and
Technical Information
Office of Information Services
P.O. Box 62
Oak Ridge, TN 37831